CRANFIELD UNIVERSITY

Luis Gallar

Gas Turbine Shaft Over-speed / Failure Performance Modelling

Aero/Thermodynamics Modelling and Overall Engine System Response

School of Engineering

Ph. D. Thesis

SCHOOL OF ENGINEERING
DEPARTMENT OF POWER AND PROPULSION

Full time Ph. D.

Academic Year 2007- 2010

Luis Gallar

Gas Turbine Shaft Over-speed / Failure Performance Modelling

Aero/Thermodynamics Modelling and Overall Engine System Response

Academic supervisors: V. Pachidis, R. Singh
Industrial advisors: A. Rowe, S. Brown

October 2010

This thesis is submitted in partial fulfilment of the requirements for the degree of Doctor of Philosophy

Executive summary

A gas turbine engine can over-speed due to various reasons, including shaft failure, variable geometry mal-schedule or fuel system malfunction. In any case, engine manufacturers are required to demonstrate that a shaft over-speed event will not result in an uncontained failure with high energy debris being released from the engine.

Although the certification authority can be satisfied that the engine is shaft failure safe by conducting large scale tests, a purely experimental approach would be very complex and expensive. Moreover, today's poor understanding of the event leads to conservative designs that exert unavoidable penalties on the engine performance and weight. It is in this context that the need for an analytical approach and small scale testing arises to model the progression of the event.

This work is part of a wider long term research collaboration between Cranfield University and Rolls-Royce that attempts to enhance today's modelling capability of gas turbine shaft over-speed/failure events. The final aim of the project is the development of a generic advanced performance prediction tool able to account for all the complex and heavily interrelated phenomena to ascertain the terminal speed of the over-speeding turbine. This multidisciplinary "all in one" tool will allow to include the shaft failure scenario early into the design process and eliminate current conservative design approaches while maintaining the high standard of airworthiness required for certification.

This thesis focuses on the aerothermal performance modelling of turbomachinery components at the extreme off-design conditions experienced during a shaft over-speed event. In particular, novel modelling techniques and methodologies at the forefront of knowledge have been developed to simulate the performance of turbine vanes at high negative incidence angles, derive the extended compressor characteristics in reverse flow and calculate the response of the air system during rapid transient among others. These component models are ready to be integrated into a generic single computational tool that, once validated against engine data available from the sponsor, can be applied to different engines and scenarios.

The collaboration with Rolls-Royce provided the opportunity to conduct research on other areas related to performance engineering apart from the shaft failure modelling. The present study makes several noteworthy contributions on compressor variable geometry loss, deviation and stall modelling, compressor variable geometry schedule optimisation and on the effect of using real gas models instead of the perfect gas assumption in engine performance simulation codes.

Acknowledgments

It is only fair to acknowledge and thank a vast number of people that have contributed in many ways to this research.

Professors Singh and Pilidis provided the opportunity to conduct this research and I am grateful for the trust deposited on me.

Dr. Vassilios Pachidis supervised the project from its beginning. He provided effective guidance and constant help, and the relationship with him has inevitably evolved into a valued friendship, as it could not be otherwise.

Steve Brown, Richard Tunstall and Arthur Rowe supported the project since its inception and provided technical advice, data, knowledge and encouragement. Especially important was Arthur's contribution to my education and understanding of the performance of gas turbines and for this I am indebted to him. I can only express him my sincere admiration and gratitude for his patience.

Roy Meads faced with a grin my constant pestering. RRAP was significantly less crude and easier to understand with him seating two metres away from me. Dr. Nicholas Merriman saved me precious time by discussing the inner workings of the algorithm he developed during his doctoral studies. Steve Curzons and Tim Scanlon were always available to share their expertise and throw some light on the design and analysis of internal air systems.

Roger Sutherland and Drs. Ian Griffins, Shane Regunath and Marko Bacic were kind as to devote some of their time to outline the role of the controls system architect in the engine design.

Eric W. Lemmon lent his altruistic help and provided the otherwise impossible to fetch 1525 experimental $p-v-T$ points for air that are the basis of chapter 10.

Dr. Timoleon Kipouros provided a useful and enthusiastic insight into stochastic optimisation techniques in engineering problems. Dr. Ioannis Templalexis shared his expertise on turbomachinery design and analysis.

Professor Pablo Rodríguez de Francisco and Mariano Ayora did an impeccable job manufacturing the turbine blades for the test rig, within a very tight deadline and in a very professional manner. The success of the experimental trials is largely because of them.

Bernard Charnley made things happen in the test area. His ample hands-on expertise building experimental rigs and instrumentation proved very useful. On a personal note, he is an inexhaustible source of interesting stories, jokes and information of all sorts. I am fond of the memories of the time spent with him in Seville, Glasgow and Brussels, and I will miss such a noble person.

Aida Álvarez tried to introduce me to the world of systems integration and robust design methodologies, although perhaps not always successful due to my inability to understand anything that is not termed mathematically. Her frankness and cheerful mood made life in Derby a tad easier.

Professor José Luis Montañés and Abel Jiménez have been instrumental in my education. Their career advice, in the past and in the present, has taken me further than whatever I could have thought not so long ago. Thank you.

The staff of the department of Thermodynamics, Fluid Mechanics and Propulsion of the School of Aeronautics in Madrid lied the foundations that have enabled me to complete my doctoral studies. To this regard, Professors A. Liñán, J.J. Salvá and Á. Velázquez and Drs. E. Moreno, J.R. Arias and G. Corchero are thankfully acknowledged. Emilio Isidoro was always willing to lend a hand and is also acknowledged with thanks.

José Javier Álvarez and Óscar Córdoba provided a useful insight into the operation of internal air systems and numerical methodologies.

Óscar Sanz dug out experimental data, shared his knowledge of Fluid Mechanics and was always willing to help in his own time with nothing to gain besides my admiration and gratitude.

Scott Booden, Derek Brown and Dick Lutley did a splendid job manufacturing and putting together the cascade rig.

Rachel Smith, Sam Broe, Gillian Hargreaves and Maria Negus provided vital administrative support, words of encouragement and, in brief, took care of me. Everybody knows that administrators rule the world behind the scenes, and these four did so smoothly and beautifully.

Aerospace engineer and MSc student Manuel Arias possibly taught me more than what I taught him. I am honoured with his friendship and grateful for many disinterested favours.

Over the past three years I have had the privilege to work with some bright and devoted mechanical engineers that have contributed notably to the progress of the project. Cristina Calcagni, Guillermo Torres, Carmen Llorens, Marco D'Erasmo, Valentino Volpe, Carlos Soria, Ioannis Tzagarakis and Martino Salussolia followed my not always completely reasonable guidance and came up with original points of view that have left a distinct mark on this thesis.

Dio Antille crossed long ago the threshold of friendship and became family. His tireless, brave and hard working nature set the example to be imitated. Meeting him, his wife Jose and his mutinous son Dio is one of my greatest achievements during my time at Cranfield without a trace of doubt.

Antonio Cantarero was my flat mate during the last year of my doctoral studies, and had a fundamental role in the success of the cascade tests. I am grateful for his support and friendship.

Jesús María Blanco and Eurico Gonçalves were fine friends throughout these past four years. We shared many coffees, squash games, conversations and meals I cannot even count. Chris Binch and Wayne Mitchell managed that waking up early in the morning was not an effort but a pleasure.

María Pardo, Marcos Latorre, José María Cecilia, Antonio Sánchez and Juan Lozano are the people I long to see and spend time with whenever I manage to put more than two vacation days together. They have contributed enormously to my mental health over the course of the doctoral programme.

Finally, I owe a great deal to my family and relatives who support every single one of my harebrained ideas and choices even when they know beforehand that some are bound to backfire.

Luis Gallar

Bedford, September 2010

Contents

List of Figures

Nomenclature

Abbreviations

$AIAA$	American Institute of Aeronautics and Astronautics
ACJ	Acceptable means of compliance and interpretation
ASL	Above sea level
$ASME$	American society of mechanical engineers
BS	British standard
CAA	Civil aviation authority
CC	Combustion chamber
CFD	Computational fluid dynamics
CFL	Courant-Friedrichs-Lewis parameter
ECU	Engine control unit
EOS	Equation of state
ER	Expansion ratio
$EVI-GTI$	European virtual institute for gas turbine instrumentation
FAR	Fuel to air ratio
$FSOV$	Fuel shut off valve
GA	Genetic algorithm
HP	High pressure
HPC	High pressure compressor
HPT	High pressure turbine
IGV	Inlet guide vane
IP	Intermediate pressure
IPC	Intermediate pressure compressor
IPT	Intermediate pressure turbine
ISA	International standard atmosphere
$ISABE$	International symposium of air breathing engines
JAR	Joint aviation requirement
$l.e.$	Leading edge
LF	Low flow
LP	Low pressure

LPC	Low pressure compressor
LPT	Low pressure turbine
MF	Moderate flow
MTO	Maximum take-off conditions
$NASA$	National aeronautics and space administration
ND	Non dimensional
NGV	Nozzle guide vane
$PIWG$	Propulsion instrumentation working group
PS	Pressure surface
R	Rotor
RL	Running line
$RRAP$	Rolls-Royce aerothermal performance suite
S	Stator
SAS	Secondary air system
SFC	Specific fuel consumption
SL	Surge line
SLS	Sea level static
SM	Surge margin
SS	Suction surface
$t.e.$	Trailing edge
TET	Turbine entry temperature
UTC	University technology centre
VSV	Variable stator vane

Latin symbols

a	$m^3Kg^{-1}mol^{-1}$	Attractive EOS coefficient
A	m^2 *or* J	Area / Helmhotz function or potential
A, B, C		Raley's stalling incidence correlation constants
b	$m^6PaKg^{-2}mol^{-2}$	Covolume EOS coeffcient
B		Uncertainty bias limit
c	m	Blade chord
c_d		Drag coeffcient
c_p	$JK^{-1}Kg^{-1}$	Pressure coefficient / Specific heat coefficient at constant pressure
c_v	$JK^{-1}Kg^{-1}$	Specific heat coefficient at constant volume
C	ms^{-1}	Characteristic curve
V_x	ms^{-1}	Axial velocity
C_T		Tangential force coefficient
C_w		Mass flow coefficient
e	J	Energy
e_t	J	Total energy

F	N	Force
F_d	N	Drag force
F_N	N	Force in the normal direction
F_d	N	Drag force
G	J	Gibbs function or potential
GGC		Generalised compressibility chart
h	JKg^{-1}	Specific enthalpy
H	JKg^{-1}	Enthalpy
i	$\circ$	Incidence
k	$WK^{-1}m^{-1}$	Thermal cinductivity
k_{coeff}		Pressure loss coefficient
k_T	Pa^{-1}	Isothermal compressibility coefficient
l	m	Characteristic length
L	m	Length
m	Kgs^{-1}	Mass flow
M		Mach number / Outlet ports
n		Vortex exponent coefficient
$\vec{n}$		Surface normal vector
N	rpm	Rotational speed / Inlet ports / Number of experimental measurements
NRT	$s^{-1}K^{-0.5}$	Aerodynamic speed
p	Pa	Pressure
Pr		Prandtl number
q	Wm^{-2}	Heat input per unit area
Q	W	Heat input
r	m	Radius
R	$JK^{-1}mol^{-1}$	Riemann invariant / Blade reaction / Universal gas constant
Rg	$JK^{-1}Kg^{-1}$	Specific gas constant
Re		Reynolds number
s	$JK^{-1}Kg^{-1}$	Specific entropy
S	JK^{-1}	Entropy / Standard deviation
$S_{\bar{x}}$		Standard deviation of the mean
St		Strouhal number
t	s *or* m	Time / Blade spacing / t-student distribution parameter
td	s	Characteristic discharge time
T	K	Temperature
u	ms^{-1} *or* JKg^{-1}	Flow velocity (modulus) / Specific internal energy
U	ms^{-1} *or* J	Blade speed / Internal energy potential / Uncertainty
v	m^{-3}	Volume
v	m^3Kg^{-1}	Specific volume
V	ms^{-1} *or* m^3	Velocity / Volume

w		Riemann invariant
W	Kgs^{-1} *or* ms^{-1}	Mass flow / Relative velocity
X, Y, Z		Raley's optimum incidence correlation constants
y^+		Non dimensional distance to wall
Y		Turbine pressure loss coefficient
Z		Compressibility factor
$A_0, B_0, C_0, a, b, c,$		EOS parameters

Greek symbols

α	m^2s^{-1}*or* K^{-1}	Flow angle / Yaw angle / Thermal diffusivity / Expansion coefficient / Alpha function
β		Pitch angle / relative flow angle / blade metal angle / bias error
γ		Specific heat coefficient / Stagger angle
δ	m	Depth of penetration of the viscosity effects
δ_k		Measurement error
δ_t	m	Depth of penetration of the thermal effects
Δ		Variation
ϵ		Error tolerance
ϵ_k		Random error
η		Adiabatic efficiency
η_c		Compressor adiabatic efficiency
η_p		Politropic efficiency
η_t		Turbine efficiency variation per % NRT
Θ		Blade camber
λ	ms^{-1}	Characteristic curve / Mass flow coefficient / Proportionality constant
μ	$Kgm^{-1}s^{-1}$	Kinematic viscosity / Fraction of separated flow
ν	m^2s^{-1}	Dynamic viscosity
π		Pressure ratio
ρ	Kgm^{-3}	Density
σ	m^2	Domain surface differential element / Blade row solidity
Σ	m^2	Domain surface
τ		Characteristic non dimensional time
$\overline{\overline{\tau'}}$	$Kgs^{-2}m^{-1}$	Tensor of viscous stress
φ		Angle of rotation - IGV and VSV settings
Φ	$\frac{V_x}{U}$	Flow coefficient
Φ_v	$Kg^2s^{-3}m^{-1}$	Rayleighs dissipation function
Ψ_{tt}	$\frac{p_{t1}-p_{t2}}{1/2\rho v_1^2}$	Total to total pressure coefficient

Ψ_{ts}	$\frac{p_{t1}-p_2}{1/2\rho v_1^2}$	Total to static pressure coefficient
Ψ_{ss}	$\frac{p_1-p_2}{1/2\rho v_1^2}$	Static to static pressure coefficient
Ψ_θ	$\frac{T_{t1}-T_{t2}}{1/2\rho v_1^2}$	Total temperature coefficient
ω		Acentric factor
ω	$\frac{p_{t1}-p_{t2}}{1/2\rho v_1^2}$	Pressure loss coefficient (compressors)
Ω	s^{-1} or m^3	Rotational speed / Domain volume

Subscripts and superscripts

0	Rotor inlet absolute / Initial conditions / Conditions in a region close to the outlet of the vessel / Free stream
1	Rotor inlet relative / Inner radius / Fan inlet
18	Secondary nozzle throat
2	Rotor exit relative / Outer radius
24	Intermediate pressure compressor inlet
26	High pressure compressor inlet
3	Rotor exit absolute
32	Combustion chamber inlet
40	High pressure turbine inlet
42	Intermediate pressure turbine stator outlet
43	Intermediate pressure turbine rotor inlet
45	Low pressure turbine inlet
60	Primary nozzle inlet
80	Primary nozzle throat
c	Control volume / critical conditions
e	Exterior / ambient
i	Inlet
L	Left
n	Generic time step
o	Conditions at the outlet
p	Perfect gas / Profile
r	Reduced magnitude
R	Residual property / Right
$real$	Real gas
s	Static
sp	Semiperfect
t	Total / Conditions in the bulk of the vessel

w	In the whirl or tangential direction
x	Axial
$*$	Over-speed conditions / Critical conditions / Saturation
θ	Tangential direction

A Martín Redondo, que me enseñó a jugar al Tute, ordeñar vacas, destazar marranos, coger moras en la pala y tantas otras cosas valiosas.

Ojalá algún día sea como él.

Chapter 1

Introduction to the shaft over-speed event

1.1 Background

A shaft over-speed is any event during which any of the engine shafts reaches a speed over its design value. Potential causes of over-speed are various and can be related to shaft failure, mal-schedule of the engine variable geometry or mal-function of the fuel control system. Shaft failure events in particular result in a sudden decoupling of the compressor and turbine with no instantaneous change in the power flow. Under these conditions the turbine is likely to accelerate to high terminal speeds and result in a disc burst or blade release. Whichever the cause of the failure, the engine manufacturer needs to demonstrate to the certifying Authority that the event will be handled safely without release of highly energetic material.

The gas turbine operation at over-speed conditions remains substantially unexplored. No reference to the event can be found in the public domain and all data available is proprietary. This chapter is a qualitative introduction to the shaft over-speed/failure event of three shaft large civil turbofans. Most of the focus is put on the IP shaft failure since this is by far the most difficult case to analyse. Shaft failure events are characterised by the strong and complex interrelation existent between engine components and the dependency of the progression of the event on the particular failure and engine geometry under analysis. This substantiates the need for a detailed and thorough introductory chapter that serves as a literature review to this thesis.

Most of the content of this chapter is the fruit of numerous private conversations with engine specialists [159][22] and constitutes the current understanding of the shaft failure/over-speed event.

1.2 Engine certification

The certifying Authority must be satisfied that the engine is safe to be operated within declared limits, even in the event of component or shaft failure. For most likely failures the engine is required to attain at least 50% of the rated thrust and that such thrust can be modulated in a controlled manner. Less likely failures may result in engine run down but this must occur safely and the event must not result in the release of high energy debris or uncontrollable fires.

Appendix 1A contains the current regulations and advisory material regarding shaft failure. Besides allowed rates of failure and descriptions, two very useful comments can be extracted from it. First, the Authority can be satisfied that the engine is shaft failure safe by either running a whole scale test in a similar fashion to bird strike or fan blade off tests, or by analysis if it is claimed that the engine will be controlled by means of mechanical interaction of turbomachinery components in contact, engine surge/stall or by the activation of over-speed protection devices. Second, if the certification is to be carried out by analysis, all possible failure cases (drive arm, shaft spline coupling, stub-shaft,...) must be scrutinised on an individual basis.

Certification requirements are prone to change over time, usually to become more stringent. At the time of writing this manuscript, the Authority accepts the declaration of the failure of some components of the shaft assembly to be Extremely Remote (probability not greater than one failure per hundred million hours of operation), and allows for the engine to be certified accordingly (see Appendix 1A). Under the current certification directives the strategy to certify three spool engines is based on fuel limiting devices for LP shaft failures and surge and subsequent run down in stall for IP and HP shafts. The latter can be triggered either mechanically (initial vibration after the failure or blade tangling) or thermodynamically by the mismatch between spool speeds. However, the position of the CAA for new products has been announced to be changing shortly and the manufacturer will be required to demonstrate that the failure is contained regardless of the probability of failure of the parts. This change in legislation has a deep impact on the certification strategy because failure modes that have been cleared in the past because of their alleged low occurrence probability become the worst case scenario. To this regard, a failure of the turbine drive arm that is rated as a Extremely Remote event would leave the turbine and the compressor located both axially and radially, with low initial vibration levels to surge the engine and little or no disc friction or blade tangling available as speed limiting mechanisms. In these cases the engine must rely solely on its intrinsic thermodynamic behaviour to arrest the over-speed. This failure constitutes the worst case scenario under the new certification directives. It is evident that exhaustive modelling work is required to guarantee the engine's compliance to the new airworthiness requirements.

1.3 Shaft over-speed and shaft failures

Two types of failures can lead to a shaft over-speed event, namely control system failures and shaft breakage. The latter can occur not as a primary cause only but late in the failure event, perhaps ensuing an oil fire. In any case, there is a substantial difference between the two that arises from the location of the speed probes in the engine. The engine control obtains measures of the speed of the shafts from probes that are located on the compressor end of the shaft, typically housed in the internal gearbox. If the shaft is severed behind the location of these probes they can only read the falling speed of the compressor end of the spool, and the engine control has no notion that the turbine is over-speeding. Quite differently, control failures in which the shaft remains integral can be arrested by the activation of over-speed protection devices that shut down the fuel flow when the speed probes read values over a prescribed threshold. This is also possible because the engine's response to control system failures is milder and slower than to an instantaneous shaft breakage. Characteristic times of shaft over-speed events are of the order of hundreds of milliseconds, whereas the shaft failure develops over times around tens of milliseconds - one order of magnitude less. The characteristic times of fuel metering valve and variable geometry actuator failures are sufficiently long for the protection devices to be able to arrest the turbine within an adequate time in shaft over-speed events.

An alternative approach to this would be to install two sets of speed probes per shaft at both ends of the spool. This is relatively easy to do and is in fact done (see 1.8) on the low pressure shaft since the tail bearing housing provides an ideal location to mount the probe. For IP and HP shafts the installation of an additional turbine speed probe is rather troublesome due to the high temperatures, space available and hostile environment inside the HP/IP bearing housing, although it has been done on the IP shaft of some industrial machines.

1.4 Causes of failure

1.4.1 Control system failures

Over-speeds can arise from two types of control failures - fuel metering valve to fail open to the hard stop position or engine variable geometry commanded closed for high power settings. If the fuel system failure happens at low powers the fuel flow increases fast enough for the compressor to surge as it would do in a fuel spike test and this curtails the over-speed. On the other hand, variable geometry and fuel system malfunctions at high powers are protected against by the activation of an over-speed protection system that chops back the fuel to very low predetermined values of the fuel flow.

1.4.2 Shaft breakage

[1]The origin of a shaft failure is important in that it has decisive role in the strength of the initial vibrations induced on the engine, and this in turn in the stability of the compression system (see 1.7.1.1). To this regard it can be distinguished between “dirty” and “clean” breakages and this is discussed below. On the other hand, shaft failures can be the primary cause of failure or can result from some other primary failure later in the event sequence. The former type includes shaft resonances, fatigue, corrosion and undetected material defects and manufacturing tolerances. The latter can occur as a result of oil fires, bearing failure, spline wear due to insufficient lubrication or loose bits of other components that can trepan the turbine drive arm or sever the shaft.

Disc burst and blade release speeds are obtained from rig testing. The failure mode of a particular design is determined by the disc material; ductile discs (steel, Waspalloy) will grow significantly and are likely to release blades by spragging prior to disc burst whereas less ductile discs (Nickel based alloys) will tend to burst before releasing the blades. For the former, the blade release will leave the disc with no means of accelerating any further and hence disc burst is unlikely to happen.

---

[1] Refer to the engine cutaway attached at the back of this manuscript for an illustration of the mechanical arrangement described in this chapter.

1.4.2.1 “Clean” breaks

This type of fracture is likely to happen as a result of a fire that overheats the shaft locally, weakens it and makes it snap, leaving two clean halves (figs. 1.1 and 1.2) and causing only local damage. The failure is characterised by high initial levels of vibration that push the engine into surge. However, the initial vibrations fade away as the event progresses and the residual vibration can be sufficiently low for the compressor to be able to recover from surge.

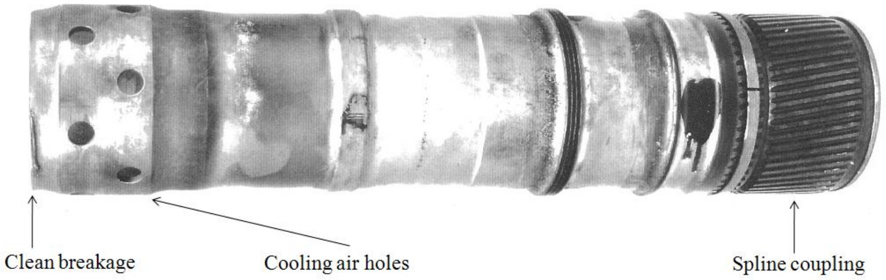

Figure 1.1: *“Clean” shaft failure - Spline coupling end. From [158]*

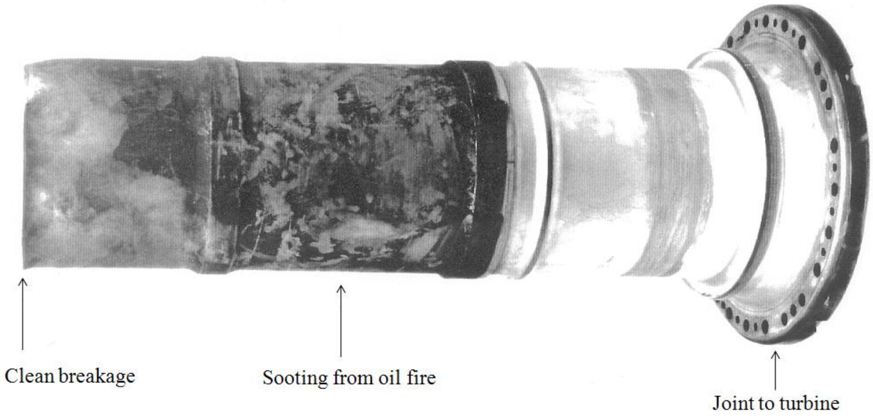

Figure 1.2: *“Clean” shaft failure - Turbine end. From [158]*

The exact location of the failure depends on the extent of the fire and the rate at which the metal heats up. To this regard, the thin sections around the cooling air holes are particularly prone to suffer this mode of failure.

Fires are susceptible of happening in bearing chambers and compartments that are lubricated by oil. If for whatever reason (oil starvation because of pipe blockage, leaks, increased friction from the bearings) the oil flow is not sufficient to evacuate the heat generated in those compartments the oil can ignite and a fire can be declared in the engine. This ignition can occur spontaneously[2] or because of a spark caused by mechanical failure. This is not likely to be a concern for the HP shaft because it is not close to oil lubricated parts. Also, if a fire breaks out in the HPC cavity the internal air system will drive it towards the engine axis to impinge on the IP shaft.

---

[2] The spontaneous ignition temperature for oil is $300^\circ - 400^\circ C$ at one atmosphere falling to $250^\circ C$ at three atmospheres.

An oil fire in the IP/HP bearing chamber can torch the IP turbine drive arm or the shaft portion downstream of the inter shaft seal leaving the compressor operating normally, axially and radially located between the front bearing and the shaft spline coupling. A fire declared in the front bearing housing can sever the IP compressor drive arm or the stub-shaft leaving the compressor unlocated. The main difference between the two is the higher vibration levels induced in the latter case that are likely to push the engine into surge.

1.4.2.2 “Dirty” breaks

Failures originated by purely mechanical causes - manufacturing defects, over-torque, acoustic, fatigue, corrosion - are likely to suffer “dirty” breaks. These fractures are characterised by a significant buckling of the shaft over a considerable extent of its length (fig. 1.3). The breakage is very violent and like clean breaks the engine surges immediately after the failure. However, high vibration levels persist throughout the event since their onset and prevent the engine from recovering from the initial surge.

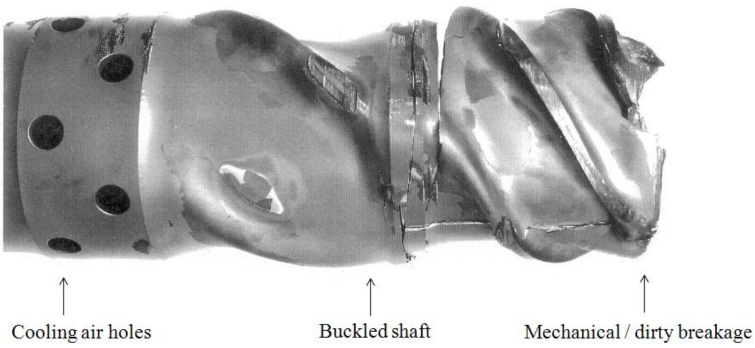

Figure 1.3: *“Dirty” shaft failure - Buckled shaft. From [158]*

1.4.2.3 The location of the shaft failure

The possible progression and outcome of a shaft failure is strongly dependent on the location of the breakage. Any shaft location must be at one position only to prevent the fight of tolerances, mechanical movement and thermal distortion. Each engine shaft is axially located on a single ball bearing whereas radial location is provided for by the ball bearings and by roller bearings located at the opposite end of the shaft. The concentric IP and LP shafts are manufactured in two separate parts that are joined together at the end of the engine assembly sequence by spline couplings secured by locking nuts. Also, IP and LP shafts can be very long and have additional branches secured by bolted flanges. All these joints introduce a play in the radial movement of the shaft and hence additional roller bearings are needed to guarantee radial location.

The progression of the event depends strongly on whether the shaft fails upstream or downstream of the thrust ball bearings. Generally speaking it can be distinguished between located and unlocated shaft failures. As a rule of thumb, failures upstream leave the turbine axially located with no possibility of blade tangling to limit the over-speed whereas failures downstream allow the turbine end of the shaft to move rearwards and collide with any downstream structure. Depending on the exact location of the breakage the amount of metal that must be ground down before blade tangling occurs may differ significantly. All the possible cases are explained thoroughly later in the chapter.

The exact location of the failure also determines the split of the shaft inertia between the turbine and the compressor ends. Modelling work carried out within the company reveals that the size of the inertias will affect the time taken to reach a determined speed, but it is the ratio of inertias between both ends that determine the actual value of the terminal speed reached. Evidently, a greater compressor to turbine inertia ratio will produce a higher terminal speed.

1.5 Engine control, bleed valves and variable geometry responses

Apart from the fuel chops activated when the engine suffers an over-speed event, there are no special measures taken by the engine control to limit the terminal speed after a shaft breakage other than the normal control logics. The reason behind this is that any limiting intervention commanded by the engine control takes too long compared to the characteristic time of the shaft failure event.

In a shaft failure the response of the control system with regard to fuel flow depends on the magnitude to which the engine is controlled. Industrial machines are controlled to HP shaft speed and after a shaft breakage demand a reduction in fuel flow that may keep the HPC out of surge. Aeroengines, on the other hand, are usually controlled to overall pressure ratio. After the severance of the drive between the turbine and the compressor the control system detects a loss of power and prompts an increase in fuel flow in an attempt to recover the commanded power setting. However, the rate at which the fuel flow can be increased is generally significantly slower than the acceleration rate of the over-speeding turbine. For these cases, running engine performance models to constant fuel flows can be an adequate assumption. However, the engine is also equipped with a topping fuel schedule that is devised to take over the fuel flow control to prevent excessive hot section temperatures when the ECU is disconnected from the engine during rapid engine malfunctions, including surge. This is typically achieved by limiting the maximum values admissible for the ratio of fuel flow upon compressor delivery pressure. Where the IPC surge is the limiting mechanism, this reduction in fuel flow would result in a lower terminal speed as fuel flow does not affect the IPC surge mechanism but does reduce the power to the turbines. Quite the contrary, for cases where the HPC surge is the limiting mechanism, a rapid reduction in fuel flow results in a higher terminal speed. This is because the vibration after the failure lowers the surge line of the HPC whereas the reduction in fuel flow lowers the running line and can keep the engine out of surge.

The response of the compressor variable geometry is characterised by a dead time followed by a travel at maximum slew rate to the closed stop position. The full travel from open to close of the variable vanes extends over around a second, and so the VSV movement lags behind during the event trying to catch up with their schedule. The impact of a mal-schedule of the variable geometry is twofold: on the one hand it lowers the IP compressor surge line; on the other it modifies the nominal IPC characteristics resulting in higher working lines during decels. The impact of a VSV mal-schedule on the IPC surge lines is geometry dependent and is generally derived by compressor tests and expressed as exchange rates. In turn, these rates can be an input to any shaft breakage performance model. On the other hand, the effect of the variable geometry mal-schedule can also be accounted for by integrating different compressor maps for a range of geometry settings into the engine performance deck.

The response of bleeds is even slower. Bleed valve operating times are of the order of several hundreds of milliseconds, and therefore have a limited impact on the outcome of the event. Opening the bleed valves make the IPC more likely to recover, whereas the contrary applies for the HPC.

1.6 High pressure shaft failures

Although simpler to analyse than IP failures, the high pressure shaft failure is potentially more dangerous than any other shaft breakage since the energy available to accelerate the relatively low inertia HP turbine assembly is greater. This is so because jet engines unchoke progressively from the rear to the front as power falls. For a typical modern engine the HPT chokes at idle, and consequently, for a constant turbine efficiency[3], operates at the same pressure and temperature ratios for any power setting. This is of paramount importance for HP spool failures, for the engine operating in rotating stall still generates considerable HP power and hence cannot be considered as a valid mechanism to arrest the over-speeding turbine safely.

Current protection against this type of failure in large civil turbofans relies on the drastic reduction of the compressor delivery pressure by means of the destruction of the compressor blading. This is achievable by designs whose HP shaft bearings are located at both ends of the shaft. In these cases any breakage leaves a considerable mass of metal off balance with no axial or radial restraint to its displacement, and as a result the compressor blading is substantially destroyed. Older engines than the RB211/Trent families may not have this design and can be at risk of a located HP failure where the failed shaft continues operation on two bearings. However, this risk is partially offset by the lower pressure ratios and ample disc capability margins characteristic of earlier designs. It is very desirable that the shaft is manufactured as a single part and that static seals, shaft spline couplings or any other design features that can lead to a located compressor after the failure must be avoided to guarantee a safe outcome to the event.

1.7 Intermediate pressure shaft failures

An IP shaft breakage is by far the most difficult shaft failure case to analyse for a number of reasons. Fuel flow chops are in the limit of being effective because the turbine remains choked longer and the power available to it is greater than in LP failures. Furthermore, the failure can be located or unlocated, and unlike HP shaft breakages it cannot be assured that the destruction of the compressor blading will arrest the over-speed. Finally, there is no proof that compressor surge will undoubtedly occur and limit the air flow through the engine.

In the early days of three shaft engines it was believed that IP shaft failures would inevitably lead to HPC surge and this would limit the over-speed. However, the understanding of the event has progressed to reveal a number of possible scenarios that do not necessarily involve compressor surge (see 1.7.2). Component behaviour and interrelation need to be accounted for; essentially, it has

---

[3] It is straightforward to demonstrate that for $\frac{W\sqrt{T}}{p} = constant$ and $\eta = constant$ then T_{outlet}/T_{inlet} and P_{outlet}/P_{inlet} across the turbine are also constant.

become clear that a greater degree of aerothermal and mechanical integration between components is required for an improved simulation of the event. Figure 1.4 and the following sections summarise the behaviour of the different engine components in an IP shaft breakage event.

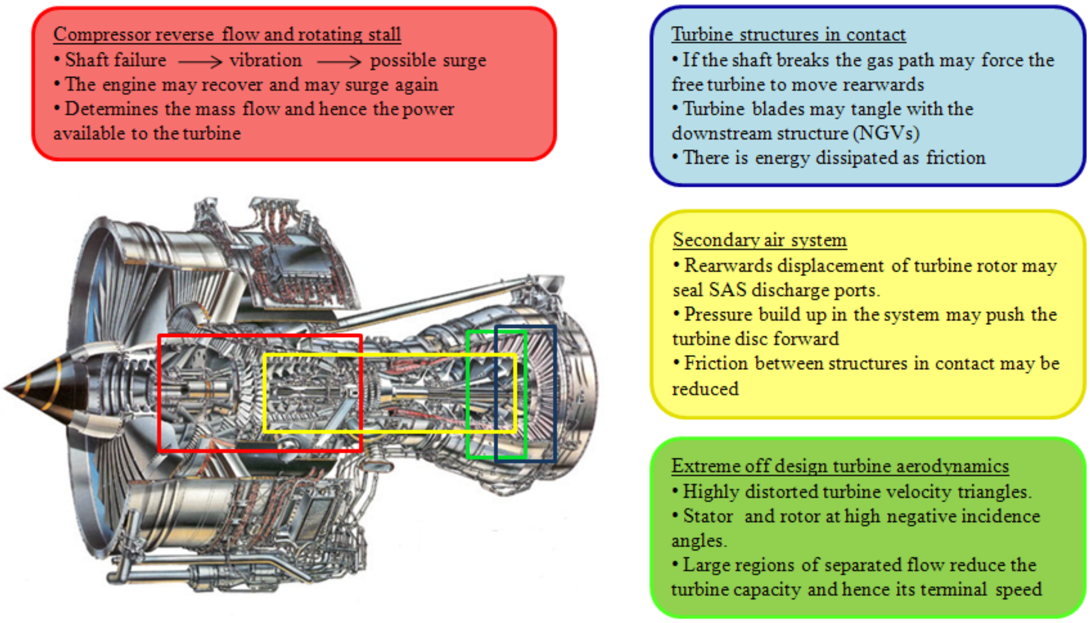

Compressor reverse flow and rotating stall
- Shaft failure ⟶ vibration ⟶ possible surge
- The engine may recover and may surge again
- Determines the mass flow and hence the power available to the turbine

Turbine structures in contact
- If the shaft breaks the gas path may force the free turbine to move rearwards
- Turbine blades may tangle with the downstream structure (NGVs)
- There is energy dissipated as friction

Secondary air system
- Rearwards displacement of turbine rotor may seal SAS discharge ports.
- Pressure build up in the system may push the turbine disc forward
- Friction between structures in contact may be reduced

Extreme off design turbine aerodynamics
- Highly distorted turbine velocity triangles.
- Stator and rotor at high negative incidence angles.
- Large regions of separated flow reduce the turbine capacity and hence its terminal speed

Figure 1.4: *Engine component behaviour during an IP shaft failure event*

1.7.1 Engine component performance during a shaft failure event

1.7.1.1 Compression system

The compressor delivery pressure (P30) is considered the principal factor influencing the outcome of an over-speed event. To this regard surge after a shaft failure is regarded as very desirable because it constitutes a very rapid means of starving the turbine of air flow. During surge the compressor delivery pressure falls exponentially to around a third of its design value. Typical surge characteristic times are of the order of 50ms - comparable with the time it takes for the turbine to reach its terminal speed. The timing of the surge inception plays a critical role in the effectiveness of surge to limit the terminal speed of the turbine. Simulations carried out by the industrial sponsor suggest that a lag of just 5ms can translate in an increase of the terminal speed of around 2.5%.

The failure of the IP shaft is in most cases violent enough to push the engine into surge (fig. 1.5). High vibrations after the rupture cause large distortions and deflections of the shaft and casings that alter compressor tip clearances significantly. In turn, compressor tip clearance changes lower the HP compressor surge line considerably allowing surge to happen. To this regard, the HP compressor is more likely to surge than the IP because it is much smaller and lighter, and hence more sensitive to vibration.

The ability of the compression system to recover from stall is determined by the residual vibration once the initial vibration has died away. It is likely that the compressor recovery line is affected by vibration in a similar fashion as the surge line is (fig. 1.5). In "dirty" breaks high

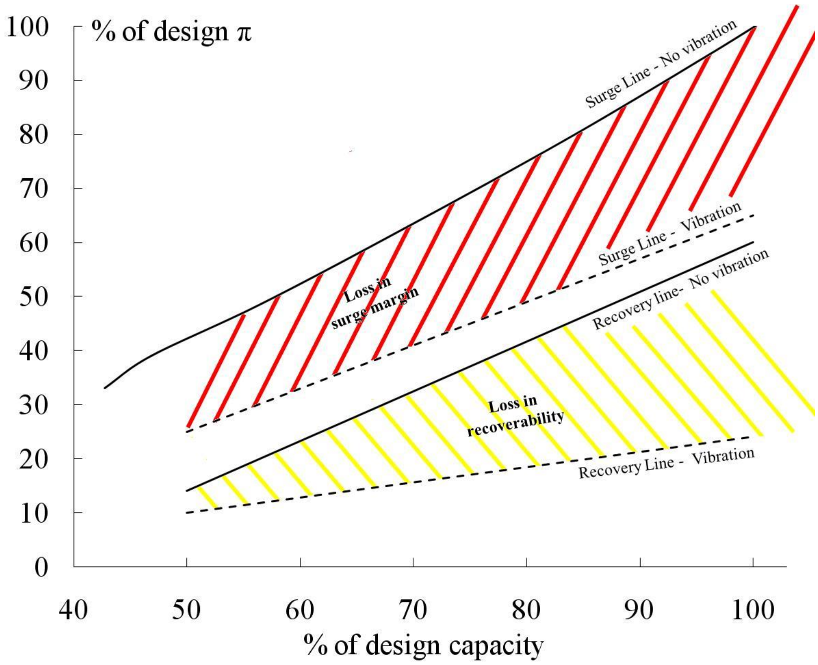

Figure 1.5: *Effect of vibration on surge and recovery lines - notional map*

vibration levels persist through the event keeping the HPC stall drop-out boundary too low for the compressor to be able to recover. In "clean" failures, however, the IP shaft can remain relatively stable, the initial vibration can decay rapidly and stall clears. The IP shaft accelerates until a second thermodynamic surge triggered by the mismatch between spool speeds or by the tangling of turbine blades occurs.

Vibration can be included in performance simulations by using exchange rates that relate vibration amplitude and frequency to tip clearance changes and these in turn to surge margin. The relation between tip clearance changes and vibration can be derived from whole engine model analyses. On the other hand, the displacement of the surge line with the change of tip clearances can be obtained from compressor rig tests. In any case, predicting the intensity of the vibrations during a particular event is something that can only rely on proprietary data extracted from previous failure events.

1.7.1.2 Turbine aerodynamics

There are two different aspects of interest related to the turbine aerodynamics during a shaft failure/over-speed event. First, there is a loss of flow capacity and efficiency associated to the highly distorted flow velocity triangles. Second, there is an increase in capacity and loss of efficiency generated by the disengagement of the blade tip seals that open the radial tip clearances. Both of these aspects are discussed below.

When a turbine disc over-speeds the velocity triangles of the rotor and any vane immediately downstream are distorted and flow angles depart to values far away from design point and opposite to the normal sense (fig. 1.6 and 1.7). As a result the flow is forced to detach from the rotor and NGV surfaces and merges into big separation bubbles and recirculation zones that offer a severely increased blockage to the flow passage (fig. 1.8). Such loss in turbine capacity throttles the upstream over-speeding turbine rotor to a lower pressure ratio, liming the speed of the shaft. On the other hand, the whirl velocity across the turbine rotor falls during the event, changes its sense and after sometime acts as a brake rather than accelerate[4]. However, it is suspected that for the incidence onto the NGV to be high enough to introduce a considerable loss in capacity not only a high spool speed is required but a reduction in axial speed as well. Therefore, the turbine capacity loss may only be a valid speed limiting mechanism if the compressor has surged. This is substantiated by the CFD and rig experiments described in chapter 4.

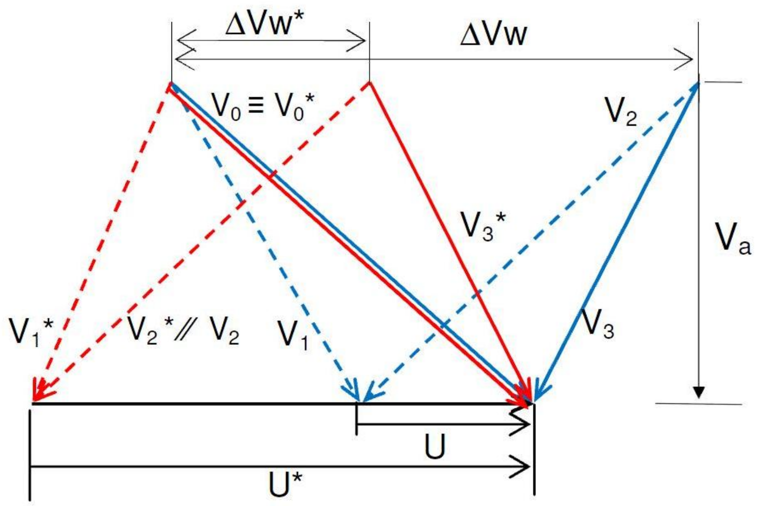

Figure 1.6: *Turbine rotor velocity triangles at nominal (blue) and over-speeding conditions close to free running speed (red)Flow velocity triangles on the turbine stator blade immediately downstream of the over-speeding rotor.*

For unlocated failures where the turbine disc is able to move rearwards the rotor blades disengage from their tip seal and tip clearances rise. Moreover, if blade tips are lost by tangling with the NGVs or by "spragging" with the casing tip clearances will also increase. As a result of the greater over tip leakage through these abnormal clearances, turbine flow efficiency deteriorates and capacity rises.

For modelling purposes and to a first order these two phenomena can be termed as a function of the flow incidence and velocity and as a function of the axial displacement respectively. The study of the loss in capacity and pressure originated by the high negative incidences is the main subject of chapter 4 whereas the capacity and efficiency changes due to tip clearance variations can be derived from experimental data available to the company.

1.7.1.3 Mechanical interaction of turbines in contact

In unlocated shaft failures the absence of axial tension in the shaft allows the IP rotor disc to slam back into any downstream structure - possibly the LP NGV platform. In particular, blade tangling can constitute an effective braking mechanism to arrest the over-speed provided it happens in a

---

[4] Euler's turbomachinery equation shows that the power extracted from a turbine rotor is proportional to the change in tangential (swirl) velocity of the fluid, Δv_θ. If the swirl velocity changes its sense the turbine brakes rather than accelerate.

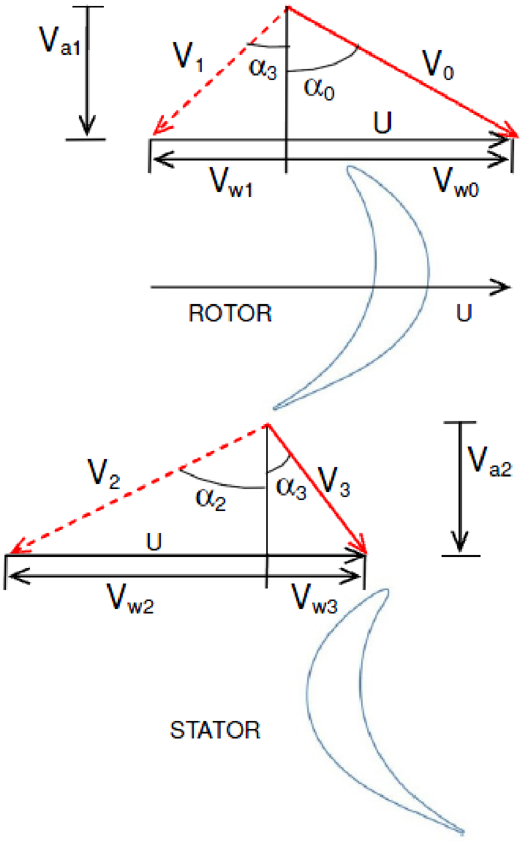

Figure 1.7: *Flow velocity triangles on the turbine stator blade immediately downstream of the over-speeding rotor.*

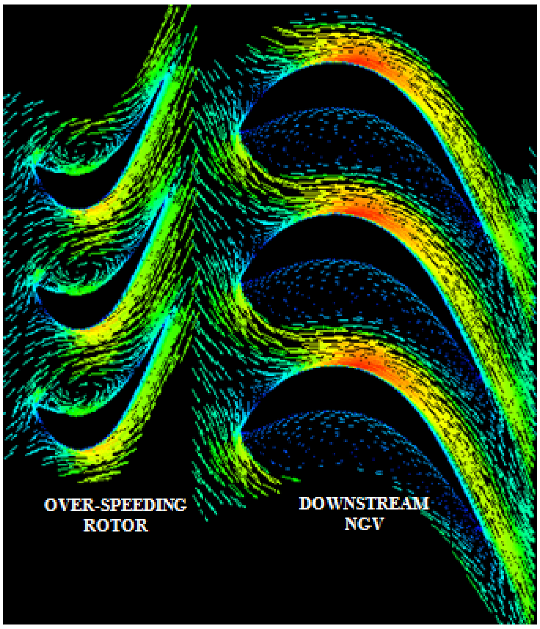

Figure 1.8: *Velocity vectors across an over-speeding turbine rotor and its downstream NGV obtained with hi-fi 3D CFD at blade mid span*

controlled manner. Tangling is a specific type of friction that arises from the contact of the over-speeding turbine blade tip trailing edges with the downstream turbine NGVs (fig. 1.9). This type of contact is particularly desirable because it occurs at high radii and hence the power dissipated as friction is greater. However, tangling can occur only after any structure between the rotor and NGV blades has been melted away. In some failure cases (turbine horizontal drive arm and failure downstream of the inter-shaft seal) the turbine remains axially located on the remaining portion of the shaft and this needs to be eroded before blade tangling occurs. However, this contact occurs at a low radius, it is not efficient and it can take an unacceptable long time for the shaft to be eroded and blade tangling to occur. Moreover, these two cases are specially important because the vibration after the breakage is likely to be low and thus vibration induced surge cannot be relied on to limit the spool speed.

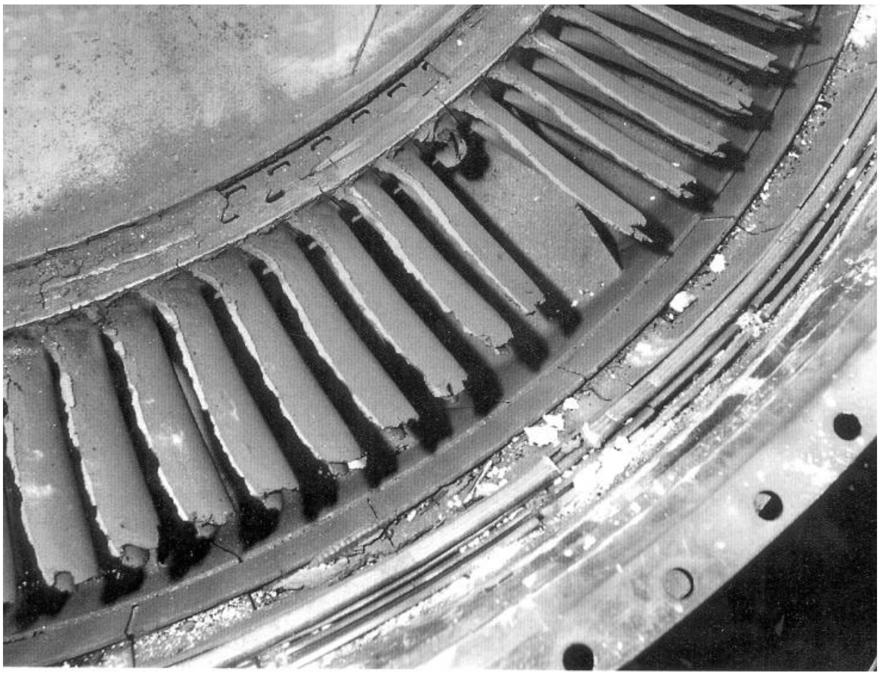

Figure 1.9: *Evidence of blade tangling between IP rotor and NGV blades - Intermediate pressure turbine rotor viewed from the rear. From [158]*

Blade tangling is also an effective means of introducing strong vibrations on the compression system and force it to surge or avoid its recovery. In cases where a second surge is required it can be promoted by blade tangling or thermodynamically by the mismatch between spool speeds. In either case the timing of the inception of surge is important; surge needs to occur rapidly to guarantee that the shaft speed will remain low.

As aerofoil machining takes place the mechanical loads to decelerate the turbine rise. Eventually the load is such that some blade tips break off and become loose. Blades can also be knocked off if radial distortion of the structures allows blade “spragging” with the casings. In any case, the blade portions loose within the turbine assembly have a considerable tangential velocity but a small axial with little possibility of coming out through the rear of the turbine. These loose bits impact the adjacent blades breaking them off and this propagates circumferentially very quickly. Almost instantaneously the turbine has all its blades knocked off at around 75% of their span and this causes a drastic drop of turbine efficiency, and therefore a very significant reduction of the driving torque, further braking the turbine.

Finally, the frictional force braking the turbine depends on the net axial load acting on the turbine disc. The dynamics of the internal air system play a major role in the determination of this load and this is discussed next.

1.7.1.4 Internal air system

The frictional force between rotating components depends on the net axial load that pushes them together. On a turbine disc the net axial load is the sum of the load exerted on the blades by the air of the main gas path and the load on the turbine disc. These two loads are normally of the same order of magnitude in modern turbine designs. The turbine displacement rearwards that follows an unlocated shaft breakage may seal the discharge ports of the internal air system, in particular the gap at the rear turbine rim. Should this happen the pressure inside the system cavities increases and exerts a forward force on the unencumbered turbine rotor that reduces the frictional force between the structures. As a result the power that can be dissipated as friction and heat may then not be enough to arrest the over-speed. However, after the initial collision the turbine disc can bounce back or move radially and open the port again, preventing the detrimental build up of pressure in the LPT cavity.

From all the previous it is clear that in “surge free” cases where the engine relies on blade tangling to run down claim for an accurate modelling of the secondary air system dynamics for an adequate simulation of the event.

1.7.2 Possible scenarios and likely progression

It can be deduced from what it has been exposed so far that the possible scenarios and the likely progression of an IP shaft failure are very geometry and event dependent. The possible outcomes of the event are:

- *Engine does not surge or surges and recovers leading to an uncontained failure.* This is obviously not an acceptable outcome and must be avoided.
- *Engine surge and no recovery.* This is the most desirable outcome of the event since it is likely to be contained regardless of any other speed limiting mechanism (turbine capacity loss or blade tangling).
- *Engine surge and recovery followed by a second surge triggered by thermodynamics.* The compressor end of the IP spool can be considerably faster to run down than the HP shaft that is being driven by the HPT. Obviously this is more marked in designs with greater compressor inertias. The difference in spool speeds consumes the HPC surge margin progressively until the stable operation of the compressor is not possible. If this happens before the bottom part of the initial surge cycle the engine is prevented from recovering from surge and runs down in stall.
- *Engine surge and recovery followed by a second surge triggered by blade tangling.* The violent collision and contact between the IPT disc and any static structure downstream generate strong vibration pulses that are enough to push the engine into surge and prevent the recovery. As in the previous case, the timing of the inception of the second surge is important in order not to reach a hazardous speed.

The progression of the event depends heavily on the location of the failure. Sorted by location, from the front to the rear, the possible scenarios are (see engine cutaway attached):

1. *Failure of the compressor rear stub-shaft.* This failure is characterised by the axial and radial location of the turbine on the front and rear bearings. In this case turbine friction and blade tangling are not available as speed limiting mechanisms. Also, unlike HP failures, there is little room available for radial or axial movement of the IP compressor and hence the destruction of the IP compressor blading is not a dependable option either. The engine relies on running down in stall to control the event, induced either by high initial vibrations of the off balance compressor or shaft speeds mismatch.
2. *Failure of the shaft upstream of the inter-shaft seal.* In this case the compressor is located only on its front bearing and this results in the initial vibrations being high enough to stall the compressor. Depending chiefly on the cause of failure (see 1.4.2) vibrations may fade away and the engine may be able to recover where thermodynamically possible.
3. *Failure of the shaft spline coupling.* Wear of the splines can make them skid and lose the drive between the compressor and the turbine whilst maintaining the axial location. Lack of out of balance means that the initial vibration induced surge may not happen and the engine must rely on stall as the speed limiting mechanism. An altogether different strategy is to assure that if the spline fails the locking nut of the shaft would unwind and allow the turbine end of the shaft to move rearwards for blade tangling to occur.
4. *Failure of the shaft downstream of the inter-shaft seal.* This event is characterised by low vibrations throughout the event because the compressor remains axially and radially located reasonably well on the front bearing and the inter-shaft seal. Initial surge may happen or not, but it is likely that vibration decays rapidly and the engine may be able to recover from stall.
5. *Failure of the horizontal turbine drive arm.* From a vibration viewpoint this failure type is unlikely to present an initial surge. Furthermore, there is a significant amount of metal that needs to be ground down before the turbine blades can become into contact. Unfortunately the friction takes place at a very low radius, the wear rate is very low and it may take an unacceptable time for blade tangling to happen.

1.8 Low pressure shaft failures

These are the most common shaft failure events and are the only for which real scale engine testing has been carried out in the past. Some proprietary data is available from tests carried out in the Spey, Olympus, RB211 and FJ44 engines.

LP shaft failures are characterised by the length of the shaft and the relative position of the thrust bearings that make this mode of failure susceptible to being unlocated. However, located failures are also possible. On the other hand, these shaft failures have little or no effect on the core matching, and thus compressor surge is not a dependable limiting mechanism to the over-speed. The fan is not likely to surge either since it is well located on the front bearing. Turbines where the core spool kinetic energy is large compared to the LP kinetic energy are subjected to higher terminal speeds because the gas generator is slower to run down that the LP spool. This means that the LP turbine has high power flows at its disposal for longer. Typical acceleration rates for LP failures are around 700%/sec. Finally, modern designs characterised by higher pressure ratios and loadings raise the terminal speed of the low pressure shaft. Because of all these reasons the low pressure shaft failure requires the intervention of an independent over-speed protection mechanism to prevent blade release.

The engine is equipped with two speed probes on the LP shaft. One is located at the compressor end and the other is located in the tail bearing housing at the other end of the shaft. The control unit counts the difference in pulses from the compressor and turbine speed probes and trigger an over-speed fuel shutoff when a critical number of excess turbine pulses have been counted. The length of the event and the finite time required by the fuel to be chopped back make the aid of variable geometry and bleed valves in LP shaft failures very desirable.

1.9 External shaft failures

For the sake of completeness, it is not out of place to mention the failures of any output or drive shafts connected to the gas turbine. Breakage of the propeller shaft in marine applications, turboshafts and turboprops or the drive shaft between the power turbine and the generator in industrial machines can lead to over-speeds, as a result of a sudden drop in the load driven by the engine. Depending on the location of the failure - in front or behind the power turbine - the engine control detects either a deceleration or an acceleration respectively, since the speed probe is generally mounted at the front of the engine. The engine control unit reacts accordingly, metering more or less fuel to catch up with the power setting demanded.

The engine is protected against this type of failure with an over-speed trip that commands the Fuel Shut Off Valve (FSOV) to close when a certain speed is exceeded. Besides to the time response of the fuel flow control software mentioned above, the amount of over-speed attained is a function of the time lags along the system. These are three: first, the time it takes after the breakage for the shaft to reach the over-speed trip set; second, the delay introduced by the electronics to command the FSOV to activate; and third, the rate at which the FSOV closes to give $0lb/h$ fuel flow. From a modelling viewpoint these failures are relatively easy to simulate since the engine remains matched during the event.

1.10 Desirable design features

There are certain design traits that can help limit the terminal speed of a free running turbine. For each shaft failure considered these are discussed next.

1.10.1 High pressure shaft failures

It has been discussed in a previous section (see 1.6) that given the high energy available to a modern HPT from even a stalled compressor the event needs to be brought to a halt by the rapid and contained destruction of the HPC blading. Therefore, design features that can compromise the compressor blading contact are to be avoided. In particular:

- There should not be an axial location bearing between the compressor and the turbine.
- There should not be any static seals between the compressor and the turbine.

1.10.2 Intermediate pressure shaft failures

The most desirable feature of an IPC from a shaft failure viewpoint is to have a big rise in working line and large reduction in surge line during the run-down to assure that the engine surges and does not recover. Design features that can limit the over-speed are:

- Low ratio of IP compressor to turbine inertia. The objective is to promote a rapid HPC surge triggered by the mismatch between HPC and IPT as the compressor runs down faster than the IPT accelerates. Thanks to the use of lighter materials and smaller cores the general tendency in modern engines is towards lower shaft inertias. However, the inertia split ratio between the turbine and the compressor has risen with time and this is beneficial from a shaft failure viewpoint.
- Rapid opening of core bleeds and slew of variable geometry to its closed stop position to push the HPC towards surge.
- Adequate fuel flow management - the fuel flow reduction must be controlled and not too rapid. This is not of importance for cases where IPC surge limits the over-speed, but it can keep the HP compressor out of surge.
- Low mass of metal between IPT rotor and LPT NGV that needs to be ground down before blade tangling occurs. Particularly important is to avoid any ineffective contact of metal parts at low radii because the power dissipated as friction is proportional to the radius of the contact.

1.10.3 Low pressure shaft failures

This type of failure relies on a rapid fuel shut off to reduce the air flow across the gas generator as rapidly as possible. Design features that would limit the terminal speed of the low pressure turbine are:

- Low turbine design loading that promotes lower terminal speeds for a given pressure drop across the turbine.
- Low ratio of core kinetic energy to LPT kinetic energy. This means that the gas generator is quick to decelerate in comparison with the LPT acceleration rate.
- Appropriate response of the bleed valves and variable geometry vanes to reduce the air flow through the engine core.

1.11 Concluding remarks

The dominant idea through the current chapter is that the possible outcome of a shaft over-speed/failure event is very case specific and the possible scenarios are many. Whereas over-speed and HP and LP shaft failures are relatively straightforward to study, the IP shaft breakage poses one of the most difficult problems in the engine to analyse. The event is characterised by the heavy interrelation between the different engine components that operate at far off-design conditions where their behaviour is poorly understood. Given the large number of possible scenarios an over-speed report needs to be thorough and can never be too detailed.

In many cases the event is dominated only by some of the phenomena described previously (surge, blade tangling, turbine capacity and efficiency changes). However, all cases share the prime requirement to throttle the over-speeding rotor to a very low pressure ratio as quickly as possible to limit the terminal speed of the turbine. The safest and most effective way of achieving this is by promoting a timely surge of the compression system and avoiding its recovery so that the air flow available to the accelerating turbine falls rapidly. There are a number of ways of achieving this that include VSV mal-schedule, tip clearance changes caused by mechanical vibrations, shaft speeds mismatch and blade tangling. However, the availability of these mechanisms depends on the particular case being considered.

This chapter described the current understanding of the shaft over-speed/failure event and forms the basis to understand the need for an integrated tool that accounts for all the different phenomena present during the event. This is covered in detail in chapter 3.

Appendix 1A - Certification regulations on shaft failure

The following sections contain the current regulations and advisory material relevant to the shaft failure event.

JAR-E-850 Compressor, fan and turbine shafts

Date: August 15, 1999

1. It shall be shown that any failure of a shaft system will not lead to a condition producing a Hazardous Effect at a rate in excess of that defined as Extremely Remote. Unless it is agreed by the Authority that the consequences of shaft failure are readily predictable a test will be required.
2. It shall be established that shaft failures will not occur at a rate in excess of that defined as Remote.

ACJ E 850 Compressor, fan and turbine shafts

Date: August 15, 1999

1. A shaft is the system that transmits torque between the disc driving flange or shaft attachment member of the system that produces power (e.g. turbine) and the system that uses this power (e.g. compressor/fan or driving flange) and for which the mechanical restraints are mainly torsional. This includes any Engine gearbox in that transmission system. The exclusion of discs in this definition of a shaft does not preclude the requirement that any failure thereof must be Extremely Remote.
2. Clarification of terms and probabilities used in JAR-E 850 may be found in JAR-1 and ACJ E 510. The possible shedding of blades is also covered in the paragraph JAR-E 810(b).
3. Where it is claimed that Hazardous Effects are avoided by ensuring that rotating components are retained substantially in their normal plane of rotation and the control of over-speed is by means of:
   - Disc rubbing.
   - Blade interference, spragging or shedding.
   - Engine surge/stall.
   - Over-speed protection devices.

   this may be substantiated by analysis. This analysis should be based upon relevant service or test experience.
4. To substantiate compliance by analysis, it should be shown that all likely failure zones (including any gearboxes supplied by the aircraft manufacturer) and failure modes have been identified in the analysis. The failure analysis should take into consideration the effect of

failures in terms of contact and loads on the surrounding structure of the engine and determine whether the affected rotor components are retained substantially in their rotational plane. It should also demonstrate that the structural components, when the loads resulting from the failure are applied, do not exceed their ultimate stress capability and lead to a hazardous failure.

5. In general, experience has shown that failures of shafts occur at a rate in excess of Extremely Remote. Where, however, it is claimed that the probability of a shaft failure is Extremely Remote, the requirements of JAR-E 515 will be applicable. An assessment should show:
    - The prevailing stress levels are below the fatigue limit for infinite life for the material concerned.
    - The surrounding environment is such that a shaft failure can be discounted.
    - The applicant has sufficient service experience of similar designs that have demonstrated the required integrity or can be expected to do so in combination with approved maintenance/operational procedures.
6. The following design aspects should be included when assessing causes and probabilities of shaft failures:
    - The potential for undetected material defects and for manufacturing tolerances.
    - Rubbing between any torque-loaded section of the shaft and adjacent surfaces (e.g. other shafts, oil seals, air seals) to the extent that significant over-heating or reduction in strength could occur.
    - The effect on the shaft of bearing failure and the desirability of provision (e.g. by maintenance techniques and/or flight instrumentation) for the detection of incipient bearing failure. The possibility of isolating the bearing from the shaft and thus increasing the damage tolerance of the system should be considered.
    - The effect on the shaft of any likely engine fire and the necessity for provision of an early warning of any internal fires that may occur.
    - The effect on the shaft of loads which could be transmitted by shock loading resulting from bird strikes, blade failures, etc.
7. The shaft system should be subjected to the following investigations and/or testing:
    - Strain gauge or other suitable means of investigation in order to satisfy the vibration survey requirements of JAR-E 650 and to ensure that shaft whirling is not present to any significant degree at any likely engine operating condition.
    - Fatigue evaluation of each shaft in torsional modes representing the normal maximum steady state torque in order to confirm its predicted safe life. An oscillatory torque of a magnitude equal to the maximum envisaged in a representative installation, but not less than 5% of the normal maximum steady state torque should be superimposed on that steady state torque. In addition, consideration should also be given to any high frequency vibrations and any possible shaft bending.
    - Where necessary, confirmation of stress assumptions by static strength tests.
    - Where necessary, substantiation by test of the design considerations above such as to demonstrate that shaft failure is acceptably remote.

Chapter 2

Thesis structure

This chapter provides a brief outline of this thesis so that it can be easily followed. The manuscript is structured as sketched in figure 2.1. Chapters 1 and 3 constitute the raison d'etre of this research and try to answer some fundamental questions about the purpose, management and planning of the research project. Chapters 4 to 10 give account of the technical work carried out during the doctoral program, each focusing on the performance of a different component during the shaft over-speed event. Chapter 11 includes the conclusions that can be extracted from this work, lists the deliverables of the research to the sponsor and discusses some recommendations for future work. The detailed content of each chapter is covered next.

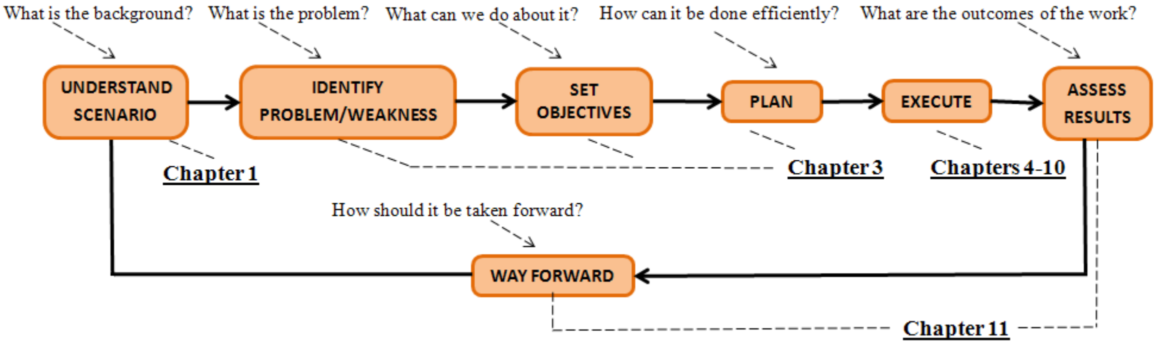

Figure 2.1: *Thesis structure and chapter content*

Chapter 1 describes the current understanding of shaft failure events in modern large turbofan civil engines. This includes engine certification requirements issued by the certifying Authority and strategies of compliance adopted by the company. The response of the control system during the event and the behaviour of the engine components is outlined and discussed. Possible outcomes and the likely progression of any shaft breakage event are also thoroughly reported here.

Chapter 3 puts this work into context within the Rolls-Royce Cranfield University Technology Centre (UTC) and links it with some parallel research activities that are ongoing at Cranfield University on shaft failure modelling. This chapter describes the project objectives that are pursued by this research and the potential benefits that can stem from this work. There is also a section dedicated to cover the management of the project both with the sponsor and internally - meetings, reporting, MSc students' contribution and management are described here. The chapter ends with detailed comments on the generation and transfer of knowledge into the company and the open domain.

Chapter 4 renders the studies carried out on turbine aerodynamics during a shaft over-speed event. These include the design, manufacture and test of a NGV cascade rig at high negative incidences and comparison against numerical data, development of an extended loss model for turbine vanes at high negative incidences and numerical simulations of the shaft failure event.

Chapter 5 reports on the development and validation of a stand-alone modular software to simulate the response of the dynamics of internal air systems to rapid transients. The development of the tool encompasses the modelling of the components that form the air system in isolation and their careful modular integration into a whole network. The chapter concludes with the estimation of the axial loads on turbine discs during a shaft breakage event.

Chapter 6 discusses the methodology that has been followed to derive the compressor characteristics for reverse flow. It begins with the investigation of the suitability of 2D analytical methodologies to capture all the important flow phenomena that occurs in backflow and moves on to describe some 3D CFD studies that have been completed across two axial compressor stages to establish a data base for compressor characteristics in backflow. This allows for the application of a stage stacking technique to derive the compressor map in reverse flow for its inclusion in the shaft over-speed simulation tool.

Chapter 7 elaborates on the development and extension of compressor inlet guide vane loss, stall and deviation models as a necessary step to produce reliable compressor maps for mal-scheduled variable geometry vanes. Such enhanced models have been integrated into a mean line compressor performance prediction tool that has been validated against experimental data and delivered to the sponsor. These improved models allow for the variable geometry optimiser described in chapter 9 to provide reliable results.

The eighth chapter of this manuscript describes the state of the art of whole engine simulation during shaft failure. It also discusses the work that was carried out to investigate the capability of an existing in-house whole engine model to capture the compressor and combustor performance for pre and post stall conditions.

Chapter 9 goes through the development of a genetic algorithm optimiser to derive the most flow efficient schedule of the compressor variable geometry that conforms to a user defined minimum surge margin. The application of the proposed methodology has shown promising results when applied to a modern eight stage axial compressor.

Chapter 10 gives account of additional research conducted by the author in the area of gas turbine performance to investigate gas compressibility effects on the accuracy of the prediction of gas turbine performance. The chapter begins with the scrutiny of the accuracy of different gas models to predict the thermodynamic state of air at the conditions of operation of modern gas turbines. The study concludes with the evaluation of the deviation from the ideal gas assumption of predicted performance employing different equations of state.

The final chapter of this thesis summarises the contribution to knowledge made by the research. Suggestions and recommendations on how to continue the research follow.

Chapter 3

Research scope, methodology and project management

3.1 Research scope and background

The dominant idea conveyed by chapter 1 is the heavily interrelated behaviour at far off-design conditions of the different engine components during a shaft failure event. Standard transient modelling techniques are not suited to tackle the problem mainly because of the limited knowledge of the performance of the engine components at such abnormal conditions that include compressor surge, mechanical interaction of rotating components, highly distorted turbine aerodynamics and rapid internal air system changes. Actual strategy to guarantee the safe outcome of a shaft failure reads across some proprietary data from development engines to other engines and scenarios. This methodology generates a substantial amount of uncertainty that is catered for by designing oversized turbine discs and parts. This in turn exerts some penalties in terms of weight, size and operational costs.

Although engine shaft over-speed/failure tests are carried out in some cases and a purely experimental approach to the problem would satisfy the Authority, large scale tests under those conditions tend to be prohibitively expensive and complex. Hence, the need for an analytical, semi-empirical approach and small scale testing arises to ascertain the terminal speed of the turbine after a shaft breakage. It has been identified that an improved understanding of the components behaviour and a greater degree of aerothermal and mechanical integration between components are required for an improved simulation of the event.

This thesis is the starting point of a longer term research collaboration between Rolls-Royce and Cranfield University towards the development of an automated computational tool to model the behaviour of gas turbine engines during shaft failure (fig. 3.1). The modelling of the event will encompass two separate tasks. First, engine component models must be developed or extended to cover the wider range of operating conditions present during the over-speed. The second task is the vertical integration of all the findings and engine components into a whole engine transient model. Once completed, the multidisciplinary tool will be calibrated against event data available to the research and applied to other engines and operating conditions.

The initial intent of the tool is twofold: on the one hand, the tool will be employed in the certification of gas turbines against core shaft failures and on the other a better over-speed assessment will promote and improved design capability to account for shaft failure early in the design process. There are other additional benefits that can be gained from the research that are discussed later in the chapter (see 3.2.1).

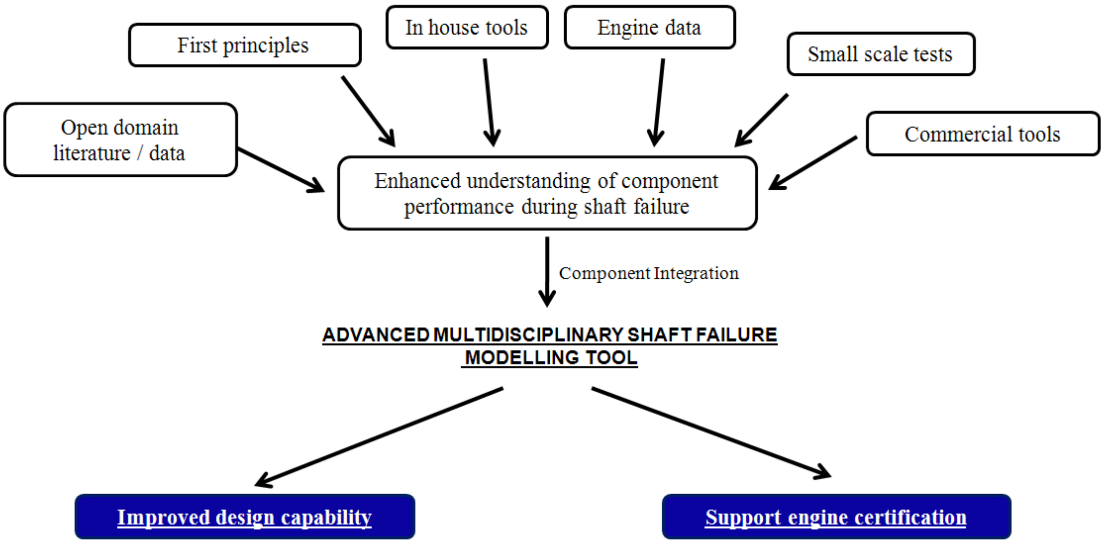

Figure 3.1: *Research scope and intent*

One of the main challenges that the project presents is the scarcity of data at the operating conditions of interest. The study of such extreme[1] failure cases has not attracted the attention of the research community because of the limited applicability of component testing and modelling at such far off-design conditions. This is aggravated by the fact that due to the unique three shaft architecture of Rolls-Royce large turbofans IP shaft failures are a technical problem of no interest to other engine manufacturers. The sources of information and tools available to the research are:

- *Open domain literature / data.* There is only one reference in the open literature on shaft failure modelling [72] and this will be discussed in chapter 8. Other publications particularly relevant to this research are limited to the work of Yamamoto on turbine blades at high negative incidence [199][197][198][195][196], some references on stalled blade performance [132][96][97][62][63][37] and some generic literature on air systems modelling [100][4]. The applicability of each piece of work to this research will be discussed in the relevant chapters.
- *First principles.* As applied to compressor blades in reverse flow in chapter 6 or to the modelling of internal air systems in chapter 5.
- *In-house tools.* These are Rolls-Royce's Aerothermal Performance suite ($RRAP$) and a mean line compressor performance prediction tool ($VU59$).

---

[1] It has to be borne in mind that there is a fundamental difference between usual off-design and extreme off-design conditions. Whereas for the former there are well documented and consolidated calculation methodologies this is not so for the latter. After a shaft breakage in particular the flow breaks away from the blade surfaces, reverse direction and behaves many times in an erratic manner where well established off-design methodologies fail to generate an adequate answer.

- *Engine data.* Available to the research from the industrial sponsor.
- *Small scale tests.* Particularly the low speed tests of turbine nozzle guide vanes at high negative incidences carried out at Cranfield and reported in chapter 4.
- *Commercial tools.* Publicly available software and tools used include programming languages Fortran and Matlab and CFD codes Fluent and CFX.

3.2 Project objectives

The objective of the shaft over-speed research is to improve the performance modelling capability of shaft failure events to include:

- Prediction of compressor pre-stall and post stall performance.
- Effects of extreme swirl and blade tip clearance on turbine capacity and efficiency.
- Methodology to derive compressor reverse flow characteristics.
- Internal air system dynamic response to rapid transients including calculation of axial loads.
- Model of friction and wear progression of turbines in contact.
- Improved prediction of compressor performance for IGV/VSV mal-schedule.
- Integration of findings into a full model.

3.2.1 Benefits gained from the research

Besides the immediate benefits of engine certification support and design optimisation there are other potential benefits that can be gained from this research. All the benefits gained from the research are (fig. 3.2):

- *Optimised design.* A better over-speed assessment allows for an optimised turbine disc, control system and engine architecture in terms of weight, performance and size. Weight in particular is a major driver of modern engine designs in the pursuit of lower fuel consumptions.
- *Reduced costs of operation.* Lower SFC promoted by optimised designs offers an evident financial reward. This is true not only for the engine operator but for the engine manufacturer as well with the popularisation of “power by the hour” schemes
- *Support engine certification.* The “all-in-one” tool can be used to demonstrate the Authority that the engine conforms to the required standards in a fast and efficient way.
- *Predictive designs* as opposed to reactive designs. The availability of a multidisciplinary tool early in the engine design process would allow to respond appropriately to future threats such as, for example, changes in legislation.

- *Controlled design parameters.* Understanding and measuring the impact of design parameters on the terminal speed allows to carry out trade-off studies early in the design process, and make design decisions accordingly.

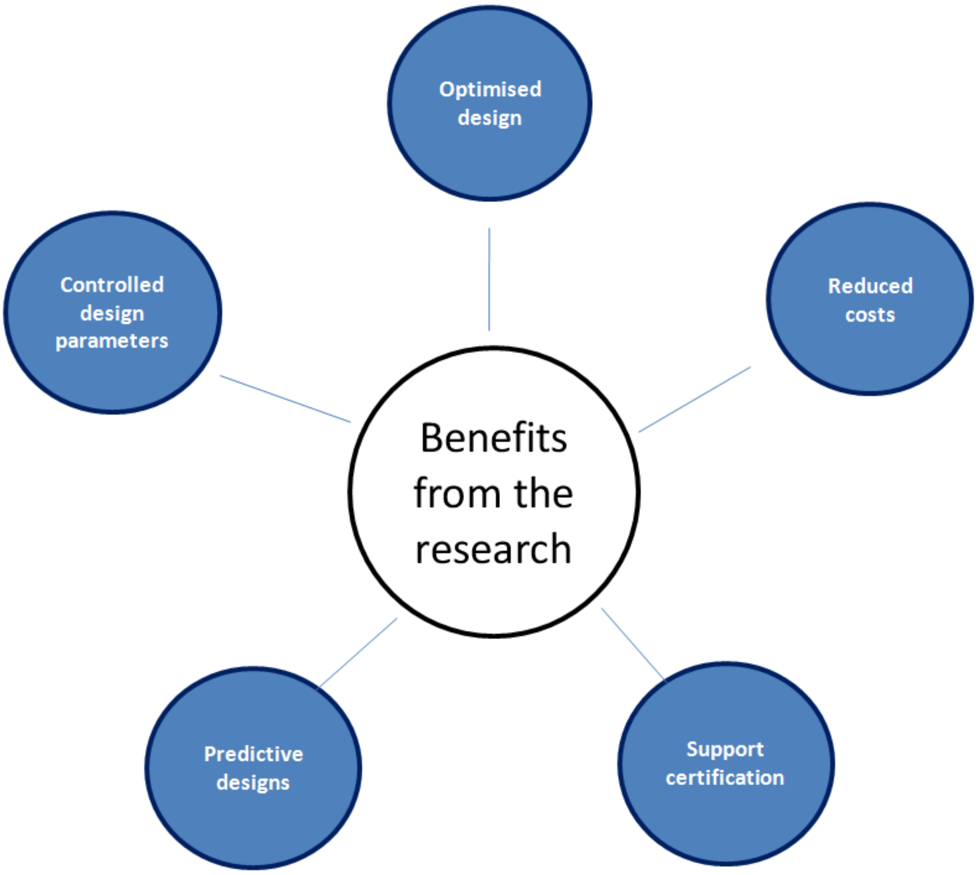

Figure 3.2: *Benefits of the research*

3.3 Work plan

Two possible approaches to develop the "all in one" tool were pondered when the project kicked off, both showing advantages and pitfalls. On the one hand, a simplified transient engine model could be written from scratch in a modular fashion to tailor the shaft breakage needs. This standalone code would have the benefits of greater simplicity, easier use and could be entirely controlled and managed by the researcher, at the expense of limited applicability and accuracy. On the other hand, the research could use a transient engine model included in Rolls-Royce's Aerothermal Performance suite (*RRAP*) as a baseline and modify the bricks relevant to the shaft failure. This latter option has the disadvantages of being less flexible and it requires the researcher to have a deep understanding of the inner-workings of the code. However, it presents with the outweighing advantages of greater accuracy and applicability with the added benefit of full compatibility with the company's libraries and databases. For these reasons it was the chosen alternative. The modular character of the tool allows for the engine component modules to be superseded by improved versions once these become available.

The first step in the research was be to investigate the possible integration of $BX04$[2] into the baseline three shaft transient engine model (fig. 3.3). $BX04$ is an initial attempt to provide $RRAP$ with high frequency pre and post stall modelling capability. It was developed by Nicholas Merriman in 1994 [124] and rests on rig data compiled by Alexander Wilson and Christopher Freeman [190][191] from stall experiments on a RR Viper engine. At the beginning of the project, its suitability to provide reliable results for modern three shaft engines remained to be established. The investigation of the capabilities of the program and its suitability to be integrated in a three shaft engine model is the objective of most of chapter 8.

Once all the component models are integrated into the software the next step will be to calibrate the code against engine data from events that occurred in development engines. The tool will then be suited to be applied to other engines and scenarios and will provide valuable information on the influence of relevant design features on the outcome of the event.

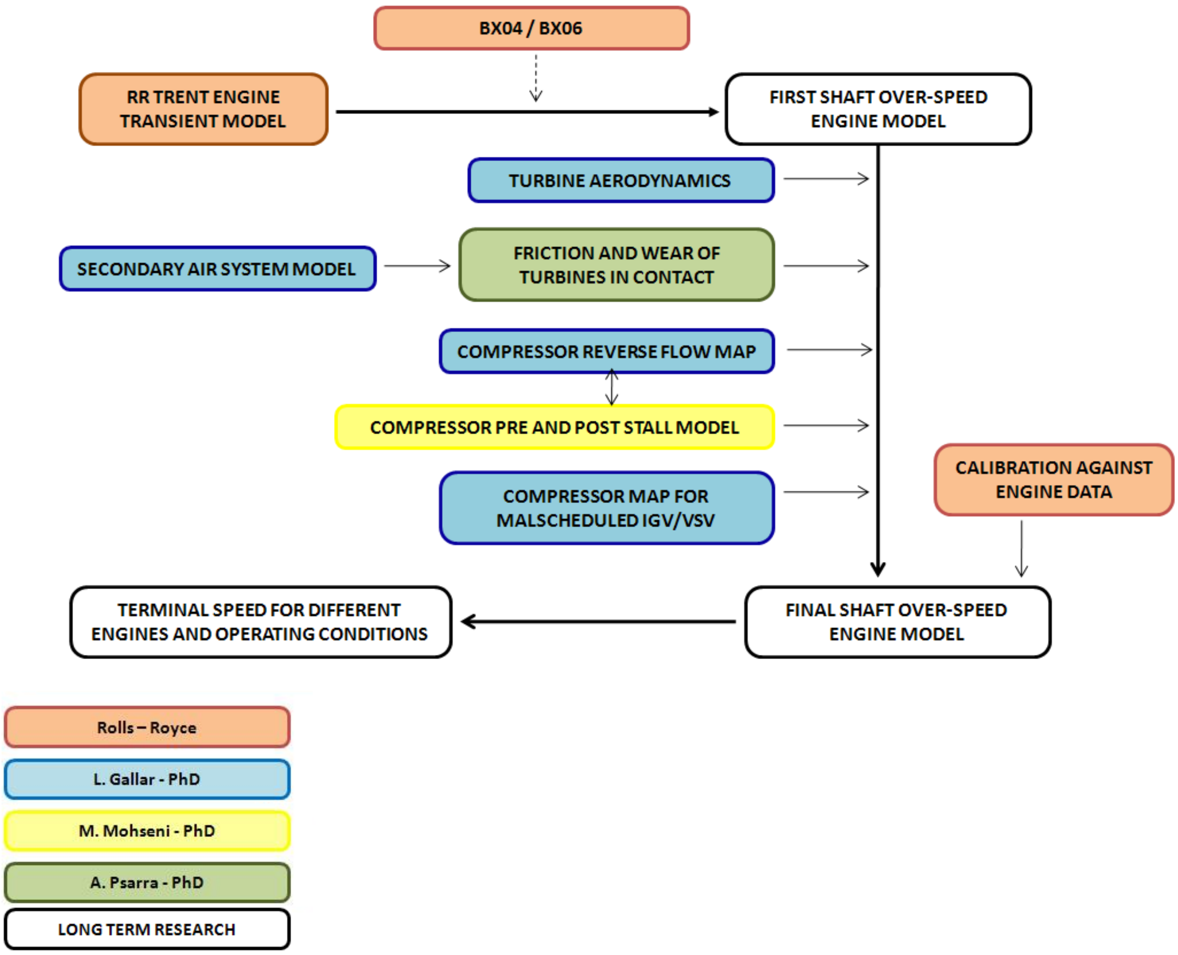

Figure 3.3: *Work plan and work split of the shaft over-speed/failure modelling project*

---

[2] The structure of $BX04$ is described in chapter 8

3.3.1 Work split

There is no harm in repeating that the accurate modelling of a shaft failure event must cover many different complex interrelated phenomena. Their thorough investigation requires an amount of work impossible to carry out by a single doctoral researcher. For this reason the project was split into three interwoven doctoral projects that have run in parallel for the past three years (fig. 3.3).

Aikaterini Psarra was entrusted with the analysis of the friction and wear modelling of turbine structures in contact. The objective of her work is to derive a map or a correlation to link the energy that can be dissipated as friction from the contact with the axial load and the operating conditions of the turbine. On the other hand, the calculation of the axial load on the turbine disc is heavily influenced by the dynamics of the air system after the shaft failure, and the SAS in turn is affected by the displacement of the turbine disc than can close some of its discharge ports (see 1.7.1.4). The highly coupled character of the two phenomena have led to a continuing synergistic collaboration between these two projects for the past three years.

Martina Mohseni is accountable for the development of a methodology to derive the compression system performance at pre-stall and post-stall conditions. This is a very important aspect of the project since the compressor delivery pressure is the principal factor influencing the flow available to the over-speeding turbine to accelerate.

The role of the author of this manuscript, Luis Gallar, is to develop methodologies to model the remaining components during shaft failure and to act as an integrator of all the component models. These models include:

- In depth study of turbine aerodynamics during shaft failure. This encompasses numerical studies of the over-speeding turbine rotor and the immediate turbine stage downstream, design and manufacture of a turbine nozzle guide vane test rig at high negative incidence, comparison of experimental results with CFD and development of an extended turbine blade loss model for far off-design conditions (see chapter 4).
- Time accurate modelling of the internal air system response to rapid air transients (see chapter 5).
- Derivation of compressor characteristics in reverse flow for their inclusion in the compressor pre and post stall model (see chapter 6).
- Prediction of IGV/VSV mal-schedule compressor maps to be included in the shaft failure modelling tool (see chapter 7).

3.4 Additional research in gas turbine performance engineering

The collaboration with Rolls-Royce provided the author with the opportunity to conduct research on other areas related to performance engineering apart from the shaft failure modelling. In some occasions the industrial sponsor expressed a timely interest to divert some research resources to investigate specific aspects of the engine performance to support the satisfaction of an immediate need. The industrial sponsor obtained innovative solutions and suggestions to a pressing problem whereas the author gained knowledge and expertise in other performance areas - in other words, a better understanding of the bigger picture. These additional projects focused on compressor variable geometry loss and schedule optimisation and on the effect of using real gas models instead of the perfect gas assumption in engine performance simulation codes. A succinct description of each is given next.

3.4.1 Compressor IGV loss, deviation and stall modelling

Section 1.5 elaborates on the impact of the variable geometry mal-schedule on the shaft overspeed event. This effect can be quantified by exchange rates that are obtained from compressor rig tests; however, testing all possible combination of geometry settings and shaft speeds is very time consuming, complex and expensive. An alternative option is to generate different compressor maps for a range of variable geometry settings and spool speeds with the help of compressor off-design performance prediction programs. This methodology relies on the accuracy of the compressor performance prediction algorithm to predict losses across the compressor blades, including uncambered IGV aerofoils. For this purpose the capability of a proprietary mean line code to provide compressor maps for variable geometry mal-schedules was investigated. The initial comparison of the computational results against experimental data revealed some weaknesses of the treatment given to loss, deviation and stall prediction across inlet guide vanes. Chapter 7 revisits such flow models and discusses the work undertaken to enhance their accuracy.

3.4.2 Compressor variable geometry schedule optimisation

This project is a spin-off of the IGV loss modelling project. The industrial sponsor expressed an interest to develop a methodology to optimise the compressor variable geometry schedule for flow efficiency and surge margin in order to save costs and testing time. Given the characteristics of the problem at hand, it was decided that the coupling of a genetic algorithm optimiser with a compressor performance prediction code would provide and adequate answer. The optimiser identifies the most flow efficient schedule that conforms to a prescribed surge margin, and reduces the amount of testing needed to derive the optimised schedule considerably. The development of the tool is reported in detail in chapter 9.

3.4.3 Thermodynamic gas models effect on gas turbine performance prediction

To the best of the author's knowledge, all engine performance simulation codes use the perfect gas assumption to link the pressure, temperature and density of the working fluid. Performance models are used extensively not only by the manufacturer but also by the customer for various purposes that include mission analysis, performance predictions and analysis and support of test data amongst many others. This justifies the need to quantify the accuracy of the perfect gas law to fit the thermodynamics of air and the departure from the ideal gas assumption of the predicted engine performance caused by the use of other gas models. This is precisely the subject of chapter 10.

3.5 Project management and planning

Only the simplest projects can succeed without strong project management and planning. However, planning of research activities is difficult since the way forward depends strongly on the findings and these most often cannot be foreseen. This section covers the management of the project both with the sponsor and internally within the university. The relationship with the sponsor was channelled through reports and quarterly and annual review meetings to monitor and control the progress against the baseline work plan. The internal management of the project included internal review meetings, work package agreement with MSc students and daily supervision.

3.5.1 The Rolls-Royce University Technology Centre in Performance Engineering at Cranfield

Rolls-Royce initiated a collaboration with Cranfield University in 1998 to undertake research in the field of gas turbine performance. The company provides funding, guidance, data and support to the researchers and these in turn carry out work on projects that are of current interest to industry. This interaction is enormously beneficial for both parties. On the one hand, results and novel methodologies developed by the researchers at the forefront of knowledge feed back into the company to be incorporated in its analysis and design processes. Researchers, on the other hand, obtain a substantial hands-on experience and very valuable guidance from world experts in their area of research that boost the quality of their work.

3.5.2 Meetings and reports to Rolls-Royce

To ensure the sponsor's expectations, requirements and objectives for the research were clearly identified, a project management meeting with the Chief of Corporate Performance and Methods and with the Corporate Operability Specialist took place in November 2007. The intent of this meeting was to discuss and agree the research scope, time line and work plan with the sponsor, as well as the work split shown in figure 3.3.

The progress of the research was controlled and monitored in technical review meetings held quarterly between the shaft over-speed researchers and the company's performance and operability specialists. The meetings included a thirty minutes presentation by the author to communicate the progress of the project that inevitably triggered very useful technical discussions. The sponsor was also available for unscheduled discussions at the researcher's request to discuss results and pressing difficulties. These meetings proved very constructive to the research thanks to the valuable feedback, advice and guidance obtained from the company specialists.

Annual review meetings had a slightly different scope. Their objective was to divulge the research activity within the company in order to maximise its impact and visibility. Senior engineers

Table 3.1: *Project review meetings held during the doctorate with Rolls - Royce*

Date	Venue	Meeting Objective	Material
31st September 2007	Derby	Project kick-off	
21st November 2007	Derby	Project management	
5th December 2007	Cranfield	Technical Review	Presentation
7th March 2008	Cranfield	Technical Review	Presentation
18th April 2008	Derby	Technical Review	Presentation
29th April 2008	Cranfield	Annual Review	Presentation and report
19th August 2008	Cranfield	Technical Review	Presentation
13th October 2008	Derby	Technical Review	Presentation
9th December 2008	Cranfield	Technical Review	Presentation
17th March 2009	Bristol	Annual Review	Presentation and report
14th May 2009	Cranfield	Technical Review	Presentation
25th June 2009	Cranfield	Technical Review	Presentation
17th July 2009	Derby	Technical Review	Presentation
19th August 2009	Cranfield	Technical Review	Presentation
8th October 2009	Cranfield	Technical Review	Presentation
11th February 2010	Derby	Annual Review	Presentation and report
6th May 2010	Cranfield	Technical Review	Presentation
22th July 2010	Cranfield	Technical Review	Presentation
19th August 2010	Cranfield	Technical Review	Presentation

and specialists across all areas and sites of the company were summoned to attend presentations given by the UTC researchers and staff for a whole day. This was useful from the technical viewpoint but also provided numerous networking opportunities.

The dates and venues for all the meetings held with the sponsor during the doctoral program are listed in table 3.1.

3.5.3 Industrial placement

The doctoral program concluded with an industrial placement of six months in the company that served several purposes:

- Collection of relevant engine data to the shaft over-speed research.
- Validation of component models and in-depth discussions with specialists.
- Use of some of the company's in-house tools, libraries and data bases, specially whole engine performance models.
- Knowledge transfer into the company. This included meetings and presentations with relevant specialists to divulge and discuss the capabilities of the models and methodologies

developed throughout the PhD (see section 11.1 for a complete list of deliverables) and possible integration with the company's tool set.

In addition to the previous, the placement proved very helpful because of the chance to create valuable relationships within the company and the opportunity to raise questions to peers who could be easily approached.

3.5.4 Internal management of the research

The internal management of the research included annual progress review meetings and reports, supervision of MSc students and handing over the research to the next doctoral researcher, Carlos Soria.

3.5.4.1 Internal progress review meetings

This research activity started on the 1^{st} of September of 2007. Internal review meetings were conducted after the submission of progress reports on the 18^{th} of September 2008 and the 10^{th} of August 2009 to assess the satisfactory progress of the research. These reviews took place in front of a panel formed by two examiners alien to the research - Drs. H. Yeung and J. A. Teixeira.

3.5.4.2 The MSc students' contribution

The shaft over-speed research is a very wide topic that encompasses the study of many different and very complex phenomena. The study of some areas of the research was amenable to be carried out by MSc students that can make a distinct contribution and provide original ideas and points of view. This involved the author of this thesis supervising a number of MSc researchers taking projects based on this research, under the overall supervision of V. Pachidis. However, given the limited time frame and scope of a masters course, the complex core aspects of the research could not be sourced out to MSc students and were carried out by the author. Figure 3.4 shows the different MSc students and the research topic they focused on.

In detail, the contribution of each MSc student is explained below:

- *Axial compressor modelling in reverse flow.* Marie-Laure Davin [40] and Ioannis Tzagarakis [180] investigated the ability of 2D codes to capture the flow phenomena and generate the extended maps of axial compressors in reverse flow.
- *Turbine aerodynamics at high negative incidence angles.* Guillermo Torres [176] ran the CFD simulations that were set up by the author to study the shaft over-speed event with CFD. Marco D'Erasmo [44] completed the numerical simulations of the NGV rig designed by the author and collaborated very actively on the development of the extended loss model for turbine vanes at high negative incidences. Antonio Cantarero [25] helped to run the experiments on the NGV cascade rig.

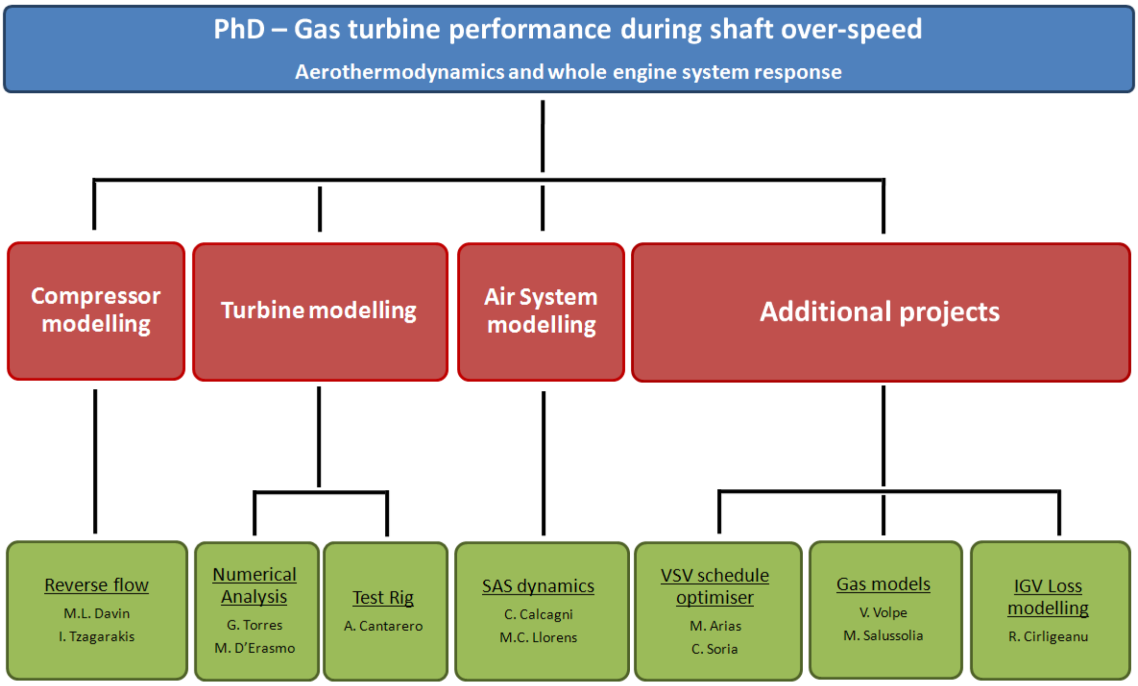

Figure 3.4: *The MSc contribution to the research*

- *Secondary air system dynamics modelling.* Cristina Calcagni [23] assembled the internal air system models developed by the author into a single network. Carmen Llorens [111] worked on the modelling of labyrinth seals and rotating flows.

- *Variable geometry schedule optimiser.* Manuel Arias [7] ran the simulations of the genetic algorithm written and developed by the author and coupled with a compressor off-design performance code to optimise the variable geometry schedule of the engine. Carlos Soria [166] translated the algorithm into Fortran and worked to make the code more efficient.

- *Thermodynamic gas models effect on engine performance simulation.* Valentino Volpe [184] and Martino Salussolia [160] ran the Turbomatch simulations presented in chapter 10.

- *IGV loss modelling.* Radu Cirligeanu [33] worked on the extension and generalisation of the inlet guide vane loss model developed by the author.

The supervision of the MSc researchers included initial meetings where the deliverables and objectives of their particular projects were discussed and agreed on an individual basis. Quite often training needs were identified and the next step involved tutorial sessions run by the author to familiarise the students with the tools and methodologies to be employed (CFD, Fortran, Labview). The progress of the MSc researchers was monitored in review meetings held at least weekly.

Finally, during the last three months of the PhD the research was handed over to Carlos Soria to be continued.

Table 3.2: *Conferences, seminars and presentations delivered to external organisations*

Date	Venue	Conference	Paper	Author	Presenter
June 2008	Berlin	Asme Turbo Expo	GT 2008 - 51008	G. Doulgeris	L. Gallar
July 2008	Cranfield	Eric Beverly Award		L. Gallar	L. Gallar
Sep. 2008	Seville	EVI-GTI / PIWG	EVI 2008 - 016	B. Charnley	B. Charnley
Sep. 2008	Seville	Sch. of Mech. Eng.	Seminar	L. Gallar	L. Gallar
June 2009	Orlando	Asme Turbo Expo	GT 2009 - 60144	K. Psarra	L. Gallar
June 2009	Orlando	Asme Turbo Expo	GT 2009 - 60049	L. Gallar et al	L. Gallar
June 2009	Orlando	Asme Turbo Expo	GT 2009 - 60058	L. Gallar et al	L. Gallar
June 2009	Orlando	Asme Turbo Expo	GT 2009 - 60051	L. Gallar et al	L. Gallar
Sep. 2009	Brussels	VKI Symposium	[58]	L. Gallar et al	L. Gallar
Sep. 2009	Montreal	ISABE 2009	Paper 1221	L. Gallar et al	L.Gallar
April 2010	Madrid	Sch. of Aeronautics	Seminar	L. Gallar	L. Gallar
June 2010	Glasgow	Asme Turbo Expo	GT 2010 - 23428	L. Gallar et al	L. Gallar

3.6 Contribution to knowledge and technology transfer

3.6.1 Deliverables to Rolls-Royce

Further to the technical meetings and presentations mentioned before, the transfer of technology, results and novel methodologies developed by the research has taken place in the form of tools, data bases, models and manuals delivered to the company. For a complete list of deliverables the reader should confer section 11.1.

3.6.2 Contribution to knowledge

In addition to the usefulness to the sponsor of the models and tools developed during the doctoral program, the research has also produced valuable knowledge and data for the research community. This is demonstrated by the peer reviewed papers published in international conferences, journal papers and presentations and seminars delivered to different organisations (see table 3.2).

3.6.2.1 Open literature publications

The research has given rise to a number of peer reviewed publications. Feedback from the referees has had a beneficial impact on the quality of the research. The papers that have already been published by the author are (in chronological order):

1. *EVI - GTI / PIWG 2nd Joint Conference on Gas Turbine Instrumentation. Paper 016.*[28] This paper describes the experimental facilities at Cranfield University and focuses particularly on the design and testing of a supersonic nozzle as an example.

2. *ASME Turboexpo GT 2009 - 60049.*[55] This paper uses a genetic algorithm to investigate the trade-off between surge margin and flow efficiency that can be obtained by restaggering the variable geometry vanes.

3. *ASME Turboexpo GT 2009 - 60058.*[57] This publication covers the development and implementation of numerical models to simulate the performance of the different components of gas turbine air systems during rapid transients. The paper explains the mathematical apparatus behind the models of the two main components of the SAS − chambers and ducts − in isolation. Then the assumptions made and the limitations that arise as a result are described thoroughly. Finally, the computational results obtained are successfully compared against experimental data available in the public domain for validation.

4. *ASME Turboexpo GT 2009 - 60051.*[24] The paper discusses the integration of the air system component models into a single modular network. The integration is successfully validated against a known numerical benchmark - the De Haller test. The paper then provides an example of the application of the tool to estimate the axial loads that arise from the air system on turbomachinery discs during a shaft breakage event.

5. *Von Karman Institute - 4th Symposium on integrating CFD and experiments in aerodynamics.*[58] This manuscript describes the detailed design of a turbine nozzle guide vane rig. The purpose is to provide an initial appreciation of the flow field and predict any unexpected behaviour or interactions in the test rig. This guarantees the reliability and representativeness of the experimental results.

6. *ISABE conference 2009 - Paper 1221.*[59] This paper reports on studies carried out with CFD to develop a surrogate loss and deviation model for the flow across an axial compressor inlet guide vane. The usefulness of the model is demonstrated by its application to an eight stage axial compressor. The contribution to knowledge of this paper is twofold: first, it demonstrates the suitability of CFD to predict trends in pressure losses and flow angles of highly separated flows to a degree of accuracy adequate for compressor performance calculation purposes. The second contribution is the provision of a set of results that constitute a starting point towards the development of a generalised loss and deviation model for compressor IGVs at far off-design conditions.

7. *ASME Turboexpo GT 2010 - 23428.*[61] This study investigates the ability of existent two-dimensional algorithms to simulate the compressor performance in backflow conditions. Three-dimensional effects and inaccuracies are accounted for by the introduction of a novel correction parameter that is a measure of the pressure loss across the blades. Results for a three stage axial compressor at reverse flow were produced and compared against stage by stage experimental data published by Gamache.

8. *Journal of Aerospace Science and Technology - Paper "Stochastic axial compressor variable geometry schedule optimisation"* [56] This paper reports on the development and calibration of a genetic algorithm to optimise the variable geometry schedule of an axial compressor as a novel and innovative methodology to save rig testing.

9. *ISABE conference 2011 - Paper "3D CFD analysis of turbine nozzle guide vanes performance at shaft over-speed conditions."*[60] The work reported in the paper investigates the combined performance of an intermediate pressure turbine rotor, low pressure nozzle guide vane and turbine rotor during an intermediate pressure shaft over-speed event of a typical three spool

high bypass ratio turbofan engine. The paper gives account of the high fidelity 3D CFD simulations carried out to evaluate the nozzle guide vane performance at high negative incidence angles. The structure of the flow that develops across the vanes is commented and successfully compared with the turbine blade cascade rig results reported by Yamamoto and Nouse [195] - [199] for a range of negative incidence angles. The turbine capacity is quantified and turbine maps are derived for an extended range of intermediate pressure and low pressure shaft speeds.

Further to the papers above, other papers are currently under review in international journals, and additional journal papers are being prepared for submission at the time of writing this manuscript.

3.6.2.2 Conferences, seminars and presentations delivered to external organisations

In addition to the presentation of the papers listed in section 3.6.2.1 in the corresponding conferences, the author has taken part in the following events:

- Presentation of two technical papers (GT 2008 - 51008[157] and GT 2009 - 60144[147]) in ASME Turbo Expo conferences 2008 and 2009 on behalf of their authors, G. Doulgeris and A. Psarra. The first paper discusses the integration of a turbofan engine into a delta wing airframe. The second describes some finite element simulations carried out to analyse the progression of the blade tangling phenomenon after a shaft breakage.
- Technical report and presentation to The Worshipful Company of Coachmakers and Coach Harness Makers of London on gas turbine shaft failure performance modelling. This was presented for the Eric Beverly's Bursary prize that was finally awarded to the author.
- Technical seminars delivered in the School of Mechanical Engineering of Seville and the School of Aeronautics of Madrid on gas turbine shaft failure performance modelling.

Chapter 4

Turbine extreme off-design aerodynamics

4.1 Background

Due to the excessive speed of the turbine and perhaps to the reduced axial velocity of the flow during the over-speed (due to a possible compression system surge), the gas velocity triangles of the over-speeding rotor and any downstream stator can be highly distorted. The NGVs can experience high negative incidence angles - as high as $-120°$ incidence and opposite to the normal sense - that will force the flow to detach from the blade surface and merge into big separation bubbles and recirculation zones. The blockage offered to the flow by the separation throttles the upstream turbine to a lower pressure ratio and hence promotes a capacity and efficiency loss that can limit the over-speed. On the other hand, in unlocated failures the rearwards displacement of the turbine may cause the turbine tips to disengage and leave increased clearances with the casings. The flow can leak over the tip of the vanes raising the flow capacity and impairing the efficiency. It is for these reasons that the proper modelling of the engine performance during a shaft failure event requires the accurate quantification of the variation in flow capacity and efficiency of the turbine.

Whereas the performance of turbine vanes for incidences close to the design is well documented and prosaic, a survey of public domain literature revealed a very limited work dedicated to high negative incidence flows across turbomachinery blades. Useful references are circumscribed to those studies undertaken by Yamamoto and Nouse [199], Yamamoto [195]-[198], Joslyn and Dring [87] and Ye et al. [200].

Atsumasa Yamamoto conducted extensive experiments on turbine rotors and stators at high negative incidences ($7.2°$ to $-53.3°$) and for a range of tip clearances. His publications elaborate on the structure of the complex highly three-dimensional flow that develops at high negative incidence and stress the fact that the flow separation on the pressure surface of the blade rapidly becomes the main source of pressure loss. However, the information contained in the papers is insufficient to give a thorough insight of the flow behaviour, especially in a quantitative manner. David Joslyn and Robert Dring [87] described the flow pattern across an over-speeding turbine rotor, with focus on the full span separation of the flow and emphasised the importance of the strong radial flow present over the blade surfaces regardless of the blade tip to casing clearance. Dajun Ye et al [200] reported on the tests carried out on two differently loaded cascades at high negative incidence. Their work shows that in the case of the strongly loaded cascade the flow separation is mild with a modest pressure loss, whereas on the lightly loaded cascade the loss incidence curve is steeper and almost vertical at high incidences. Nonetheless the flow field is strongly dependant on the blade geometry and the conclusions than can be drawn from the paper are limited.

The work presented in this chapter describes the work carried out to assess the loss in capacity and efficiency of turbine vanes operating at high negative incidence angles. The ultimate aim of the research is to produce extended turbine maps that can be integrated into the multidisciplinary tool that will simulate the engine rapid transient response after a shaft breakage.

The work commences with the CFD simulation of the combined performance of an intermediate pressure turbine rotor, low pressure nozzle guide vane and turbine rotor during an intermediate pressure shaft over-speed event of a typical three spool high bypass ratio turbofan engine. The structure of the flow that develops across the vanes is commented and successfully compared with the 2D linear turbine blade cascade rig results reported by Yamamoto for a range of negative incidence angles.

The research work includes extensive low speed testing of an experimental turbine NGV cascade rig for a wide range of negative incidence angles and speeds. The results from the rig provide a representative benchmark against which CFD techniques can be validated.

The chapter continues with the appraisal of existing turbine loss models to predict pressure losses across the vanes at high negative incidence angles. Such models have been upgraded and extended to provide a greater agreement with the numerical and experimental data at such far off-design conditions.

It is assumed that, to a first order, the high negative incidence on the NGV downstream of the over-speeding turbine alters the operation of just the first stage of the downstream turbine. It is considered that the first stage rotor accommodates the non-uniformities of the flow downstream of the NGV and leaves a reasonably clean flow at the inlet of the rear stages. The chapter concludes with the application of stage stacking and splitting techniques to replace the first stage of an LP turbine map with the extended map derived from CFD and obtain a low pressure turbine map for a range of IP and LP spool speeds.

4.2 Numerical CFD simulation of a shaft failure event

[1]The numerical simulation of the shaft over-speed event provides an initial insight into the flow field that develops across the turbine vanes as the event progresses. The 3D simulations recreate an IP shaft breakage of a modern three shaft high bypass ratio turbofan. The simulation domain includes the IPT rotor, LPT NGV and LPT first rotor with no tip clearance (fig. 4.1) using prescribed inlet pressure, temperature, spool speed and mass flow profiles as boundary conditions.

---

[1] See Appendix 4A for details and validation studies of the CFD simulations carried out in this research

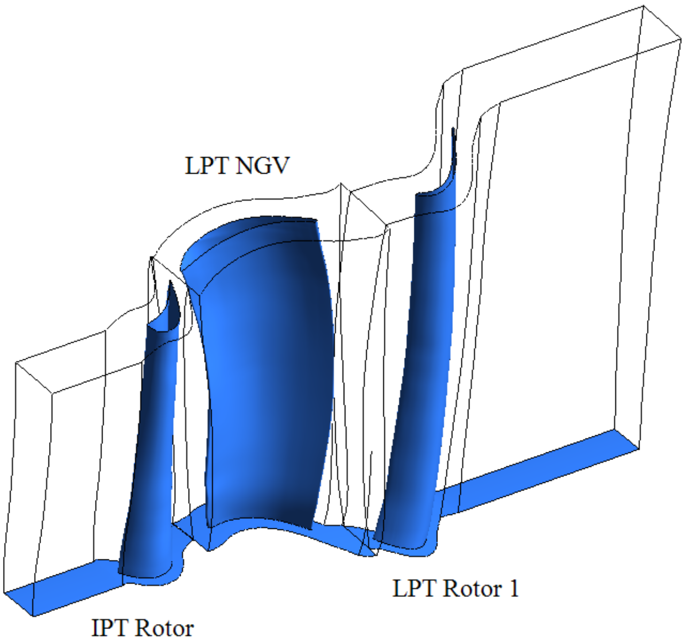

Figure 4.1: *Shaft over-speed simulation domain*

4.2.1 Calibration of the CFD against engine data at maximum take-off conditions

A first set of simulations were completed to recreate the operation of the three mentioned vane rows at maximum take-off conditions where engine data from the manufacturer is available. The main purpose is to tune the CFD meshing strategy, boundary conditions and turbulence models to set the standard for further simulations. Results predict separated flow on the suction surface of the first rotor of the LPT originated by a high negative incidence onto the blades (fig. 4.2). This is expected because the turbine blading is optimised for cruise conditions at which the spool speed is significantly lower than at maximum take-off. The deviation of the numerical total pressure and total temperature at the outlet of the NGV from engine data is 6.20% and 0.11% respectively. This is acceptable for the intent of this study.

4.2.2 Simulation of a shaft failure event

The simulation of the shaft failure event pursues the better understanding of the passage blockage phenomenon that arises from the separation of the flow at high negative incidence angles. Steady state 3D simulations are carried out for a number of time instants after the breakage prescribing six boundary conditions to the model taken from engine data: inlet pressure and temperature profiles, inlet absolute angle, mass flow and LP and IP spool speeds as specified in table 4.1. The absolute flow angle on the IPT rotor is constant since it is given by the IPT stator trailing edge angle.

The scenario under study reproduces a shaft failure event that occurs at maximum take-off conditions. Immediately after the breakage the engine surges and locks into stall with a sudden drop in mass flow and LP shaft speed while the IP spool speeds up (fig. 4.3). The combined effect

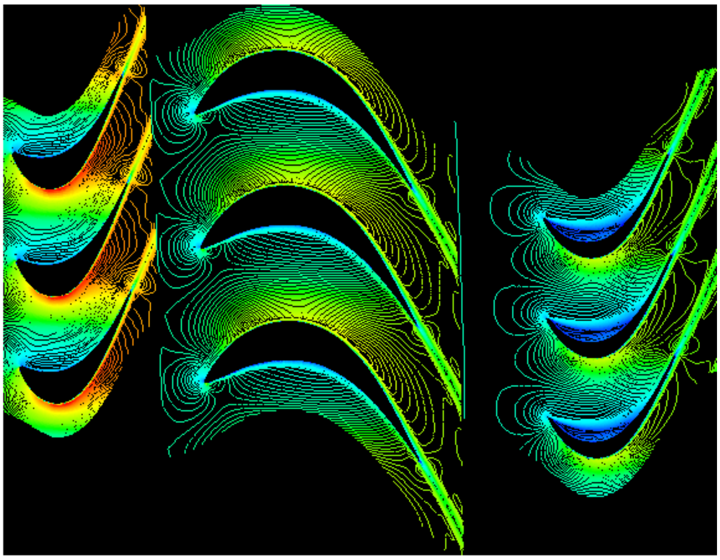

Figure 4.2: *Relative Mach number contours at mid span for maximum take-off conditions across the IPT rotor, LPT NGV and LPT rotor.*

Table 4.1: *Non-dimensional boundary conditions for the shaft over-speed steady-state analysis*

Time after the failure (s)	0	0.08	0.13	0.3	0.5	0.7	0.9	1.1	1.3	1.5
P_{42}	1.27	0.40	0.19	0.16	0.13	0.12	0.11	0.10	0.09	0.09
T_{42}	1.13	1.18	1.20	1.16	1.12	1.07	1.03	0.98	0.94	0.89
α_{42}	1.00	1.00	1.00	1.00	1.00	1.00	1.00	1.00	1.00	1.00
Mass flow	1.24	0.38	0.17	0.14	0.11	0.09	0.08	0.07	0.07	0.06
N_{IPT}	1.05	1.32	1.35	1.40	1.43	1.45	1.45	1.45	1.45	1.45
N_{LPT}	1.06	1.07	1.03	0.85	0.68	0.57	0.49	0.43	0.39	0.35

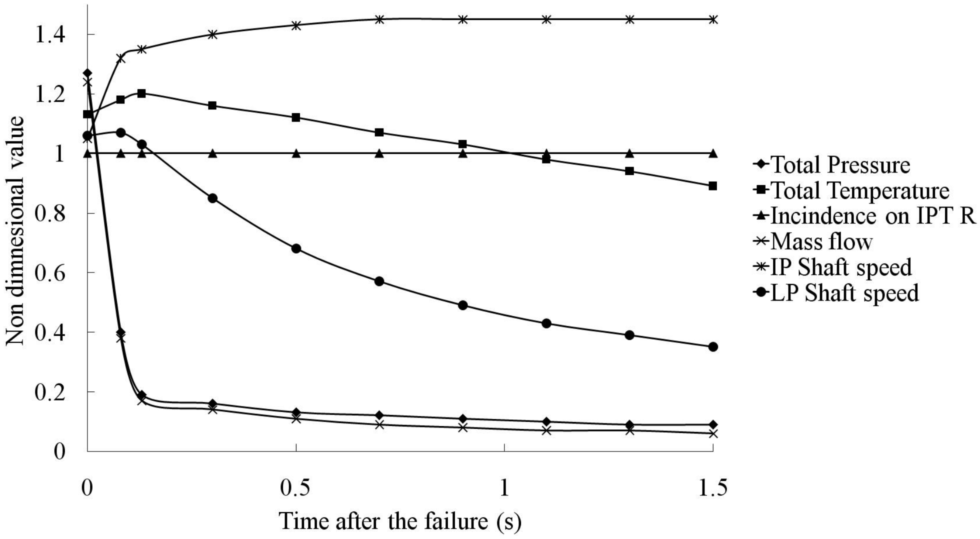

Figure 4.3: *Non-dimensional boundary conditions for the shaft over-speed steady-state analysis*

of the over-speed and reduced mass flow makes this the case most deviated from the datum from the turbine aerodynamics viewpoint. The incidence onto the different turbine blades during the simulated event is plotted in figure 4.4a. The evolution of the incidence angle onto the first rotor of the LPT exhibits a peak at 0.1s after the failure that occurs because during the first instants of the event the low pressure shaft starts to decelerate while the flow remains attached to the NGV, keeping the relative outlet angle constant. After only two tenths of a second the incidence onto the IP rotor and LP NGV deviates as much as $-50°$ from the initial value and reaches values around $-120°$ after a second. The incidence on the LPT rotor does not go further than 15° throughout the whole event. This relatively lower deviation from the design conditions substantiates the later claim that, to a first order, the first stage is able to accommodate the flow distortion and leave the rear turbine stages unaffected.

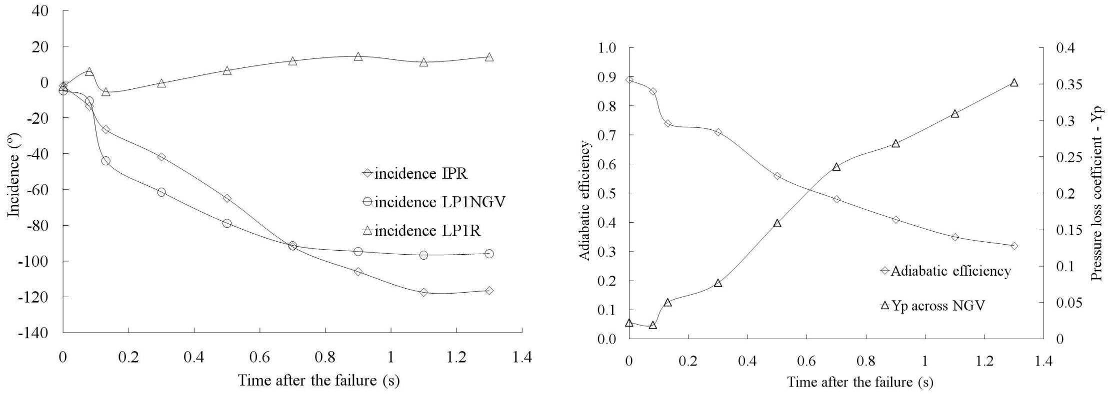

(a) *Incidence onto the IP rotor, LP NGV and LP rotor* **(b)** *LPT efficiency and pressure loss coefficient*

Figure 4.4: *Incidence and loss during the simulated shaft over-speed event*

On the other hand, the pressure loss coefficient across the NGV - defined as total pressure loss upon inlet head - rises continuously during the event (fig. 4.4b) and therefore adiabatic efficiency falls. The slight drop in pressure loss coefficient at 0.08 seconds after the breakage is consistent with the fact that the flow is still attached and with the significantly lower mass flow when compared to its value at the time of failure.

The flow field across the NGV at mid span at different instants during the over-speed is shown in figure 4.5 together with the streamlines from Yamamoto's cascade. It has been already mentioned that at maximum take-off conditions the flow over the NGV separates over the pressure surface. This separation is mild because, unlike compressor blades, incidence changes around the optimum incidence can be reasonably accommodated thanks to the favourable pressure gradient and the rounded leading edge characteristic of turbine vanes. After just 8 milliseconds the incidence decreases down to $-10.38°$ and the separated flow covers more than half of the vane chord. As the event progresses, the separation grows and occupies around 50% of the throat of the passage after 0.3 seconds. Half a second after the breakage the Mach number is not high enough for the flow to turn and follow the trailing edge of the vane and separates over the suction surface. Seven and nine tenths of a second after the failure the Mach number increases again and although the separated region on the pressure surface grows the flow on the pressure surface is able to reattach again. Despite the high Mach number, in the last simulated instant the incidence is very high and

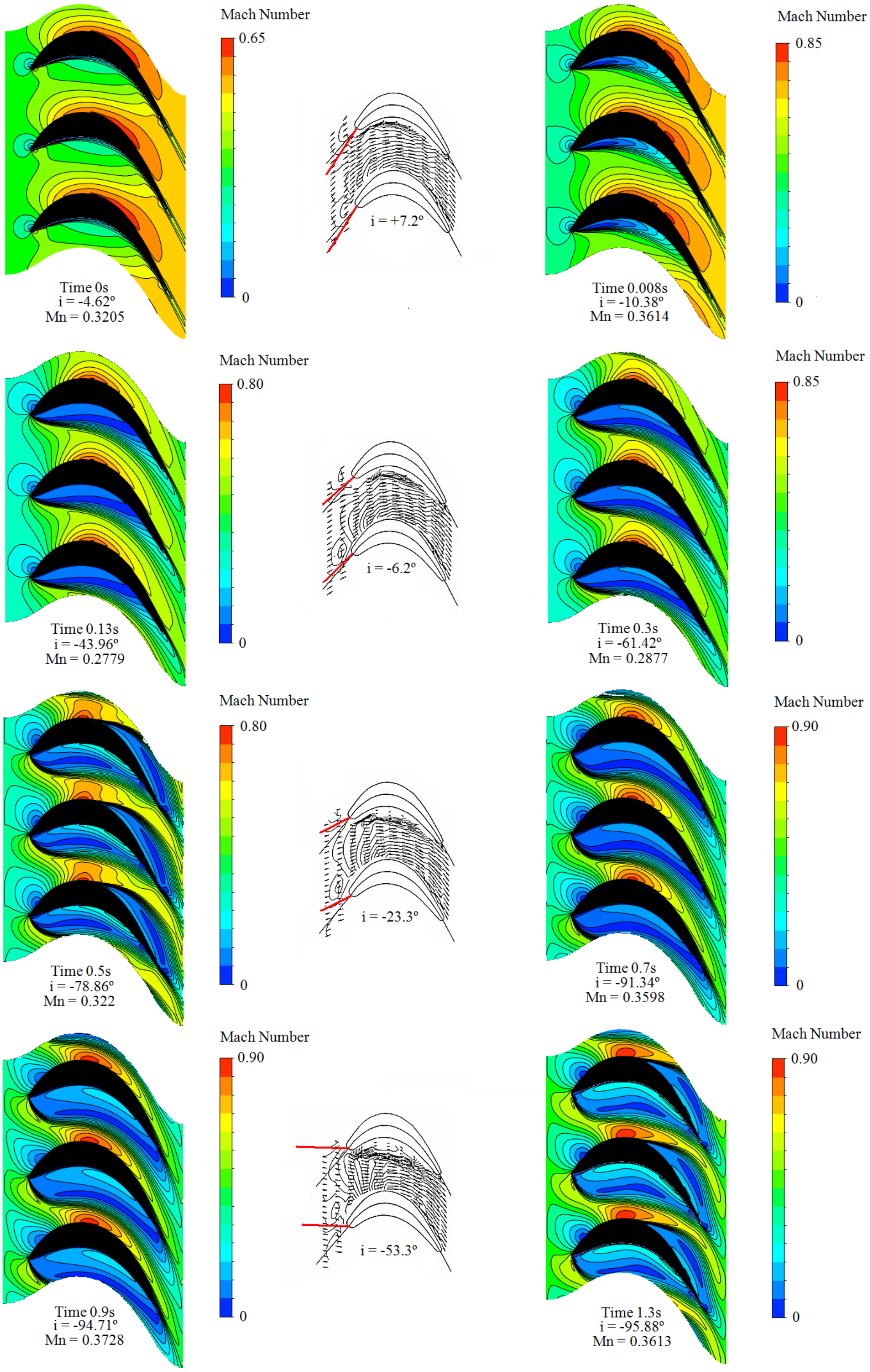

Figure 4.5: *Simulation of the shaft over-speed event - Contours of Mach number at mid-span and comparison with the data from Yamamoto [199]*

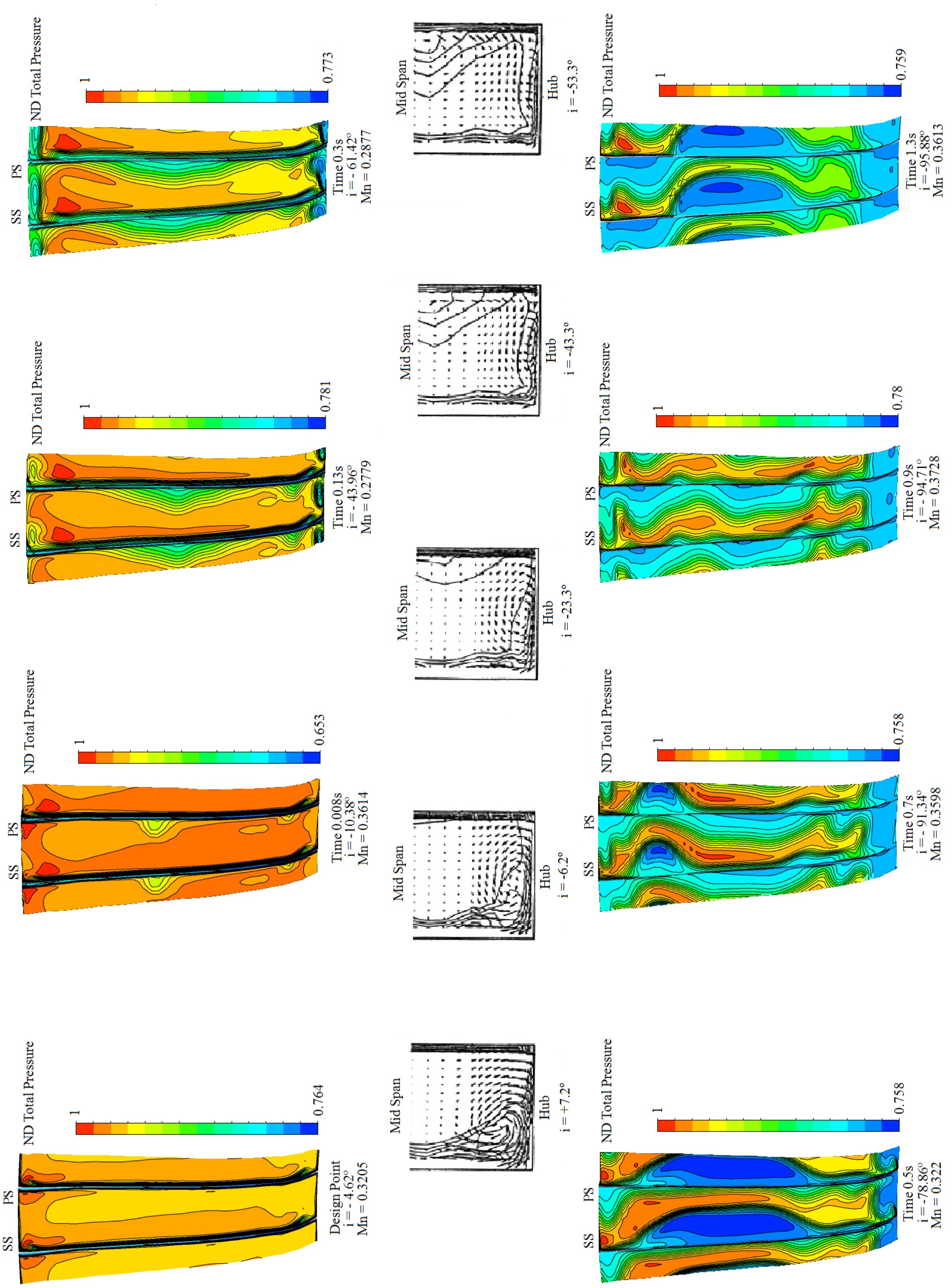

Figure 4.6: *Simulation of the shaft over-speed event - Contours of total pressure at the trailing edge and comparison with the data from Yamamoto [199]*

the flow on the pressure surface separates again. Throughout the event there is a progressive reduction in effective passage area and although the mass flow drops the Mach number at the throat section remains close to unity. The qualitative comparison with the flow structure from Yamamoto is satisfactory (fig. 4.5).

Figure 4.6 shows the total pressure profile during the event on a plane at the trailing edge of the NGV. Comparison against the experimental data from the two-dimensional linear cascade rig of Yamamoto and Nouse is not straightforward because the effect of incidence is masked by the 3D flows originated by the non two-dimensional geometry of the vane. Moreover, the experiments carried out by Yamamoto are limited to $-53°$ incidence and this is reached just two tenths of a second after the breakage. As the event progresses the passage vortex becomes weaker and the boundary layer over the endwalls thickens significantly. For moderate negative incidences the separation from the leading edge becomes stronger and reaches the trailing edge of the blade on the pressure surface at mid span. This is consistent with the loss profiles reported by Yamamoto and grouped in the middle column of figure 4.6. For incidences smaller than $-70°$ the flow breaks down at several locations along the span and it becomes very difficult to interpret, although generalised high loss regions spread throughout the passage.

4.3 Turbine nozzle guide vane rig

There is a considerable uncertainty peculiar to far off-design CFD calculations in turbomachinery components. The low speed nozzle guide vane rig constitutes an outstanding validation platform to evaluate the capability and accuracy of the numerical simulations. The experimental data is also of particular interest to the sponsor to validate their in-house numerical CFD code.

4.3.1 Rig design

4.3.1.1 Previous work carried out at Cranfield University

First attempts to design the experimental rig are due to Darragh McGrath [120] and Simone Serrajotto [163] that investigated the suitability of different rig configurations to produce reliable results, provided a first insight into the flowfield and identified the main problems that could arise from the cascade tests. They concluded that a suction cascade rig with a rectangular chamber to accommodate the wake would provide adequate results. However the simulations intended to provide a preliminary design (2D, low number of elements, first order schemes, etc.) and the final dimensions of the rig required additional higher fidelity simulations to refine the design.

4.3.1.2 Rig configuration

The test rig lay out consists of a bell mouth subsonic intake, a plenum chamber that contains the blades and an outlet duct that connects the plenum with a fan in suction mode that drives the flow across the cascade (figs. 4.7, 4.8a and 4.8b). This arrangement has been employed successfully by other researchers [69][145]. The intake was manufactured to comply with the British Standard BS 1204 and was fitted with a flow straightener to guarantee a uniform flow profile onto the blade row. The plenum chamber has been designed with the aim of providing a periodic wake between adjacent passages for all incidence angles under study. To this regard, a rectangular chamber has been found suitable to minimise the interactions from the walls and accommodate the strong shear flows present on the first and last blade passages whilst keeping a periodic wake profile. The convergent discharge duct has been engineered to receive the wake and avoid its direct impingement on the walls of the plenum. It is later demonstrated that if such impingement occurred it shall have a very pernicious effect on both the wake uniformity and the convergence of the simulations. Finally, an additional flow straightener at the fan's face provided an effective barrier to fan induced swirls.

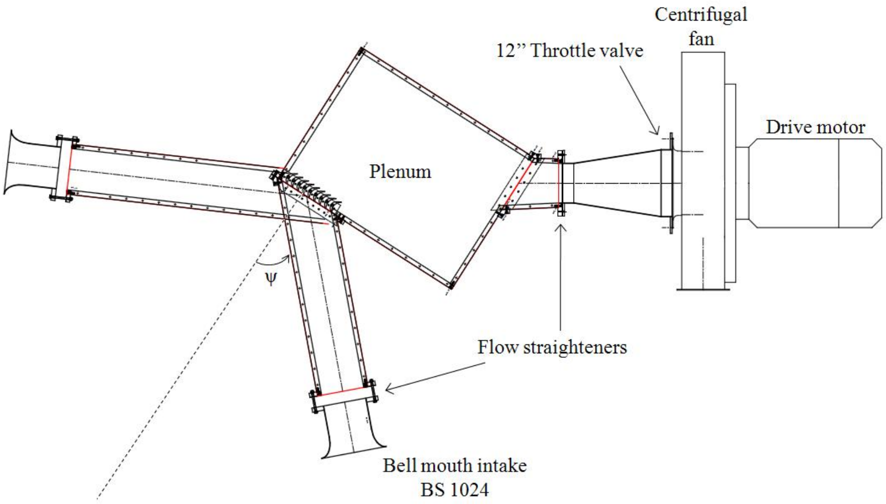

Figure 4.7: *Turbine NGV test rig assembly*

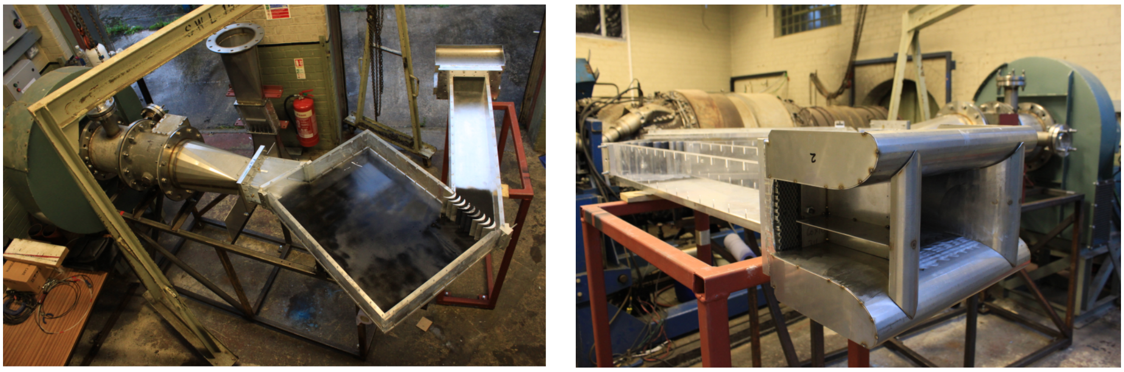
(a) *View from above*
(b) *Bell mouth intake*

Figure 4.8: *Rig assembly for the 0° incidence configuration*

It was decided to test the turbine vanes in a linear cascade arrangement as an alternative to an annular configuration. This is because, since the tests are ideated to build a calibration/validation platform for the CFD simulations rather than to provide a detailed investigation of the blade performance, the linear cascade configuration constitutes a solution easier and cheaper to design, manufacture and assemble than the annular cascade. The tested NGV vanes are straight and two-dimensional to avoid radial flows that would mask the flow separation and capacity loss that arise from the effect of incidence only. Details of the cascade geometry are grouped in table 4.2.

Table 4.2: *Cascade geometry data*

Blade chord	67mm
Maximum thickness	12.4mm
Blade spacing	30mm
Stagger	24.77°
Camberline angle at the l.e.	43°
Camberline angle at the t.e.	-59°
Leading edge radius	0.88mm
Trailing edge radius	0.62mm
Span	120mm
Aspect ratio	1.79
Solidity	2.23
Number of blades	9

Given the wide range of flow angles and velocities onto the NGV encountered during the shaft over-speed event, the experiments must cover a number of incidences and mass flows for the validation against CFD to be representative and trustworthy. Four different incidence angles - 0°, $-43°$, $-78°$ and $-113°$ - at three different Mach numbers each have been tested in the rig. For each incidence angle and flow velocity - an overall 12 different operating conditions - profiles of total and static pressures and flow direction and velocity are measured at two different locations downstream of the trailing edge of the NGVs.

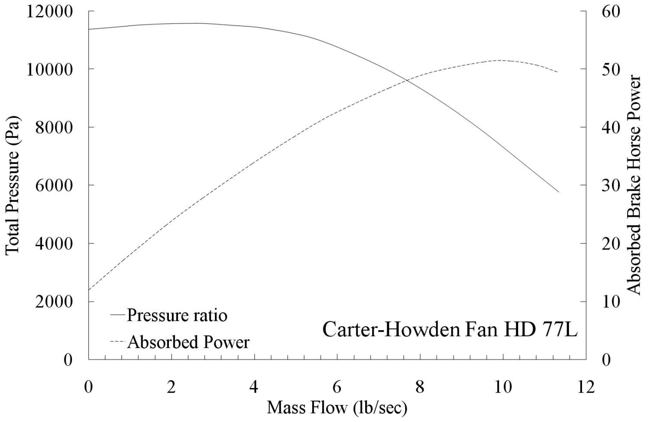

Figure 4.9: *Carter - Howden HD77L Fan Performance*

4.3.1.3 Fan performance

The fan performance is fundamental to estimate a priori the mass flow available across the cascade. The machine is a centrifugal Carter - Howden HD77L fan driven by a 50 brake horse power electric motor and capable of producing a maximum mass flow of 12 pounds per second (fig. 4.9). The fan is fitted with a 12” throttle valve that allows the user to modulate the static pressure at the outlet of the plenum chamber, and hence change the pressure drop across the cascade to attain different mass flows and Mach numbers.

4.3.1.4 Rig geometry definition

The simulation domain is delimited by both flow straighteners upstream and downstream of the test section. For the test rig to be designed and optimised for the pursued objectives (rig as a CFD validation platform) and the resources available (chiefly the power from the fan), careful consideration of other geometrical aspects is required. Particularly, the choice of the plenum width and shape, the blade aspect ratio and the number of blades to be tested demands detailed investigation.

The choice of the chamber width and its general arrangement is dictated by the need of a clear uniform wake that is allowed to develop free from any impingements on or gradients originated from the plenum walls. To this regard, if the plenum outlet was not far enough from the blades trailing edge the pressure profile at the outlet would be affected by the fan and those disturbances would propagate upstream to the test section invalidating the experimental results. In a similar fashion, if the funnel did not accommodate the wake in its whole width for the whole range of incidences to be tested the impingement with the walls, even if small, would give raise to disturbances on the flow field that would travel upstream and affect the flow profile on the measurement sections. This is demonstrated by figure 4.10a. The flow hits the plenum corner (1) and decelerates (2) to accelerate again in the convergent outlet funnel. The impingement causes a velocity deficit on the lower passages (3) and the wake is smoothly deflected (4) towards the bottom wall. As a result the cascade wake presents a severe pitchwise velocity gradient that spoils the uniformity of the wake (fig. 4.10b). Furthermore, not only the wake uniformity is compromised but the simulation convergence is hampered severely. The likely explanation is due to the transient character of the vortices that appear in the recirculation area around the impingement region. Such unsteady effect cannot be captured with steady simulations and introduces some oscillations on the simulation residuals that risk the convergence of the calculations.

On the one hand, the choice of number of blades and the cascade aspect ratio is dictated by the necessity to assure the periodicity of the wake and minimise the effect of the endwall flow on the measurements. This can be achieved for a large number of blades and high values of their aspect ratio. On the other hand, however, for wider test sections the power required from the fan to build up a pressure drive able to accelerate the flow up to the desired Mach numbers would exceed that available (fig. 4.9). Nine turbine NGV blades with an aspect ratio of 1.79 are found to be an adequate compromise to minimise endwall effects and provide representative Mach numbers.

4.3.2 Preliminary investigation of the flow field in the rig

The investigation of the flow field that develops in the test rig serves several purposes. To begin with, the preliminary insight into the flow field brings to light potential areas of concern like radial flows, impingement with the plenum walls and non periodic effects on the wake of the vanes. Furthermore, the study of the CFD simulations of the rig is paramount to make a judgement on the type and location of the instrumentation that is to be employed to obtain meaningful results.

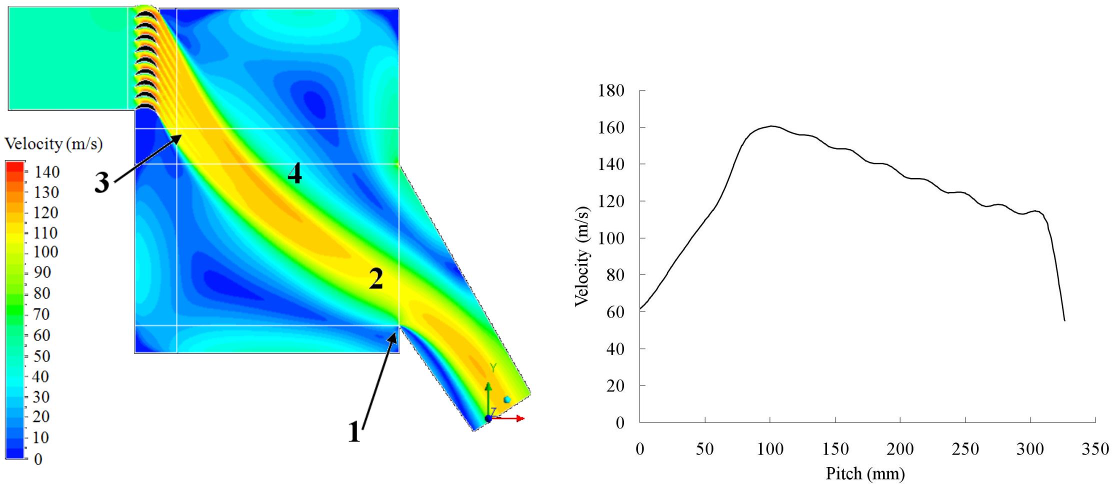

(a) *Velocity contours at mid span*

(b) *Wake profile half a chord downstream of the trailing edge*

Figure 4.10: *Effect of wake impingement on the plenum walls on the flow field - −43° incidence Atmospheric inlet conditions and 91KPa backstatic pressure*

4.3.2.1 Two-dimensional simulations

Initially the flow field was investigated by means of a set of 2D simulations whose results are depicted in figure 4.11 at 0°, −43° −78° and −113° incidence angles for a prescribed pressure gradient between the inlet and outlet interfaces. The highest peak local velocity across the cascade occurs at the greatest negative incidence resulting from the greater passage blockage induced by the recirculation flow present on the blade pressure surface. The velocity and total pressure profiles obtained half a chord downstream of the trailing edge of the blades (figs. 4.12a and 4.12b) show that the wake uniformity is guaranteed throughout the whole range of incidences to be tested. Bearing in mind that conditions at the inlet are atmospheric for all the simulations, the pressure loss increases as incidence departs from the nominal (0°) whereas the average velocity of the wake decreases. This is expected because the same pressure drop across the cascade for all the simulations must overcome the greater pressure losses that occur at −113° leaving a smaller pressure difference to accelerate the flow. It can also be observed that the wake is smoother as the incidence decreases due to the effective mixing of the flow promoted by the larger separation regions. This will be confirmed by the experimental results (see figure 4.28).

Attention is drawn to the subtle pressure rise that appears on the right side (pitch-wise coordinate around 0.18m) of the total pressure distribution for an incidence angle of −113°. This undesired behaviour of the wake is explained by the absence of a stagnation point on the surface of the rig when a certain negative incidence angle is surpassed. This will be more evident at the light of the 3D results reported in the next section.

4.3.2.2 Three-dimensional simulations

In order to investigate the interaction of the end wall flows with the free stream across the blades a set of 3D high fidelity CFD simulations was carried out for a number of different flow incidences

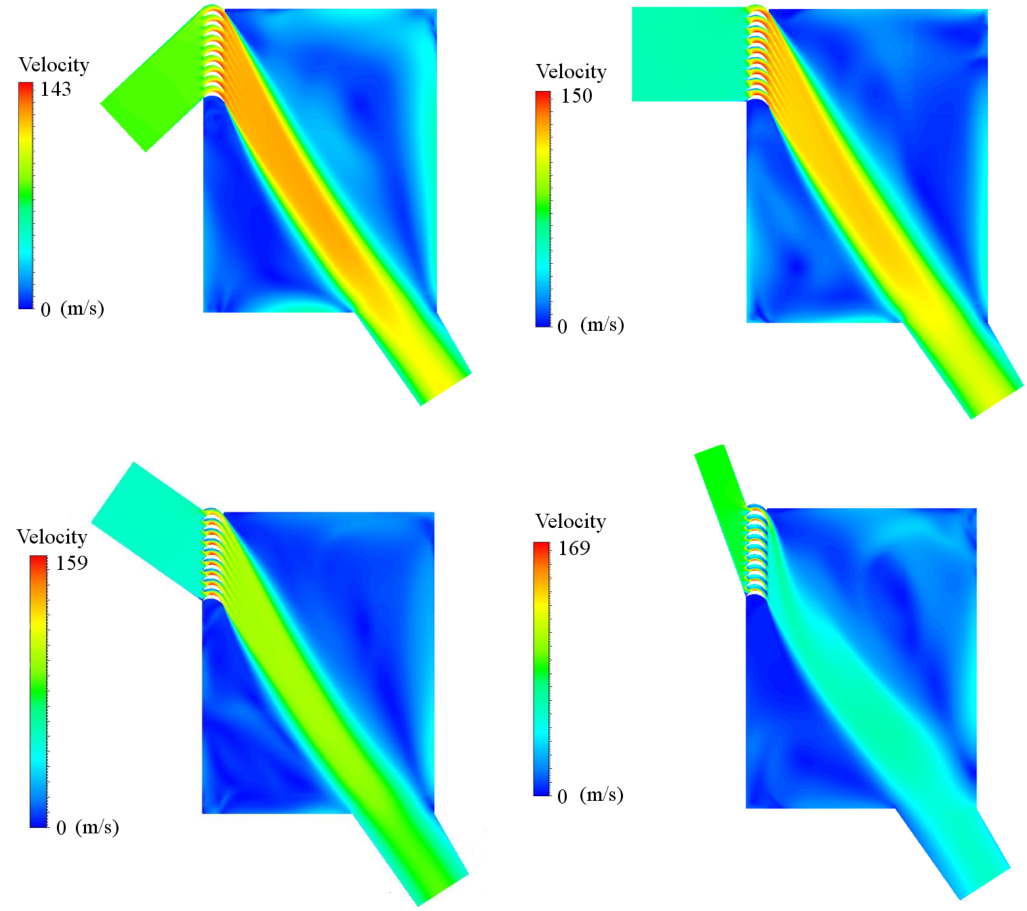

Figure 4.11: *Rig 2D CFD simulations - Mid span velocity field for* 0°, −43°, −78° *and* −113° *incidence angles. Atmospheric inlet conditions and 91KPa backstatic pressure*

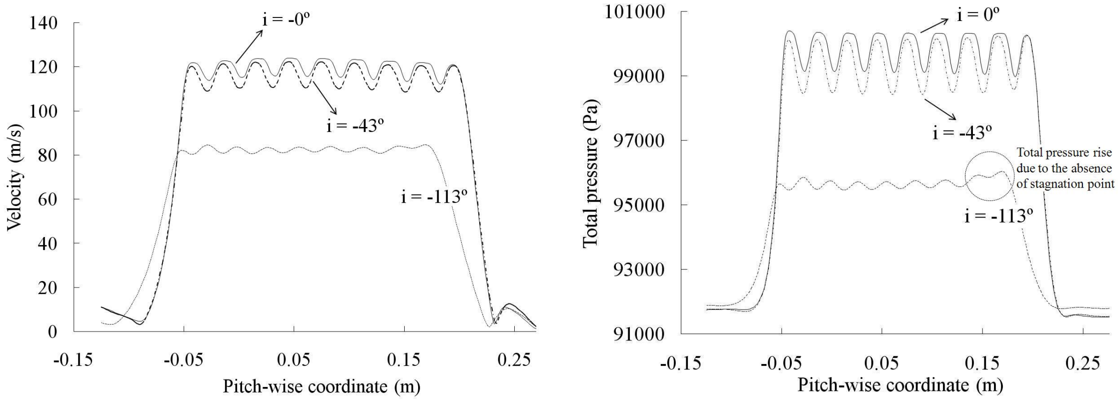

(a) *Velocity profiles at mid span* **(b)** *Total pressure profiles at mid span*

Figure 4.12: *2D rig simulations - Total pressure and velocity profiles half a chord downstream of the trailing edge for a range of flow incidence angles*

onto the blades. At mid span the flowfield for the lowest (design) and highest (far negative off-design) incidences is depicted in figures 4.13a and 4.13b respectively. The main difference between

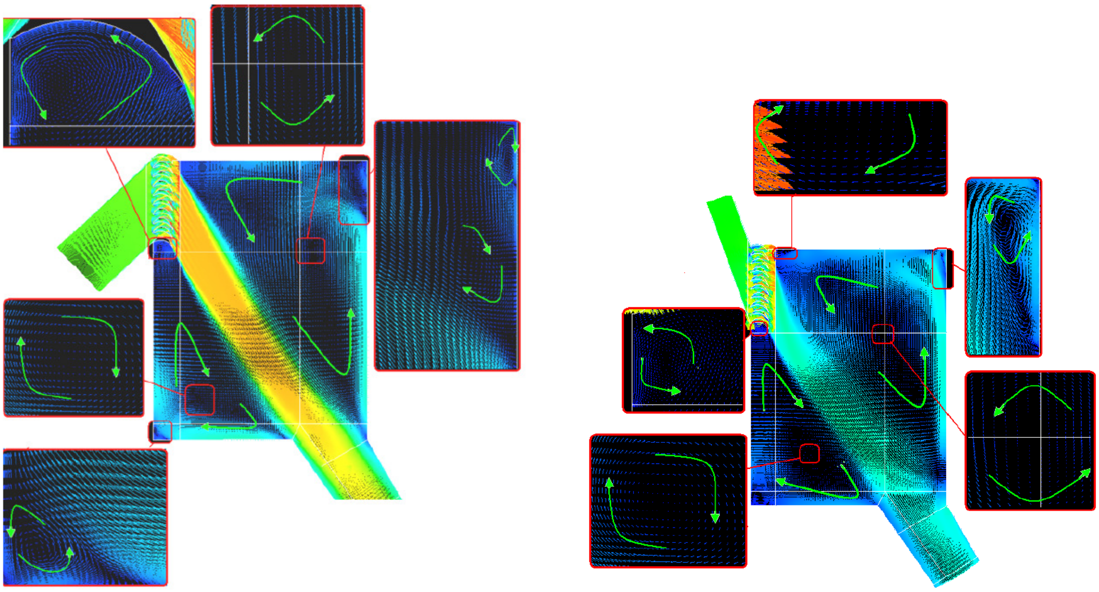

(a) *Incidence* 0° **(b)** *Incidence* −113°

Figure 4.13: *Flow velocity vectors at midspan for atmospheric inlet conditions and 91KPa backstatic pressure*

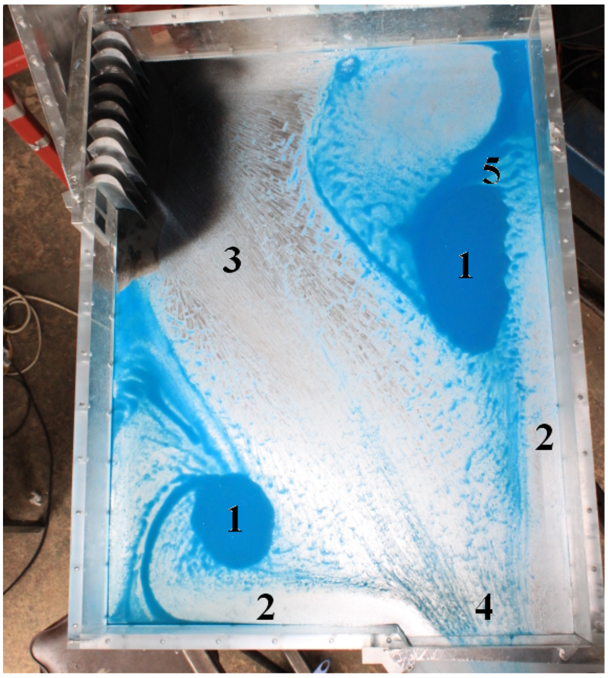

Figure 4.14: *Flow visualisation on the endwall of the chamber at* −113° *incidence angle*

the cases is the lower average wake velocity of the off-design case which is due to the reduced capacity for the same pressure drop across the cascade (increased pressure losses). Besides, another minor qualitative dissimilarity that can be observed is the different strength of the vortices that develop in the proximities of the corners of the plenum chamber. The visualisation of the flow on the endwall of the plenum with a mixture of oleic acid and acrylic paint agrees closely with the structure predicted by CFD. Figure 4.14 shows two strong counter rotating vortices (1) at both sides of the wake (3) that are fed by strong flows over the walls of the chamber (2). The wake presents a core region where the streamlines are parallel (3), surrounded by two outer shear layers where the flow decelerates to rest. The wake is straight and does not impinge on the plenum walls and is perfectly accommodated by the downstream funnel (4), avoiding the undesired behaviour explained earlier and shown in fig. 4.10a. Intermittent waves on low velocity regions (5) are due to the small vibrations induced by the fan on the rig assembly.

The abnormal velocity rise found only on the upper passage of the cascade was further investigated and at the sight of the results it was concluded that the lack of a stagnation point on the upper passage for incidences smaller than −43° leads to such acceleration of the flow. Figure 4.15 illustrates that, unlike the rest of the blade passages, the flow through the upper passage does not undergo the deceleration and turning needed to get around the leading edge. This generates a smaller recirculation bubble and a greater flow acceleration than across the remaining passages for whom the wake uniformity is guaranteed.

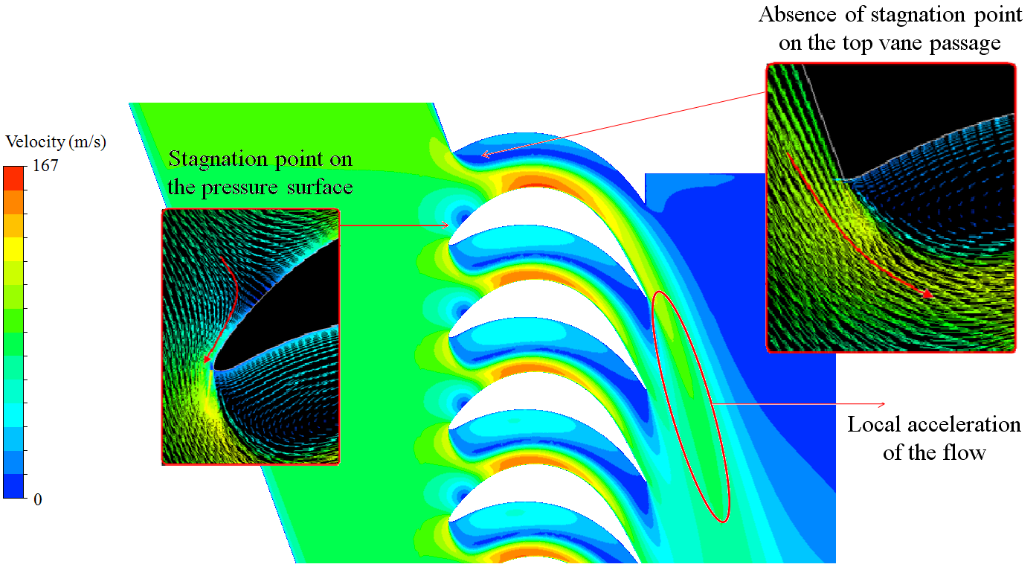

Figure 4.15: *Flow acceleration on the upper passage*

For what concerns the interaction between the end wall flows and the core flow through the cascade, the simulations show a strong radial flux that migrates towards the blade mid span as a result of the interaction between the horseshoe vortex at the tip of the blades and the boundary layer that develops over the chamber walls. The radial flow is illustrated in figure 4.16. The figure shows the intersection of a circumferential plane located at mid chord with a blade to blade plane located close to the hub and at mid span respectively. Close to the hub, the horseshoe vortex entrains the endwall boundary layer, rolls up and drives the flow towards the blade midspan. This radial flow is driven by the passage vortex into the recirculation bubbles on the pressure surface of the blades resulting in two enlarged detached high loss regions that roll up and grow towards the mid span of the cascade as the flow incidence decreases. Eventually those two build ups of low energy fluid coalesce and merge into a single high loss region on the pressure surface at mid span, as seen in figure 4.16. This structure is in accordance with that observed experimentally by Yamamoto and Nouse [199].

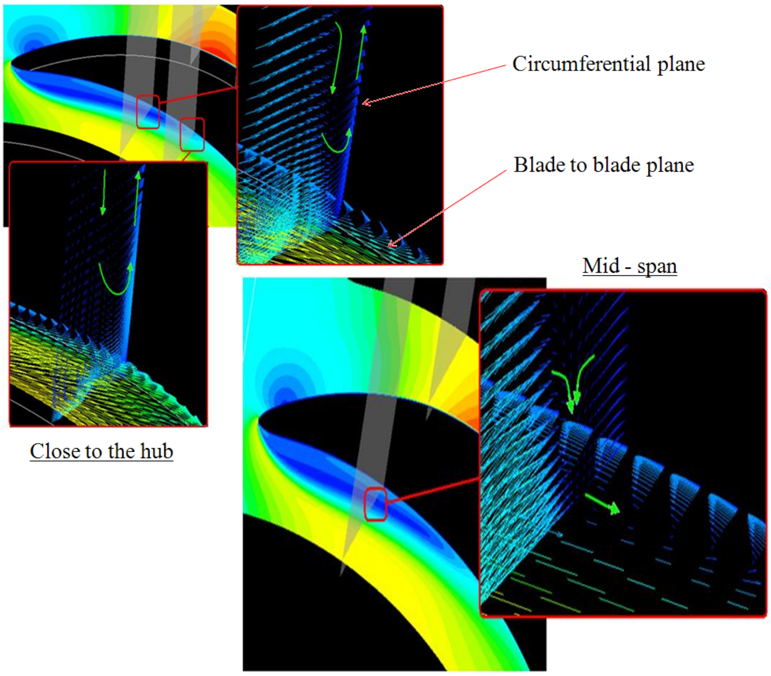

Figure 4.16: *Velocity vectors on a circumferential and blade to blade planes close to the hub (left) and at mid span (right)*

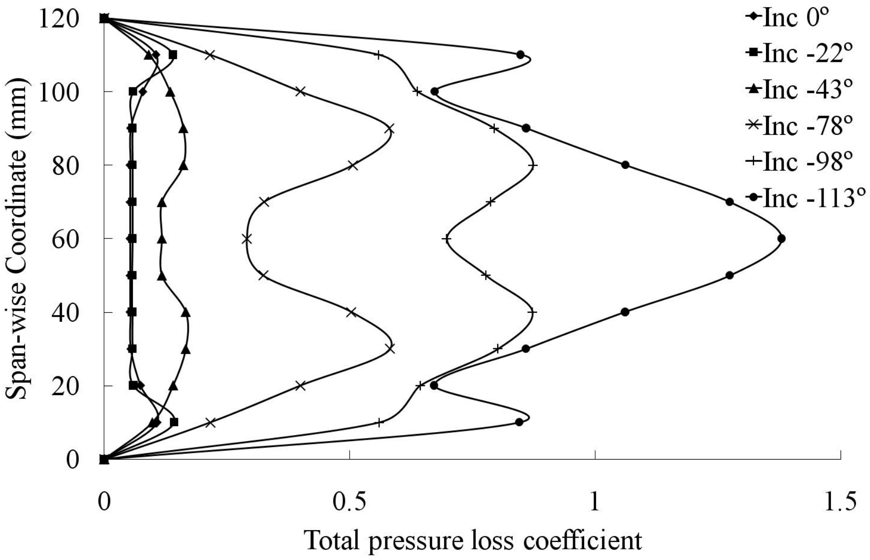

Figure 4.17: *Span-wise total pressure loss coefficient distribution at the trailing edge for a range of flow incidences*

Figure 4.17 shows the circumferentially averaged total pressure loss coefficient along the blade span at the trailing edge of the blades for a set of flow incidence angles. The pressure loss shows two incipient spikes symmetrical to the blade mid span for an incidence of 0° that progress towards the mid span as incidence decreases until they coalesce into a high loss region at mid span. The particular incidence values for which this happens depends on the Mach number of the incoming flow.

4.3.2.3 Unsteady 3D simulations

Large flow separation and wall effects can give rise to transient effects that may affect acutely the behaviour of the flow. In order to disregard the unsteadiness of the flow under study, transient simulations have been completed for the lower and upper incidences considered. The time-step is imposed to be a tenth of the time required for the flow to cover one chord length. Span-wise differences are found to be negligible for all the incidences analysed whereas the variation pitch-wise is less than 1% for all the cases under study as shown in figures 4.18a and 4.18b.

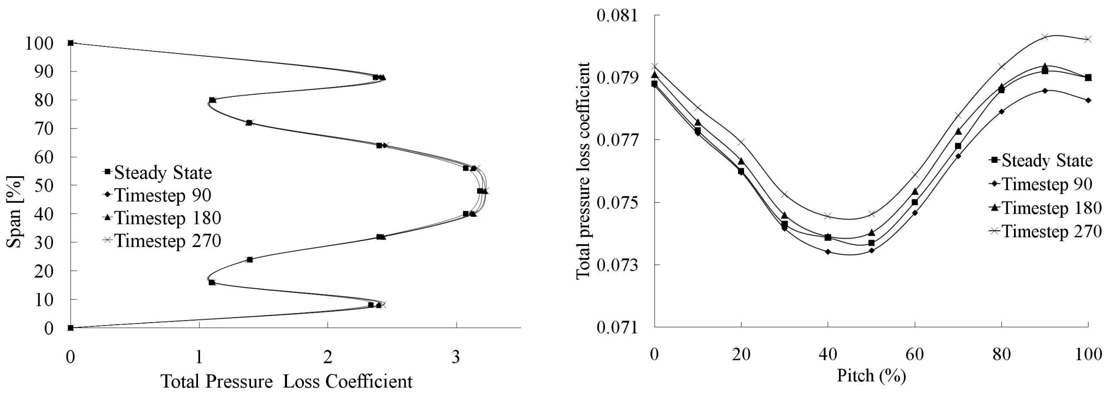

(a) *Pressure loss coefficient versus span at −113° incidence*

(b) *Pressure loss coefficient versus pitch at −113° incidence*

Figure 4.18: *Transient simulations of the NGV rig - Pressure loss coefficient at different time steps*

4.3.3 Instrumentation

The instrumentation used in the rig tests consists of the following:

- A pitot static and a five hole "L" shape pneumatic probes to measure the mass flow through the intake and the wakes downstream of the cascade.
- Static pressure tapings far upstream and downstream of the cascade.
- Piezoelectric pressure transducers that translate the gauge pressure into an electric signal by relating the mechanical stress on a crystalline material to the electrical voltage that appears across it. The range of measurement of the transducers is from 1 to 150mbars.
- A set of amplifiers and low pass filters to amplify the electric signal and eliminate any background noise.
- An analogue-to-digital data acquisition card that receives the signal from the transducers through separate channels and feeds into the post processing software. The card is capable of a maximum sampling rate of 20kHz and a 32-bit resolution.
- A personal computer to post-process the data with the help of a commercial software (Labview).

4.3.3.1 Pitot static pneumatic probe

Mass flow through the rectangular intake of the rig is measured by deriving the velocity from static and pressure measurements taken with a pitot static tube (fig. 4.19) aligned with the flow. Measurements are taken on a grid of 16x30 points spaced 1cm in the central region of the intake and 2.5mm close to the walls to capture the boundary layer with a greater accuracy (fig. 4.20). The location of the measurement plane is three chords upstream of the cascade section to capture the flow field undistorted by the blades. Assuming that the density change with respect to the atmosphere is negligible, the mass flow through the intake is found by integration of the flow velocity on the area of each grid element. A comparison between the measured and simulated mass flows through the intake is provided in table 4.3[2].

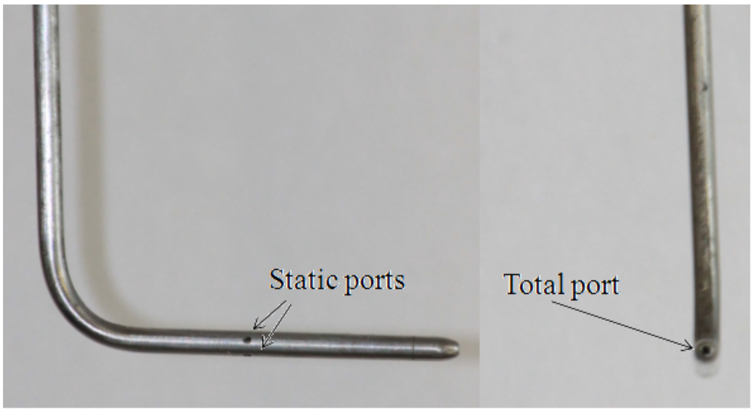

Figure 4.19: *Pitot static pressure probe*

Table 4.3: *Comparison of CFD and rig results of mass flow through the cascade intake for incidences* $0°$, $-43°$, $-78°$ *and* $-113°$ *and three Mach numbers*

	Deviation (%)			
Valve position (Mach number)	$i = 0°$	$i = -43°$	$i = -78°$	$i = -113°$
Open	-0.0070	0.9808	0.5470	0.2456
Semiclosed	0.0114	-0.0990	0.9588	-0.2252
Closed	0.6208	-0.3056	0.7538	-0.3229

4.3.3.2 Five hole pneumatic probe

The measurement of the cascade wake was obtained with a five hole probe that can be traversed at several locations downstream of the trailing edge of the blades (fig. 4.21). The use of a five hole probe instead of a simpler three whole probe is justified by the significant radial flows predicted by the CFD simulations. The choice of the location of the measurement slot is chosen to isolate as much as possible profile losses to wake mixing losses. The first measuring plane is located 5% of the chord downstream of the trailing edge and an additional set of measurements was taken one

---

[2] Positive deviations mean CFD results are greater than experimental.

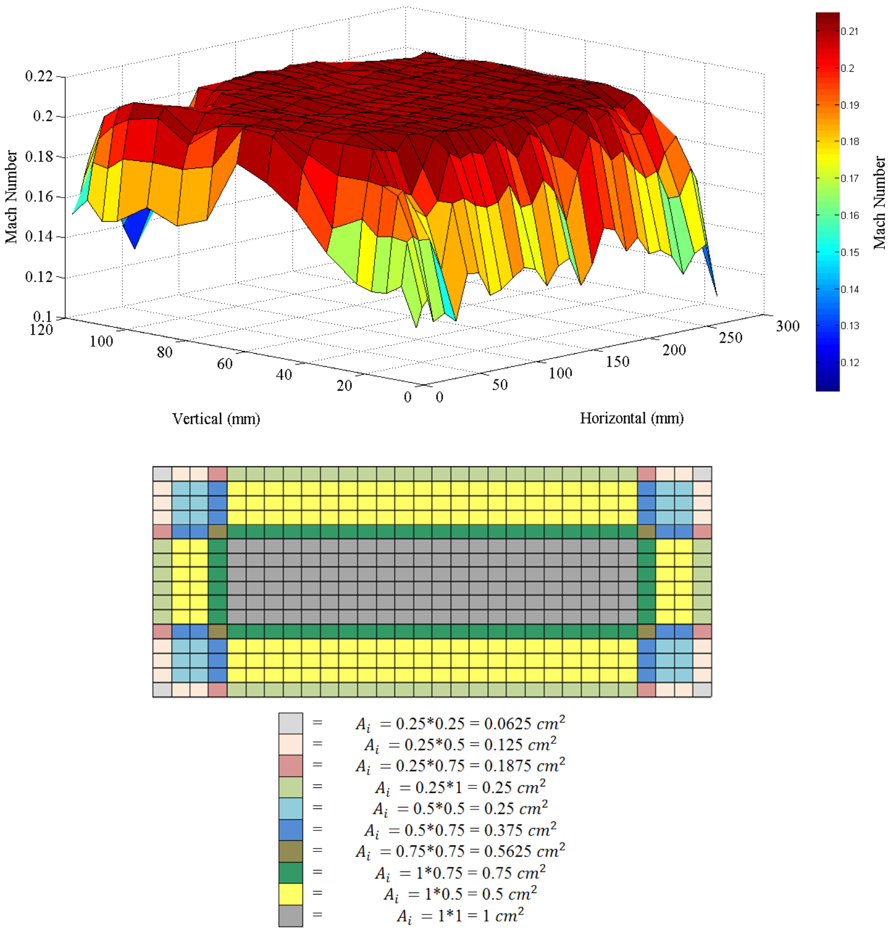

Figure 4.20: *Example of flow Mach number on a plane three chords upstream of the blade section and measurement grid. −43° incidence angle, throttling valve fully open*

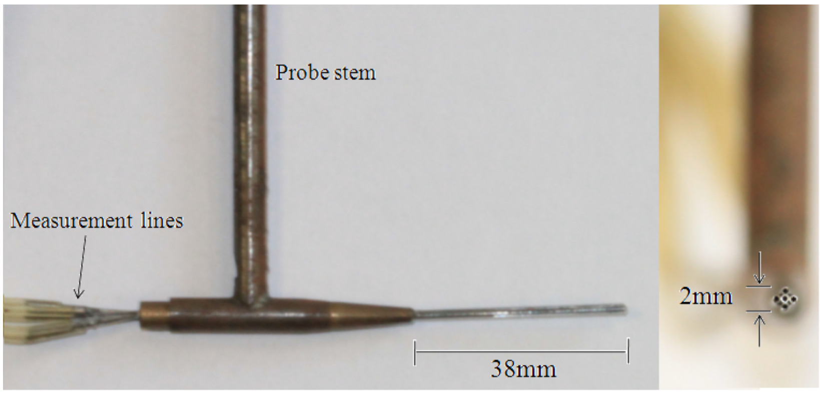

Figure 4.21: *Five hole "L" shape pressure probe*

chord downstream of the trailing edge with the aim of estimating the order of magnitude of mixing losses on the flow.

The use of five hole probes is widely documented in the literature (see for example [8]). In essence, static and total pressures and flow direction are obtained using the ratios of the pressure readings on each hole of the probe. Prior to their use pressure probes need to undergo a calibration process in which the flow incidence onto the head of the probe is varied to cover all possible combinations of pitch (α) and yaw (β) angles (fig. 4.22).

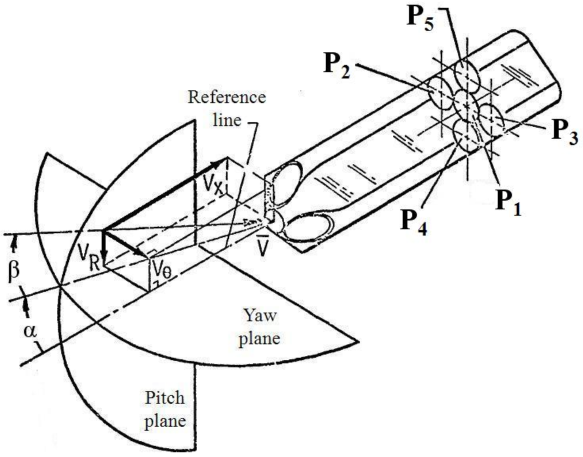

Figure 4.22: *Flow angles onto the five hole probe and hole number definition. Adapted from [177]*

The experimental points measured during the calibration are plotted into maps that manage to correlate univocally the measured pressures on the holes of the probe with the flow direction via the following pressure coefficients:

$$\overline{P} = \frac{1}{4}(P_2 + P_3 + P_4 + P_5) \tag{4.1}$$

$$C_{p\ total} = \frac{P_1 - P_T}{P_1 - \overline{P}} \tag{4.2}$$

$$C_{p\ static} = \frac{\overline{P} - P_S}{P_1 - \overline{P}} \tag{4.3}$$

$$C_{p\ \alpha} = \frac{P_5 - P_4}{P_1 - \overline{P}} \tag{4.4}$$

$$C_{p\ \beta} = \frac{P_2 - P_3}{P_1 - \overline{P}} \tag{4.5}$$

The probe was calibrated following the widely used procedure published by Treaster and Yocum in 1978 [177]. The calibration was carried out in a purposely built wind tunnel capable of achieving a Mach number of 0.5 (fig. 4.23) at three Mach numbers - 0.1, 0.2 and 0.3 - to account for the effect of Reynolds number on the calibration of the probe. An example of the calibration maps obtained for one Mach number are grouped in figures 4.24, 4.25a and 4.25b.

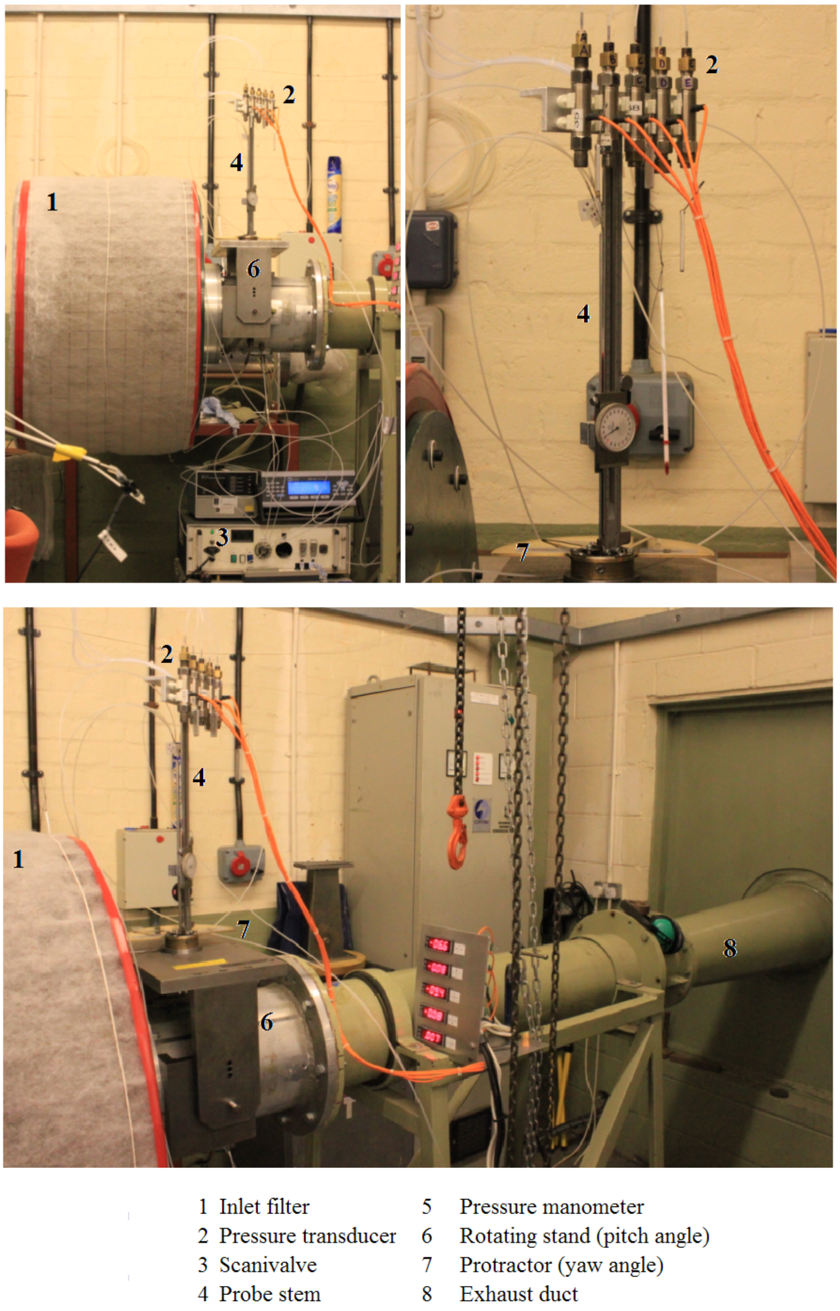

Figure 4.23: *Wind tunnel arrangement for the calibration of the five-hole probe*

4.3.4 Measurements

An overall 9672 experimental measurements were taken on the wake at two different locations downstream of the trailing edge of the vanes: 5% of the chord and one chord downstream. These are split as follows:

Two sets of measurements are taken 5% of the chord downstream of the trailing edge for each incidence angle available (0°, −43°, −78° and −113°) at three different Mach numbers. In the

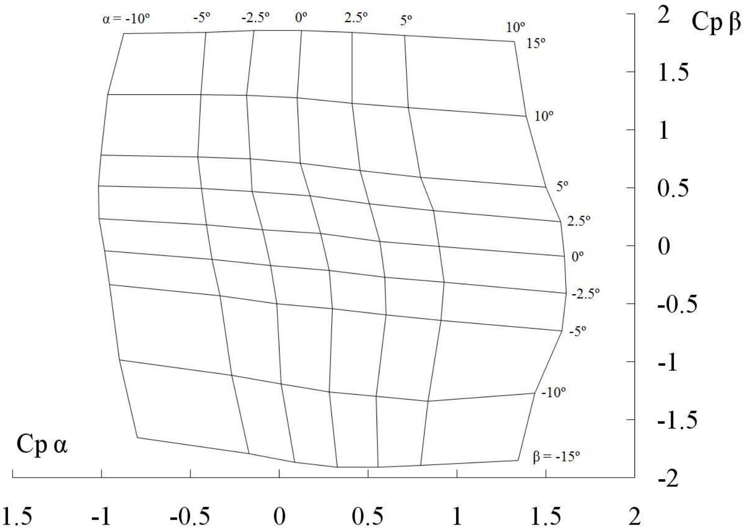

Figure 4.24: *Five hole probe calibration at 0.2 Mach number -* $C_{p\,\alpha}$ *and* $C_{p\,\beta lines}$ *for a range of pitch* α *and yaw* β *angles*

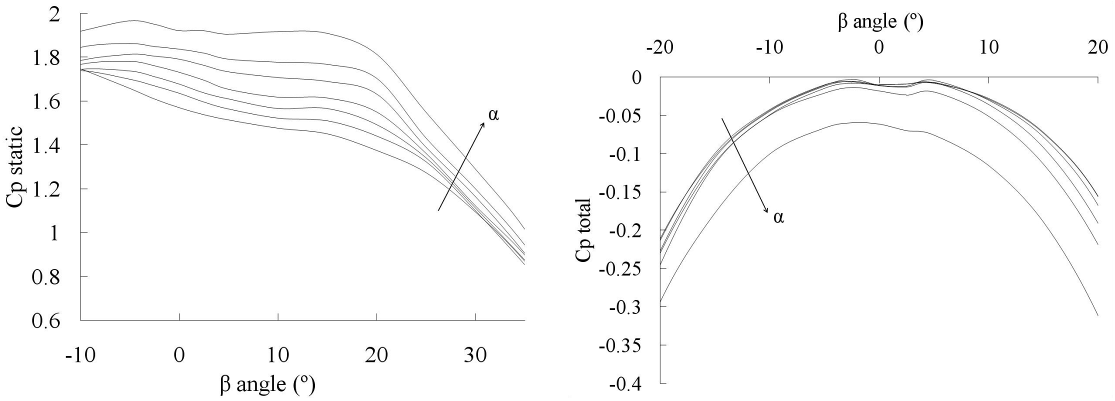

(a) $C_{p\,static}$ *coefficient vs pitch angle for a range of yaw angles*

(b) $C_{p\,total}$ *coefficient vs pitch angle for a range of yaw angles*

Figure 4.25: *Five hole probe calibration at 0.2 Mach number -* $C_{p\,static}$ *and* $C_{p\,total}$ *coefficients*

first set the periodicity of the wake is investigated by measuring 52 points spaced 4mm across the cascade pitch at mid-span. The second set of measurements consists of a grid of 26x27 points distributed pitchwise spaced 2mm and spanwise spaced 4mm respectively to cover a plane slightly smaller than two whole blade passages. These allow to identify and account for radial flows and 3D effects on the flowfield. Due to the size of the probe and its stem, the measurements could only be taken 2mm and 5mm from the hub and tip endwalls.

Measurements further downstream of the trailing edge are limited to sets of 52 points spaced 4mm across the cascade pitch at mid-span on a line located one chord downstream of the trailing edge for each incidence angle tested at three different Mach numbers. The comparison with the data obtained 5% of the a chord downstream of the trailing edge allows for the estimation of the effect of wake mixing on the pressure losses.

Due to the intrinsic unsteady nature of separated flows measurements were averaged over a period of 10 seconds at a sampling rate of 1000Hz. This is appropriate for the harmonic frequencies and amplitudes of the Fourier series decomposition of the signals[3].

Static pressure on two planes upstream and downstream of the cascade are derived by averaging three measurements obtained from 1mm pressure tapings on the intake and plenum walls.

4.3.5 Measurement uncertainty

Experimental studies must be accompanied by the assessment of the uncertainty associated to the measurements. This is essential to ascertain the degree of confidence that can be exercised when handling the rig data. The uncertainty reported here has been calculated following the uncertainty methodology published in 1985 by Abernethy et al. [1] that set the standard approved by ASME.

In essence, the total error is expressed in terms of two components: a fixed (bias) error, and a random (precision) error such that:

$$\delta_k = \beta + \epsilon_k \tag{4.6}$$

The uncertainty of the measurement represents the band within the true value of the parameter being measured is expected to lie, for a given level of confidence. In particular, for a 95% confidence level, the uncertainty is calculated from:

$$U = B^2 + (tS_{\bar{x}})^2 \tag{4.7}$$

where B is the bias of a given magnitude, $S_{\bar{x}}$ is the standard deviation of the mean of the measurements and t is the t-student distribution parameter that depends on the number of measurements.

The parameters B and $S_{\bar{x}}$ are obtained by the root sun square method to combine the standard deviation from every source of error:

$$S_{\bar{x}} = [S_{\bar{x},1} + S_{\bar{x},2} + \ldots + S_{\bar{x},k}]^{1/2} \tag{4.8}$$

$$B = [B_1^2 + B_2^2 + \ldots + B_k^2]^{1/2} \tag{4.9}$$

In the experimental arrangement described in this work the main sources of uncertainty are the five hole pneumatic probe and the piezoelectric pressure transducers, and these are described next.

---

[3] The period of the fundamental harmonic of the Fourier series decomposition of the signal in the worst case scenario analysed is 1s and the amplitude of the second harmonic is 5% of the measurement with a period of 0.2s obtained for the static pressure signal at $i = -113°$

4.3.5.1 Uncertainty associated to the five hole probe and the pressure transducers

The uncertainty associated to the operation of the five hole probe has a double origin:

- Resolution of the protractors used to calibrate the probe. In terms of pitch angle, α, the angular measurement is accurate to ±0.125° whereas the yaw angle, β, is accurate to ±0.5°.
- Systematic error associated to the instrument. This is inherent to the probe and is assessed by measuring the standard deviation of a set of measurements of the same operation point during the calibration of the probe, at the same sampling rate and during the same sampling period as the measurements taken in the rig.

The origin of the uncertainty introduced by the operation of the pressure transducers is threefold:

- Error associated to the pressure indicator manometer used to calibrate the transducers. This error is provided by the manufacturer and is ±0.05% of calibration maximum value.
- Error introduced by the least squares method used to correlate the output voltage of the transducer to the gauge pressure measured respect to the reference.
- Instrument error. This is provided by the manufacturer of the transducer and comprises several causes: combined non linearity of the measurement and hysteresis (±0.1% of the measurement), side to side error (±0.5% of the measurement) and temperature effects (±0.5% of the measurement).

4.3.5.2 Final uncertainty band of the measurements

Table 4.4) groups the values of the uncertainty of the measurements in the worst case scenario encountered in the rig, by direct application of equations 4.7, 4.8 and 4.9.

Table 4.4: *Uncertainty sources and final uncertainty band*

Pressure transducer (instrument)	±49.35Pa
Pressure transducer (calibration)	±10.00Pa
Pressure transducer (least squares)	±11.94Pa
Pressure probe	±0.32Pa
Pressure (Total)	±51.75**Pa**
α **angle**	±0.125°
β **angle**	±0.500°

4.3.6 Experimental measurements and comparison with CFD

4.3.6.1 Mid span measurements

Figures 4.27 to 4.30 group the measurements of the wake 5% of the chord downstream of the trailing edge for the four incidence angles studied at the highest Mach number that the fan can provide for each incidence. Pitchwise spacing between measurements is 4mm. The plots also contain the CFD results on the same location for the same boundary conditions at which the tests were carried out.

Figure 4.27 shows the total and static pressure profiles along the cascade pitch at mid span. For all the incidence angles the periodicity of the wake is noticeable. As the flow incidence decreases the total pressure wake becomes wider, more rounded and less distinct. The difference between the total pressure in the core jet and inside the wake drops from 3,500Pa to 500Pa. Bearing in mind that the inlet conditions for all the incidence angles tested are atmospheric, it is clear that there is a very significant rise in pressure loss as incidence falls, particularly for the smallest incidence angle studied. The mentioned effect of the absence of an stagnation point on the upper passage of the cascade is particularly evident at $-113°$ incidence: the flow does not need to get around the leading edge of the blades, accelerates further and this originates less loss across the first passage.

The different depth of the wake for each passage is attributed to the pitchwise spacing between measurements. This is particularly clear for the design incidence plot. For this case the wake is very thin and it is likely that the measurements are not taken on the exact location where the peak of the wake occurs. Wakes measured on a grid of 2mm spaced points eliminated this effect. The total pressure in the jet shows a clear plateau for the design incidence angle that becomes inclined as incidence decreases until for the smallest incidence the highly turbulent wake promotes a very effective mixing that flattens the profile of the wakes.

Static pressure results show roughly the same behaviour in an inverted manner. Double pressure peaks are thought to occur when the probe is located in the shear layer that separates the wake and the jet flow. The shear layer is thinner for design conditions and it is likely that given the finite size of the head of the probe some of its holes sit on the wake side of the layer and the others on the wake, affecting the measurement. As the turbulence rises and the mixing layer becomes thicker the double peak rounds off, particularly for $-78°$ and $-113°$.

CFD results follow closely the rig data. The different depth of the wakes with respect to the experiments can be traced back not only to the pitchwise spacing between measurements but to the size of the head of the five hole probe as well. Although the head is reasonably small - 2mm - flow measurements taken by pneumatic probes are intrusive and cannot capture steep pressure gradients accurately. This results in a tendency to round off pressure peaks. The numerical simulations predict deeper wakes than the rig data. It was first considered that this may be caused by the difference in turbulent intensity between the rig data and the simulated flow. A preliminary examination of this was carried out (see section 4.3.6.5) but given the challenges that accurate turbulence modelling poses it is suggested that this is investigated in more depth in the future.

Velocity profiles are plotted in figure 4.28. Trends are similar to those shown by the total and static pressure profiles discussed previously. This is expected since velocity is a function of the difference between static pressure and total pressure.

Figure 4.29 shows the pitchwise distribution of yaw (β) and pitch (α) angles at mid span with respect to a line located at constant span and in accordance with figure 4.26. The yaw angle oscillates around 30° for incidences down to $-78°$ with an amplitude of around $\pm5°$. This is consistent with the trailing edge metal angle of $-59°$ ($90° - 59° \approx 30°$). The location of the local peaks coincides with the wake position shown in figure 4.27. CFD manages to capture the average angle values accurately whereas the location of the peaks is slightly delayed for the three incidence values closer to zero. For an incidence value of $-113°$ the average value follows closely the rig data, but CFD fails to predict the relative location of the local peaks.

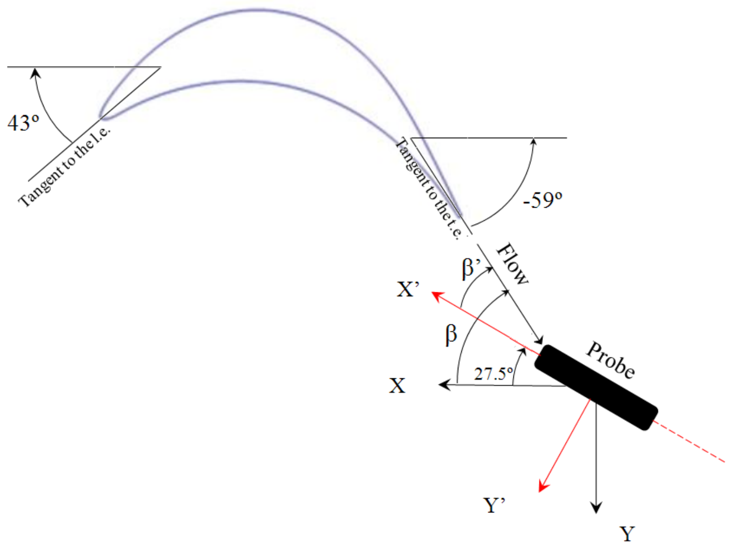

Figure 4.26: *Absolute and relative (linked to the five hole probe) reference frames*

Because of symmetry considerations the pitch angle of the flow at mid span should be zero. The CFD simulations exhibit this behaviour for all incidences simulated and this serves as an additional check of the satisfactory convergence of the numerical simulations. The pitch angle measured in the rig hovers around zero, in a range of $\pm1°$.

The pitch averaged spanwise velocity and total pressure measurements for different incidences and Mach numbers are grouped in figure 4.30. Three-dimensional flow effects are negligible at the design incidence and rise with the departure towards high negative incidences. There are two clear low velocity - high loss regions at approximately 25% and 75% of the blade span at $-43°$ incidence that roll up progressively towards mid span and finally merge into a single low velocity region that occupies most of the blade span for a flow incidence of $-113°$. This is in agreement with the flow field description discussed before (see figure 4.17). However, the rig data shows a greater wake mixing than the predictions from CFD.

The boundary layer flow over the hub endwall is thicker than over the tip of the vane because it is not affected by tip leakage flows. These are particularly important at 0° and their strength diminishes as incidence falls.

The agreement between the rig data and the CFD results is very good at zero incidence (within $2m/s$ difference along the span), and as expected the departure of both increases for far off-design incidences.

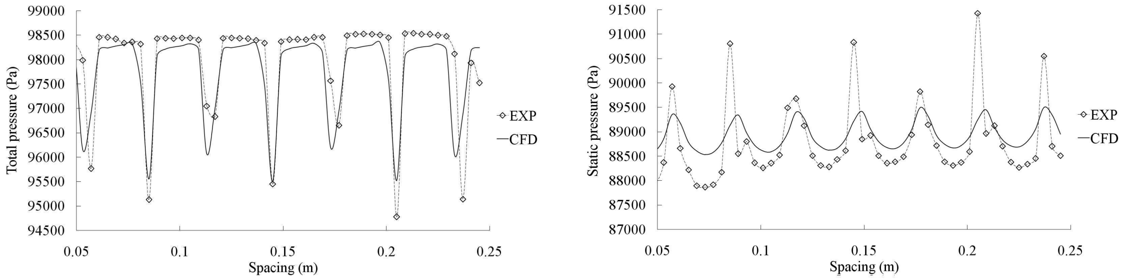

Incidence – 0 degrees
Mach number 0.22

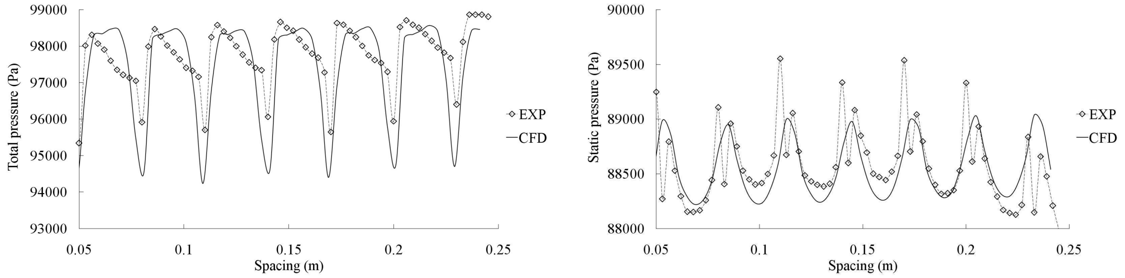

Incidence – -43 degrees
Mach number 0.16

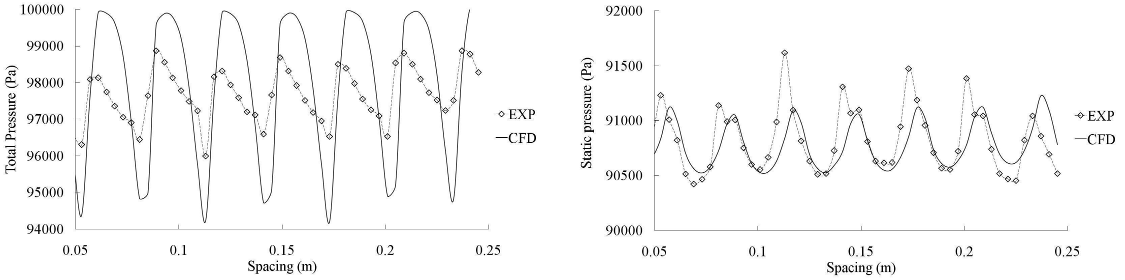

Incidence – -78 degrees
Mach number 0.18

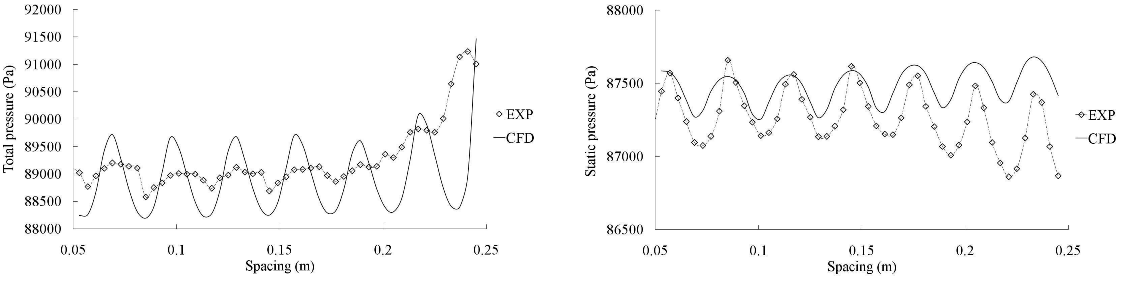

Incidence – -113 degrees
Mach number 0.25

Figure 4.27: *Rig total and static pressure profiles 5% of the chord downstream of the trailing edge at mid span for* 0°, −43°, −78° *and* −113° *incidence angles and comparison with CFD*

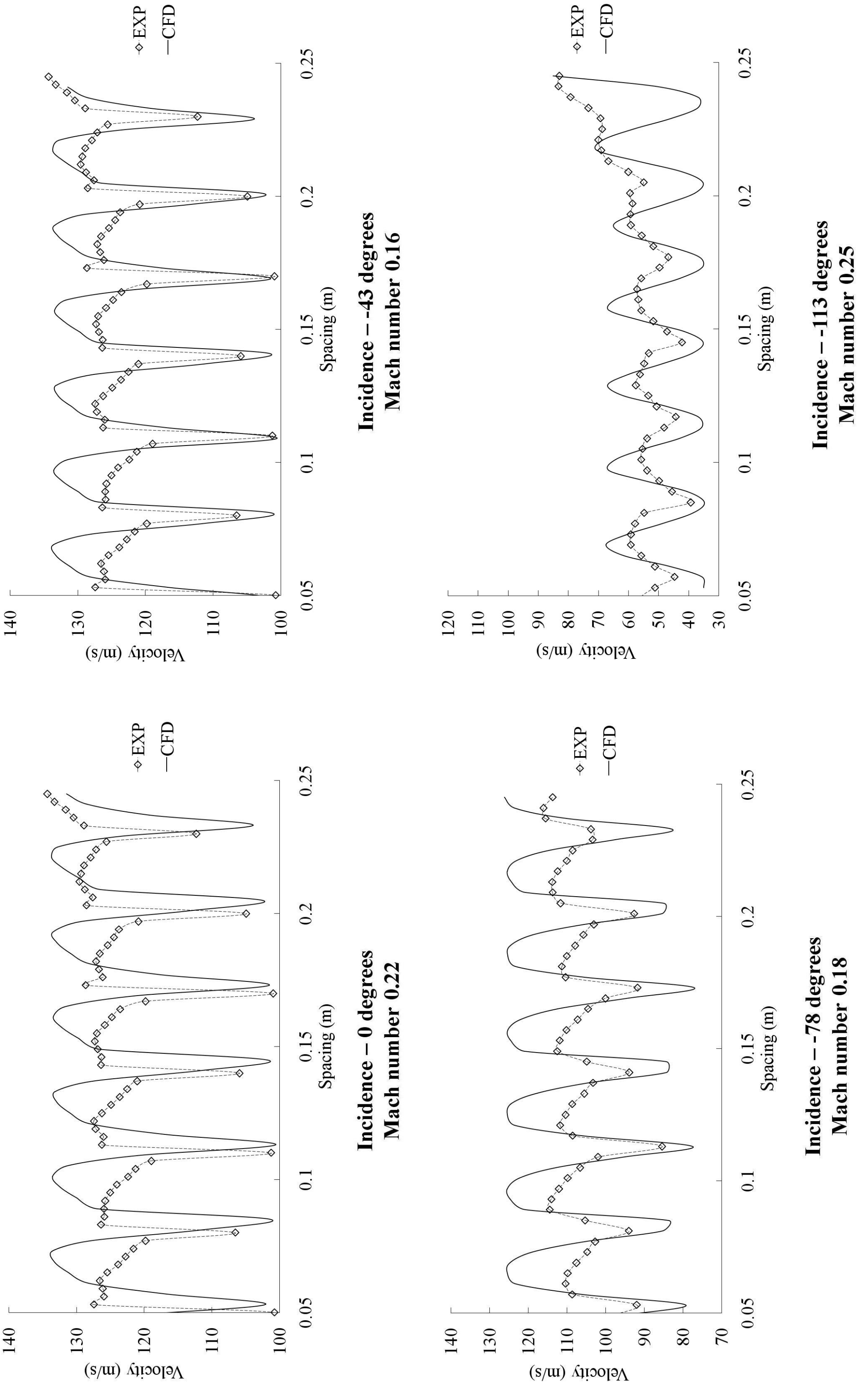

Figure 4.28: *Rig velocity profile 5% of the chord downstream of the trailing edge at mid span for 0°, −43°, −78° and −113° incidence angles and comparison with CFD*

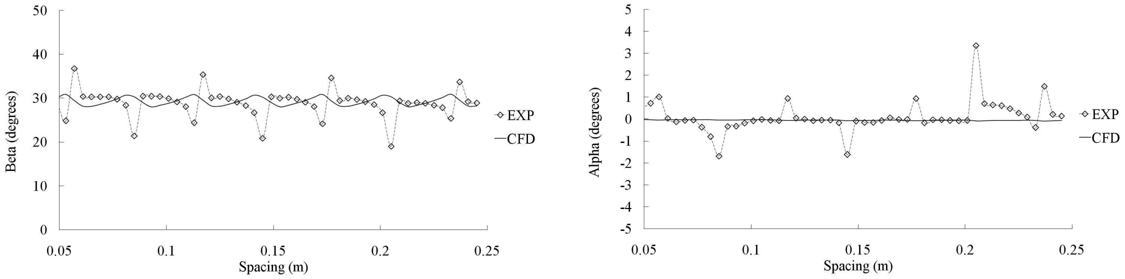

Incidence – 0 degrees
Mach number 0.22

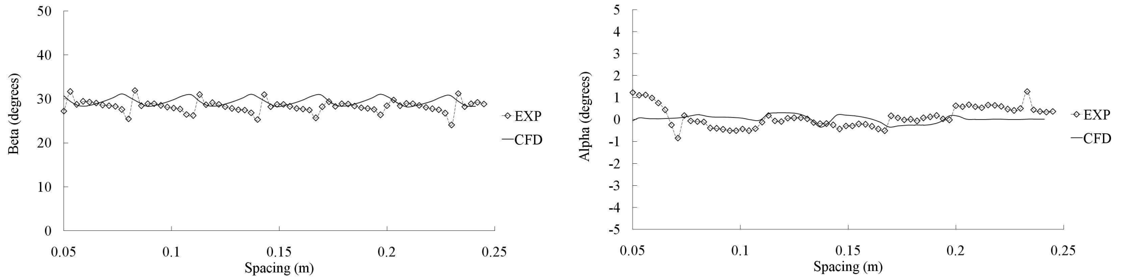

Incidence – -43 degrees
Mach number 0.16

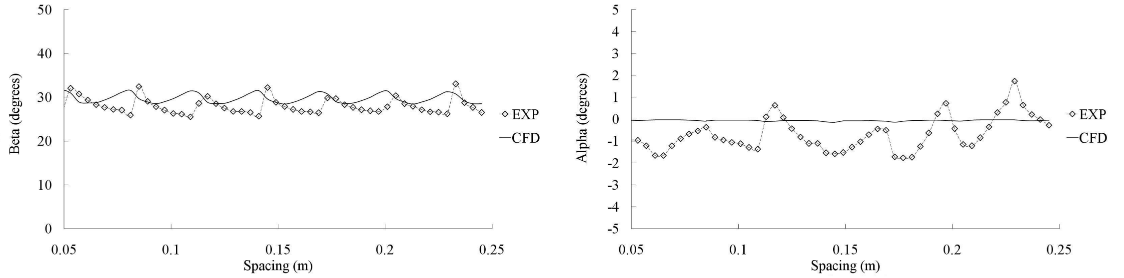

Incidence – -78 degrees
Mach number 0.18

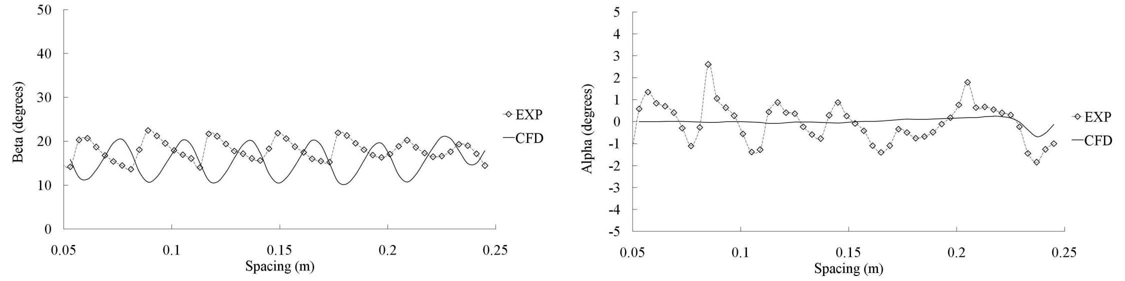

Incidence – -113 degrees
Mach number 0.25

Figure 4.29: *Rig yaw (β) and pitch (α) angle profiles 5% of the chord downstream of the trailing edge at mid span for* 0°, -43°, -78° *and* -113° *incidence angles and comparison with CFD*

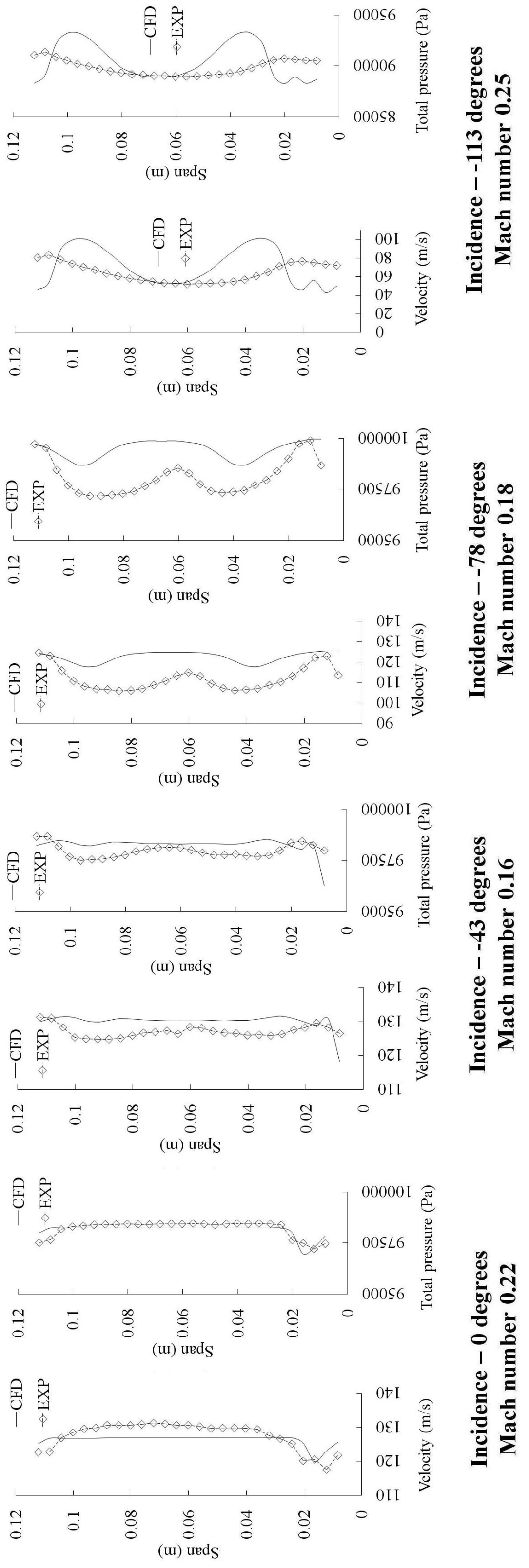

Figure 4.30: *Pitch averaged rig velocity and total pressure profiles along the span for* 0°, −43°, −78° *and* −113° *incidence angles and comparison with CFD*

4.3.6.2 Whole passage flow

Figures 4.31 and 4.32 group the total pressure contours and total pressure loss coefficient on a plane located 5% of the trailing edge, for the four values of flow incidence tested and the comparison with the CFD results. These contours and the flow visualisation studies reported in section 4.3.7 allow to identify the flow structure and the development of high loss regions across the cascade.

At 0° incidence there are two relatively small regions of high loss ($\omega \approx 1.5$) that correspond to the passage vortex that flows over the suction surface at the traililling edge of the blade. The flow away from the vane surface is very clean and the pressure loss coefficient is smaller than 0.1 in the majority of the passage.

The passage vortex becomes smaller and stronger ($\omega \approx 2.1$) as the incidence falls (incidence $-43°$) and two high loss regions develop over the pressure surface at approximately 25% and 75% of the span. For a smaller incidence the passage vortex disappears and the loss peaks over the pressure surface become larger and more intense. For the smallest incidence the loss regions on the pressure surface merge into a single high loss cell that occupies the central portion of the passage.

The vertical strip immediately downstream of the trailing edge of the vane is characterised by a high loss up to an incidence of $-78°$. For the smallest incidence tested the wake is fully mixed and no high loss downstream of the trailing edge can be distinguished.

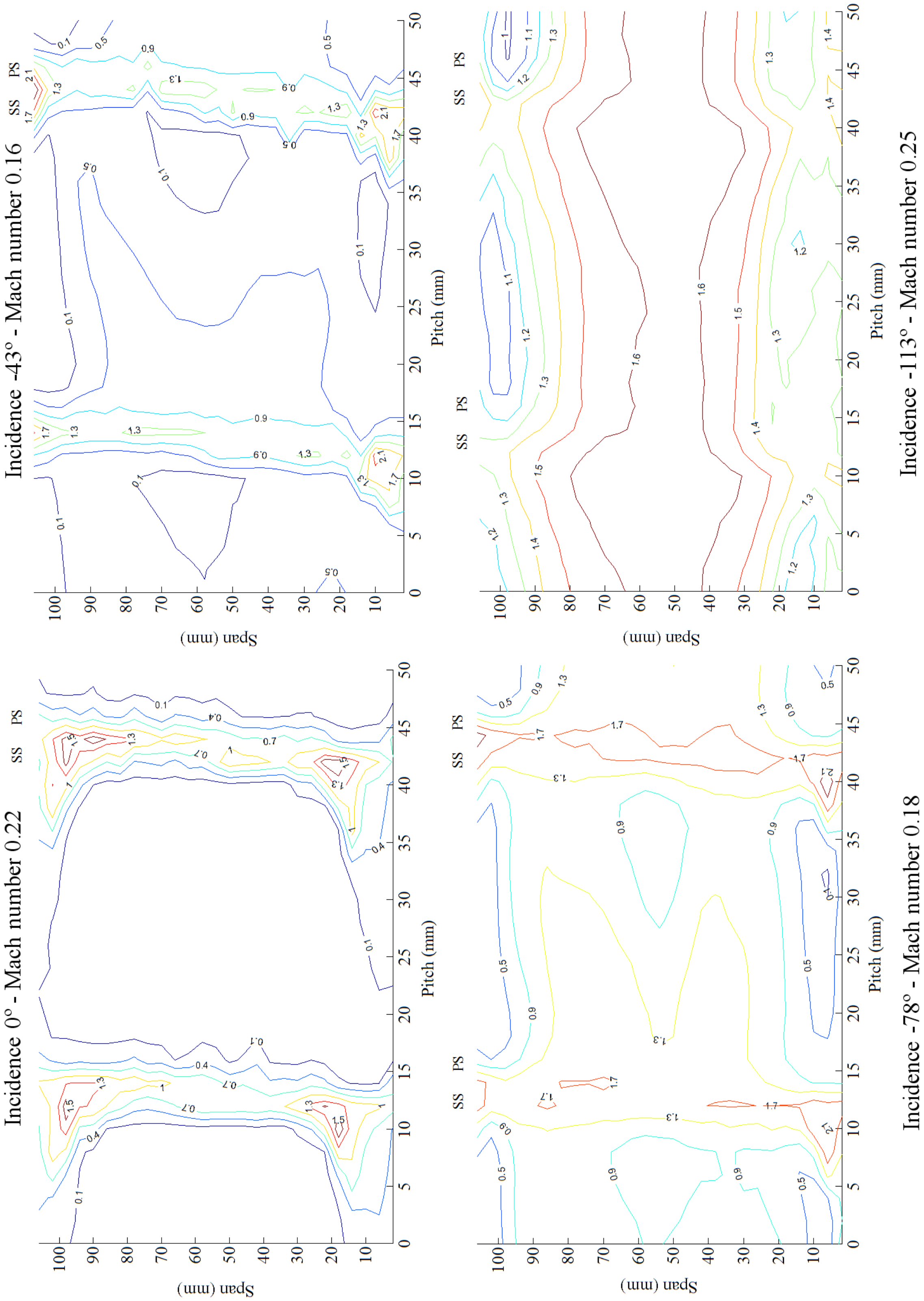

Figure 4.31: *Pressure loss coefficient contours 5% of the chord downstream of the trailing edge for* 0°, −43°, −78° *and* −113° *incidence angles*

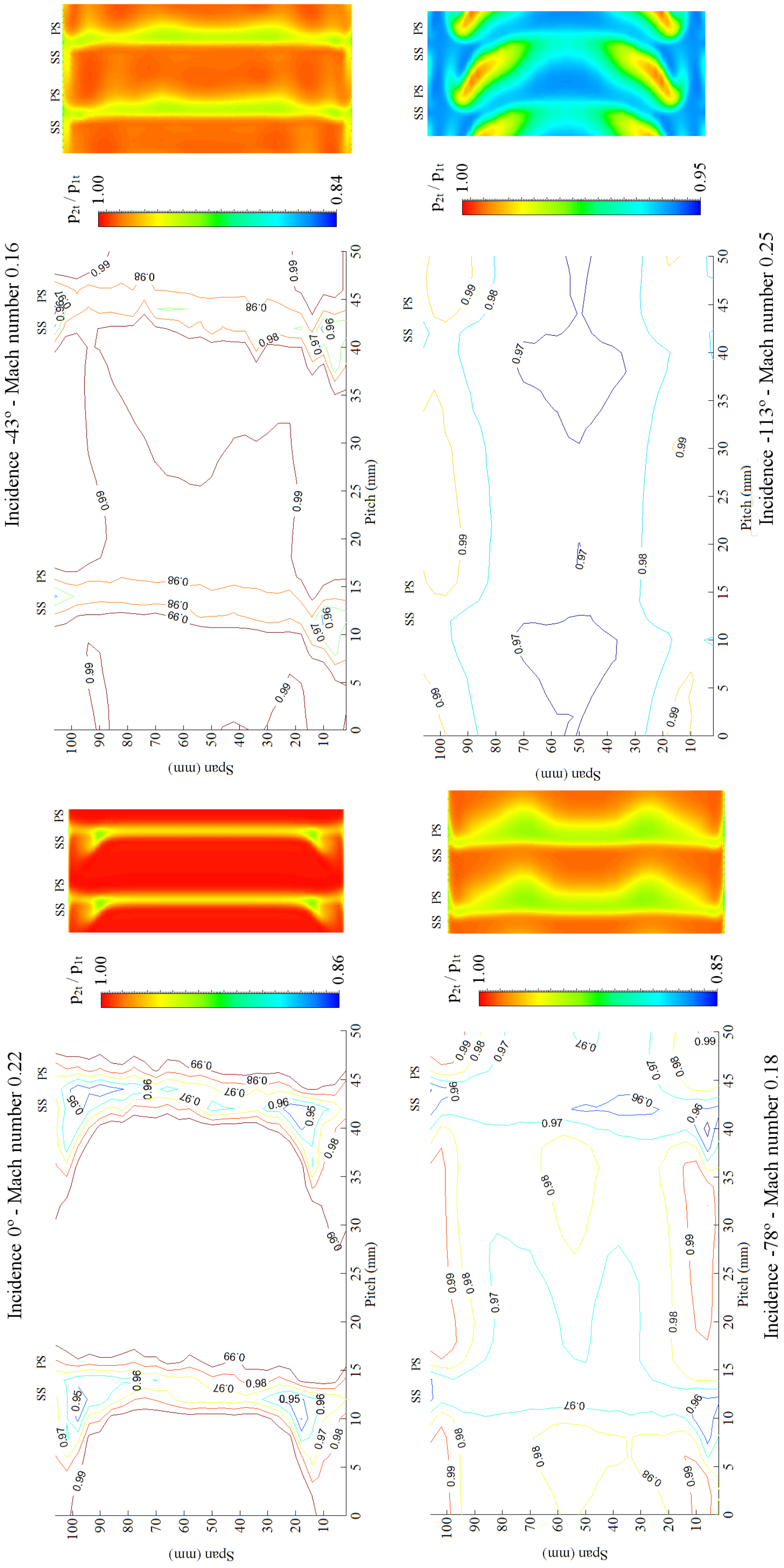

Figure 4.32: *Total pressure contours 5% of the chord downstream of the trailing edge for* 0°, −43°, −78° *and* −113° *incidence angles and comparison with CFD*

4.3.6.3 Wake mixing losses

It is expected for the wake mixing process to generate a significant loss that is accentuated the further the incidence is from its design value. The mixing loss is calculated by comparing the pitch averaged total pressure measured at two measuring slots located 5% and 1 chord downstream of the trailing edge. Table 4.5 groups the experimental and numerical values of the pressure loss coefficient across the NGV at those two locations. The larger flow separation characteristic of higher incidences promotes a stronger mixing and thus exacerbate pressure losses due to wake mixing.

Table 4.5: *Mixing losses between 5% and 100% chords downstream of the t.e of the NGV - Experimental pressure loss coefficient and comparison with CFD*

	Incidence 0°		Incidence −43°		Incidence −78°		Incidence −113°	
	Rig	CFD	Rig	CFD	Rig	CFD	Rig	CFD
ω 5% chord	0.075	0.118	0.272	0.473	1.409	1.227	1.950	1.963
ω 1 chord	0.124	0.123	0.405	0.578	1.575	1.382	2.219	2.205
Difference	0.048	0.004	0.133	0.105	0.165	0.155	0.269	0.242

On the other hand, the mixing of the fluid in the wake is very efficient. The wake is almost fully mixed and indistinct only one chord downstream of the trailing edge, even for the design incidence (fig. 4.33).

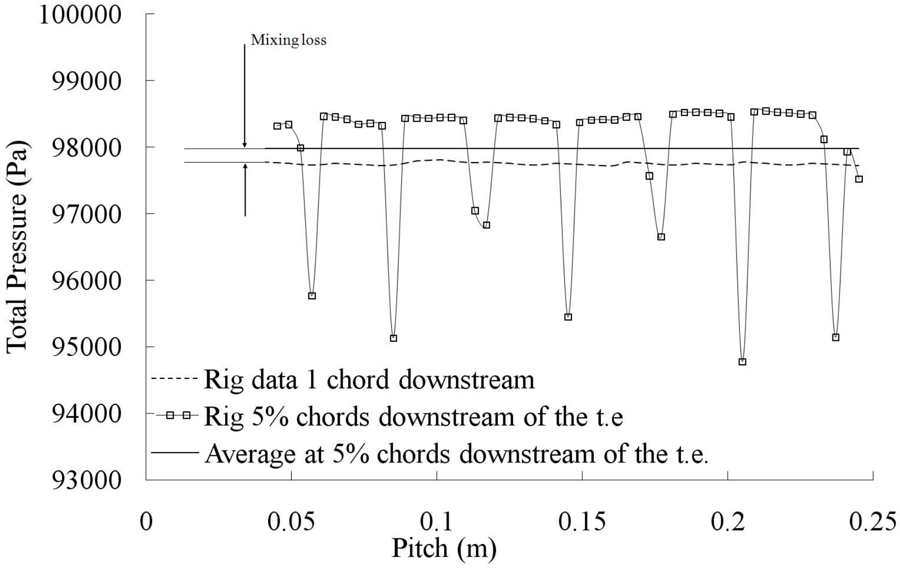

Figure 4.33: *Total pressure wake profiles 5% of the chord and 1 chord downstream of the trailing edge for an incidence of* 0° *at* 0.22 *inlet Mach number*

4.3.6.4 Inlet Mach number effect on the wake profile

Results shown in figures 4.27 to 4.31 correspond to the highest Mach number tested for each incidence angle. Analogue results were obtained for two other smaller flow Mach numbers but for the sake of conciseness only the most representative plots are included in Appendix 4B. The most remarkable effect of Mach number is the expected fall of total pressure loss with decreasing Mach numbers[4] (fig. 4.47) and the smaller depth of the wake (fig. 4.48).

4.3.6.5 Turbulence intensity effect on the CFD simulations

At the sight of the previous results it seems that CFD predicts a less effective mixing of the wake with the core flow. Since accurate measurements of turbulence intensity on the incoming flow were not available the sensitivity of the CFD calculations to the prescribed turbulence level was assessed in a series of simulations. Results show a minimal impact of the turbulence intensity on the flow field (figs. 4.34a and 4.34b).

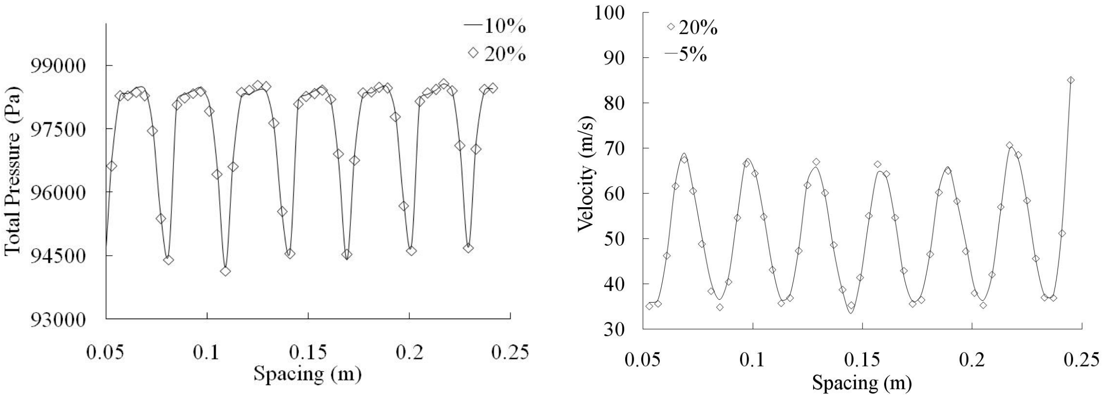

(a) *Incidence* 0°

(b) *Incidence* −113°

Figure 4.34: *Effect of prescribed turbulence intensity (5,10,20%) at the inlet on the CFD simulations*

4.3.6.6 Summary of rig results and CFD

The comparison between the rig measurements and CFD are summarised in tables 4.6, 4.7 and 4.8[5].

Table 4.6 provides a comparison of the results pitch averaged at mid span. Deviations of total and static pressure and velocity are expressed as percent variations and deviations in flow direction are expressed as absolute differences. Averaged deviations are very small because the higher values of the magnitudes predicted by CFD in the core flow are compensated by the lower values predicted in the wakes. As expected, deviations rise the farther the incidence is from design. Whole passage averaged results (table 4.7) and results at different blade span locations (table 4.8) show the same

---

[4] Flow losses are proportional to the flow velocity squared

[5] Positive deviations mean CFD results greater than experimental data and vice versa

trend. Differences between the experimental data and CFD at 25% and 75% span rise notably, and this is in agreement with figure 4.30.

Table 4.6: *Comparison of CFD and rig results of pitch averaged total pressure, static pressure, flow velocity, yaw angle (β) and pitch angle (α) for incidences* 0°, $-43°$, $-78°$ *and* $-113°$ *and three Mach numbers 5% of the chord downstream of the trailing edge*

Incidence (degrees)	Mach number	$\Delta\ p_t(\%)$	$\Delta\ p_s(\%)$	$\Delta\ v(\%)$	$\Delta\ \beta(°)$	$\Delta\ \alpha(°)$
-113	0.25	0.05	-0.25	5.54	-1.89	0.12
	0.24	0.04	-0.19	5.28	-1.48	-0.20
	0.18	0.03	-0.07	6.40	-2.07	0.63
-78	0.18	-0.34	0.04	-3.55	1.80	0.63
	0.16	-0.26	-0.01	-2.79	1.98	0.60
	0.09	-0.11	0.02	-2.58	1.82	-0.29
-43	0.16	0.36	0.01	-0.40	1.26	-0.09
	0.15	0.23	-0.12	0.46	1.40	-0.14
	0.11	0.10	0.00	1.80	1.72	0.81
0	0.22	0.19	-0.18	-0.84	0.40	-0.14
	0.19	0.17	0.02	-0.81	0.46	-0.22
	0.11	0.01	0.04	-0.82	0.44	-0.08

Table 4.7: *Comparison of CFD and rig results of whole passage pitch and span averaged total pressure, static pressure and flow velocity for incidences* 0°, $-43°$, $-78°$ *and* $-113°$ *and three Mach numbers 5% of the chord downstream of the trailing edge*

Incidence (degrees)	Mach number	$\Delta\ p_t(\%)$	$\Delta\ p_s(\%)$	$\Delta\ v(\%)$
-113	0.25	-0.35	-0.22	-3.14
	0.24	-0.43	-0.25	-3.77
	0.18	-0.16	-0.09	-0.56
-78	0.18	0.20	0.02	-0.23
	0.16	0.31	0.02	1.44
	0.09	0.08	0.02	2.54
-43	0.16	0.41	-0.03	0.08
	0.15	0.35	-0.04	0.71
	0.11	0.12	0.00	2.10
0	0.22	-0.05	0.09	-0.81
	0.19	0.02	-0.08	-1.28
	0.11	-0.07	0.00	-2.08

Table 4.8: *Comparison of CFD and rig results of pitch averaged total pressure, static pressure and flow velocity at 25%, 50% and 75% of the blade span for incidences* $0°$, $-43°$, $-78°$ *and* $-113°$ *and three Mach numbers 5% of the chord downstream of the trailing edge*

Incidence (degrees)	Mach number	Span (%)	$\Delta\ p_t$(%)	$\Delta\ p_s$(%)	$\Delta\ v$(%)
-113	0.25	0.25	-1.71	-0.42	-26.99
		0.50	0.14	-0.09	3.24
		0.75	-0.94	-0.32	-10.14
	0.24	0.25	-1.70	-0.39	-29.15
		0.50	-0.02	-0.18	2.20
		0.75	-1.03	-0.35	-11.05
	0.18	0.25	-0.82	-0.19	-25.13
		0.50	0.00	-0.06	3.35
		0.75	-0.38	-0.13	-5.65
-78	0.18	0.25	0.74	-0.02	4.35
		0.50	-0.48	0.03	-4.51
		0.75	0.94	-0.09	5.33
	0.16	0.25	0.84	0.01	6.97
		0.50	-0.18	-0.08	-1.56
		0.75	0.87	-0.06	6.59
	0.09	0.25	0.19	0.01	7.28
		0.50	-0.10	0.01	-1.79
		0.75	0.20	0.01	6.26
-43	0.16	0.25	0.37	-0.13	0.35
		0.50	0.39	0.05	-0.35
		0.75	0.29	0.02	-0.87
	0.15	0.25	0.37	-0.09	1.22
		0.50	0.29	0.09	-0.31
		0.75	0.34	-0.05	0.71
	0.11	0.25	0.09	0.00	1.75
		0.50	0.14	-0.02	2.65
		0.75	0.14	0.00	2.33
0	0.22	0.25	0.29	-0.17	-0.35
		0.50	0.16	-0.25	-0.74
		0.75	-0.41	0.20	-7.52
	0.19	0.25	0.19	0.06	-0.99
		0.50	0.22	0.05	-0.22
		0.75	-0.33	-0.15	-3.77
	0.11	0.25	-0.04	-0.06	0.49
		0.50	-0.02	-0.02	-0.09
		0.75	-0.17	0.15	-10.40

4.3.7 Secondary flow visualisation

This research aims to investigate the overall performance of turbine vanes at high negative incidences. The detailed investigation of the secondary flows that develop across the passage is somewhat out of the scope of the present work. However, to the author's knowledge there is not any study available in the public domain that discusses the structure of the flow across turbine vanes at incidences smaller than −53°. In order to provide the research community with an appreciation of the flow field at very high negative incidence angles flow visualisation surveys have been undertaken in the NGV rig at four different incidence angles, 0°, −43°, −78° and −113°, at the maximum inlet Mach number that the fan can supply.

The intricate structure of the secondary flows across turbine passages has been extensively investigated by a number of researchers [103][194]. Essentially, the flow structure at incidences close to zero can be explained with the help of figure 4.35 as follows. The inlet boundary layer flow splits at a saddle point and forms a horseshoe vortex that develops into two separate counter rotating legs at both sides of the turbine vane. The pressure side leg of this vortex is pushed towards the suction side of the adjacent vane and feeds the endwall flow forming a wider passage vortex. The suction side of the horseshoe vortex rotates around the axis of the passage vortex interacting with it. The flow immediately downstream of the saddle point at the leading edge impinges on the blade and forms two inner legs of a vortex that detaches from the leading edge of the blade. The strength of this vortex fades away before the passage throat. Further downstream, the flow adjacent to the end walls and the blade develop into corner vortices that flow gently following the blade surface down to the trailing edge. In addition, the flow over the blade tip leaks from the pressure surface through the gap into the suction surface, and rolls into a vortex that curls toward the hub. This leakage flow becomes weaker as the incidence decreases since the flow turning required from the vane is smaller.

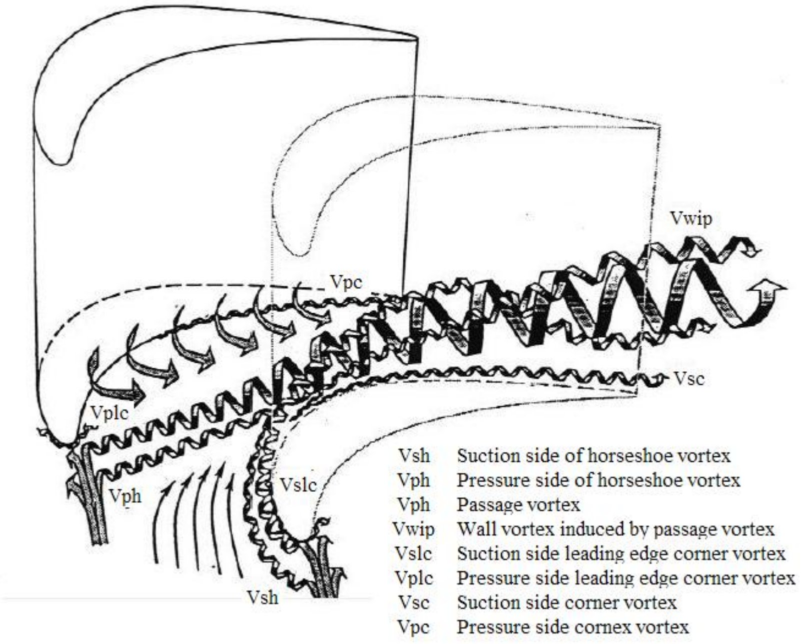

Figure 4.35: *Schematics of flows across a turbine passage at design conditions on the hub. From [186]*

Oil visualisation techniques have been employed widely in the past to investigate the flow across turbomachinery blades [104][162][116][77]. The visualisation fluid used in this work is a mixture of 50% oleic acid, 20% paraffin and 30% Titanium oxide in fine white particles of 50μm that can flow smoothly following the streamlines.

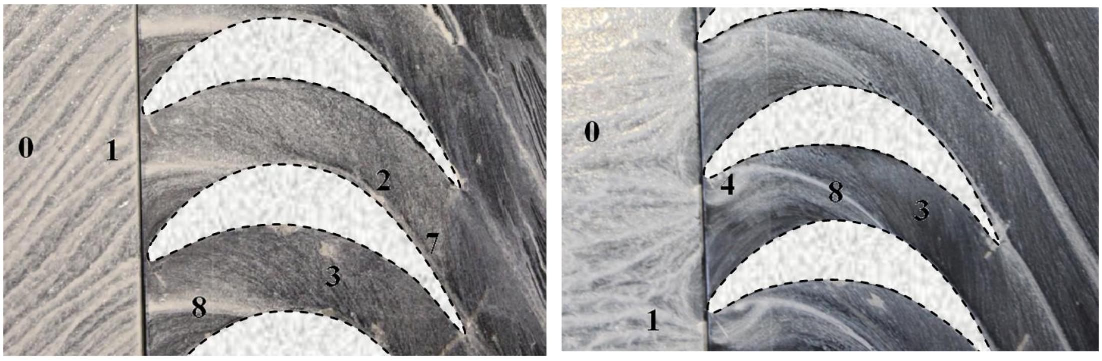

Incidence 0°
Inlet Mach number 0.22

Incidence -43°
Inlet Mach number 0.16

Incidence -78°
Inlet Mach number 0.18

Incidence -113°
Inlet Mach number 0.25

Figure 4.36: *Flow visualisation on the bottom end wall*

The endwall flow for a range of negative incidence angles is show in figure 4.36. The inlet wall flow (0) splits into a horseshoe vortex at a saddle point (1) ahead of the leading edge of the vane. As the incidence decreases the saddle point moves toward the pressure surface. The flow on the corner between the endwall and the vane forms corner vortices (2 and 5) that flow towards the trailing edge. These two counter rotating vortices are difficult to distinguish and quite insensitive to incidence changes. There is a strong flow migration from the pressure surface to the suction surface (3), but this is less clear for high negative incidences when the flow becomes more turbulent. As incidence decreases the flow separates downstream of the leading edge (4) and this separation grows until it covers half of the chord. The separated flow feeds into the corner vortex of the suction surface and as a result the flow cannot reattach again (6). The flow over the suction surface at the design incidence separates before the trailing edge (7). This happens because the amount of turning demanded from the flow cannot be achieved at the Mach number at which the test was carried out. The streamlines on the end wall group into a single line that becomes more skewed and less marked as the incidence decreases (8).

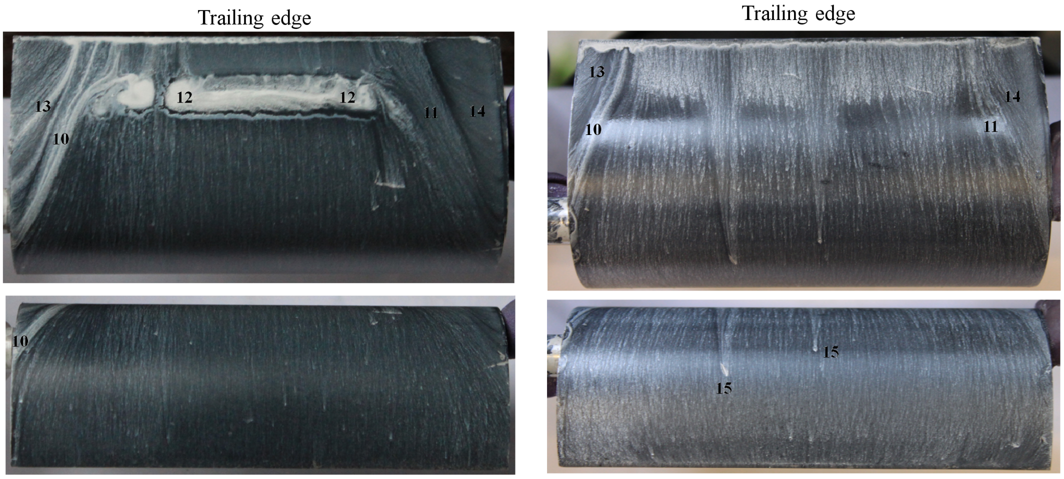

Incidence 0°
Inlet Mach number 0.22

Incidence -43°
Inlet Mach number 0.16

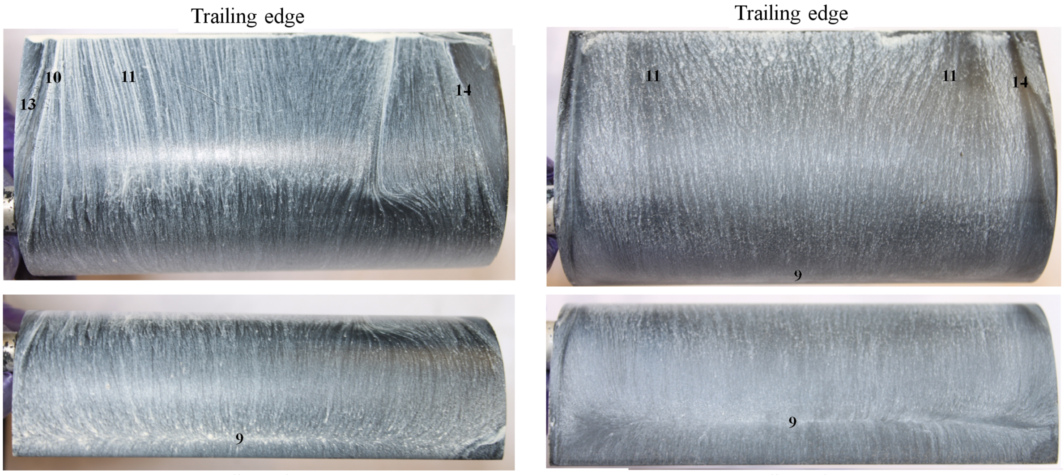

Incidence -78°
Inlet Mach number 0.18

Incidence -113°
Inlet Mach number 0.25

Figure 4.37: *Flow visualisation on the suction surface of the vanes for a number of incidences and Mach numbers*

The flow over the suction surface is shown in figure 4.37. The stagnation line of the flow on the blade is barely visible at 0° and moves rearwards as incidence falls (9). The passage vortex (10) that impinges on the suction surface becomes weaker, narrower and moves backwards as the incidence angle decreases. As a result of the vortex the streamlines over the blades converge towards the trailing edge for incidences close to the design point, and deviate progressively toward the endwalls as the passage vortex weakens (11). This is consistent with the flow structure reported by Yamamoto. At zero incidence the inlet Mach number is not high enough for the flow to achieve the required turning and the flow separates around an inch upstream of the trailing edge (12). The separation does not extend to the whole span of the blade because near to the endwalls the passage vortex energises the boundary layer over the vane avoiding the separation. A second streamline parallel to the passage vortex line can be attributed to the corner vortex on the suction surface (13). The differences between the streamlines at the hub and the tip arise from the leakage over the tip of the vane (14). This is particularly evident for the last two smallest incidence angles. For the −43° incidence case there are two dirt deposits on the vane surface that leave a visible wake of streamlines downstream (15).

The flow on the pressure surface is shown in figure 4.38. At design conditions the streamlines at mid-span are clean and straight. Close to the endwalls, the streamlines converge from the leading edge and diverge from mid-chord down to the trailing edge (16). For negative incidence angles there is a saddle point (17) that moves toward the trailing edge as incidence decreases. There is a stagnation line on the lower half of the vane that is slightly inclined to the trailing edge and moves rearwards as incidence falls (18). On the upper half of the vane there is another stagnation line that becomes more inclined and almost horizontal with the decreasing incidence (19). Strong vortical flows clock-wise (20) and anti clock-wise (21) develop from the stagnation lines towards the leading edge of the vane and collapse into a region of low energy at mid-span (22). There are two stagnation points anchored to the leading edge that move towards the mid-span as the incidence angle falls (23). The streamline at −113° incidence close to the vane tip (24) may arise from the tip leakage flow that reverses its direction at high negative incidences (from the suction to the pressure surface)

4.4 Effect of axial displacement on turbine capacity

During an unlocated shaft failure the rearwards movement of the IPT rotor disengages the tip seals of the vanes opening up the tip clearances with the casings. This allows the flow to leak more easily over the tip of the vanes, and promotes a marked loss in flow efficiency and capacity. The effect of the increased tip clearance is accounted for in performance models and turbine maps by correcting the turbine efficiency and flow capacity with experimental factors available to the sponsor. This correction factors were derived from tests carried out on a Tay turbofan engine and are proprietary data that will not be discussed here.

4.5 Concluding remarks and future work

The aerothermodynamics of the turbine assembly play a fundamental role in the evolution of a shaft over-speed event. The highly distorted velocity triangles across some of the blade rows of the turbine promote significant pressure, efficiency and capacity losses that need to be accounted for to model a shaft over-speed event. In particular, the flow across the nozzle guide vane immediately downstream of the over-speeding rotor can break away from the vane surface blocking the flow passage and reducing considerably the flow capacity of the turbine stage. As a result the upstream turbine disc is throttled to a lower pressure ratio limiting the terminal speed that the turbine disc can attain.

The study of the turbine aerodynamics during s shaft over-speed was carried out with the help of three-dimensional CFD simulations that were validated against a series of low speed cascade tests. The departure of the CFD simulations from the rig data was found to be of the order of 2% in terms of the absolute total pressure in the worst case analysed. The flow visualisation of the rig flow and the CFD simulations provide an insight into the flow field across turbine blades at high

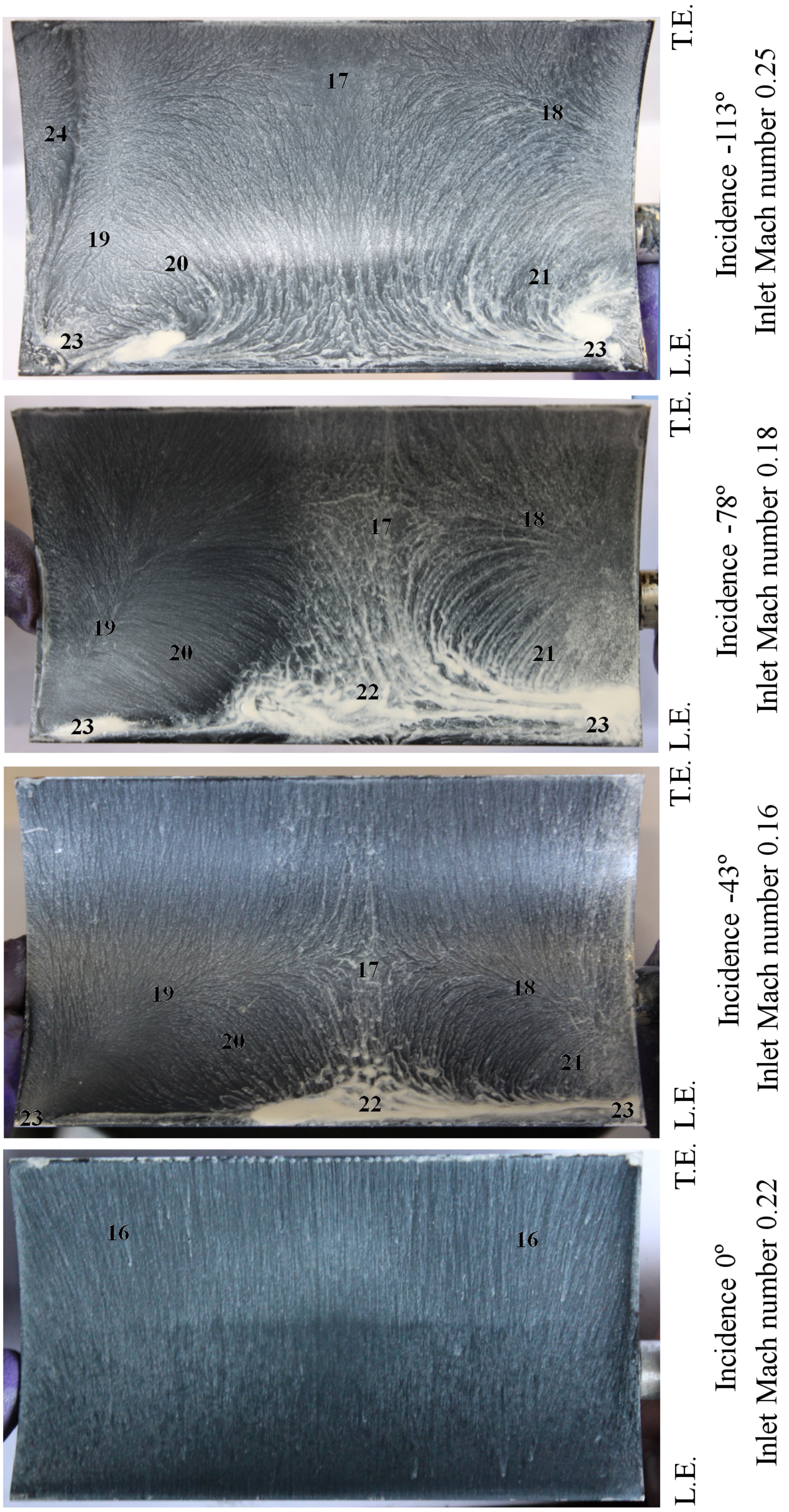

Figure 4.38: *Flow visualisation on the pressure surface of the vanes for a number of incidences and Mach numbers*

negative incidence angles that is unpublished in the open literature.

The analysis reported in the current chapter can be repeated to investigate the effect of the cascade geometry on the results. In particular, less cambered and more spaced aerofoils are expected to exhibit a stronger reduction in flow capacity, providing a more effective braking mechanism to the over-speed.

Appendix 4A - Validation of CFD techniques

The advent of CFD supposed a breakthrough to understand the complex flow across turbomachines. However, whereas CFD has been proved to predict turbine efficiencies at design point with an error of 2% [171], the application of CFD to off-design scenarios is still in its early stage of development [43]. Nonetheless, some studies have shown that for high negative incidence cascades the agreement that can be obtained between numerical predictions and experiments can be pinned down to 8% [201]. This research draws heavily on CFD to analyse the performance of engine components at off-design conditions. It is therefore reasonable to include a small appendix to comment on the CFD methodology employed, validate it and provide an estimation of its accuracy. However, it has to be borne in mind that CFD is employed in this work to obtain component performance maps and not to reveal the flow loss mechanisms or fundamental structure. It is therefore the critical appraisal of the capability of CFD to obtain off-design performance maps that is the aim of this section.

Mesh strategy, turbulence models and wall treatment.

Mesh strategy, turbulence modelling and near wall treatment are interrelated aspects of CFD simulations that must be considered as a whole; the mesh generation strategy must be in accordance with the turbulence model and the wall treatment. The vast majority of the simulations reported in the current work were carried out with Ansys CFX CFD suite. The solver code includes $k-\epsilon$ and $k-\omega$ two coefficient turbulence models that are the standard in CFD simulations of turbomachinery.

$k-\epsilon$ turbulence models are useful for free-shear layer flows where the pressure gradient is not substantial, and accuracy degrades for flows containing large adverse pressure gradients, typically underpredicting flow separation. Hence, this model is not best suited for compressor blades and intake calculations. $k-\omega$ models on the other hand, are more accurate to predict transitional and separated flows, although are less robust than the $k-\epsilon$ model.

Transitional flows are largely affected by the behaviour of the viscous sublayer, and under these circumstances the most appropriate simulation strategy is to fully resolve the viscous-affected region with a low Reynolds number turbulence model such as $k-\omega$ SST or $k-kl-\omega$. This low Reynolds models are also significantly more accurate to predict flow separation and reattachment and this in turn have a very marked impact on the prediction of losses. On the other hand, wall function approaches, where the near-wall region is approximated by empirical correlations, are inappropriate when low-Reynolds effects dominate the flow because the assumptions on which they are based are not valid under these conditions. Near-wall approaches require a fine resolution of the mesh in the viscous affected near wall region to guarantee that the first cell is well within the viscous sublayer of the boundary layer. Usually, in terms of the non-dimensional height of the first cell, y^+, a value of 2 or less must be used in order to accurately predict shear stresses on the walls. If there is no interest in calculating transition, separation and associated magnitudes, fine meshes suffice for the application of wall functions. The first cell centroid in these cases should be located within the log-law layer; that is, y^+ should be between 30 and 300. The height of the first cell can be estimated a priori but since the thickness of the boundary layer depends on the flow velocity on the walls it must be checked that values are well within range after running the simulations (fig. 4.39).

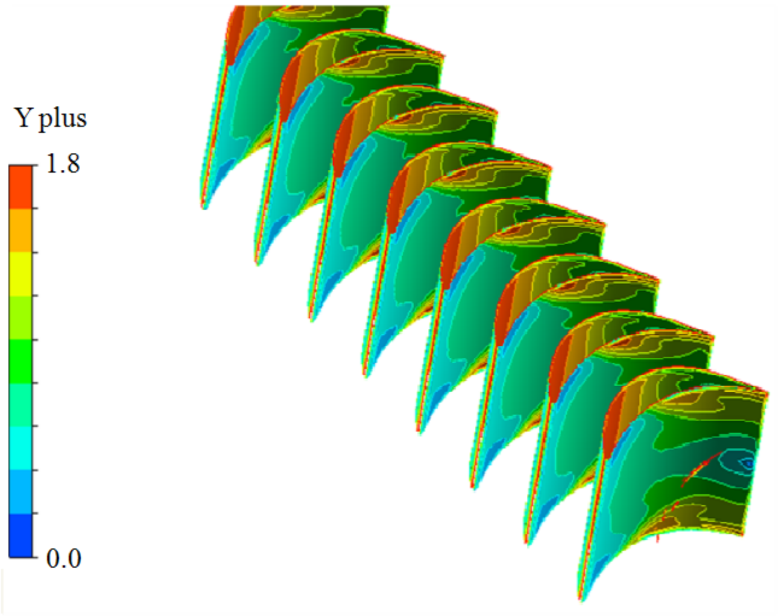

Figure 4.39: *Example of y^+ distribution over the rig cascade*

The turbulence model employed to carry out the simulations is the SST (Shear Stress Transport) $k-\omega$, first introduced by Menter in 1994 [122][123]. This model blends the robustness of Joness $k-\epsilon$ turbulence model [86] in the free flow with the precise wall treatment of Wilcox's $k-\omega$ turbulence model [189] while avoiding the typical over production of turbulence energy produced by the $k-\epsilon$ model in highly strained regions such as stagnation points and strong adverse pressure gradients. The solver is a double precision second order accurate in space to limit the acute numerical diffusivity distinctive of first order schemes. In some cases, however, first order schemes proved useful to initialise the simulations due to their enhanced robustness to capture determined features of the flow like shock and expansion waves.

Mesh independence

While coarse meshes can be useful in some cases to initialise simulations of complex flows with strong pressure gradients, separation or shock waves, accurate results require relatively fine grids to guarantee the mesh independency of the solution. The optimum mesh size is determined by monitoring some global flow magnitudes for different mesh sizes and finding an acceptable compromise between simulation time and accuracy. These studies have been completed for each geometry considered in this work - see figures 4.41a and 4.41b for an example.

Turbulence intensity

Imposing appropriate levels of turbulence intensity is important and very often quite difficult to accomplish due to the difficulty of disposing of experimental measurements. It is usually necessary

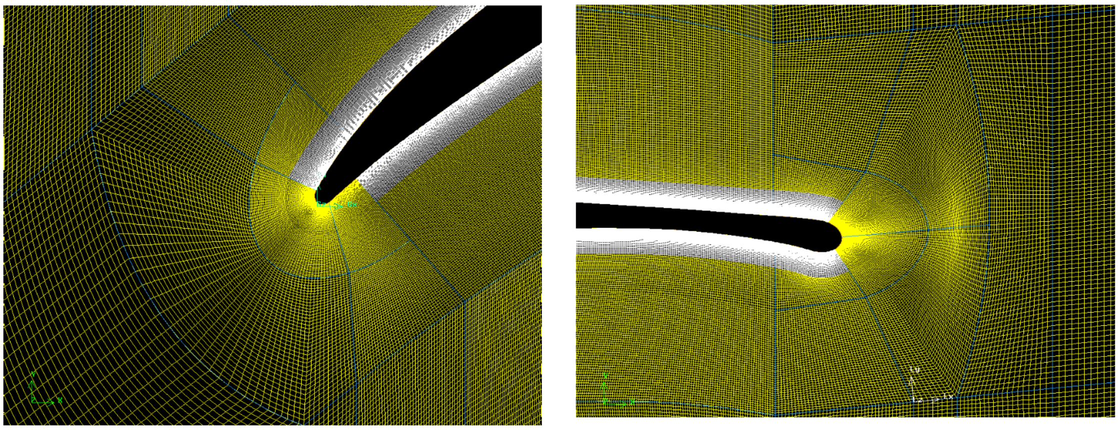

(a) *Mesh around the leading edge of the blade* **(b)** *Mesh around the trailing edge of the blade*

Figure 4.40: *Example of the mesh arrangement around the compressor rotor blade of chapter 7*

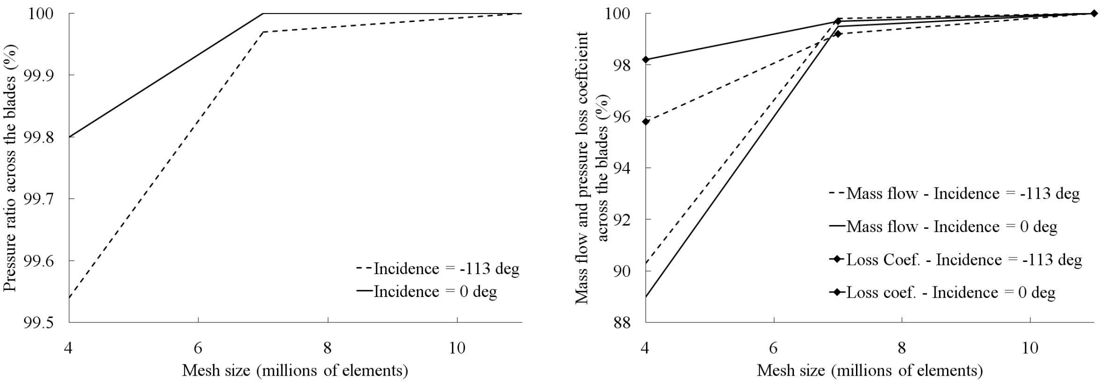

(a) *Pressure ratio across the blades* **(b)** *Mass flow and pressure loss coefficient across the blades*

Figure 4.41: *Example of a mesh sensitivity analysis - NGV test rig for atmospheric inlet conditions and* $91KPa$ *backstatic pressure*

to make an educated assumption - in this research turbulence intensities of 1% for intakes and low pressure compressor flows, 5% for high pressure compressors and low pressure turbines and 20% for flows inside and immediately downstream of combustion chambers have been prescribed. Some additional simulations have been carried out to assess the impact of turbulence intensity on the results for the NGV rig and due to the low speeds this has been found to be minimal (see section 4.3.6).

Prescribing a turbulence intensity level at the inlet of a domain can produce misleading results because the turbulence can decay along the inlet duct and be significantly lower when the flow reaches the leading edge of the blade. This is particularly important for the NGV rig simulations that feature a long inlet duct to straighten the flow. For a straight smooth duct and atmospheric inlet conditions simulations showed that the turbulence for the $k-\epsilon$ and $k-\omega$ models decays as shown in figure 4.42.

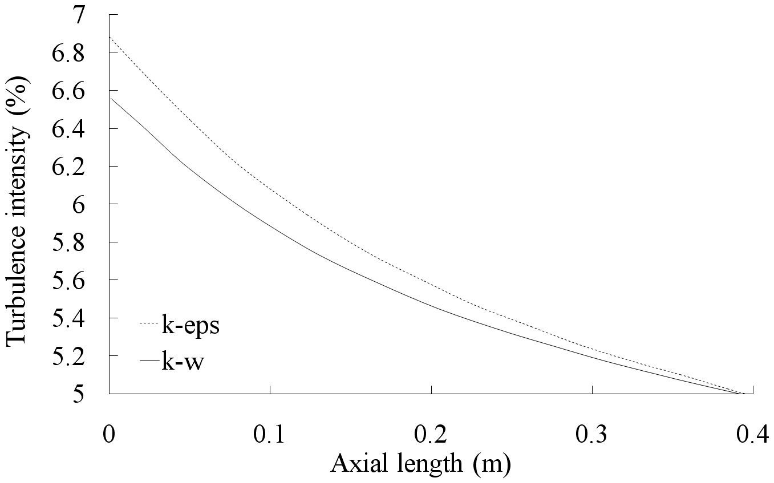

Figure 4.42: *Decay of the turbulence intensity against the streamwise direction of the flow*

Convergence

Commercial CFD codes use scaled residuals to determine the convergence of the simulations. Typically a number of residuals - usually velocity and turbulence descriptors - are compared to an average of their initial value and the simulation continues until the residuals are smaller than a given value. However, in some cases, this does not guarantee the full convergence of the simulations, and it is necessary to monitor other magnitudes like forces on the blades and mass imbalance across the domain. In the simulations reported in this work, residuals are flat and below 10^{-5}, the drag coefficient on the blades, c_d, is also constant and the mass imbalance across the domain is kept below 0.5%.

Mesh generation

Mesh generation is usually the most tedious and time consuming step of any CFD simulation. Discussion of the algorithms to generate appropriate meshes is out of scope, and the interested reader is directed to [172]. The meshes were produced adhering to the recommendations reported in [48] and [101]. As a general guideline, all the simulations reported in this thesis use hexahedral elements aligned with the flow to minimise the truncation errors characteristic of tetrahedral meshes. The preferred grid is a totally structured mesh that features an O shaped refined boundary layer mesh around the blade that allows good resolution of both the leading and trailing edges and a H structured mesh on the free flow region that is appropriate to apply far-field and periodicity conditions. The reason behind this choice is that in regions exposed to large pressure gradients tetrahedral meshes perform poorly due to their inherent larger truncation errors than quadrangular meshes which are aligned with the flow in boundary layers, jets, mixing layer and wakes. The mesh must also be finer in those areas where the greatest variations in the fluid variables are expected, because those are the regions where numerical errors will be greater. The quality of the mesh is assessed by monitoring four grid parameters (aspect ratio of cell side, maximum and minimum element angles, and size ratio of adjacent cells) and guaranteeing that they are within acceptable limits (see table 4.9).

Table 4.9: *Mesh parameters allowed ranges*

Aspect ratio	Maximum element angle	Minimum element angle	Size ratio
≤ 100	$\leq 150°$	$\geq 30°$	≤ 1.2

Validation against NASA's rotor 37

The AIAA guide defines validation as the process of determining the degree to which a model is accurate representation of the real world from the perspective of the intended uses of the model [2]. Unfortunately, the number of turbomachinery benchmarks available for validation of numerical techniques is very scarce and limited to design point conditions. Among them, perhaps the most popular is NASA's transonic rotor 37 [153][168] since it was the object of a detailed study on CFD validation carried out by numerous experts whose findings were reported in [48]. The complexity of the transonic flow field - strong shock wave anchored to the leading edge of the blade that impinges on the boundary layer of the blade and separates the flow after the lambda foot structure that develops over the surface of the blade (fig. 4.43) - and the very complete amount of experimental data publicly available makes Rotor 37 a widely used benchmark nowadays [73][6]. The software and meshing strategy used in this work has been compared against such benchmark for a range of normalized mass flow, and the agreement between the simulations and the experimental data has been found to be rather good as illustrated by the red markers in figures 4.44, 4.45 and 4.46.

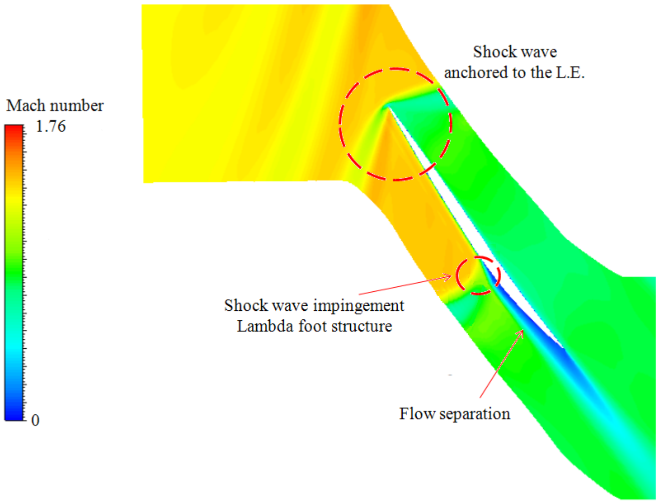

Figure 4.43: *CFD validation - Rotor 37 Contours of relative Mach number at mid span*

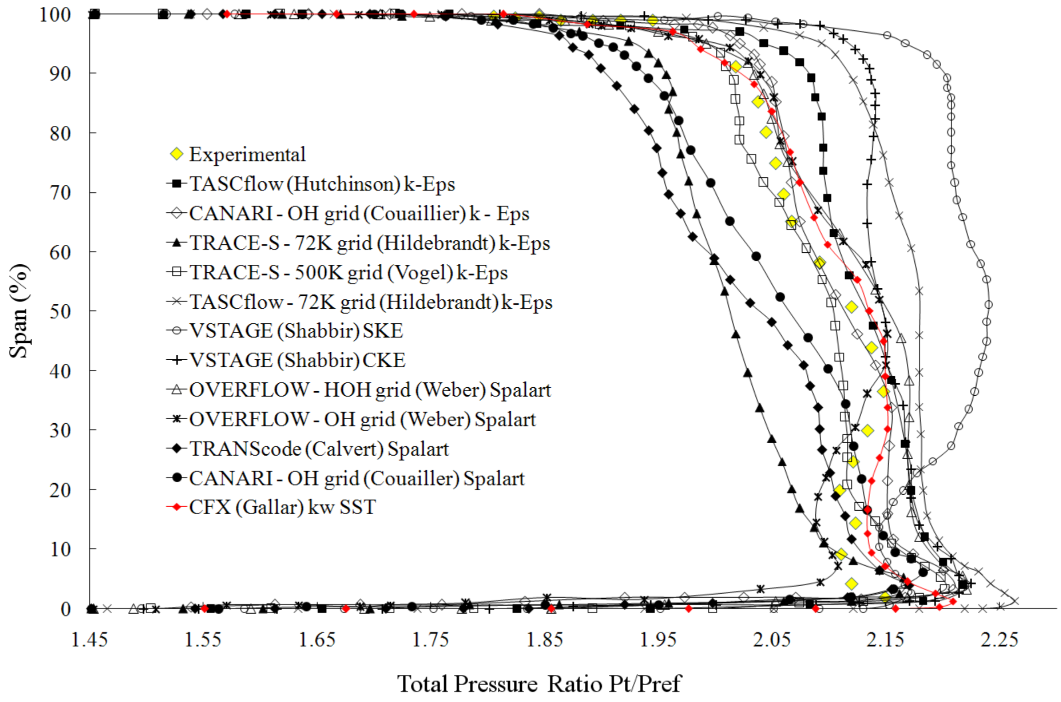

Figure 4.44: *CFD Validation - Rotor 37 Pressure Ratio versus span for 0.98 normalised mass flow*

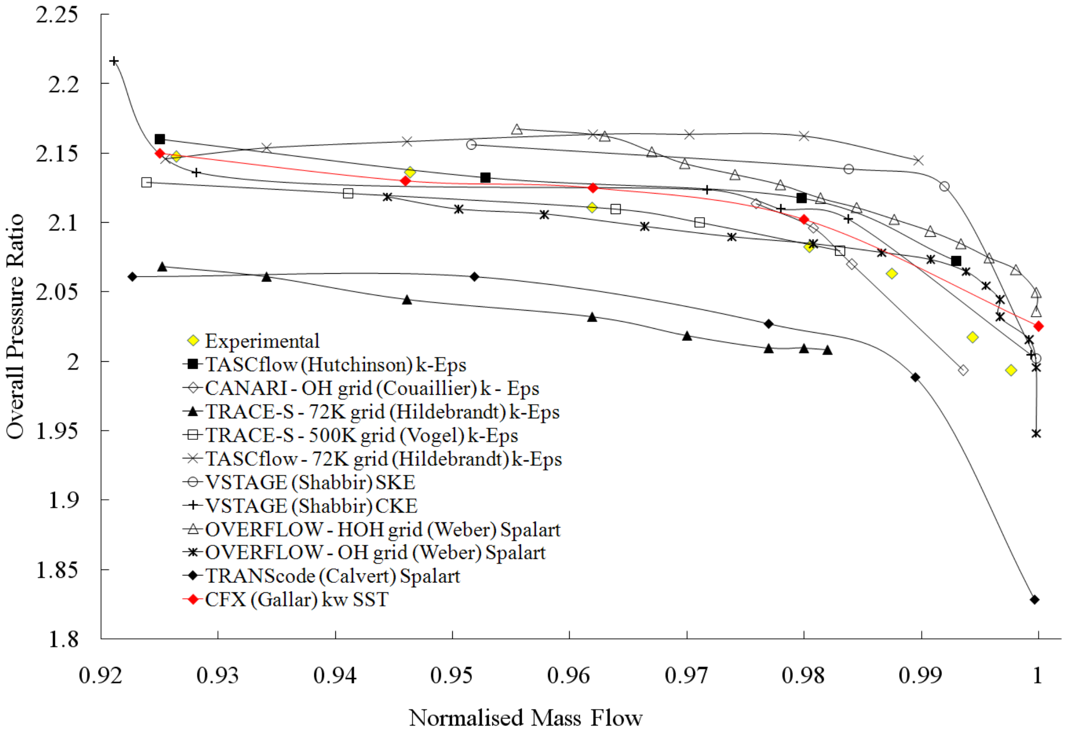

Figure 4.45: *CFD Validation - Rotor 37 Pressure Ratio versus normalised mass flow*

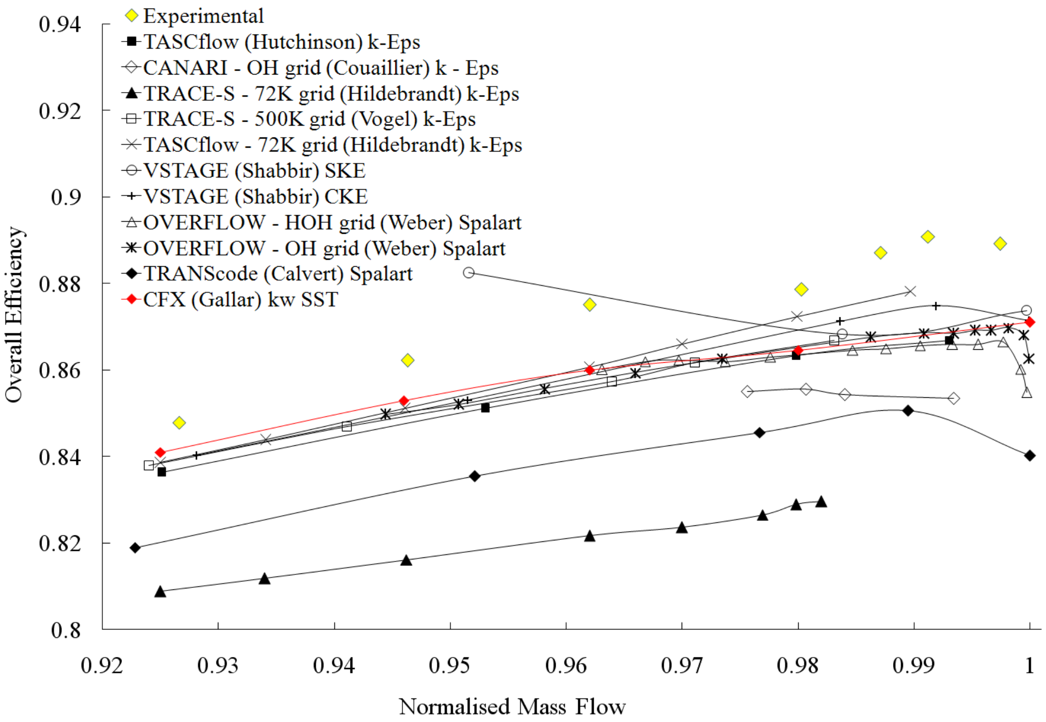

Figure 4.46: *CFD Validation - Rotor 37 Efficiency versus normalised mass flow*

Appendix 4B - Effect of Mach number on the rig results

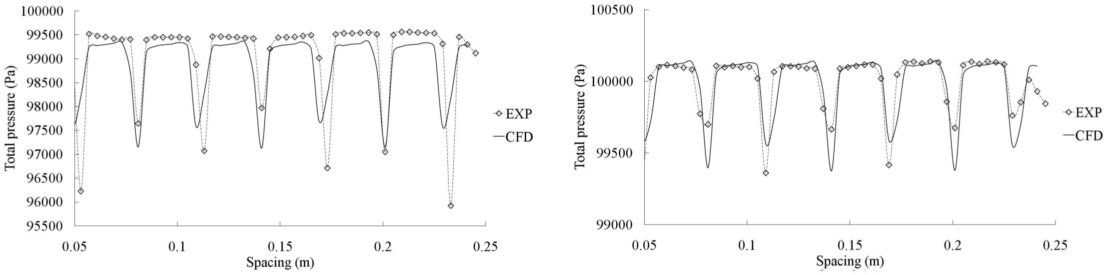

Incidence – 0 degrees
Mach number 0.20 (left) and 0.11 (right)

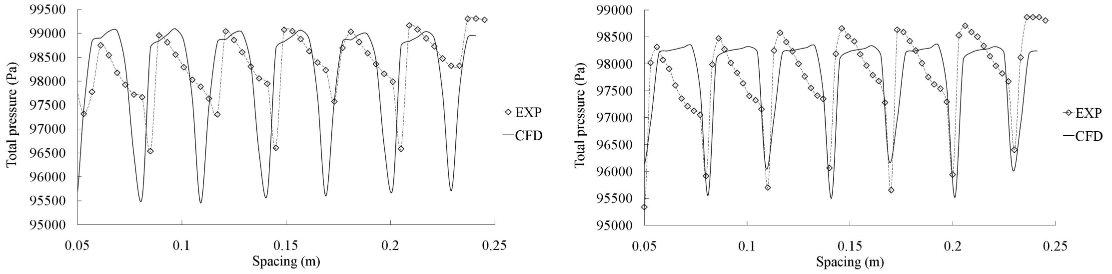

Incidence – -43 degrees
Mach number 0.15 (left) and 0.11 (right)

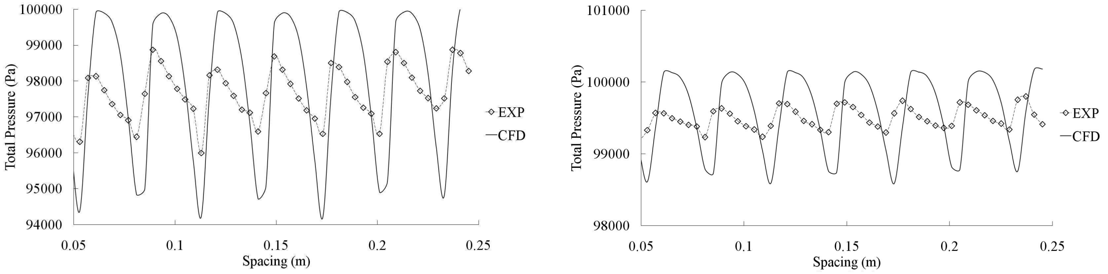

Incidence – -78 degrees
Mach number 0.16 (left) and 0.09 (right)

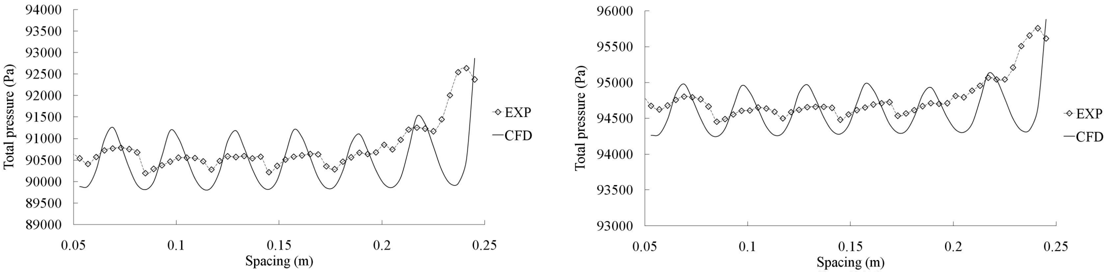

Incidence – -113 degrees
Mach number 0.24 (left) and 0.18 (right)

Figure 4.47: *Rig total pressure 5% of the chord downstream of the trailing edge at mid span for* 0°, −43°, −78° *and* −113° *incidence angles versus inlet Mach number and comparison with CFD*

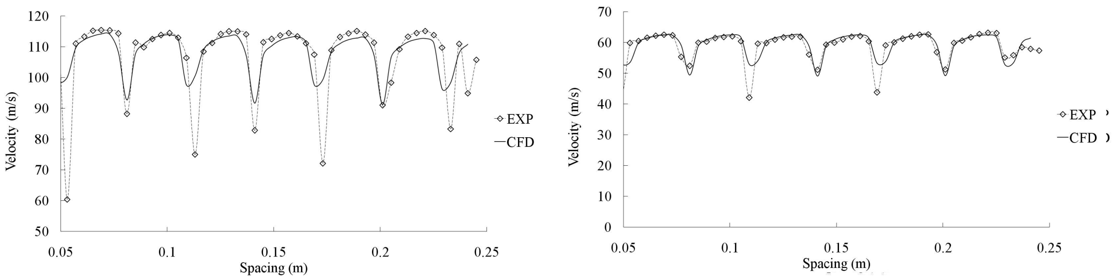

Incidence – 0 degrees
Mach number 0.20 (left) and 0.11 (right)

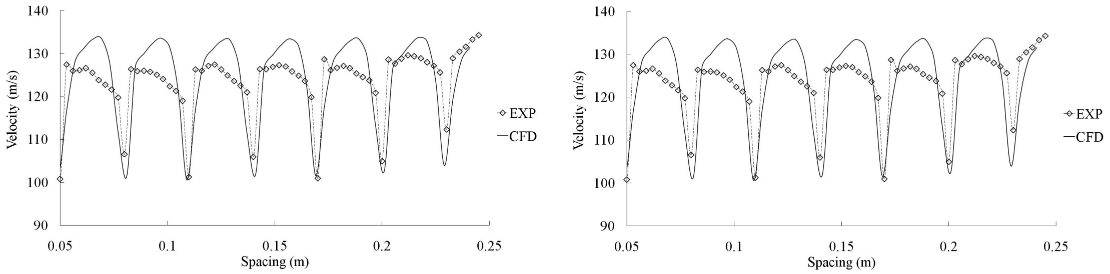

Incidence – -43 degrees
Mach number 0.15 (left) and 0.11 (right)

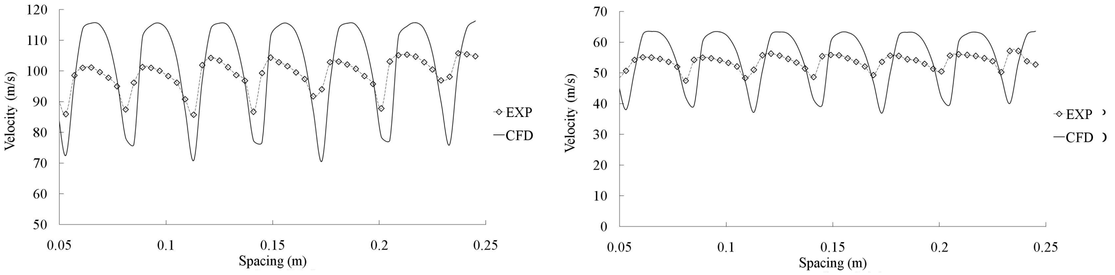

Incidence – -78 degrees
Mach number 0.16 (left) and 0.09 (right)

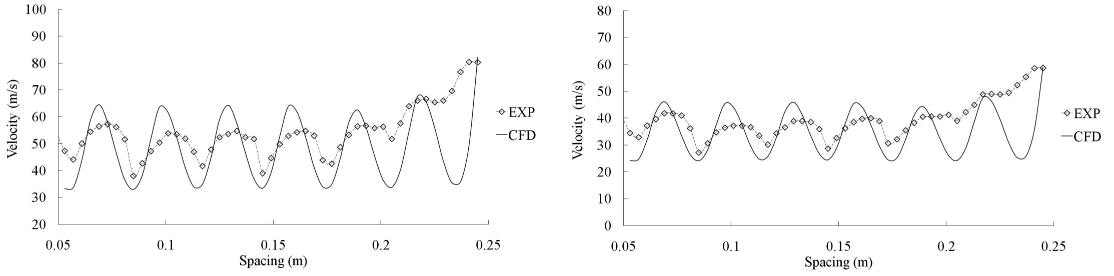

Incidence – -113 degrees
Mach number 0.24 (left) and 0.18 (right)

Figure 4.48: *Rig velocity 5% of the chord downstream of the trailing edge at mid span for* $0°$, $-43°$, $-78°$ *and* $-113°$ *incidence angles versus inlet Mach number and comparison with CFD*

Chapter 5

Secondary air system dynamics performance modelling

5.1 Introduction

The Secondary Air System (SAS) of a gas turbine is designed to perform several functions important for the safety, reliability, mechanical integrity and performance of the engine. The amount of air bled from the main gas path of a gas turbine, although necessary, impairs the engine performance because it is purged from the main engine cycle. In order to quantify and minimise its effect, during the design stage the SAS is typically modelled as a steady one-dimensional gas flow network of nodes and connections that represent the various flow components the air meets along its path. Consistent works based on that approach are those undertaken by Kutz and Speer [100], Muller [133] and Alexiou and Mathioudakis [4]. To the authors knowledge the models published hitherto are only valid for steady or quasi steady state and this is perfectly adequate for usual engine transients when the time constant of the air system is insignificant compared with the turbomachinery characteristic time. In these cases the flow is not supposed to reach sonic conditions anywhere within the network and most important, flow reversal anywhere throughout the system does not occur. It is then the case that the differential equations that govern the fluid movement are not time discretised and thus can be solved in a relatively straightforward fashion.

Nonetheless, the rapid changes that occur during slam accelerations or some failure scenarios call for a different approach to calculate the fluctuations of the endloads on the turbomachinery discs. A strategy based on empirically derived correlations and parameters such as discharge coefficients for every single component is unfeasible at the present day due to the lack of data at reverse flow conditions when a model able to deal with flow that may pulsate indistinctly forwards and backwards is required.

In the event of a shaft failure the sudden decoupling between the turbine and the compressor may result in a dangerous shaft over-speed scenario whose outcome can be severely influenced by the response of the internal air system. If the shaft fails behind its axial location bearings the turbine is no longer axially constrained and is free to move rearwards driven by the force imposed by the air across it. Such movement may result in the free turbine disc and rotor blades contacting with any other rear static structure. In the event of an IP shaft failure in particular, the blades of the IPT rotor may tangle with the LP NGV blade row. Such interaction, if it occurs in a controlled manner, is desirable since it will dissipate energy as friction and will reduce the terminal speed that the turbine is able to reach.

However, the turbine displacement rearwards may seal some of the outlet ports of the downstream turbine secondary air system cavity. Should this happen the pressure inside the cavity will increase, exerting a forward force on the disc that will reduce the frictional force on the tangling structures. The energy that can be dissipated as friction will then be lower and the beneficial effect of the blades tangling with the downstream structure may be lost. Therefore the need for a dynamic simulation tool of the whole air network arises.

This chapter covers the development of a dynamic model for gas turbine secondary air systems capable of capturing the sudden changes in the flow properties that occur along the system during rapid transients. The final aim of this area of the research is the provision of a simplified methodology to calculate the turbine endloads exerted by the air system during rapid transients.

5.2 Flow in internal air systems during a shaft over-speed event

The air system of a jet engine is an open system: there is a bleed off take from the compressor - at the lowest possible pressure compatible with the sink where the flow is to be discharged -, the air then travels through the internal cavities of the engine cooling down the compressor and turbine discs and sealing and cooling bearing chambers. Eventually, the air is discharged at the turbine rims preventing the hot air of the main gas path from entering the internal turbomachinery cavities that would damage the turbine assembly. Ultimately the system is also primarily responsible for determining the endloads exerted on the turbine discs. The following sections provide a brief description of the flow across the main components of the internal air system during a shaft over speed event.

5.2.1 Flow in rotating cavities

The flow inside the cavities of internal air systems is very complex and is still a matter of very intense research activity by the gas turbine community. The structure within a rotating cavity with radial outflow and axial inflow was first described by the flow visualisation experiments of Owen and Picombe [138] and the CFD simulations by Chew [30]. Similar flow structures were reported for laminar and turbulent flows by Ong and Owen [135][136], Morse [131], and Iacovides and Theofanopoulos [83].

The basic streamlines that develop inside the cavity are sketched in figure 5.1. Essentially, the flow enters the cavity and impinges on the downstream disc, rolls up over the walls and feeds the boundary layer. At some distance over the walls a portion of the boundary layer reverses and feeds the boundary layer on the upstream disc. The core of the cavity forms a “spinning doughnut” of fluid that rotates at a fraction of the disc speeds with zero radial velocity. The flow eventually exits the cavity through the outer radial port. The size of the core region grows with increasing mass flows into the cavity and with decreasing rotational Reynolds number until it occupies the whole of the cavity. Quantitative results however are limited to some rough correlations and expressions to estimate particular magnitudes of interest like the flow rate necessary to be supplied to the cavity to prevent ingestion or the windage over the discs. It is clear that much additional work will be required before a complete understanding of the phenomenon is possible.

In unlocated shaft failures the rearwards displacement of the disc can very rapidly close the discharge port of figure 5.1. As the port closes a compression wave travels towards the engine shaft, interacts with the boundary layer and is likely to separate the flow over the walls, making it a very complex phenomenon to model.

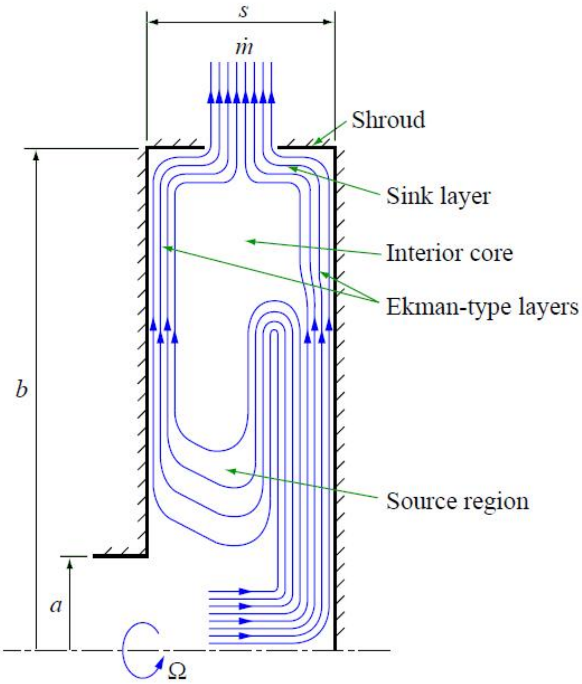

Figure 5.1: *Schematics of the streamlines in a rotating cavity with through flow and an outlet flow. From [11]*

5.2.2 Flow in the inter-shaft gap

Flows through long rotating conduits with axial through flows were characterised by the experimental work of Kaye and Elgar [89] that linked the structure with the axial and rotational Reynolds numbers of the flow. The flow along the inter-shaft gap can be analysed by the superposition of a rotating Couette flow and an axial Poiseuille flow. This results in a skewed, helical flow structure (fig. 5.2).

During a shaft over-speed event the abnormally high speed of the shaft causes the total distance covered by the air within the inter shaft gap to increase significantly and the effect of friction with the walls can become important.

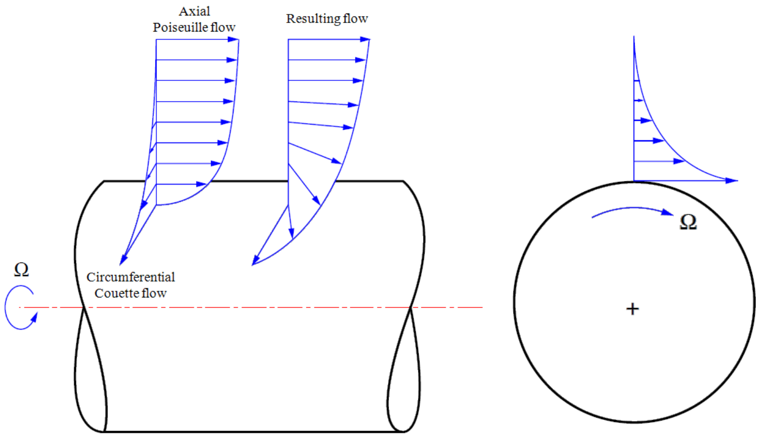

Figure 5.2: *Through flow over a rotating cylinder. From [11]*

5.2.3 Flow through seals

A typical labyrinth seal consists of a series of radial fins that restrict the annular flow of fluid (fig. 5.3). The flow must accelerate to pass through the seal and in so doing some of the energy associated to the static pressure of the flow is converted into kinetic energy. The flow expands downstream of the throat of the fin and forms eddies that dissipate some of the energy of the flow reducing its total pressure. This process is repeated through the subsequent cavities of the seal until the flow exhausts downstream of the last fin. The design and analysis of labyrinth seals was the subject of a book by Trutnovsky and Komotori [178].

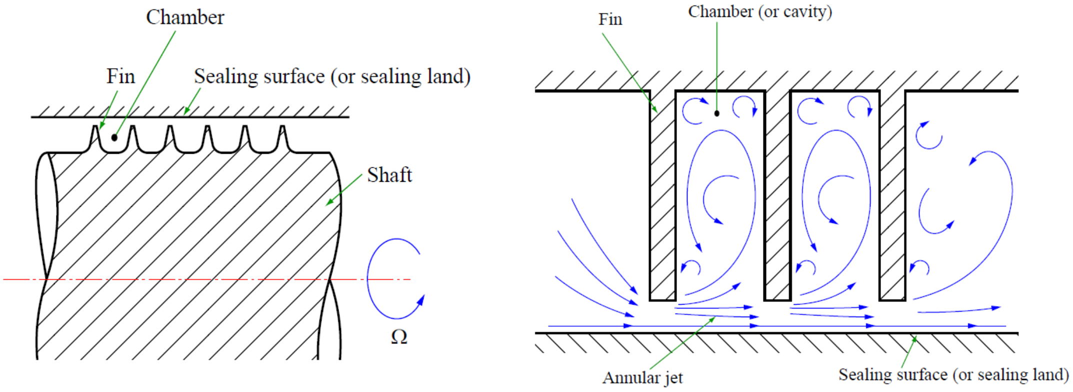

Figure 5.3: *Typical axial labyrinth seal arrangement and characteristic flow through the seal. From [13] adapted from [174]*

5.2.4 Flow through rotating orifices

In order for the flow bled from the compression system to reach the low pressure turbine cavity it must travel along the inter-shaft gap through cooling holes on the outer shaft (fig. 5.4). As with any other flow restriction element, rotating cooling holes are characterised by discharge coefficients that can be as low as 0.3. This means that only a third of the ideal flow through an orifice of the same area does actually pass through the hole. Alex Alexiou et al. carried out some experiments and CFD calculations to correlate the discharge coefficient through rotating holes with the conditions of operation of the system [3].

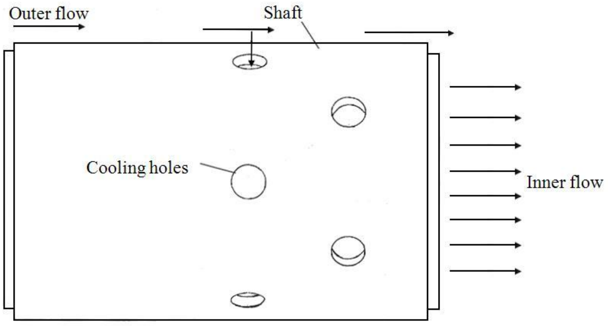

Figure 5.4: *Configuration of the cooling holes on the intermediate pressure shaft*

5.3 Secondary air system components dynamic modelling

For modelling purposes the whole system is initially broken down into a series of chambers of a finite volume connected by pipes that are initially modelled in isolation and then interconnected. The effects of rotation in the system and flow strangulation through labyrinth seals are included in the network as well at a later stage. The resulting tool constitutes a baseline onto which further improvements and modifications will be implemented in subsequent works.

The chapter also focuses on the challenges encountered integrating the single components into a network to predict the transient operation of the air system. The flow regime - subsonic or supersonic - and its direction have deemed the choice of the appropriate numerical and physical boundary conditions at the components interface for each time step particularly important. The integration is successfully validated against a known numerical benchmark - the De Haller test. A parametric analysis is then carried out to assess the effect of the length of the pipes that connect the system cavities on the pressure evolution in a downstream reservoir. Finally, the work concludes with the analysis of the flow evolution in the secondary air system during a shaft failure event.

5.3.1 Simultaneous charge and discharge of a pressurised vessel

5.3.1.1 Assumptions and mathematical apparatus

[1]The secondary air system contains a number of volumes that have a filling time that must accompany a pressure change. The assumption upon which the mathematical models for the charge and discharge of a vessel are built is the fact that all the thermodynamic properties of the flow can be considered uniform inside the vessel - they do not change spatially and are only time dependent - during the whole process. This is paramount since the uniformity of the properties in the tank allows for the Navier-Stokes equations to be solved in their integral form.

---

[1] See appendix 5A for complete details of the mathematical model

As deduced from the state principle first enounced by Kline and Koening [95], it is enough to demonstrate the uniformity of two thermodynamic properties in a simple homogeneous system to ensure the uniformity of all of them. First, it is considered that the flow velocity in the bulk of the vessel is low apart from small localised regions such as the outlet area in the case of the discharge and the inlet jet in the case of the charge. This assumption is satisfied for both charges and discharges as long as the ports of the vessel are small compared with its volume in both processes ($A/V^{2/3} << 1$). In such case, it can be demonstrated that in the region close to the port (small compared with the volume of the vessel) the Reynolds number is high and despite the value of the Reynolds number in the bulk of the vessel the pressure inside can be considered uniform. The physics behind the finding of a second uniform thermodynamic property are however different depending on the event under study. In the case of a discharge, the application of the entropy equation to the fluid that remains in the reservoir yields:

$$\frac{DS}{Dt} = \frac{\nabla \cdot (k\nabla T)}{\rho T} + \frac{\Phi_V}{\rho T} \tag{5.1}$$

Due to the fact that the Reynolds number at the outlet is high ($Re >> 1$) the entropy generation due to viscous dissipation can be disregarded in eq. 5.1. On the other hand, the entropy rise due to heat conduction into the control volume can be estimated as follows:

$$\frac{\nabla \cdot (k\nabla T)}{C_V \rho T} t_d \approx \frac{\Delta}{T} \frac{\delta_t}{V^{1/3}} \tag{5.2}$$

The magnitude $\delta_t \approx \sqrt{\alpha t_d}$ is the depth of penetration of the thermal effects. At the sight of equation 5.2 two limit cases can be distinguished. In the first case δ_t is small compared with the vessel length; that is, the effect of heat conduction is confined to a thin layer close to the walls and equation 5.1 shows that the entropy can be considered constant within the vessel and equal to its initial value. On the contrary, in the second case the bulk of the fluid attains the temperature of the walls quickly enough for the process to be isothermal. In any case, for both scenarios two thermodynamic magnitudes are found to be uniform - pressure and entropy in the first and pressure and temperature in the second - enabling the discharge to be modelled as an isentropic or isothermal process respectively. For the purpose of this work, the transient events for which this model is ideated are rapid enough for the discharge to be considered adiabatic.

Conversely and unlike the discharge, under no circumstances the charge is isentropic because the mixing of the inlet jet with the surrounding fluid makes the viscous and heat transfer effects in equation 5.1 to be considerable. However, such mixing process that takes place is extremely effective and forces the temperature in the vessel to be uniform, although not necessarily constant.

Assuming that the control volume is not moving, and that the heat addition, buoyancy forces and flow velocity in the vast majority of the vessel are negligible, the application of the mass flow continuity and the total energy equations in their integral form to the vessel with N inlet and M outlet ports sketched in figure 5.31 eventually yields:

$$\frac{d}{dt}(\rho V) + \sum_{l=1}^{M} W_{o,l} - \sum_{r=1}^{N} W_{i,r} = 0 \tag{5.3}$$

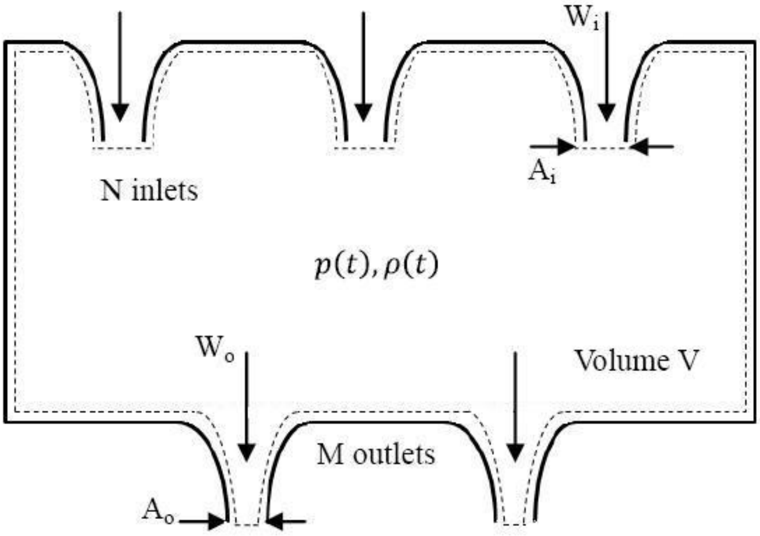

Figure 5.5: *Simultaneous charge and discharge of a pressure vessel. Control volume*

$$\frac{d}{dt}(\rho e_t V) + \sum_{l=1}^{M} W_{o,l} h_{o,l} - \sum_{r=1}^{N} W_{i,r} h_{i,r} = 0 \tag{5.4}$$

Furthermore, utilising the perfect gas equations for the total enthalpy and entropy, the total energy equation can be rearranged to give:

$$V\frac{dp_t}{dt} + \sum_{l=1}^{M} \gamma(\frac{p_t}{\rho}) W_{o,l} - \sum_{r=1}^{N} (\gamma - 1) W_{i,r} h_{i,r} = 0 \tag{5.5}$$

Provided that the inlet and outlet mass flows are known, the mass flow equation can be solved with the help of an explicit Euler scheme:

$$\rho^{n+1} = \rho^n + \frac{\Delta t}{V}(\sum_{l=1}^{M} W^n_{o,l} - \sum_{r=1}^{N} W^n_{i,r}) = 0 \tag{5.6}$$

And once the density evolution is known the pressure can be obtained in a similar fashion to that in equation 5.6:

$$p^{n+1} = p^n + \frac{\Delta t}{V}[(\gamma - 1)\sum_{r=1}^{N} W^n_{i,r} h_{i,r} - \gamma \sum_{l=1}^{M} W^n_{o,l} \frac{p^n_t}{\rho^n} = 0] \tag{5.7}$$

5.3.1.2 Nozzle behaviour

The previous methodology provides the thermodynamic conditions inside the vessel given that the mass flows at the interfaces are known. It is assumed that the vessel is connected to the outside on each port by a convergent nozzle. It is the study of these nozzles that determines the mass flows entering and leaving the vessel at each time step. For every time step, the inlet to tank and outlet to tank pressure ratios are compared to the sonic throat pressure ratio to determine whether the mass flow through the nozzle is the critical, W^*, or not, W. In the case of a discharge the mass flow for both cases is given by:

$$W_o^{*,n} = A_o(\frac{2}{\gamma+1})^{\frac{\gamma+1}{2(\gamma-1)}}\sqrt{\gamma\rho^n p_t^n} \tag{5.8}$$

$$W_o^n = A_o\sqrt{\gamma\rho^n p_t^n\frac{2}{\gamma-1}[\frac{p_e^n}{p_t^n}]^{\frac{\gamma+1}{\gamma}}[(\frac{p_t^n}{p_e^n})^{\frac{\gamma-1}{\gamma}}-1]} \tag{5.9}$$

Whereas in the case of a charge the mass flow is obtained from:

$$W_i^{*,n} = A_i(\frac{2}{\gamma+1})^{\frac{\gamma+1}{2(\gamma-1)}}\sqrt{\gamma\rho_e p_e^n} \tag{5.10}$$

$$W_o^n = A_i\sqrt{\gamma\rho^e p_e^n\frac{2}{\gamma-1}[\frac{p_t^n}{p_e^n}]^{\frac{\gamma+1}{\gamma}}[(\frac{p_e^n}{p_t^n})^{\frac{\gamma-1}{\gamma}}-1]} \tag{5.11}$$

To analyse the outcome of some possible operating scenarios such as a shaft failure the closure of some of the ports of the secondary air system may need to be considered. Should that be wished, it would be enough to replace the area A in any of the previous equations by a known function of time, A^n, so that this effect is accounted for in every time step.

5.3.1.3 Validation of the model

The experimental data available in the literature for charging and discharging vessels is limited to cases where either of the processes is considered in isolation but not simultaneously. In order to seize that data to validate the code issued for the simultaneous charge and discharge process of a reservoir, simulations have been carried out imposing either the inlet or the outlet ports to be closed ($A = 0$).

In [49] Dutton and Coverdill described a set of experiments carried out for didactic purposes in which the isolated charge and isolated discharge of several pressure vessels is monitored and also modelled as isothermal and adiabatic. In particular, one of the tests consisted of a pressure vessel that is hastily discharged through a convergent nozzle to the atmosphere. The results for the Dutton and Coverdill's models, the rig data and the model developed in the present work are grouped in figure 5.6. In this particular case both adiabatic models agree with each other and fit satisfactorily with the rig data; however, in a general case where the discharge may not be so quick the rig data would come closer to, but never trespass, the isothermal model line that represents the theoretical process in which heat transfer is effective enough for the temperature to be constant and equal to the environment's.

The second experiment reported in [49] relevant to the study under consideration explores the charge of an initially vacuum reservoir from the atmosphere through a convergent nozzle. In

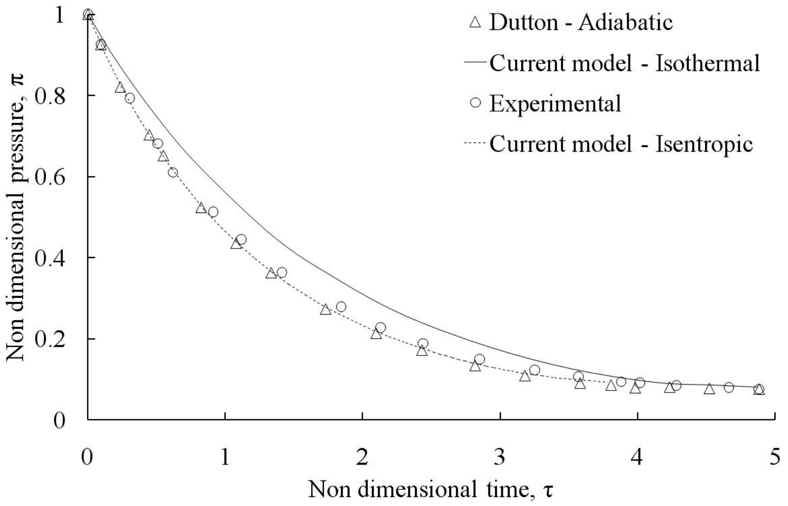

Figure 5.6: *Dynamic model validation of a discharging vessel in isolation*

this case, the rig data seems to be better approximated by the isothermal model developed by Dutton and Coverdill (fig. 5.7); nevertheless, the agreement between the adiabatic model and the model developed herein is remarkable, and such model is expected to deal with the rapid charging processes that occur in the SAS adequately.

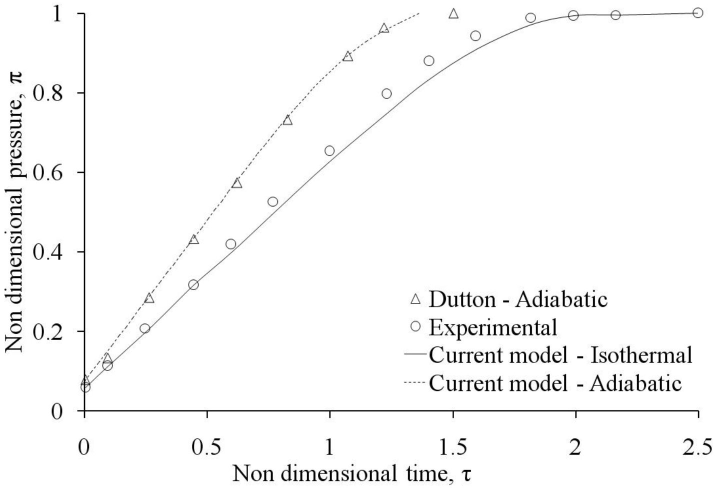

Figure 5.7: *Dynamic model validation of a charging vessel in isolation*

5.3.2 Unsteady one-dimensional flow of a gas through a tube

5.3.2.1 Assumptions and mathematical apparatus

[2]The necessity to model the flow through a duct as a transient phenomenon arises from the fact that the flow is affected by the fluid inertia because a finite time is required for any perturbation exerted in the flow at one end of the duct to be transported to the other end. In particular, if during a transient scenario there is an undesired pressure overshoot along the system the existence of long

---

[2] See appendix 5B for complete details of the mathematical model

and narrow conduits that connect the SAS cavities will exacerbate the problem. Whereas the SAS reservoirs act as pressure fluctuation dampers similar to a well damped spring-mass-damper system or an electrical capacitor, the tubes induce a lag and magnify such pressure overshoots.

To analyse the unsteady movement of the gas through a duct the Navier-Stokes equations evolve to the Euler equations by applying the following assumptions [102]:

- $\vec{v} = u \cdot \vec{i}$. One-dimensional flow.
- $p = \rho R_g T$. Perfect gas model applicable.
- $Re >> 1$. Inviscid flow.
- $RePr >> 1$. Heat conduction negligible.
- $St \geq 1$. Unsteady flow.
- $Fr >> 1$. Buoyancy forces negligible.
- No chemical reactions.
- The tube is not moving.

Consequently, the system of equations, in its characteristic form is reduced to:

$$\frac{\partial w_i}{\partial t} + \lambda_i \frac{\partial w_i}{\partial x} = 0 \;\; \forall\, i = 1, 2, 3;\; \lambda_i = \frac{dx}{dt} \tag{5.12}$$

Where the Riemmann invariants and the characteristic curves are given by:

$$\delta w_1 = \delta p - a^2 \delta \rho; \quad \lambda_1 = u = C^0 \tag{5.13}$$

$$\delta w_2 = \delta u + \frac{1}{\rho a} \delta p = \delta R^+; \quad \lambda_2 = u + a = C^+ \tag{5.14}$$

$$\delta w_3 = \delta u - \frac{1}{\rho a} \delta p = \delta R^-; \quad \lambda_3 = u - a = C^- \tag{5.15}$$

The first equation can be integrated to yield that the entropy of the particles, although different amongst them, does not change along their movement. On the other hand, the second and third equations show that the invariant R^+ will be constant as we travel towards the positive direction of the x axis at speed a, whereas R^- will not change with respect to an observer that moves towards $-x$ at speed a. This discussion provides the necessary background to understand why the choice of boundary conditions is profoundly influenced by the flow regime. The characteristic lines given by equations 5.13 to 5.15 can be interpreted as the directions along which small disturbances are propagated within the flow, and it is evident that their slope - particularly that of C^- - and hence their direction, depend on the relationship between u and the speed of sound a. Due to the fact

Table 5.1: *Tube flow model - Boundary conditions as a function of the flow regime*

	Subsonic		Supersonic	
	Physical	Numerical	Physical	Numerical
Inlet	w_1, w_2	w_3	w_1, w_2, w_3	$--$
Outlet	w_3	w_1, w_2	$--$	w_1, w_2, w_3

that information is only transported along characteristics that enter the domain (fig. 5.8), for the system of equations to be mathematically closed there is the need in some cases to add numerical boundary conditions (table 5.1). Such conditions can be derived utilising several methods such as the characteristics [53] or extrapolation methods [154]. Moreover, while the boundary conditions that are usually known refer to primitive measurable variables such as pressure or velocity, the boundary conditions that are to be inputted into the system of equations must be formulated in terms of the characteristic variables and therefore they need to be constructed from those elemental variables.

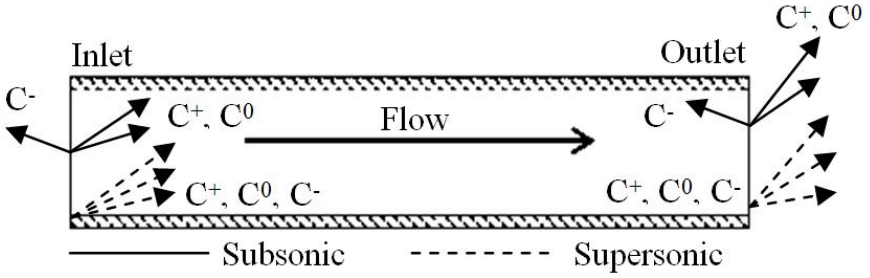

Figure 5.8: *Tube characteristics into and out of the domain*

The Euler equations constitute a non linear hyperbolic partial differential equations system that can be formulated in a conservative or a non-conservative form. On top of the fact that the applicability of numerical schemes based on the latter formulation is restricted to cases exempt of discontinuities - i.e. shock waves - at the risk of not reaching convergence otherwise, the conservative approach benefits from some computational advantages that deem it the right choice for the present study where flow reversal is likely to occur in some of the SAS branches at off-design conditions. It is for these reasons that a so called Roe's approximate upwind Riemann solver has been chosen as the baseline algorithm employed in the simulations [51]. Furthermore, Roe's scheme is a finite volume method fit to tackle flow discontinuities in contrast to finite difference methods [137]. The method is too lengthy to be contained here, and the interested reader should confer [75][154][175][121] for a comprehensive description.

To guarantee the numerical stability of the scheme, the Courant-Friedrichs-Lewis (CFL) condition is utilised[3], as suggested in [75][175][26]. According to such approach, for the scheme to be stable the CFL factor should be smaller than unity and the couple Δx and Δt must obey the

---

[3] This is a mathematical condition that establishes the compatibility of the spatial and time discretisations in terms of convergence and stability of the numerical schemes used.

following relation:

$$(|u| + a)\frac{\Delta t}{\Delta x} \leq CFL \tag{5.16}$$

In order to unequivocally define the numerical scheme the numerical fluxes at the boundaries, $x = 0$ and $x = l$ for the following time step are required. In the present scheme two fictitious cells have been introduced upstream and downstream of the inlet and the outlet respectively, and the numerical fluxes have been calculated in the same manner as for any other interior cell.

5.3.2.2 Validation of the model

To validate the tube code two different comparison tests have been carried out. The first aims to assess the numerical error associated with the numerical scheme utilised to model the flow whereas the second is in turn carried out against the experimental data obtained by Felling et al. [51] for a shock tube and investigates the validity of the Euler equations to model the flow. In [75] Hirsch produces the solution for the so called Riemann problem; that is, the evolution of the flow thermodynamic properties for a 10 metres shock tube compartmented by means of a thin membrane as sketched in fig. 5.9. The same gas is initially confined by such diaphragm at two different states:

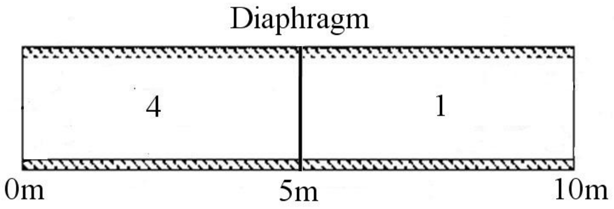

Figure 5.9: *Shock tube*

$$For \quad x < \frac{l}{2} \quad \rho(x, t = 0) = 1\frac{Kg}{m^3}; \quad u(x, t = 0) = 0\frac{m}{s}; \quad p(x, t = 0) = 10^5 Pa; \tag{5.17}$$

$$For \quad x > \frac{l}{2} \quad \rho(x, t = 0) = 0.125\frac{Kg}{m^3}; \quad u(x, t = 0) = 0\frac{m}{s}; \quad p(x, t = 0) = 10^4 Pa; \tag{5.18}$$

Suddenly, as the diaphragm is ruptured a shock wave propagates to the right compressing the flow left behind and, at the same time, an expansion wave travels towards the left end of the tube expanding the flow. After 6.1 milliseconds have elapsed, Hirsch's solution and the results produced by the code for the density, velocity and pressure evolutions of the flow are compared in figures 5.10, 5.11 and 5.12 and show that the numerical convergence and stability of the scheme is excellent.

The ability of the model to capture the physics of the flow movement was assessed by comparing

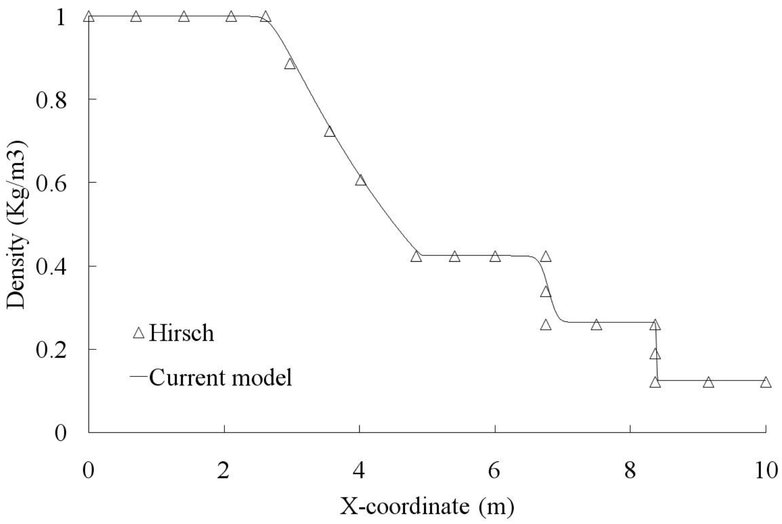

Figure 5.10: *Shock tube. Numerical validation - Density at 6.1mS*

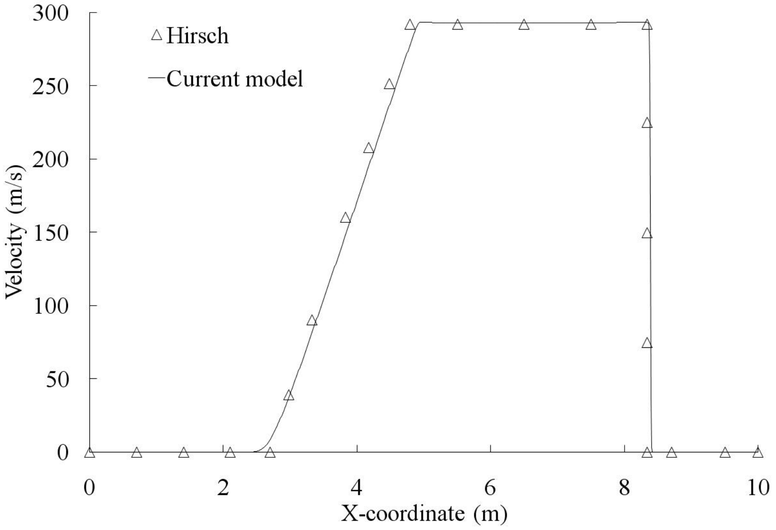

Figure 5.11: *Shock tube. Numerical validation - Velocity at 6.1mS*

the computational data with the test data published by Felling et al. [51]. In such work, the evolution of the flow properties within a shock tube was recorded and two different computational models were engineered to describe the movement. The computational results obtained follow the trend exhibited by the rig data although a difference in the height of the pressure plateau does exist (fig. 5.13). However, the agreement attained with the tube code is still better that the results produced by the two codes developed by Felling - Shtube.exe and Meltube.exe.

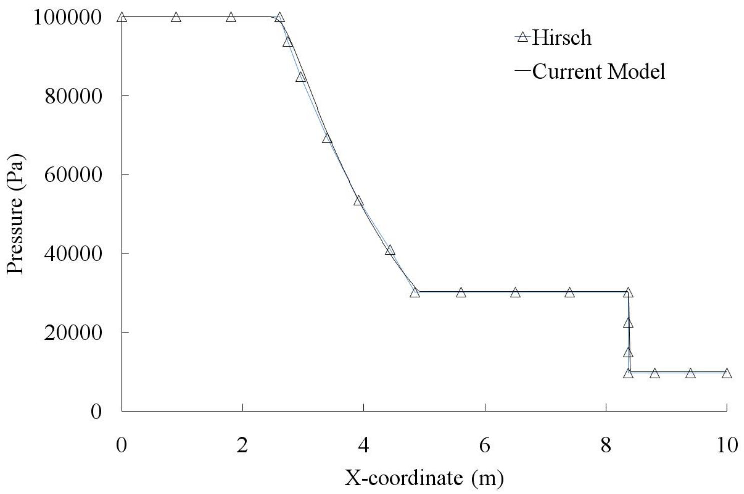

Figure 5.12: *Shock tube. Numerical validation - Pressure at 6.1mS*

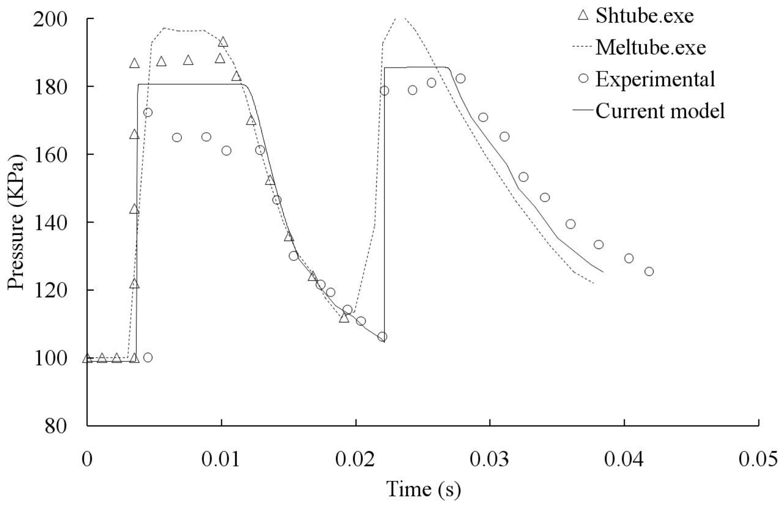

Figure 5.13: *Shock tube. Experimental validation*

5.4 Network assembly

5.4.1 Boundary conditions

The coupling between the models developed presents some challenges, the main issue being the heavy interrelation between components. In fact, the mass flow transfer between the vessels is affected by the flow inertia and the pressure waves in the pipes, but in turn the boundary conditions of the transient flow through the pipes are defined by the charge and discharge process of the vessels. The coupling of the components is hence achieved by means of the boundary conditions. It is therefore necessary to find the appropriate formulation of such conditions representative of the interaction of the tube with the neighbouring vessels.

As seen in section 5.3.2, three boundary conditions have to be imposed at each boundary of the pipe. These are split into physical and numerical boundary conditions. The physical boundary conditions are those physical variables that can be freely imposed at the boundaries and will depend on the way the information transported along the characteristics interacts with the boundaries. However, for the numerical problem to be unequivocally defined, the values of all the variables at the boundaries are required and hence additional conditions of numerical origin, referred to as numerical boundary conditions, must be added [76][173]. A wide variety of methods can be used for the definition of the boundary conditions, depending on the variables used in the definition of the physical boundary conditions and the method used for the imposition of the numerical conditions. The choice of the boundary conditions infers some challenges since their definition can have a remarkable effect on the accuracy, stability and convergence of the numerical scheme used. The number of physical boundary conditions that are required is also dependent on the flow condition at a given boundary. Namely, for subsonic inflows, the mass flow and energy conservation equations between the nozzle exit and the tube inlet section are imposed. The additional numerical condition is obtained by the discretisation of the compatibility equation that corresponds to the negative characteristic, C-, approximating the space derivatives by one-sided second order difference formulas. For subsonic outflows the tank pressure is imposed as a physical condition, while a zero order extrapolation in space and time is used to obtain the two numerical boundary conditions. In the case that the flow reaches sonic conditions, three physical boundary conditions at the inlet, and three numerical boundary conditions at the outlet are required. The resulting system of equations for the left and right boundaries of the tube is summarised in tables 5.2 and 5.3.

Table 5.2: *Physical boundary conditions for the movement of a gas in a duct*

	Flow regime	Physical BCs
Inflow	$M < 1$	$W_{N1} = \rho_L u_L A$
boundary		$\frac{\gamma}{\gamma-1}\frac{p_1}{\rho_1} = \frac{\gamma}{\gamma-1}\frac{p_L}{\rho_L} + \frac{u_L^2}{2}$
	$M \geq 1$	$\rho_L = \rho N1$
		$u_L = uN1$
		$p_L = pN1$
Outflow	$M < 1$	$p_R = p_2$
boundary	$M \geq 1$	$None$

Table 5.3: *Numerical boundary conditions for the movement of a gas in a duct*

	Flow regime	Numerical BCs
Inflow	$M < 1$	$\frac{\delta u}{\delta t} - \frac{1}{\rho a}\frac{\delta p}{\delta t} + (u-a)(\frac{\delta u}{\delta x} - \frac{1}{\rho a}\frac{\delta p}{\delta x}) = 0$
boundary	$M \geq 1$	$None$
Outflow	$M < 1$	$\rho_R = \rho(\rho_{i\,max}, \rho_{i\,max-1}, \rho_{i\,max-2}, \cdots)$
boundary		$u_R = u(u_{i\,max}, u_{i\,max-1}, u_{i\,max-2}, \cdots)$
	$M \geq 1$	$\rho_R = \rho(\rho_{i\,max}, \rho_{i\,max-1}, \rho_{i\,max-2}, \cdots)$
		$\rho_R = u(u_{i\,max}, u_{i\,max-1}, u_{i\,max-2}, \cdots)$
		$p_R = p(p_{i\,max}, p_{i\,max-1}, p_{i\,max-2}, \cdots)$

For the system of equations to be mathematically closed the mass flow at the inlet boundary must be specified. The mass flow is determined by the discharge process of the vessel connected to that tube end that is a function of the outlet pressure, which in this case is not easily defined. The numerical algorithm proposed for the inlet boundary involves an iterative procedure to couple the tank solution with the boundary conditions: the discharging mass flow must be varied until the nozzle outlet conditions are equal to the left boundary conditions. As a result, the mass flow will not just be a function of a state but will be determined based on information from inside the domain reaching the boundary along the negative characteristic.

5.4.2 Assembly validation

Before applying the model to complex networks, the numerical algorithm proposed is applied to the reservoir discharge problem described in [19] known as the De Haller problem. As sketched in figure 5.14 a pipe of $0.01m$ diameter and $1m$ length is connected to a large reservoir pressurised to $150kPa$. A valve is fitted at the other end of the pipe to separate it from the ambient at a pressure of $100kPa$. Initially the valve is closed and the system is in equilibrium. The exact theoretical solution of the unsteady flow in the pipe when the valve is suddenly opened is derived by assuming homoentropic flow and was produced by Bessel [19].

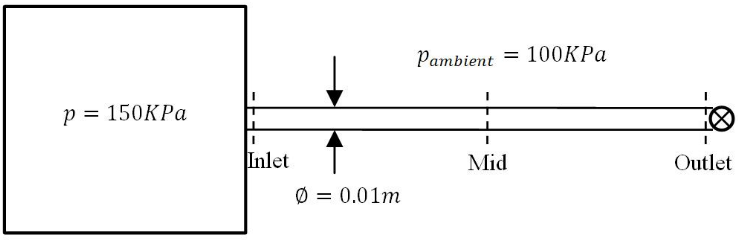

Figure 5.14: *The De Haller problem*

The solution shows the existence of pressure waves travelling in the pipe that are reflected at the boundaries. The theoretical and numerical pressure evolutions at three different locations (inlet, mid length and outlet) along the tube are presented in figure 5.15, while the associated velocity profiles are shown in figure 5.16. It is evident that, although the numerical solution slightly rounds off the sharp edges, it tends to follow the theoretical solution quite closely. These results therefore validate the network assembly methodology that has been explained previously in 5.4.1.

5.4.3 Test cases

In order to assess the influence of the main geometric parameters of the SAS on the dynamic behaviour of the system, a series of test cases are carried out for the modelling of simple networks.

First, the transient response of a vessel of a volume and discharge area similar to a typical LPT drum cavity to a step change in the boundary ambient pressure has been analysed. Although the real LPT cavity has a number of different boundaries, the results show that the time taken for a cavity of this size to adapt to the new pressure is comparable to the characteristic time of rapid transients such as a shaft failure (fig. 5.17).

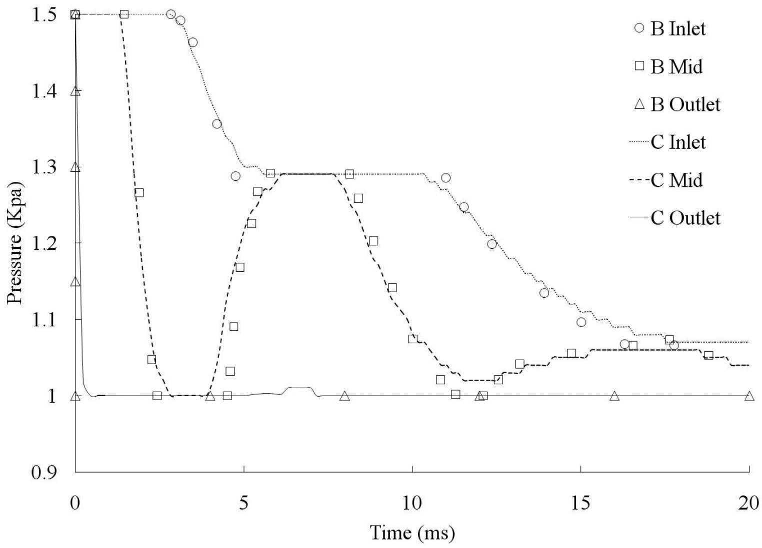

Figure 5.15: *Network assembly validation - Pressure evolution in the De Haller problem*

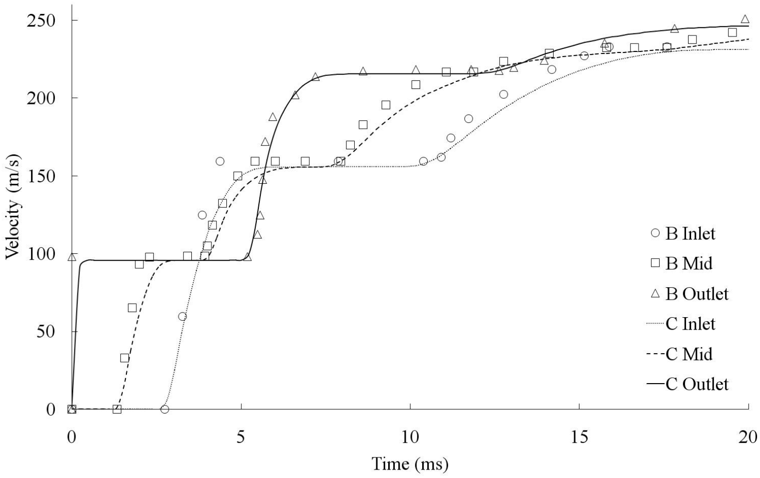

Figure 5.16: *Network assembly validation - Velocity evolution in the De Haller problem*

Secondly, a simple system is analysed in order to reproduce the gas transfer between the IPC and LPT cavities, which are connected through the inter-shaft gap in the IP system. To that end a high pressure vessel and a low pressure vessel similar in size to the air system cavities are considered. The two chambers are connected by a 0.6m long, thin flow conduit (fig. 5.18a). The transient flow through such conduit may affect the gas transfer between the two chambers because of the flow inertia and the possible presence of shock waves pulsating up and downstream of the tube. Although in reality the IPC cavity is continuously fed by the IP compressor and the LPT cavity has several ports, at this stage this simple approximation suffices. It is assumed that initially a valve separates the LPT cavity from the rest of the system which is stagnated. At t=0 the valve is suddenly opened and the system is allowed to reach equilibrium (fig. 5.18b). The resulting pressure evolution in the LPT cavity plotted in figure 5.18b oscillates around the final value. In fact, because of the inertia of the flow through the tube, a finite time is required for any change at one end of the tube to be transported to the other end and therefore, the pressure in the LPT

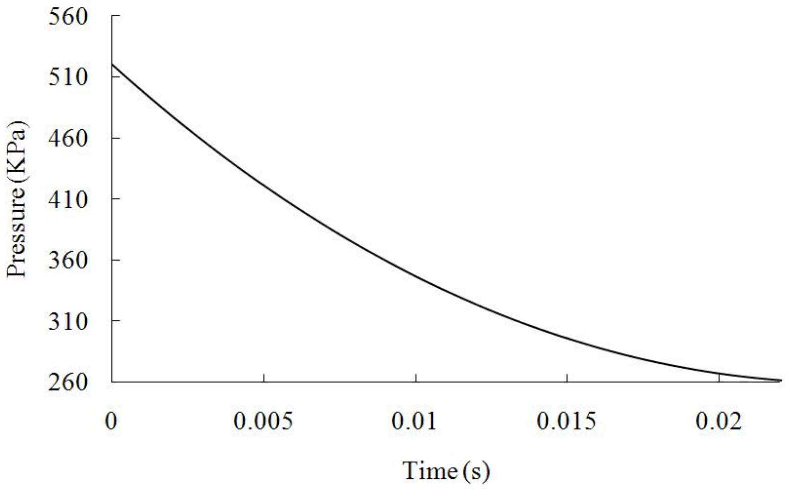

Figure 5.17: *Response of a typical LPT drum cavity to a step change of the ambient pressure*

cavity continues to increase although the IPC pressure is lower. As a result, after a certain time the flow in the tube reverses and the pressure in the chambers fluctuate around the equilibrium pressure until the equilibrium state is reached.

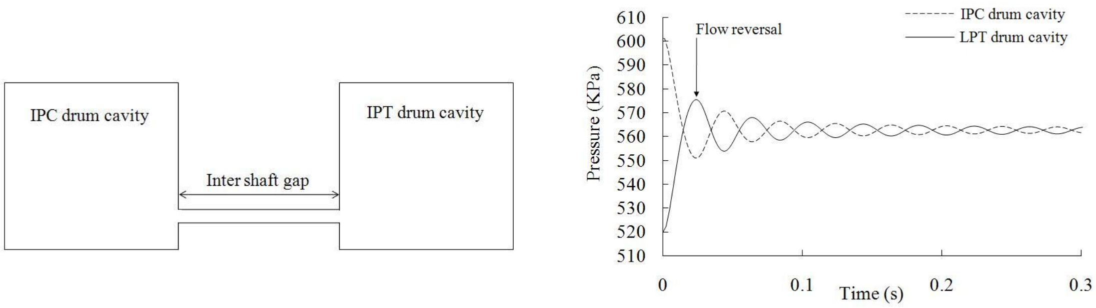

(a) *Simplified network*

(b) *Response for* $l = 0.6m$

Figure 5.18: *Simplified air system network and associated response*

It is interesting to see what happens if a shorter tube links the two vessels or even in the limit case, when just an orifice between the reservoirs is considered. The pressure evolution for these two cases is presented in figures 5.19a and 5.19b respectively. As expected, the overshoots are considerably reduced. On the other hand, the speed of response of the systems is very similar regardless of the duct length. In fact, although a slight increase can be noticed for the longest pipe the time to reach the target pressure is almost the same, the main difference between the two cases being the inertia exerted by the tube length on the flow progression that will force the pressure to overshoot. The amplitude of the overshoots will depend on the length of the tube. Consequently the settling time, defined as the time to get to and stay within 10% of the target value, is different for each system.

To account for the fact that the LPT cavity is connected to several chambers that are usually of a smaller size rather than isolated, a small volume vessel is added to the system analysed (fig.

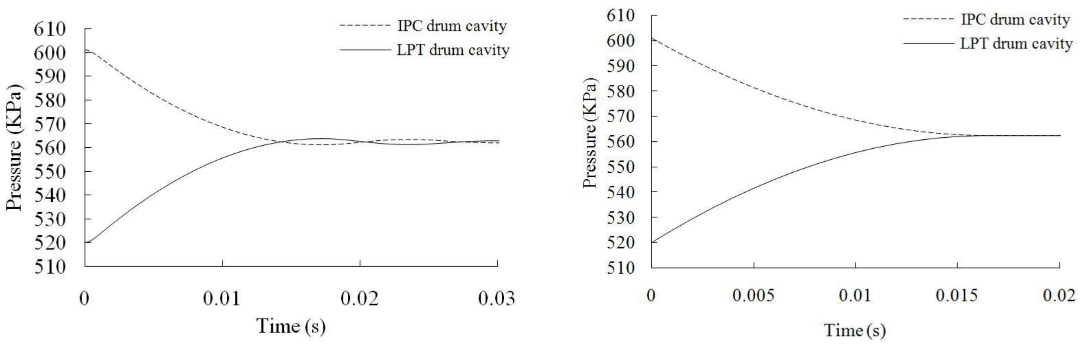

(a) $l = 0.06m$ **(b)** *No intershaft gap,* $l = 0$

Figure 5.19: *Effect of the length of the inter-shaft gap in the response of the system*

5.20a). The predicted pressure evolutions in the three cavities are represented in figure 5.20b. As would be expected the system now tends to reach a lower target pressure. However, the pressure overshoots in the LPT cavity are of the same order than in the two cavities case. It can be seen that the pressure in the cavity V tends to rapidly assimilate the LPT cavity pressure, due to its small capacity, and follows its behaviour effortlessly afterwards. This is due to the fact that, because of the big difference in the volume capacity between the LPT and the additional cavity, the response of the latter is very fast and the pressure in the cavity V tends to oscillate around a final pressure that is very close to the LPT initial pressure. The pressure overshoots in the LPT cavity do not seem affected by the presence of this smaller volume.

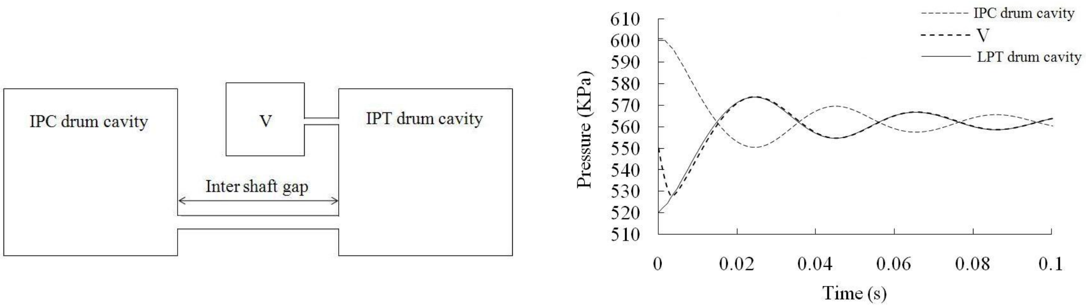

(a) *Network configuration* **(b)** *Response for* $l = 0.6m$

Figure 5.20: *Simplified air system network with three cavities*

5.5 Labyrinth seals

[4]Most labyrinth seal models are based on the work carried out by Martin [117][118] that considered the leakage through labyrinth seals as expansions of an ideal gas through a series of orifices.

---

[4] See appendix 5C for complete details of the mathematical model of the ideal flow through a labyrinth seal

Martin's equation provides the leakage through the seal:

$$\dot{m} = Ap_{t0}\sqrt{\frac{1-\left(p_n/p_{0t}\right)^2}{RT_{0t}\left[n-ln\left(p_n/p_{0t}\right)\right]}} \tag{5.19}$$

where m is the mass flow rate, A is the annular clearance area of the seal, p_{t0} is the upstream total pressure, p_n is the downstream static pressure, R is the characteristic gas constant, T_{t0} is the upstream total temperature, and n is the number of labyrinth fins.

Several authors have modified Martin's model by using different discharge coefficients [202][149][183] that are correlated against the geometry of the seal and the flow conditions. However, these seal models were developed some decades ago and hence do not cover all the geometries and conditions of operation of modern engines. Engine manufacturers use extensive confidential data bases that are obtained from experimental rigs. The methodology used to model the operation of labyrinth seals in this work uses an algorithm developed by the sponsor that gives the conditions downstream of the seal for a given set of thermodynamic conditions upstream of the seal and a given mass flow. This guarantees the accuracy of the results since the correlations were developed from data obtained from modern test rigs.

On the other hand, the volume of the cavities of the labyrinth seals is very small compared to the characteristic volumes of the main cavities of the air system. This allows for the transient effects on the operation of the seals to be disregarded with respect to the transient operation of the main cavities of the air system.

5.6 Rotating cavities

[5] The equations presented in the previous sections idealise the flow in the cavities of the air system as containing static fluid with no radial pressure gradient. In reality the cavities in the system rotate and induce vortices in the flow that lead to significant radial pressure gradients in the flow field. Not including the effect of rotation in the model is recognised as a serious weakness in the prediction of the performance of the internal system because the vortex introduces a retard in transient pressure overshoots in the cavities.

5.6.1 The transient character of the vortex

At steady state conditions is common place to model the radial pressure distribution on the turbine discs by assuming that it obeys a general law of the form:

$$\frac{p_2}{p_1} = \left\{1+\frac{k^2}{2nc_pT_1}\left(r_2^{2n}-r_1^{2n}\right)\right\}^{\frac{\gamma}{\gamma-1}} \tag{5.20}$$

The coefficient n can be related to the through flow over the disc with the help of the coefficient

---

[5] See appendix 5D for complete details of the equations to characterise vortical flows in internal air system cavities

$\lambda = \frac{C_w}{Re^{0.8}}$ where C_w is a non dimensional mass flow coefficient given by $C_w = \frac{\dot{m}}{\mu r}$:

- $-0.001 < \lambda < 0.01$ This describes low through flows for which the vortex is approximated by a forced law.
- $\lambda < -1$ or $\lambda > 0.4$ This characterises high through flows that can be approximated by a free vortex.

The meaning of intermediate values of λ is not clear - specialists [38][161] suggest that the relationship between n and λ for those values is certainly not linear and it is suggested it may be approximated by an exponential law (fig. 5.33).

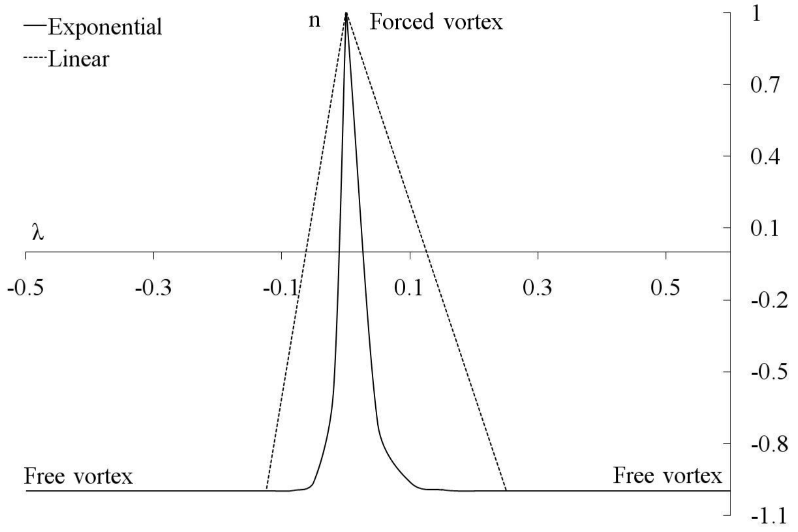

Figure 5.21: *Proposed general vortex law exponent as a function of the through flow into a rotating cavity*

For the limit cases in which $n = 1$ (force vortex) and $n = -1$ (free vortex) the nondimensional pressure distribution along the radius is plotted in figure 5.22

The determination of n at transient conditions is even more obscure. The change of rotational speed of the discs is transmitted to the fluid inside the cavity and changes the character of the vortical flow. The viscosity of the fluid is the mechanism that drags the flow particles in the boundary layer and transmits the change of velocity through the fluid in the cavity. However, the momentum transfer across the boundary layer is not instantaneous and takes a finite time for the flow to adapt to the new conditions.

The process is analogous to stirring a cup of tea with a spoon to dissolve a lump of sugar. Initially the liquid in the cup is at rest, and as the spoon is stirred the fluid spins progressively further away from the spoon and it takes some time until the movement reaches the rim of the cup. The analysis of simpler problems, like Stokes' flow problem[6] shows that there is a characteristic length, δ, known as the charateristic length of penetration of the viscous effects, that is the distance

---

[6] Stokes' flow is the name given to the unidirectional movement of an incompressible flow of constant viscosity that occupies the semispace limited by an infinite plate that oscillates parallel to its length with a constant frequency.

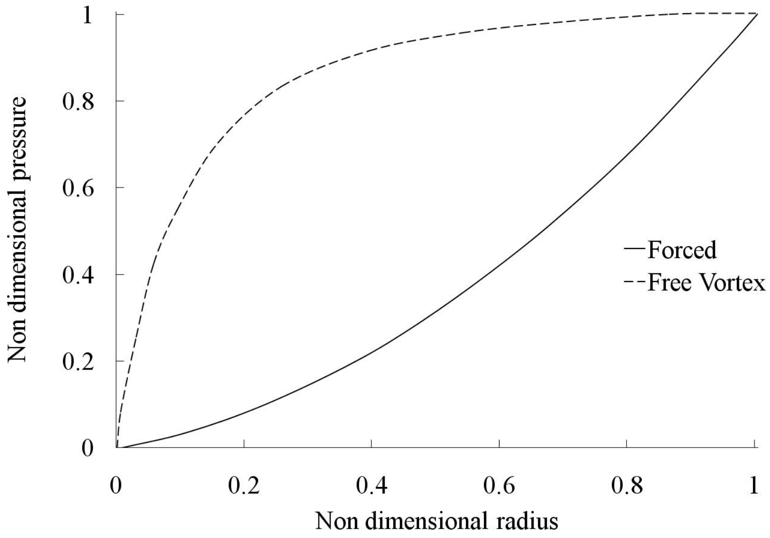

Figure 5.22: *Non dimensional pressure distribution along the radius for several vortex laws*

away from the wall where changes of velocity are of the order of the characteristic velocity of the movement. It can be demonstrated that this length is of the order of

$$\delta \approx \sqrt{\nu t_c} \approx \sqrt{\nu/\omega} \tag{5.21}$$

The kinematic viscosity of air at high temperatures is of the order of $10^{-4} m^2/s$, and for a characteristic time of 1 second equation 5.21 shows that viscous effects can only be noticed 1cm away from the walls.

There are, however, two limit cases for equation 5.21:

- $\delta << 1$. In this case the effects of viscosity are confined to a very thin layer close to the disc during the whole event. To a first order it could be considered n is constant during the over-speed; that is, the character of the vortex does not change during the event.
- $\delta >> 1$. In this case changes of disc velocity are transported instantaneously to the whole bulk of fluid in the cavity. The event can be modelled as a superposition of infinite steady states for which λ and n need to be evaluated.

5.7 Implementation of the rotation and seal models

The implementation of the rotation model into the code has been carried out as shown in figure 5.23. Prior to the analysis of the transient response of the network, calculations run until the network is in equilibrium with the steady state conditions prescribed at the boundaries. Once the equilibrium has been reached the conditions for the next time step of the transient are obtained by superposing the vortex distribution given by λ and figure 5.33 to the pressure in the cavity. The averaged pressure in the cavity is obtained by integration over the radius of the disc. This fixes the conditions upstream of the seals of the cavity and the leakage through the seals in the next time step is then calculated with the help of the seals model. Equations 5.6 and 5.7 calculate then the density and pressure of the fluid left inside the cavity, and the process is repeated for the next time step.

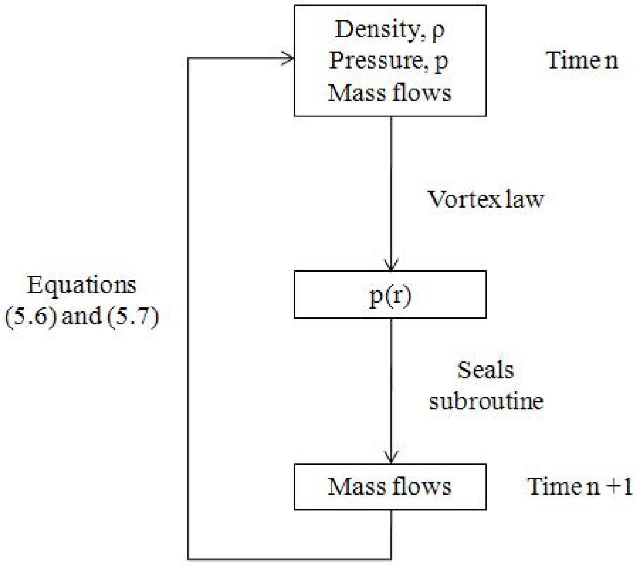

Figure 5.23: *Flow chart of the calculations in rotating cavities*

The vortex subroutine provides the pressure downstream of the seal for a known pressure and temperature upstream of the seal and the leakage flow. In the simulation of whole networks, however, it is the mass flow across the seal that is unknown whereas the conditions downstream are given by the discharge of the flow into the main gas path. The calculation of seals is therefore iterative - mass flow through the seal is changed until the pressure downstream of the seal converges to 0.1% of the downstream pressure.

5.8 Shaft over-speed simulations

Simulations to investigate the performance of the air system during a shaft over-speed event were carried out in the research. Axial loads on the turbine discs were calculated from the pressures produced by the simulations, and are an input to the finite element code used by K. Psarra [146] to analyse the mechanical interaction of turbine discs in contact (see sections 3.3.1 and 5.10).

5.8.1 Network geometry

The model simulates the whole intermediate and high pressure branches of the air system of a modern high bypass ratio turbofan engine. The geometry consists of 16 cavities and 16 tubes connected by nozzles and labyrinth seals (fig. 5.24).

Volumes 1, 11, 12, 13, 14 and 15 represent the engine main gas path stations and are boundary

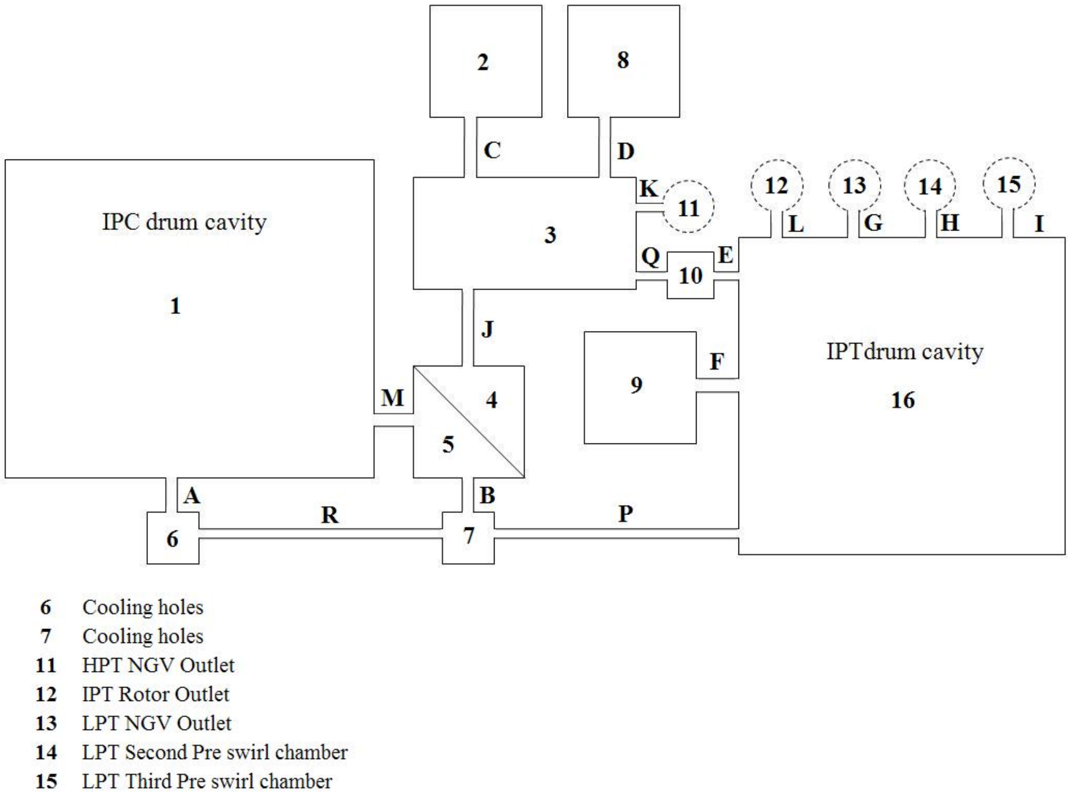

Figure 5.24: *Whole air system model network configuration*

conditions to the simulations of the air system. These volumes are modelled as having an infinite volume so that they are perfect pressure and temperature sources that are not affected by the behaviour of the secondary air system.

5.8.2 Boundary conditions

The main aim of this chapter is to demonstrate the capabilities of the model developed to model the transient performance of the SAS prior to its inclusion into a whole engine performance model. The boundary conditions prescribed in the simulations were chosen with this in mind, so that they represented the most challenging scenario from the SAS modelling viewpoint. Although a simulation where the engine surges, recovers and continues operating unstalled during the event is worse from a terminal speed point of view, a scenario where the engine surges, recovers and surges again is more challenging for the air system model to capture. This is because at the bottom of the first surge cycle there is likely to be flow ingested by the LPT cavity.

The notional boundary conditions imposed in the shaft over-speed simulations are shown in figure 5.25. These are taken from engine data available to the research. At maximum take-off conditions the engine surges, recovers after 200ms, surges again a tenth of a second later and subsequently runs down in stall. Boundary conditions in cavities 11 to 15 are obtained from running a whole engine model imposing the pressure profile shown in figure 5.25.

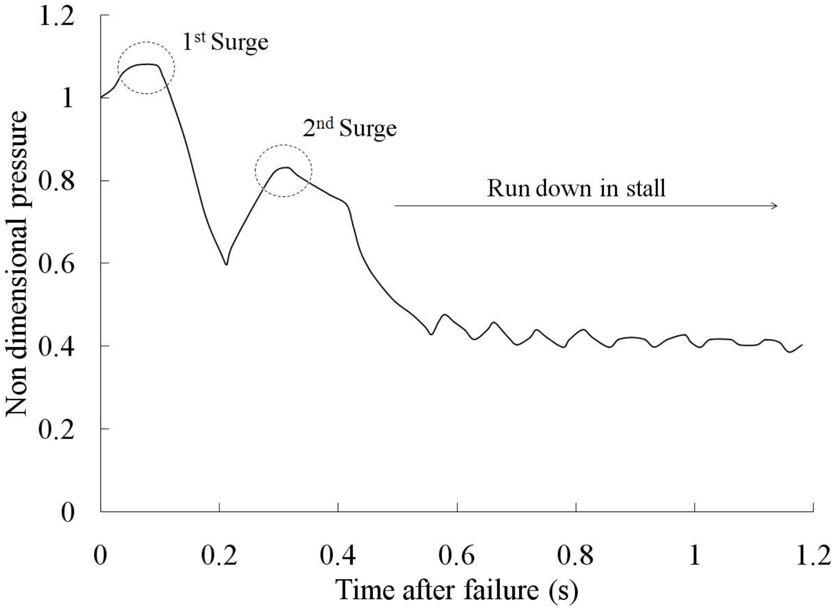

Figure 5.25: *Prescribed pressure profile in the LPC drum cavity for the internal air system shaft over-speed simulations*

5.8.3 Case $\delta << 1$ - Constant vortex modelling

If the charateristic length of penetration of the viscous effects is very small the character of the vortex and hence the vortex exponent, n, does not change during the over-speed event. The simulation of the event for the free and forced vortex will limit the real case since any vortex distribution will lie between such vortex laws (see figure 5.22). The free vortex case depends on the initial tangential velocity of the fluid entering the cavity - in this case the disc does not do any work on the fluid and the tangential velocity of the fluid is constant along the radius. For the geometry studied, the inter shaft gap discharges into the LPT cavity very close to the engine shaft and hence the tangential speed of the fluid entering the cavity can be disregarded. On the opposite end, the forced vortex law guarantees that the fluid in contact with the walls rotates at the velocity of the disc and hence the flowfield depends strongly on the shaft speed. It is evident that the departure between the two vortex laws is greater the higher the spool speed is. Figure 5.26 shows the pressure evolution in the LPT cavity for the free and forced vortex laws for a constant speed of the intermediate pressure shaft that is twice the nominal. These two simulations set the limits between which any shaft failure event would be contained.

As expected, there is an initial build up of pressure in the LPT cavity as a consequence of the sudden rise of pressure in the IPC cavity at the at the onset of the first surge sequence. Then the LPT cavity pressure starts to decrease following the IPC cavity pressure evolution. After a delay, due to the flow inertia, the flow in the inter-shaft gap reverses. When the second surge is triggered, the IPC cavity pressure increases again, restoring the initial flow direction in the inter-shaft gap and causing the LPT cavity pressure to increase again.

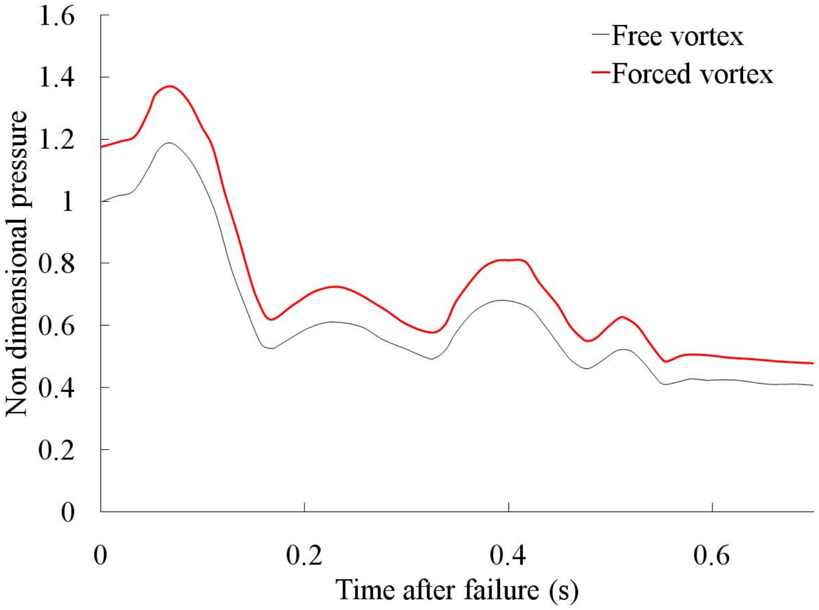

Figure 5.26: *Pressure profile in the low pressure turbine cavity for constant free and forced vortex laws for the boundary conditions of figure 5.25 - IP shaft speed 200%*

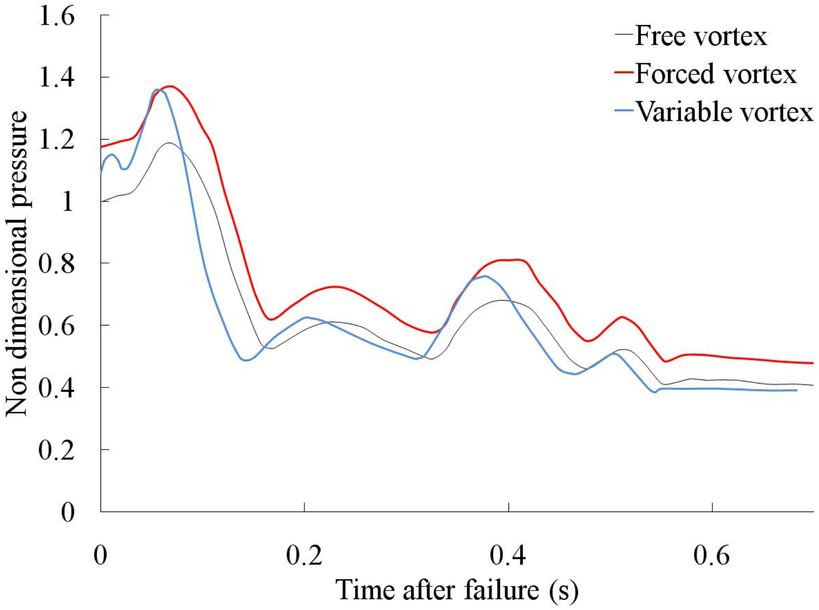

Figure 5.27: *Pressure profile in the low pressure turbine cavity for constant free and forced vortex laws and for a quasy steady variable vortex for the boundary conditions of figure 5.25 - IP shaft speed 200%*

5.8.4 Case $\delta >> 1$ - Quasy steady vortex modelling

In the cases where the length of penetration of the viscosity effects is big, the movement of the disc is transmitted instantaneously to the fluid in the cavity and the event can be modelled as a sequence of steady states where the whole of the fluid inside the cavity obeys a given vortex law. At each time step the vortex exponent n is evaluated as a function of the mass flow entering the cavity through the coefficient λ. Figure 5.27 shows the evolution of the pressure inside the LPT drum cavity and compares them with the fixed free and forced vortex law of the previous section. Results oscillate between the forced and free vortex laws, with more acute pressure peaks that happen around 20ms earlier.

5.8.5 Effect of closure of the discharge port

During an unlocated shaft over-speed event pressure build ups in the cavities of the internal air system arise not only from the pressure rise at the beginning of the surge event but from the closure of some of the ports of the secondary air system too. To account for the rearward displacement of the turbine disc, the area of the ports of the air system can be specified in the equations as a function of time; that is, the area A in equations 5.8 to 5.11 and equation 5.19 can be expressed as $A = A(t) = A^n$.

The effect of the closure of the IPT rotor rear gap after an unlocated IP shaft failure has been investigated by means of a sensitivity analysis of the pressure evolution in the LPT cavity for different constant areas of the IPT rotor rear gap during the event (fig. 5.28). The average pressure inside the cavity rises for smaller gaps and the initial pressure build up following the first surge is aggravated significantly (up to 40%).

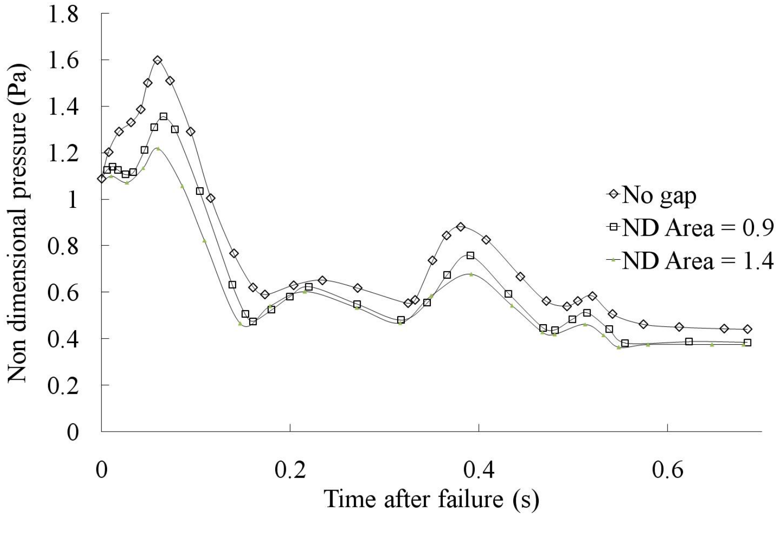

Figure 5.28: *Effect of the discharge port area. Pressure profile in the low pressure turbine cavity for a quasy steady variable vortex for the boundary conditions of figure 5.25*

However, the accurate determination of the area of the ports of the SAS against time is not immediate. The performance of the system is coupled to the progression of the event from a mechanical point of view. This will be discussed in section 5.10. Furthermore, after the breakage the impact of the turbine disc may be violent enough for the disc to bounce back and open up the rotor rear gap again. The forwards movement of the disc would result in opening the seal and equalising the pressure with the gaspath, limiting the axial load on the turbine disc and the energy dissipated as friction from the contact.

5.9 Calculation of turbine endloads

The problem of predicting the transient response of the air system mainly arises in the calculation of endloads. During steady state or normal transients the endloads are derived from non dimensional plots of load versus pressure ratio that are obtained from a number of steady state performance points. However, this is not adequate for very rapid transient manoeuvres.

The air system model reported here is capable of providing the evolution of pressure along the system during a shaft failure event. The pressure distribution at both sides of the disc can be integrated over the radius to yield the axial load exerted on the turbine disc:

$$F_{axial,\ disc} = \int_{r_{in}}^{r_{out}} p(r) 2\pi r dr \tag{5.22}$$

The net axial load acting on the free turbine disc depends on the gas load on the blades and the gas load on the disc:

$$F_{axial,\ net} = F_{axial,\ disc} + F_{axial,\ blades} \tag{5.23}$$

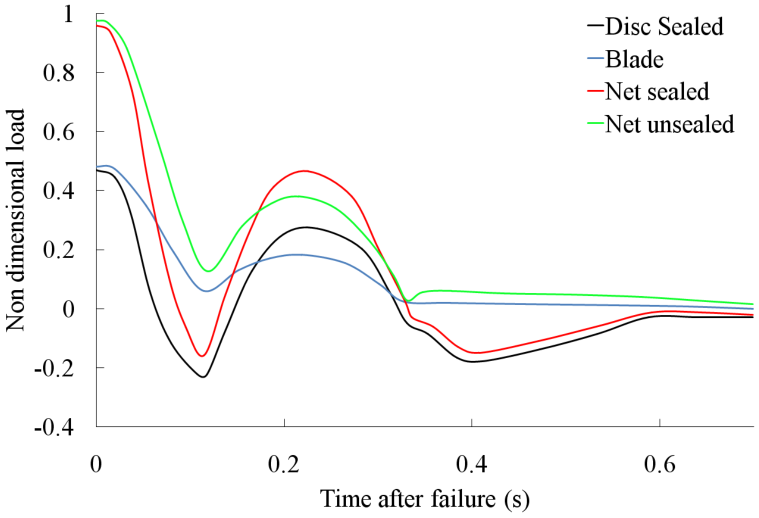

Figure 5.29: *Axial load on the IP rotor disc, blades and net load for a sealed and unsealed IPT rotor rear gap during an unlocated IP shaft failure. Surge, recovery and* 2^{nd} *surge scenario*

Figure 5.29 shows the calculated loads on the blades and on the disc that add up to a net axial load when the over-speeding turbine seals the front port of the LP turbine drum cavity. The comparison between the sealed and unsealed lines illustrates the effective difference in load calculated depending on whether or not allowance is made for the LPT cavity being sealed and its pressure being decoupled from the gas path. In the sealed case, the initial build up of pressure in the LPT cavity is such that the disc load at a certain time tends to be opposed to the blade load so forcefully that it will result in a net axial forward load on the IP turbine. This would cause a further opening of the gap, contrary to what was imposed in the simulation, with the possible subsequent equalisation of the cavity pressure with the main gas path, limiting the frictional wear rate on the rear static structure. This would be a poor feature for a design which relied on friction for controlling the terminal speed. Then the LPT cavity pressure decreases and hence the axial load is restored in the main flow direction pushing the turbine rearwards again. However, if the port is unsealed the air system is able to vent enough mass flow to the main gas path so that the net axial load on the turbine disc acts rearwards during the whole event.

5.10 Coupling with finite element analysis simulations

In unlocated shaft failures the performance of the internal air system is coupled with the mechanics of the wear and friction of turbine parts in contact after the breakage. Both phenomena are linked through the size of the discharge ports that in turn has a strong influence on the pressure in the system and the endloads on the disc.

The analysis of wear and friction between turbine discs in contact is the object of a doctoral project carried out by Aikaterini Psarra. This work has been running in parallel with this research for the past three years. The main outcome of this work is a surrogate model that relates the energy dissipated as friction with the axial load on the turbine disc [146]. This has been achieved by the thorough investigation of the event with finite element simulations.

It is advised that further research includes the integration of the air system model with the surrogate model of the wear and friction progression of turbines in contact. A plausible integration scheme is sketched in figure 5.30. At each time step, the FEA surrogate model uses an initial guess of the net axial load, $F_{net,\,1}$, to calculate the area of the turbine rotor rear gap, A. This in turn is an input to the SAS model to calculate the pressure inside the cavity, p_2, and hence a new estimate of the axial load, $F_{net,\,2}$. The calculation loop continues until the difference between p_1 and p_2 ,or the net axial loads for that matter, is within a given tolerance.

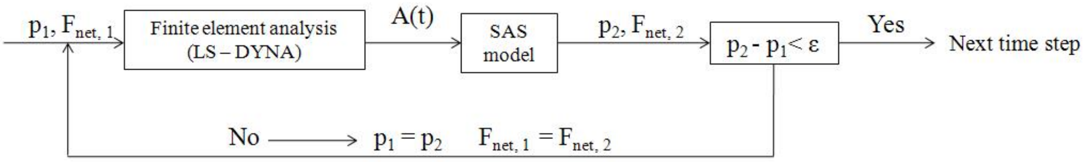

Figure 5.30: *Proposed coupling algorithm between the FEA model of turbines in contact and the SAS transient model*

5.11 Concluding remarks and future work

The study of the performance of internal air systems of gas turbines is commonly limited to steady state conditions. This is so because the characteristic time of the system is very small compared to the characteristic time of normal transient manoeuvres. However, rapid transients that are arise from failure events are fast enough for the air system to play a significant role in the outcome of the event. This is particularly true in the event of a shaft breakage.

If a gas turbine shaft is severed its turbine end may be able to move rearwards and seal some of the discharge ports of the air system. As a result, pressure may build up in the cavities of the system and exert a forward force on the over-speeding turbine disc that may limit the beneficial effect of blade tangling to arrest the over-speed. It is for these reasons that the accurate modelling of a shaft over-speed event requires the study of the dynamics of the secondary air system.

This chapter has discussed a workable approach to the estimation of the internal air system response during rapid transients and in particular, turbine endloads during a shaft failure event. The main novelty of this work compared to any SAS model published in the literature is the capability of the model to capture the transient performance of the system.

The work covers the development for transient operation of models of the basic components that conform the SAS network: pressure vessels, ducts and labyrinth seals. The validation of the models against experimental data has also been covered and has been demonstrated to be successful. The code is able to handle the possible reversal in the flow direction and supersonic conditions. It also accounts for the effects of flow inertia on the response of the system as the main contributions with respect to prior works.

The methodology followed to assemble the elements into a single network has been properly validated too against a known numerical benchmark - the De Haller test. The extensive investigation carried out on the impact of the boundary conditions on the solution and the behaviour of the equations allows for the network of tanks and tubes to be readily modified making it a flexible tool. Moreover, its modular character allows the user to explore a number of design possibilities and assess the behaviour of different configurations of the secondary air systems during rapid transient operation. It is recommended that the research continues with the inclusion of other system components in the network such as rotating holes, junctions and brush seals.

The effect of rotation is included in the calculations and the transient character of the vortical flow that develops in the cavities of the air system has been investigated. Two limit cases - constant and quasy steady vortex - provide the boundaries for the range of possible responses of the system.

The method involves several estimates and uncertainties. The heat input into the system is neglected as it is considered to have a second order effect in the results. Anyhow, this adiabatic assumption is believed to be a pessimistic approach as any heat transfer with the air system will introduce pressure losses that will alleviate any pressure overshoot along the SAS conduits. CFD and rig test investigations are suggested as valid means to quantify this pessimism of the assumption.

The model has been utilised to estimate the performance of the SAS and the endload on the IPT disc during an IP shaft failure event. In this particular case, the predicted pressure build up in the LPT cavity following the closure of the gap between the IPT and the LPT platform and the prompt compressor surge suggest that the net rearwards load on the IPT turbine may be significantly reduced, because the disc load tends to be opposed to the blade load. To this regard, the beneficial friction between the over-speeding turbine with the downstream structures to reduce the terminal speed would be limited. Moreover, the transient endload predicted when the inter turbine gap is sealed is considerably different to that calculated when the port is not allowed to seal. This underlines the importance of accounting for the SAS dynamics on engine designs which rely on blade tangling to limit the terminal speed in the event of a shaft failure.

More important than these particular results is the fact that it has been demonstrated that the methodology is able to capture the flow phenomena in the air system during rapid transients. Consequently, the code constitutes an excellent baseline tool to study the dynamics of internal air systems.

Appendix 5A - Equations of the charge and discharge of pressure vessels

In this appendix the hypotheses that allow the use of the Navier-Stokes in their integral form to determine the charge and discharge processes of pressurised vessels are explained and justified. The fact that the integral form can be used is based on the assumption that the thermodynamic magnitudes are uniform inside the vessel (they only vary with time) and that speeds in the bulk of the vessel are small compared with those in other regions, particularly close to the charge and discharge orifices. Once the assumptions are justified, the equations for the simultaneous charge and discharge of a vessel are derived.

Discharge of vessels

In the discharge process of a pressure vessel of volume V through an orifice of area A (provided that $A/V^{2/3} << 1$), two different regions can be distinguished (fig. 5.31). Region (I) is formed by the bulk of the volume, it is characterised by low speeds compared with the outlet region and its characteristic length is $V^{1/3}$. Region (II) is reduced to the neighbourhood of the outlet orifice of the vessel. Its characteristic length is $\sqrt{A}$ and the flow speed in this region can reach sonic conditions ($M_o \approx 1$).

Calling v_t and v_o the characteristic velocities in regions (I) and (II) respectively, the continuity equation provides

$$\rho_t v_t V^{2/3} \approx \rho_o v_o A \tag{5.24}$$

The density ratio, ρ_t/ρ_o, is of the order unity, and hence equation 5.24 gives:

$$\frac{v_t}{v_o} \approx \frac{A}{V^{2/3}} << 1 \tag{5.25}$$

The Strouhal number in region (I) is of the order one, because the characteristic time of the discharge is the discharge time, t_d, and it is of the same order of the residence time of a particle in the vessel, $V^{1/3}/v_t$. However, the residence time in region (II) is of the order of $\sqrt{A}/v_o$ and is much smaller than the residence time in region (I), and as a result the movement can be considered stationary in (II).

The Reynolds number in (II) is big compared to one

$$Re_o \approx \frac{\rho_o v_o \sqrt{A}}{\mu} >> 1 \tag{5.26}$$

In region (II) the thermodynamic magnitudes along the flow streamlines because the flow is quasy-stationary and at high Reynolds numbers, as long as the work done by the mass forces is disregarded (in this case only the gravitational forces are present and its effect can be disregarded for gases; this changes if the volume rotates) and heat addition and chemical reactions are not considered.

In the region (I) the flow is not stationary and Reynolds number, Re_t, is such that

$$Re_t \approx \frac{\rho_t v_t V^{1/3}}{\mu} \approx Re_o \frac{\sqrt{A}}{V^{1/3}} \tag{5.27}$$

Equation 5.27 is the product of a number much greater than one, Re_o, and a number smaller than one. The Reynolds number in the vessel can be either big, small or of order one. However, in practice, it is commonly much greater than unity, since $Re_o >> \sqrt{A}/V^{1/3}$.

The order of magnitude of spatial variations of pressure in the vessel are of the order

$$(\Delta p)_t \approx \rho_t v_t^2 \tag{5.28}$$

if $Re_t >> 1$, and of the order

$$(\Delta p)_t \approx \frac{\mu v_t}{V^{1/3}} \tag{5.29}$$

if $Re_t << 1$. However, the order of magnitude of spatial variations of pressure in (II) are such that

$$(\Delta p)_o \approx \rho_o v_o^2 \tag{5.30}$$

Comparing equations 5.28 and 5.29 with 5.30 it can be written that

$$\frac{(\Delta p)_t}{(\Delta p)_o} \approx (\frac{v_t}{v_o})^2 \approx (\frac{A}{V^{2/3}})^2 << 1 \quad if \quad Re_t >> 1 \tag{5.31}$$

$$\frac{(\Delta p)_t}{(\Delta p)_o} \approx \frac{\mu v_t}{\rho_o v_o^2 V^{1/3}} \approx \frac{1}{Re_o} \frac{A\sqrt{A}}{V} << 1 \quad if \quad Re_t << 1 \tag{5.32}$$

Consequently, the pressure in (I) can be considered uniform independent of the Reynolds number.

The entropy equation in region (I), in the absence of external heat sources, is

$$\underbrace{\frac{1}{c_v}\frac{DS}{Dt}}_{\frac{\Delta S}{c_v}} = \underbrace{\frac{\nabla \cdot (k \nabla T)}{\rho c_v T}}_{\frac{\Delta T}{T}\frac{k t_d}{\rho_t c_v V^{2/3}}} + \underbrace{\frac{\Phi_v}{\rho c_v T}}_{\frac{\mu v_t^2 t_d}{\rho_t c_v T V^{2/3}}} \tag{5.33}$$

where the order of magnitude of each of the terms of the equation have been written below, multiplied by the characteristic time of the discharge process, t_d.

The contribution to the entropy gain of the viscous dissipation is

$$\frac{\mu v_t^2 t_d}{\rho_t c_v T V^{2/3}} \approx \frac{M_o^2}{Re_o} \frac{A\sqrt{A}}{V} << 1 \tag{5.34}$$

This is because M_o is of order one and Re_o is big. From equation 5.34 it is therefore concluded that the entropy rise due to viscous dissipation is negligible.

The contribution of the heat conduction to the entropy rise is

$$\frac{\Delta T}{T} \frac{k t_d}{\rho_t c_v V^{2/3}} \approx \frac{\Delta T}{T} \frac{\alpha t_d}{V^{2/3}} \approx \frac{\Delta T}{T} (\frac{\delta_t}{V^{1/3}})^2 \tag{5.35}$$

where α is the thermal diffusitivity and $\delta_t \approx \sqrt{\alpha t_d}$ is the depth of penetration of the viscous effects. Two limit cases can be distinguished:

- If δ_t is small compared to the characteristic length of (I), $V^{1/3}$, the effects of heat conduction remain confined to a thin layer close to the walls of the vessel where temperature changes from its value in (I) to the value at the wall. In this case entropy rise are negligible except in this thin layer, and entropy is conserved through the discharge process. This corresponds to $Re_t >> 1$.
- If $\delta_t >> V^{1/3}$ the effects of heat conduction, during the discharge time t_d, affect the whole fluid contained in region (I). The fluid temperature equals the temperature of the walls of the vessel, and given that $\Delta S/c_v$ is of order one, equation 5.35 yields that $\Delta T/T \approx (V^{1/3}/\delta_t)^2 << 1$. In this case the discharge process is isothermal.

In both limit cases there is a thermodynamic variable that is uniform in (I), and since it has been demonstrated that pressure is uniform in (I) independently of the Reynols number in the vessel all thermodynamic variables are uniform during the discharge (see [95]).

It is evident that the discharge will not be isentropic even if $\delta_t >> V^{1/3}$ if heat transfer of the vessel with its surroundings is significant. In such case Q should be included in the energy equation.

Charge of vessels

The charge of a vessel is not isentropic due to the presence of a jet that mixes with the fluid in the vessel. In this mixing process the viscous and heat transfer effects are important and hence the process is no longer isentropic.

During the charge of a pressure vessel there are three different regions clearly distinguishable. Region (I) constitutes the bulk of the vessel and its characteristic length is $V^{1/3}$. Region (II) is the entry nozzle whose characteristic length is $\sqrt{A}$ and where the speed can reach the speed of sound. Region (III) is formed by the entry jet whose characteristic volume is of the order $AV^{1/3} << V$ and where the speed is of the same order as the entry.

In region (I), in a similar fashion as the discharge, spatial variations of pressure are negligible compared to the pressure variation in (II), and so pressure in (I) can be considered uniform. The jet drags the fluid from its surroundings and entrains and mixes with it. The drag from the jet generates slow recirculation areas in the bulk of the vessel producing a very effective mixture that makes temperature in (I) practically uniform, but different, in general, to that in the entry and in the jet. Therefore, and for reasons different to those in the case of a discharge, thermodynamic magnitudes in (I) can be considered uniform when the vessel is charging.

Equations

The continuity equation in its integral form applied to the control volume formed by the internal walls of the tank of figure 5.31 and the inlet and outlet ports is

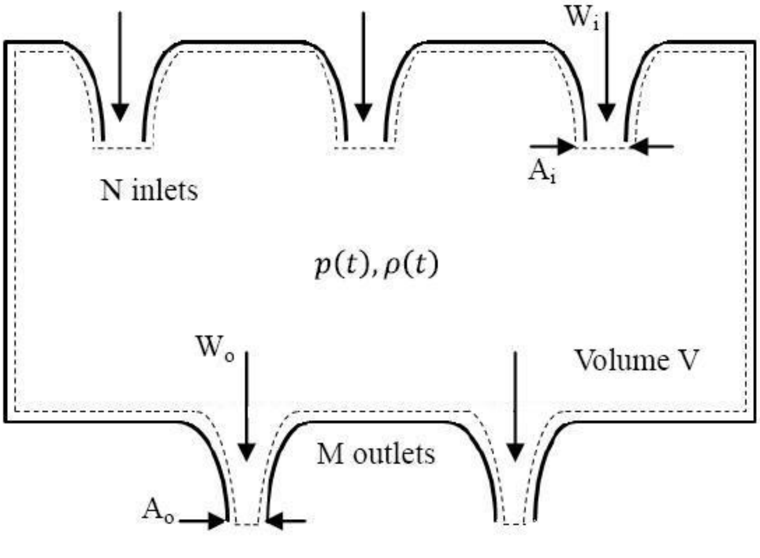

Figure 5.31: *Simultaneous charge and discharge of a pressure vessel. Control volume*

$$\frac{d}{dt}\int_V \rho d\Omega + \int_\Sigma \rho(\vec{v} - \vec{v_c}) \cdot \vec{n} d\sigma = 0 \tag{5.36}$$

The volume integral is extended to the total volume, (I) and (II) for the discharge and (I), (II) and (III) for the charge. Density is not uniform except in (I), but since this volume is of the order of V, much greater that the volume (II) and (III). Therefore, and to a first order, it can be written that

$$\frac{d}{dt}\int_V \rho d\Omega \approx \frac{d(\rho_t V)}{dt} \tag{5.37}$$

where $\rho_t(t)$ is the uniform density in the bulk of the vessel. The surface integral is zero everywhere except at the entry and outlet sections where $\vec{v_c} = 0$ and $\vec{v} \cdot \vec{n} = \pm v$. The positive sign is valid for the discharge and the negative is valid for the charge. Equation 5.36 then gives

$$\int_{\Sigma} \rho(\vec{v} - \vec{v_c}) \cdot \vec{n} d\sigma = \pm \int_{A} \rho v dA = \pm W \tag{5.38}$$

where W is the mass flow that crosses a section of area A. The continuity equation is then

$$\frac{d(\rho_t V)}{dt} \pm W = 0 \tag{5.39}$$

The total energy equation in its integral form applied to the same control volume of figure 5.31, in absence of mass forces or heat addition, takes the form

$$\frac{d}{dt}\int_{V} \rho(e+\frac{1}{2}v^2)d\Omega + \int_{\Sigma} \rho(e+\frac{1}{2}v^2)(\vec{v}-\vec{v_c})\cdot\vec{n}d\sigma = -\int_{\Sigma} p\vec{v}\cdot\vec{n}d\sigma - \int_{\Sigma} \vec{q}\cdot\vec{n}d\sigma + \int_{\Sigma} \vec{n}\cdot\overline{\overline{\tau'}}\cdot\vec{v}d\sigma \tag{5.40}$$

Since the working fluid is a compressible gas, $P_r \approx 1$, viscous effects and heat conduction can be disregarded in region (I). The last two terms of equation 5.40 are then taken as zero. The most important part of the volume integral is that extended to region (I), but in this region the flow velocity is very small compared to the velocity in the surroundings of the outlet and inlet ports. Hence the kinetic energy can be disregarded against the thermal energy in the vast majority of the vessel. Hence

$$\frac{d}{dt}\int_{V} \rho(e + \frac{1}{2}v^2)d\Omega \approx \frac{d(\rho_t e_t V)}{dt} \tag{5.41}$$

where $e_t(t)$ is the internal energy that is uniform in the bulk of the vessel.

The surface integral that accounts for the convective flow of energy through the walls is zero on every surface except on the outlet and inlet port sections where $\vec{v_c} = 0$. Therefore it could be written that

$$\int_{\Sigma} \rho(e + \frac{1}{2}v^2)(\vec{v} - \vec{v_c}) \cdot \vec{n}d\sigma = \pm \int_{A} \rho(e + \frac{1}{2}v^2)\vec{v} \cdot \vec{n}dA \tag{5.42}$$

where, same as with the continuity equation, the positive sign corresponds to the discharge and the negative sign is valid for the discharge. The work per unit time of the pressure is zero on all surfaces if these are not moving, and hence on them $\vec{v} = \vec{v_c} = 0$, except on the interface ports where it holds that

$$-\int_{\Sigma} p\vec{v} \cdot \vec{n}d\sigma = \mp \int_{A} p\vec{v} \cdot \vec{n}dA \tag{5.43}$$

Grouping integrals 5.42 and 5.43 the energy can be rearranged to give:

$$\int_{\Sigma}[\rho(e+\frac{1}{2}v^2)\vec{v}\cdot\vec{n}+p\vec{v}\cdot\vec{n}]d\sigma=\pm\int_{A}\rho(e+\frac{p}{\rho}+\frac{1}{2}v^2)\vec{v}\cdot\vec{n}dA=\pm\int_{A}\rho h_0\vec{v}\cdot\vec{n}dA \tag{5.44}$$

where h_0 is the stagnation enthalpy on the section A that is equal to the enthalpy upstream of region (II) where stagnation magnitudes are uniform. Hence, in the case of a discharge $h_0 = h_t$ being $h_t(t) = \gamma p_t(t)/\rho_t(t)$ the enthalpy in the vessel. In the case of a charge, h_0 takes the value that it has out of the vessel. In both cases h_0 is uniform and it yields

$$\pm\int_{A}\rho h_0\vec{v}\cdot\vec{n}dA=\pm W h_0 \tag{5.45}$$

Finally, for N inlets and M outlets, the continuity and energy equations can be expressed as

$$\frac{d}{dt}(\rho V)+\sum_{l=1}^{M}W_{o,l}-\sum_{r=1}^{N}W_{i,r}=0 \tag{5.46}$$

$$\frac{d}{dt}(\rho e_t V)+\sum_{l=1}^{M}W_{o,l}h_{o,l}-\sum_{r=1}^{N}W_{i,r}h_{i,r}=0 \tag{5.47}$$

Appendix 5B - Equations of the transient flow of a compressible gas through a duct

The equations that govern the unsteady flow of a gas through a duct are known as the Euler equations. These are obtained from the following starting assumptions:

1. $\vec{v} = u \cdot \vec{i}$. One-dimensional flow.
2. $p = \rho R_g T$. Perfect gas model applicable.
3. $Re >> 1$. Inviscid flow.
4. $RePr >> 1$. Heat conduction negligible.
5. $St \geq 1$. Unsteady flow.
6. $Fr >> 1$. Buoyancy forces negligible.
7. No chemical reactions.
8. The tube is not moving.

The evolution of the gas through the duct is better analysed by the Navier-Stokes equations in their differential form. With the previous assumptions the continuity equation gives

$$\frac{\delta \rho}{\delta t} + \nabla \cdot (\rho \vec{v}) = \frac{\delta \rho}{\delta t} + \rho \frac{\delta u}{\delta x} + u \frac{\delta \rho}{\delta x} = 0 \tag{5.48}$$

The momentum equation takes the form

$$\rho \frac{\delta \vec{v}}{\delta t} + \rho \vec{v} \cdot \nabla \vec{v} = -\nabla p + \underbrace{\rho \vec{f_m}}_{\approx \vec{0}\ (Fr>>1)} + \underbrace{\nabla \overline{\overline{\tau'}}}_{\approx \vec{0}\ (Re>>1)} \tag{5.49}$$

Projected on the x and y and z axes the equation yields

$$\vec{i}) \quad \rho \frac{\delta u}{\delta t} + \rho u \frac{\delta u}{\delta x} + \frac{\delta p}{\delta x} = 0 \tag{5.50}$$

$$\vec{j}, \vec{k}) \quad \frac{\delta p}{\delta y} = \frac{\delta p}{\delta z} = 0 \rightarrow p = p\,(x, t) \tag{5.51}$$

The energy equation can be retermed into what is known as the entropy equation

$$\rho \frac{Ds}{Dt} = \underbrace{\Phi_v}_{\approx 0 (Re>>1)} + \underbrace{\nabla \cdot (k \nabla T)}_{\approx 0 (RePr>>1)} + \underbrace{Q_r}_{\approx 0 (without\ chemical\ reactions)} = 0 \tag{5.52}$$

Hence, for each fluid particle the entropy is conserved and equal to its initial value. This fact coupled with equation 5.51 reveals that, since $\frac{p}{\rho^\gamma}$ the density is constant. With the aid of the perfect gas equation, equation 5.52 can be expressed as

$$\frac{Ds}{Dt} = 0 = \frac{D}{Dt}\left(\frac{p}{\rho^\gamma}\right) = \frac{1}{\rho^\gamma}\frac{Dp}{Dt} - p^\gamma \frac{1}{\rho^{\gamma+1}}\frac{D\rho}{Dt} \overset{\times\rho^\gamma}{\rightarrow} \frac{Dp}{Dt} + \frac{\gamma p}{\rho}\frac{D\rho}{Dt} = 0 \tag{5.53}$$

The total derivative in equation 5.53 can be expanded in accordance with:

$$\frac{Dp}{Dt} = \left(\frac{\delta p}{\delta t} + \vec{v}\cdot\nabla p\right) = \frac{\delta p}{\delta t} + u\frac{\delta p}{\delta x} \tag{5.54}$$

Therefore, the final system of equations is

$$\frac{\delta\rho}{\delta t} + \rho\frac{\delta u}{\delta x} + u\frac{\delta\rho}{\delta x} = 0 \tag{5.55}$$

$$\rho\frac{\delta u}{\delta t} + \rho u\frac{\delta u}{\delta x} + \frac{\delta p}{\delta x} = 0 \tag{5.56}$$

$$\left(\frac{\delta p}{\delta t} + u\frac{\delta p}{\delta x}\right) - a^2\left(\frac{\delta\rho}{\delta t} + u\frac{\delta\rho}{\delta x}\right) = 0 \tag{5.57}$$

Appendix 5C - Ideal gas flow through a series of orifices

This appendix provides the calculation of the flow of an ideal gas through a series of orifices (fig. 5.32). It is assumed that process is isothermal and that the kinetic energy of the flow is dissipated before the next cavity.

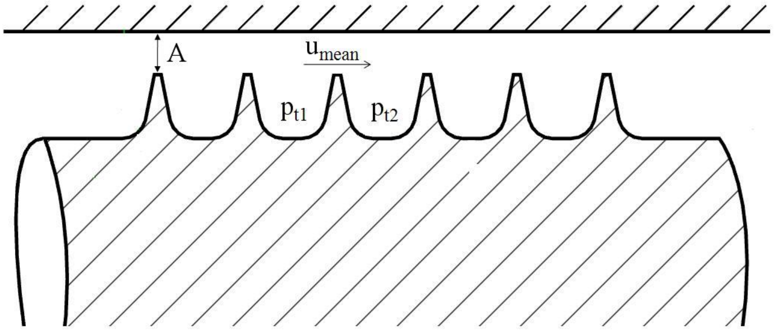

Figure 5.32: *Labyrinth seal configuration*

The mean velocity u_{mean} of the flow that expands adiabatically through an ideal orifice of area A from an upstream total pressure p_{1t} to a lower total pressure p_{2t} is given by:

$$\frac{u_{mean}^2}{2} = \int_{p_{1t}}^{p_{2t}} v dp_t \tag{5.58}$$

By using the perfect gas equation to an isentropic process, $pv^{\gamma} = constant$:

$$\frac{u_{mean}^2}{2} = p_{1t}v_1 \frac{\gamma}{\gamma - 1}\left[1 - \left(\frac{p_{2t}}{p_{1t}}\right)^{(\gamma-1)/\gamma}\right] \tag{5.59}$$

The term $\left(\frac{p_{t2}}{p_{t1}}\right)^{(\gamma-1)/\gamma}$ can be expanded using a Taylor series:

$$\left(\frac{p_{2t}}{p_{1t}}\right)^{(\gamma-1)/\gamma} = 1 + \frac{\gamma-1}{\gamma}\frac{p_{2t}-p_{1t}}{p_{1t}} + \frac{[(\gamma-1)/\gamma]\left\{[(\gamma-1)/\gamma]-1\right\}}{2}\left(\frac{p_{2t}-p_{1t}}{p_{1t}}\right)^2 + \dots \tag{5.60}$$

To finally yield:

$$\left(\frac{p_{2t}}{p_{1t}}\right)^{(\gamma-1)/\gamma} \approx 1 + \frac{\gamma-1}{\gamma}\frac{p_{2t}-p_{1t}}{p_{1t}} \tag{5.61}$$

and hence:

$$\frac{u_{mean}^2}{2} = -v_1(p_{2t} - p_{1t}) \tag{5.62}$$

Mass flow through the seal is given by:

$$\dot{m} = \frac{u_{mean}A}{v_2} \tag{5.63}$$

The specific volume v_2 after the adiabatic expansion can be found from:

$$v_2 = v_1 \left(\frac{p_{1t}}{p_{2t}}\right)^{1/\gamma} \tag{5.64}$$

The term $\left(\frac{p_{t1}}{p_{t2}}\right)^{1/\gamma}$ can expanded using a binomial series and equation 5.64 then yields:

$$v_2 = v_1 \left(\frac{p_{1t}}{p_{2t}}\right)^{1/\gamma} = v_1 \left[1 - \frac{1}{\gamma}\left(\frac{p_{2t} - p_{1t}}{p_{1t}}\right)\right] \tag{5.65}$$

Equations 5.65 and 5.62 can be substituted back into the continuity equation to give:

$$\left(\frac{\dot{m}}{A}\right)^2 = \frac{-2(p_{1t} - p_{2t})}{v_1\left[1 - \frac{2}{\gamma}\left(\frac{p_{2t}-p_{1t}}{p_{1t}}\right)\right]} \tag{5.66}$$

Assuming that $pv = constant = p_{1t}v_1 = p_{0t}v_0$ equation 5.66 becomes:

$$\left(\frac{\dot{m}}{A}\right)^2 = \frac{2p_{1t}(p_{2t} - p_{1t})}{p_{0t}v_0\left[1 - \frac{2}{\gamma}\left(\frac{p_{2t}-p_{1t}}{p_{1t}}\right)\right]} \tag{5.67}$$

In its differential form equation 5.67 can be rearranged to give:

$$\left(\frac{\dot{m}}{A}\right)^2 \frac{1}{\delta x} - \left(\frac{\dot{m}}{A}\right)^2 \left(\frac{2}{\gamma}\right) \frac{1}{p_{1t}} \frac{dp_t}{dx} = \frac{-2}{p_{0t}v_0} p_{1t} \frac{dp_t}{dx} \tag{5.68}$$

Equation 5.68 can be integrated over the length of the seal:

$$\left(\frac{\dot{m}}{A}\right)^2 \frac{1}{\delta x} \int_{x_0}^{x_n} dx - \left(\frac{\dot{m}}{A}\right)^2 \left(\frac{2}{\gamma}\right) \int_{p_0}^{p_n} \frac{dp_t}{p_t} = \frac{-2}{p_{0t}v_0} \int_{p_{0t}}^{p_{nt}} p_t dp_t \tag{5.69}$$

And for a seal with n fins such that $\frac{x_n - x_0}{\delta_x} = n$, assuming that the velocity in the cavity is small ($p_t \approx p$) and taking that $2/\gamma \approx 1$ the flow through the seal is given by (Martin's equation):

$$\dot{m} = Ap_{0t}\sqrt{\frac{1-\left(p_n/p_{0t}\right)^2}{RT_{0t}\left[n - ln\left(p_n/p_{0t}\right)\right]}} \tag{5.70}$$

Appendix 5D - Equations to characterise vortical flows in internal air system cavities

Consider a cavity of the internal air system that extends from radius 1 to radius 2. From the Euler equation of turbomachinery and the steady flow energy equation it can be written that

$$Work = \dot{m}\Omega\left(v_1 r_1 - v_2 r_2\right) = \dot{m}c_p\left(T_{1t} - T_{2t}\right) \tag{5.71}$$

This expression is applicable to any swirling flow but it is only of use when some assumption regarding the relationship between v and r is made. Two particular cases are of great interest: that of the forced vortex where the fluid rotates at a constant angular velocity at all radii, and that of a free vortex where no work is done on the fluid and that maintains a constant angular momentum. These are the two limit cases possible and any real vortex will lie somewhere between the two. They are discussed next.

Forced vortex

The forced vortex is described by a constant velocity of the fluid at all radii, as a solid body rotation motion. This occurs for cavities with small through flows; the residence time of the particles over the rotating surface is long enough for the drag of the discs to bring the particles to the local disc speed. The tangential velocity is proportional to radius, $v_i = \Omega r_i$, and the change of angular momentum required for this to happen comes from the work done by the rotor on the air or vice-versa when there is through flow. In this case it holds that

$$T_{1t} - T_{2t} = \frac{\Omega^2}{c_p}\left(r_1^2 - r_2^2\right) \tag{5.72}$$

and since the relationship between total and static temperatures is given by $T_t = T_s + \frac{v^2}{2c_p}$ equation 5.72 can be rearranged to yield

$$\frac{T_2}{t_1} = 1 - \frac{\Omega^2}{2c_p T_1}\left(r_1^2 - r_2^2\right) \tag{5.73}$$

By further assuming that the process is isentropic the pressure ratio along the vortex is

$$\frac{p_2}{p_1} = \left[1 - \frac{(\gamma - 1)\,\Omega^2}{2R_g\gamma T_1}\left(r_1^2 - r_2^2\right)\right]^{\frac{\gamma}{\gamma-1}} \tag{5.74}$$

Free vortex

On the other extreme, if through flow is high enough, the drag of the discs is not sufficient to impose any perceptible change of angular momentum. In this case the tangential velocity of the air is inversely proportional to radius; that is, $v_i r_i = constant$. Moreover, since there is no work done in a free vortex, the total temperature is maintained, $T_2 t = T_1 t$. This leads to

$$T_1 - T_2 = \frac{v_2^2 - v_1^2}{2c_p} = \frac{v_1^2}{2c_p}\left[\left(\frac{r_1}{r_2}\right)^2 - 1\right] \tag{5.75}$$

The pressure ratio along the vortex, assuming an isentropic process, takes the form

$$\frac{p_2}{p_1} = \left\{1 - \frac{v_1^2}{2c_p T_1}\left[\left(\frac{r_1}{r_2}\right)^2 - 1\right]\right\}^{\frac{\gamma}{\gamma-1}} = \left\{1 - \frac{(\gamma-1)\,v_1^2}{2R_g \gamma T_1}\left[\left(\frac{r_1}{r_2}\right)^2 - 1\right]\right\}^{\frac{\gamma}{\gamma-1}} \tag{5.76}$$

General vortex laws

A general vortex will obey the following law

$$\frac{p_2}{p_1} = \left\{1 + \frac{k^2}{2nc_p T_1}\left(r_2^{2n} - r_1^{2n}\right)\right\}^{\frac{\gamma}{\gamma-1}} \tag{5.77}$$

where $v = kr^n$ is the general velocity profile. Equation 5.77 can be reduced to equations 5.74 and 5.76 by substituting $n = 1$ and $n = -1$ respectively.

Vortex characterisation

Any vortex between the two extreme cases exposed previously can be characterised by a value of the n variable. It is reckoned that significant work needs to be done to define the dependency of such variable for a range of conditions. The actual understanding is that n can be loosely related to the flow with the help of a coefficient that measures the through flow in the cavity , λ, as follows:

- $-0.001 < \lambda < 0.01$ This describes low through flows and as discussed previously the vortex is approximated by a forced law.
- $\lambda < -1$ or $\lambda > 0.4$ This characterises high through flows that can be approximated by a free vortex.

Values for n for intermediate values of the through mass flow are obscure and further experimental work is needed. Experts [38][161] however, indicate that the variation is far from linear and suggest an exponential function as a more appropriate and representative fit to reality. This means that the vortex is free for a greater range of through flows than it would if the dependency was assumed to be linear. This behaviour is illustrated by figure 5.33.

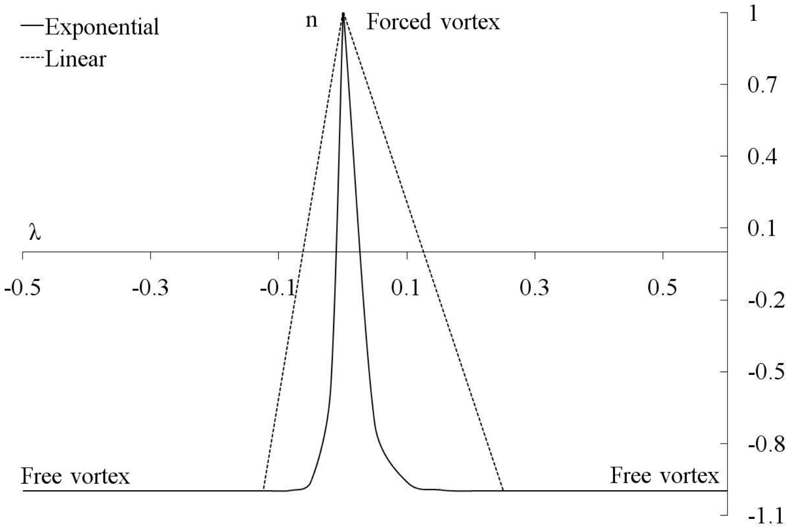

Figure 5.33: *General vortex law exponent as a function of the through flow into a rotating cavity*

Chapter 6

Compressor reverse flow modelling

6.1 Introduction

Immediately after a shaft breakage the compression system of a gas turbine is likely to surge. This happens because the violent vibrations and radial imbalance of the shaft alter the tip clearances of the compressor blades lowering both the surge and recovery lines. Depending on the strength of the residual vibrations after the failure the compressor may not recover, recover and run unstalled or recover and surge again as a result of the contact between the turbine vanes or the mismatch between shaft speeds. However, unlike at any other conditions of operation, compressor surge during a shaft failure event is regarded as desirable as it limits the air flow across the engine and hence the power available for the free turbine to accelerate.

The evolution of the compressor delivery pressure, p_{30}, is regarded as the main parameter influencing the terminal speed of the free turbine after a shaft breakage. A reliable compressor dynamics model is therefore a fundamental input item to any performance model of the event.

Most compressor pre and post stall performance models require the specification of the steady state characteristics to yield the trajectory of the transient on the compressor map. This is in keeping with the assumption that the high-frequency transient performance of any engine component is equal to its instantaneous steady-state performance. The unstalled forward flow portion of the compressor characteristic (Fig. 6.1 - region (I)) can be easily obtained either by rig tests or with the help of compressor performance models. On the other hand, the steady axisymmetric reverse flow portion of the characteristic (region (III)) is considerably more difficult to obtain experimentally since the sheer power to drive a modern multi stage axial compressor in reverse flow is prohibitively large. Hence, the compressor performance in reverse flow has to be calculated numerically and supported by small scale test data.

The flow in the stalled and unsteady portion of the compressor characteristic (region (II)) is inherently unstable and very difficult to measure. Most performance models use an interpolated characteristic in this region that connects the characteristic in region (I) with the stall point of the characteristic in forward flow.

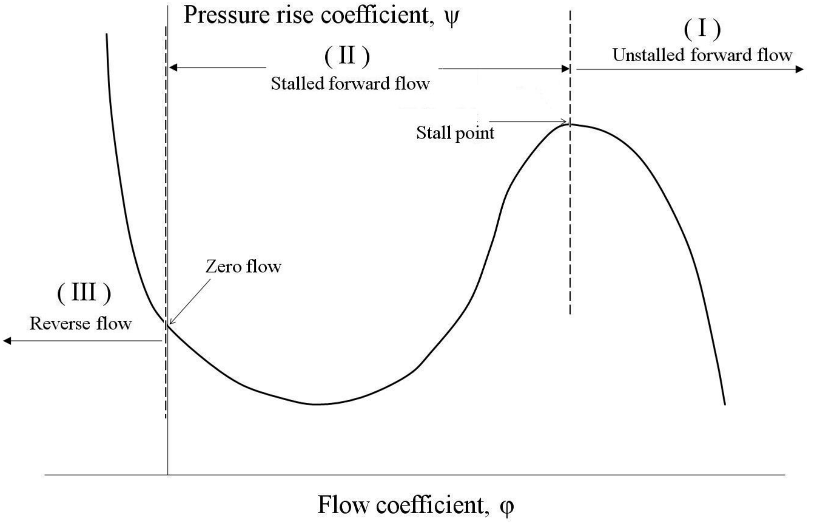

Figure 6.1: *Notional compressor characteristic in quadrants (I) and (II) of the compressor map*

In the context of the shaft over-speed modelling, this research is responsible for the provision of the reverse flow characteristics that will be used in the compressor pre and post stall model developed by Martina Mohseni [129].

This chapter reports on the calculation of axial compressor maps at reverse flow conditions for their inclusion in the "all in one" shaft over-speed/failure model. The maps are obtained by stacking the performance of two stages that have been modelled by high fidelity CFD simulations for a range of mass flows and shaft speeds.

The study continues with the investigation of the ability of the existent two-dimensional algorithms to simulate the compressor performance in backflow conditions. Results for a three stage axial compressor at reverse flow were produced and compared against stage by stage experimental data published by Gamache [63][62].

The research shows that due to the strong radial fluxes present over the blades, two-dimensional approaches are inadequate to provide satisfactory results. Three-dimensional effects are accounted for by the introduction of a correction parameter that is a measure of the pressure loss across the blades. Such parameter is tailored for rotors and stators and enables the satisfactory agreement between calculations and experiments on a stage by stage basis.

6.2 Compressor performance in reverse flow

6.2.1 Published experimental data

The availability of experimental data in the public domain on compressor reverse flow operation is scarce and hence conclusions that can be drawn from the literature are limited. This is partly because the sheer power required to drive the flow across a full scale axial compressor in reverse flow is prohibitively large and partly because of the limited interest of the turbomachinery community in the reverse flow performance in comparison with the study of design flows. The data sources of relevance to the current work are summarised in this section.

The work by Turner and Sparkes [179] was the first experimental attempt to derive the four quadrant flow characteristics of an gas turbine compressor. The machine tested was a single stage (inlet guide vane, rotor and stator) low speed axial fan. To achieve backflow conditions the blades were rotated 180° while its shaft, inlet and outlet sections were those of design. However, rather than the provision of a detailed set of measurements, the authors' aim was to provide notional qualitative results that would trigger further research.

The data published by Steven Koff and Edward Greitzer [96][97] was derived by post processing the surge cycle data produced by Greizer. The data was obtained from a three stage axial compressor rig and shows a strong negative slope in reverse flow that becomes zero at small negative flow angles prior to forward flow.

Robert Gamache's PhD thesis in 1985 [62] is still the only published detailed investigation of compressor reverse flow operation, in which a complete set of overall performance characteristics is presented. In his work, experiments were carried out on two builds of a three-stage, constant annulus compressor, preceded by an IGV, but each with a different blade reaction (R=0.64 and R=0.74). The compressor was operated at steady reverse flow using an auxiliary fan to draw the air backwards, while a conical nozzle was each time adjusted to give the desirable mass flow rate. The tests took place at three different rotational speeds, 1170, 1800 and 2400 rpm, and measurements were taken at five radial (spanwise) and eleven circumferential stations, with high-response probes and hot wires used to measure the instantaneous total and static pressure and velocity of the flowfield. From the results obtained, it was observed that there is no significant difference between the two compressors; it was then concluded that the influence of the compressor reaction on reverse flow is not so severe. Also, the transition from rotating stall to reverse flow seemed to take place at a flow coefficient $\Phi = -0.04$, accompanied by a large reduction in pressure rise. The shape of the reverse flow characteristic derived was slightly parabolic and negatively slopped. Moreover, it was shown that the backflow compressor characteristics are not dependent on the shaft speed and fit into a single line for the whole range of rotational speeds tested. Finally, one of the most important conclusions reached was that in multistage axial compressors, the reverse flowfield is dominated by radial effects, especially across rotor blades. It was also brought to light the fundamental difference in the flow through rotors and stators in terms of pressure ratio (see section 6.3).

In 1994 Ivor Day [41] carried out his experiments to investigate the boundary between stall and surge on a four-identical stage, constant annulus compressor, again preceded by a lightly loaded set of IGVs. As part of the results the reverse flow characteristic of the compressor was measured by averaging the measurements of six hot wire probes at the inlet of the compressor.

6.3 Flow structure

It is not the objective of this work to elucidate the nature of stall and surge. However, it is necessary to have an appreciation of the most relevant features of the flow field across axial compressors in reverse flow to understand and interpret the results provided by CFD, the stage stacking technique and the two-dimensional models developed by the research.

The study of the experimental data summarised in the previous section reveals that the backflow characteristic is strongly negatively sloped (15:1 on a Φ, Ψ basis for a three stage compressor [63]). The greater slope of the characteristic in the second quadrant indicates that the stationary compressor offers more resistance to back flow than to forward flow. This is also supported by the much higher temperature rise (fig. 6.2b) and hence enthalpy rise across the blades in reverse flow compared to unstalled forward flow conditions for the same overall pressure ratio ($\frac{C_p \Delta T}{U^2}$ rises from 0.577 at design point to 2.954 in reverse flow).

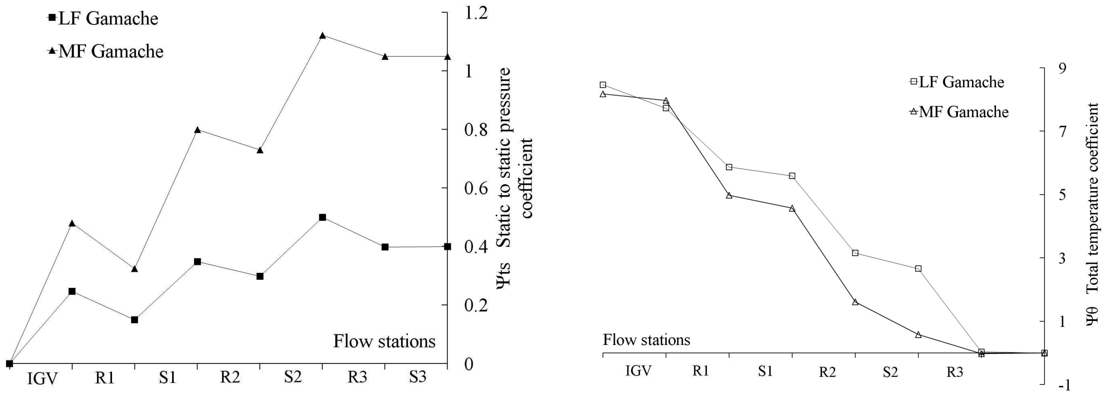

(a) *Pressure rise coefficient* **(b)** *Temperature rise coefficient*

Figure 6.2: *Pressure and temperature rise coefficients along Gamache's compressor in reverse flow at moderate ($\Phi = -0.04$) and low ($\Phi = -0.1$) flows*

The study of the individual stage characteristics of Gamache's three stage compressor [63] shows that the performance of the first two stages is almost identical whereas the performance of the last stage shows a negative pressure coefficient[1] out of a reverse flow coefficient of -0.2 (fig. 6.3). This can be explained because the trailing edge angle of the last stator of the compressor is zero (outlet flow is axial in forward flow) and the flow is therefore reasonably attached to the blade in reverse flow, minimising the pressure loss across the last stator. At these conditions the pressure loss across the rotor of the last stage is not enough to overcome the pressure rise imparted into the fluid by the rotation of the shaft, and as a result the pressure across the last stage in reverse flow rises and the pressure rise coefficient is therefore negative. On the other hand, the incidence onto the stators of the following stages is very high and the pressure loss across the stator exceeds the small pressure rise attained across the rotor. This results in a net loss of pressure across the stage and hence a positive pressure rise coefficient (fig. 6.2a). An additional paramount difference between rotor and stator flows arises from the fact that radial pumping may occur in the rotors, and this reduces the pressure drop of the backflow characteristic. Two-dimensional models are unable to capture these strong radial flows, and the accuracy of such models is therefore limited (see section 6.5)

The effect of the stagger angle of the blades on the characteristic is not certain. Preliminary calculations carried out by Koff and Greitzer [97] suggest that high stagger angles offer a greater resistance to the reverse flow and hence promote stronger losses. This results in a steeper characteristic in reverse flow (fig. 6.4). This claim, although it has not been

---

[1] Pressure coefficient defined as the pressure rise (pressure at the outlet of the stage in forward flow minus pressure at the inlet) particular to that coefficient (static to static, total to total, static to total) upon $1/2 \rho U^2$

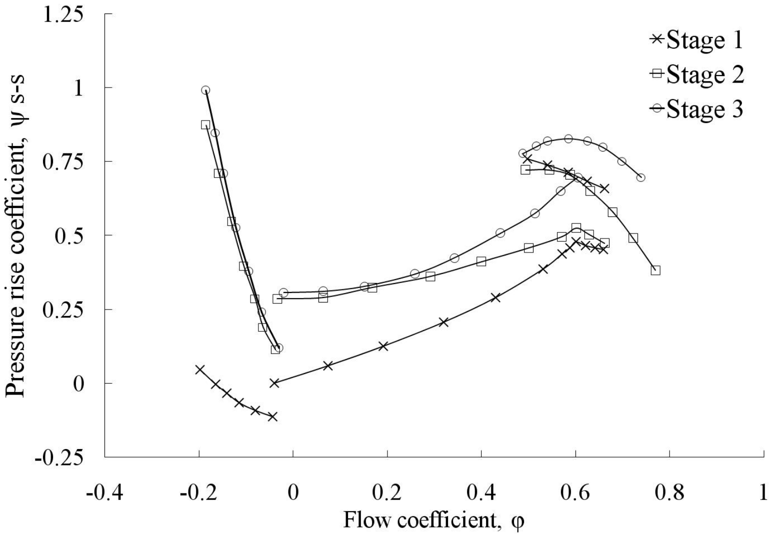

Figure 6.3: *Stage static to static characteristics of Gamache's compressor R=0.64 build. From [63]*

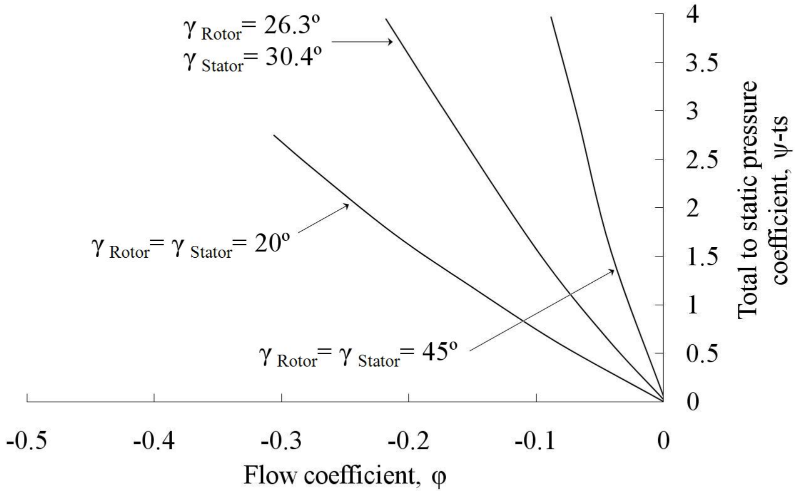

Figure 6.4: *Effect of blade stagger on predicted backflow characteristics. From [97]*

supported unequivocally by experimental evidence, is consistent with the fact that the reverse flow characteristics of Gamache's compressor fit into the same line because they have very similar staggers (0.7° difference for the rotors and 2° for stators). This allows to take the performance of the penultimate stage of the compressor in reverse flow as representative of the performance of all the stages, assuming that the blade rows are staggered similarly in modern compressors.

At high flow incidences the effect of the camberline angle on the pressure losses is considered of second order. This assumption has already been proven reasonable in the literature [81]. However, the effect of blade spacing remains unexplored. It is suspected that greater cascade solidities suppress the flow separation across the passage, and hence limit pressure loss giving rise to less steep reverse flow characteristics.

6.4 Stacking of CFD derived stage characteristics in reverse flow

In this research, the reverse flow characteristics of a multistage compressor are obtained by stacking the performance of single stages derived from CFD. In accordance to that exposed in the previous section (fig. 6.3) an axial compressor can be considered to be formed by two types of stages: the last stage and the remaining front stages. The former is characterised by the attached flow across the last stator and by a negative value of the pressure coefficient whereas the front stages are characterised by strong separated flows across both rotors and stators and positive pressure coefficients. The stage stacking technique adds up the characteristic of the last stage followed by the characteristic of the front stage repeated as many times as necessary to build the whole compressor.

The assumption that the performance of the penultimate stage can be extrapolated to represent the performance of all the front stages is made on the grounds that the stagger angle of the blades in modern axial compressors is very similar for all the blade rows. Figure 6.3 supports this claim.

6.4.1 CFD simulations

CFD is used to build a data base of compressor characteristics in reverse flow, for a range of flow conditions and shaft speeds. The 3D CFD simulations comprise the last two stages of a modern eight stage axial compressor for a range of reverse flows at three shaft speeds - 3,500, 5,000 and 6,500 rpm (fig. 6.5). Frozen rotor interfaces [2] between blades have been used to capture the effect of the impingement of the separated wake onto the following blade row.

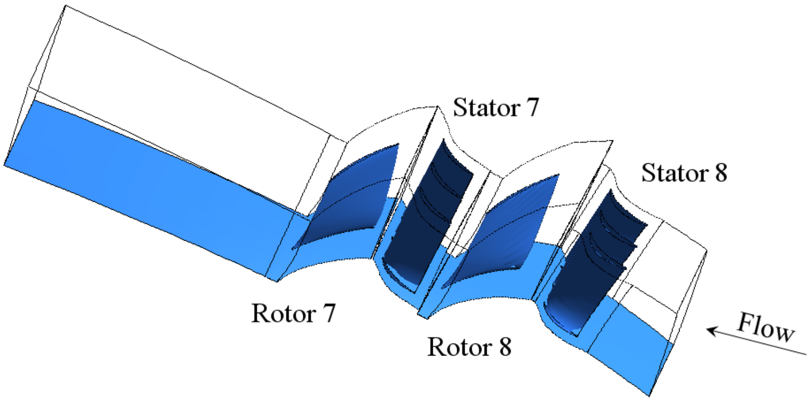

Figure 6.5: *Reverse flow CFD simulation domain*

Relative velocity vectors at midspan are shown in figure 6.6a. As expected there is no separation over the last stator whereas across the following blade rows the flow is strongly detached and form big separation bubbles that cover the whole chord of the blade. Attention is drawn to the weaker

---

[2] Three stator blades for every rotor have been found as an adequate approximation for a pitch ratio between domains of 1

separation across one of the stator passages that results from the different impingement of the rotor wake onto the stator and captured by the frozen rotor interface.

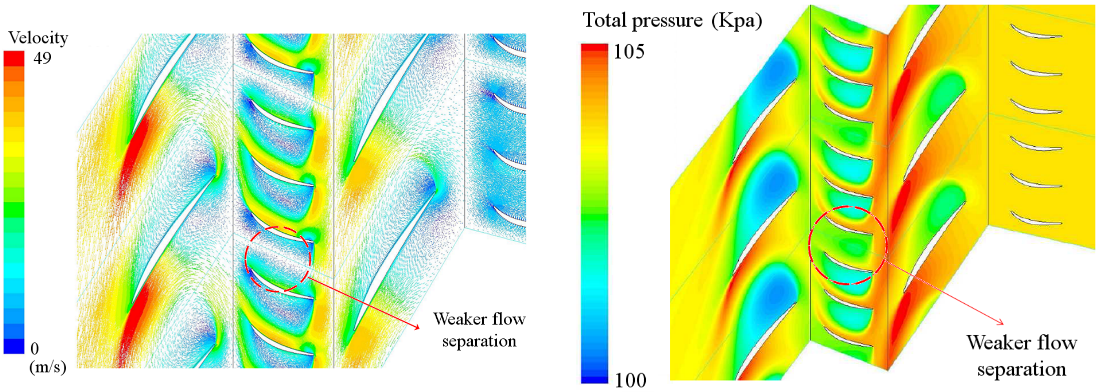

(a) *Relative flow velocity vectors* **(b)** *Total pressure contours*

Figure 6.6: *Flow field at mid span across the last two stages of an eight stage axial compressor in reverse flow at 5,000 rpm*

The CFD simulations also shows the strong radial fluxes over rotor blades reported previously in the literature, particularly over the suction surface towards the hub (fig. 6.7).

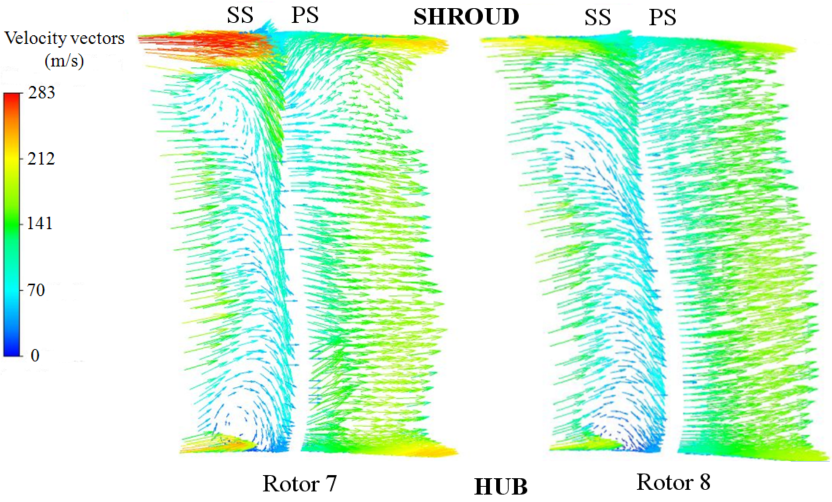

Figure 6.7: *Flow velocity vectors on two circumferential planes at mid chord of rotor 7 and 8 at mid chord at 5,000 rpm*

6.4.2 Stage stacking technique

The stage stacking technique employed to build the whole compressor characteristic in backflow uses ten equations to derive the flow conditions at the inlet (station 2 in figure 6.8) of the stage given that the conditions at the outlet (station 1 in figure 6.8) are known. Two of those equations are replaced by graphic correlations that are derived from CFD - pressure rise coefficient and adiabatic efficiency as a function of the flow coefficient. These graphic correlations need to be different for the last stage and for any other stage as a result of the attached flow over the last stator.

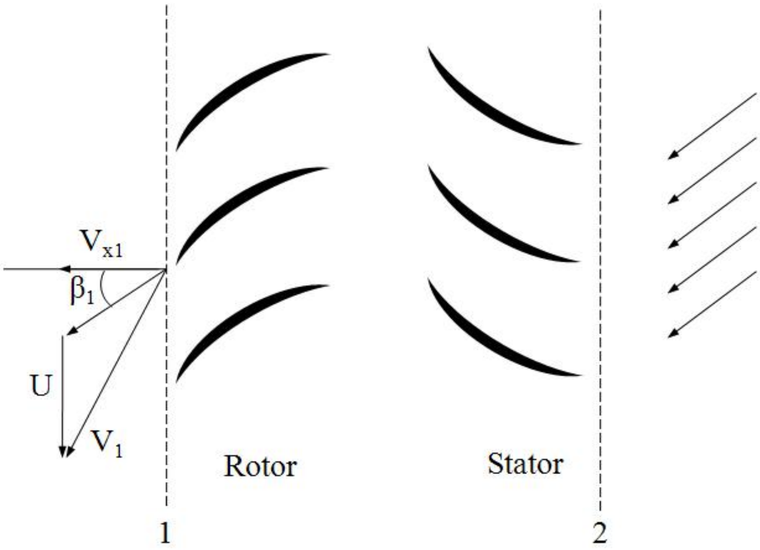

Figure 6.8: *Compressor stage in reverse flow - Station numbering*

Figures 6.9a and 6.9b group the pressure rise coefficient as a function of the flow coefficient at 3,500, 5,000, and 6,500 rpm for the last compressor stage and for mid and front stages respectively. The pressure rise coefficient is shown to be independent of the shaft speed and this is in agreement with the flow behaviour reported by Gamache and mentioned previously. The pressure coefficient is significantly smaller across the last stage because the last stator barely introduces loss into the flow.

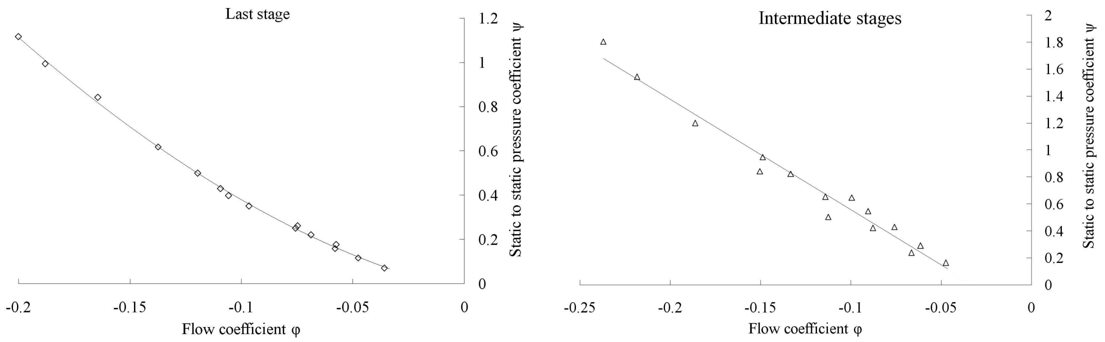

(a) *Last stage* **(b)** *Mid and front stages (from stage 7)*

Figure 6.9: *Static to static pressure rise coefficient ψ_{ss} versus flow coefficient ϕ for several shaft speeds*

The flow efficiency versus flow coefficient for the last and the mid and front stages is plotted in figures 6.10a and 6.10b for the same spool speeds. The usual forward flow definition of flow efficiency is kept. Whereas in forward flow the efficiency is a measure of the work needed to raise the flow pressure compared to an isentropic compression, the definition loses its meaning in reverse flow. However, although deprived of a physical meaning it is still a valid expression to correlate the temperature rise as a function of the pressure change across the blades. Results show that the efficiency across the last stage can be considered independent of the shaft speed but this is not the case for the mid and front stages.

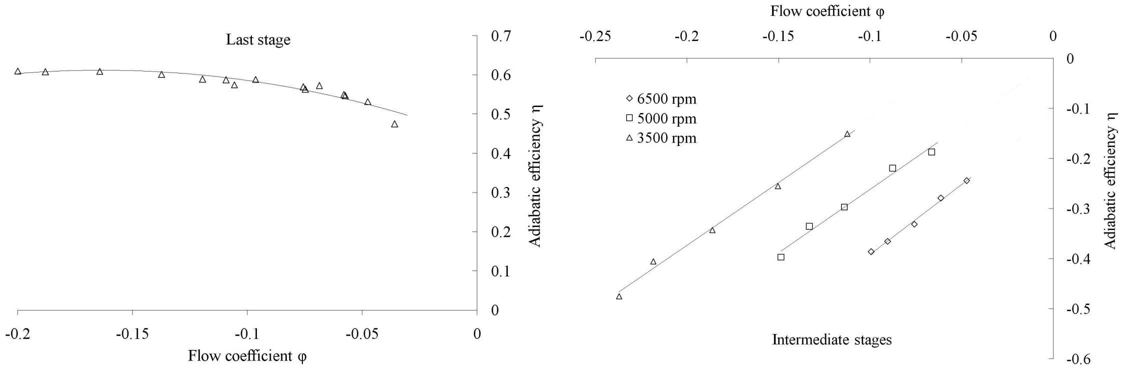

(a) *Last stage* **(b)** *Mid and front stages (from stage 7)*

Figure 6.10: *Adiabatic efficiency η versus flow coefficient ϕ for several shaft speeds*

The system of equations to calculate the flow at the inlet of the stage are:

$$Mass\ flow\ continuity\ \dot{m} = \rho_1 V_{x,1} A_1 \tag{6.1}$$

$$Speed\ of\ sound\ a_1 = \sqrt{\gamma R T_1} \tag{6.2}$$

$$Mach\ number\ M_1 = \frac{V_1}{a_1} \tag{6.3}$$

$$Static\ to\ static\ pressure\ coefficient\ \psi_{ss}(\phi_2) = \frac{p_2 - p_1}{\frac{1}{2}\rho_2 U^2} \tag{6.4}$$

$$Graphical\ correlation\ of\ \psi_{ss} = \psi_{ss}(\phi_2) \tag{6.5}$$

$$Adiabatic\ efficiency\ \eta = \frac{\frac{p_{2t}}{p_{1t}}^{\frac{\gamma-1}{\gamma}} - 1}{\frac{T_{2t}}{T_{1t}} - 1} \tag{6.6}$$

$$Graphical\ correlation\ of\ \eta = \eta(\phi_2) \tag{6.7}$$

$$Velocity\ triangle\ V_1 = \sqrt{V_{x,1}^2 + \left[(V_{x,1} tg\beta_1) + U\right]^2} \tag{6.8}$$

$$Stagnation\ pressure\ p_{1t} = p_1 \left(1 + \frac{\gamma - 1}{2} M_1^2\right)^{\frac{\gamma}{\gamma - 1}} \tag{6.9}$$

$$Stagnation\ temperature\ T_{1t} = T_1 \left(1 + \frac{\gamma - 1}{2} M_1^2\right) \tag{6.10}$$

$$Perfect\ gas\ equation\ p_1 = \rho_1 R T_1 \tag{6.11}$$

Flow variables at station 2 are known. Equations 6.1 to 6.11 are a system of eleven equations with eleven unknowns: a_1, T_1, M_1, V_1, $V_{x,1}$, p_1, p_{1t}, T_{1t}, ρ_1, η and ψ_{ss}. The system is solved with the help of a Newton scheme to provide the flow conditions at station 1, that become the conditions at station 2 for the next stage. Two of the equations of the system are the correlations of the static to static pressure coefficient, ψ_{ss}, and the adiabatic efficiency, η, with the flow coefficient, ϕ obtained from the CFD simulations.

The reverse flow characteristics for the whole compressor obtained from the stage stacking technique are plotted in figures 6.11 and 6.12. These maps have been obtained from CFD data that is particular to a given compressor blading. However, given that the most important parameters that affect the performance of the compressor in reverse flow are cascade solidity and stagger angle, it is straightforward to run a series of CFD simulations to build a database that could be used to derive the reverse flow map for any compressor geometry. Once again the value of this chapter lies especially in the methodology proposed, in addition to the particular results obtained for the geometry under scrutiny.

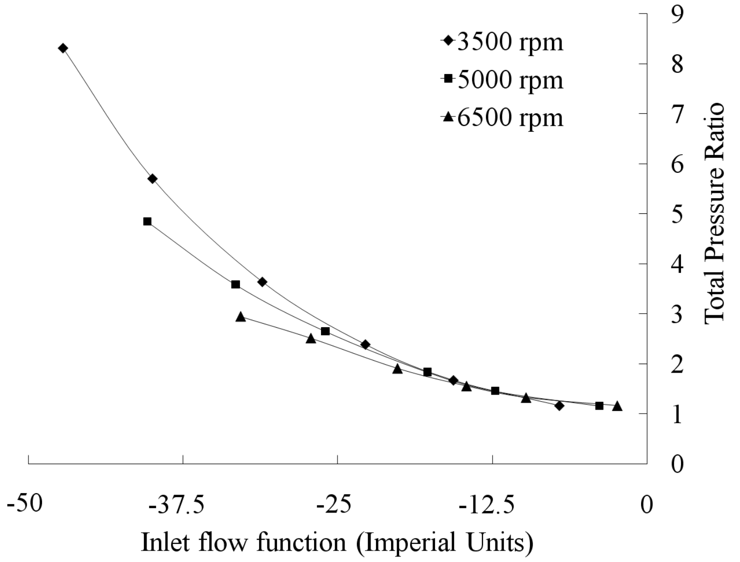

Figure 6.11: *Eight stage axial compressor map in reverse flow for a range of shaft speeds*

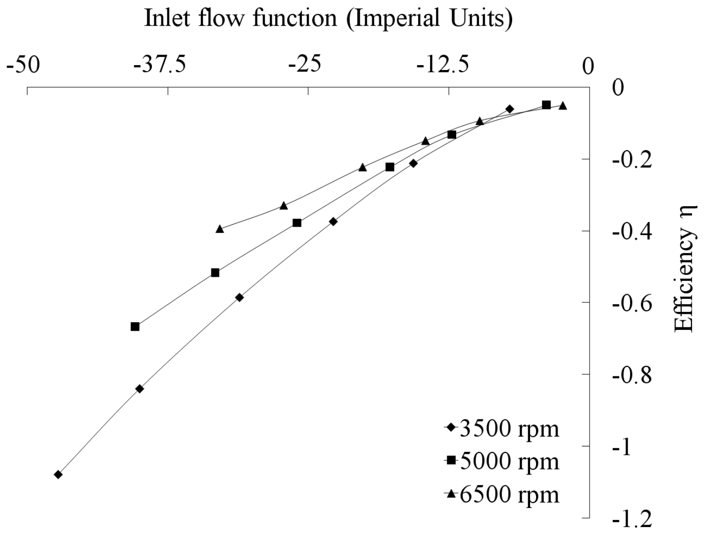

Figure 6.12: *Eight stage axial compressor efficiency map in reverse flow for a range of shaft speeds*

6.5 Analytical modelling of compressor performance in reverse flow

Further to the stage stacking technique described before, an assessment of the ability of two-dimensional models to calculate the reverse flow compressor characteristics was carried out towards the development of a method based on first principles and that would not require to run extensive CFD simulations to derive the compressor map in reverse flow. The first studies carried out on the topic were authored by Koff and Greitzer [96][97] based on the analysis of stalled cascades published by Cornell [37]. The main advantage of the numerical model proposed by Koff lies on its simplicity, rapidity and robustness. However, the two-dimensional methodology described by Koff is flawed by its inability to capture the important three-dimensional effects present in compressor backflow. This important radial flux was reported by Gamache and Greitzer [62][63].

6.5.1 Description of the model and assumptions

The reverse flow model is based on the numerical models of Koff [96][97] and Moses and Thomason [132]. In 1983, Steven Koff [96] reported an axisymmetric two-dimensional reverse flow model and derived the compressor characteristics in such conditions. His cascade model was based on Cornell's analysis of stalled cascades [37]. Each blade row is divided into two different regions 6.13: station 1 is located at the trailing edge of the blade, station 2 is at the leading edge of the blade and station 3 is at the trailing edge of the next blade. Flow conditions at station 3 are the inlet boundary conditions to station 1 of the next blade row. In the passage, the flow is conceived as fully separated from the trailing edge of the blade (assumed as a thin flat plate). A free streamline demarcates a region of separated and stagnated flow from a potential flow jet. The wake and the jet are then mixed out downstream of station 2 in a highly entropic process. The losses across the cascade (between stations 1 and 2) are assumed to be zero, with the only losses of the model being introduced by the mixing process.

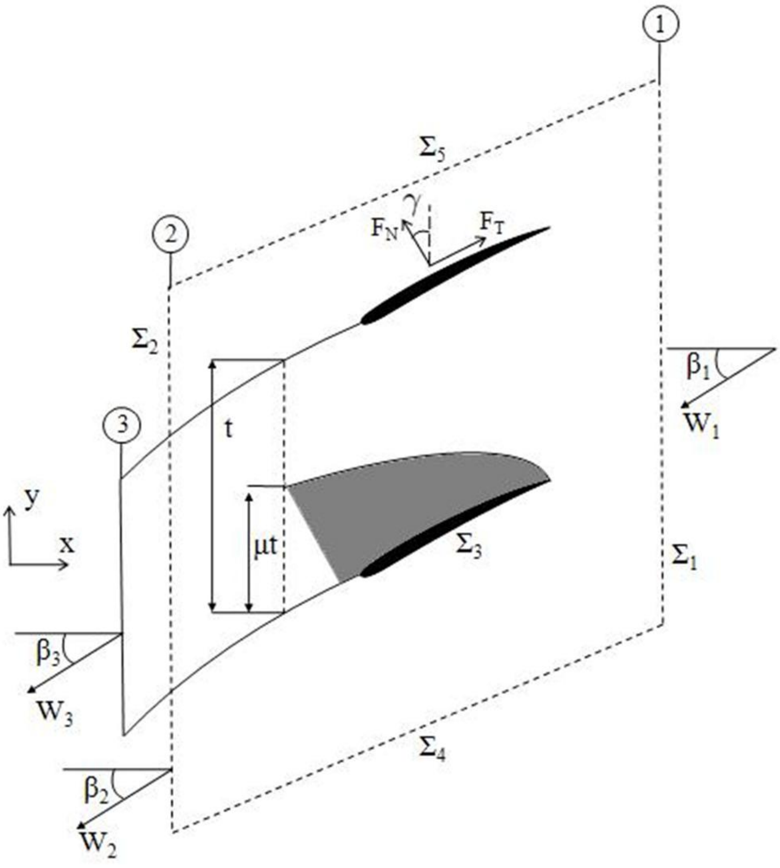

Figure 6.13: *Compressor reverse flow model - Control volume*

The model is based on three main assumptions:

- The flow in the jet is considered as potential and hence isentropic.
- No friction is considered in the direction parallel to the plate. No losses are considered between stations 1 and 2 so that $p_{1t} = p_{2t}$ at the expense of a static pressure drop $p_2 < p_1$.
- The mixing occurs at constant momentum in the circumferential direction and promotes a static pressure rise $p_3 > p_2$.

In the Moses and Thomason model [132], the velocity, static pressure and angle of the flow are calculated for a cascade in stalled forward flow, but the model can be easily modified to be applied to reverse flow conditions. The pressure and shear forces in the direction parallel to the plate are zero. The effects of pressure loss across the blade passage are modelled as a fraction of the dynamic head. The value of k is obtained from a fit of very limited experimental data and is proposed to be $0.15\sigma/cos(\beta_1)$. The expression is based on the assumption that the relative pressure losses within the blade passage should be proportional to the width of the free shear layer, and hence to the chord length c and, also, inversely proportional to the mass flow rate per blade passage, represented by $t \cdot cos(\beta_1)$. The whole expression is affected by a factor equal to 0.15 obtained from fitting the limited experimental data available at the time.

In reverse flow, the flow across the last stator vane is reasonably smooth and pressure losses are negligible since the flow approaches the vane at an angle close to the camber line angle at the leading edge. The flow angle at the inlet of the next blade row (trailing edge) can be as high as 80°, so the flow is assumed to be fully separated on the suction surface. It is considered that a fraction μ of the blade pitch t is occupied by the zero velocity wake while the bulk of the flow is channelled through the high energy jet. Between stations 2 and 3 the jet and the wake mix effectively thanks to the vortices that roll up downstream of the trailing edge of the blade. In the current work, the assumption was made that before the next blade row (station 3) complete mixing has taken place and the flow is uniform again. Finally, it is considered that the blade passage guides the flow so that the flow angle at station 2 is assumed to be equal to the stagger angle γ of the blade.

6.5.2 Mathematical model

Unlike Koff's or Moses and Thomason's models the current work accounts for non-constant diameter compressors and the effects of compressibility in the way explained below. The continuity, momentum, conservation of enthalpy (or rothalpy in case of rotors) and perfect gas state equations are applied across the blade passage in each of the two zones. As mentioned above, the flow is separated between stations 1 and 2, and the presence of the blade introduces a total pressure loss that is estimated by the following formula:

$$\frac{p_2 - p_1}{\frac{1}{2}\rho_1 W_1^2} = 1 - (1+k)\frac{\rho_2 W_2^2}{\rho_1 W_1^2} \tag{6.12}$$

where $k = k_{coeff}\sigma/cos(\beta_1)$ and k_{coeff} is an empirical coefficient that can be regarded as a measure of the pressure loss across the blades. The momentum equation is applied to the control volume shown in figure 2:

$$\int_{\Sigma} \rho\vec{V}(\vec{V}\cdot\vec{n})d\sigma = \int_{\Sigma_1,\Sigma_2,\Sigma_4,\Sigma_5} (\overline{\overline{\tau'}} - p)\vec{n}d\sigma - \int_{\Sigma_3} (\overline{\overline{\tau'}} - p)\vec{n}d\sigma \tag{6.13}$$

where the last term of the equation represents the body forces that the fluid exerts on the blade. The momentum equation, after some algebra, yields the following expression for the tangential force coefficient on the blade:

$$C_T = -\frac{2cos(\gamma)}{\sigma}\left(\frac{p_2 - p_1}{\rho_1 W_1^2}\right) + \frac{2cos(\beta_1)}{\sigma}\left[cos(\gamma+\beta_1) - \frac{W_2}{W_1}cos(\gamma-\beta_2)\right] \tag{6.14}$$

By substituting equation 6.14 into 6.12 the following quadratic equation in $\left(\frac{W_2}{W_1}\right)$ can be derived:

$$cos(\gamma)(1+k)\frac{\rho_2}{\rho_1}\left(\frac{W_2^2}{W_1^2}\right) - 2cos(\beta_1)cos(\gamma-\beta_2)\left(\frac{W_2}{W_1}\right) + 2cos(\beta_1)cos(\gamma+\beta1) - C_T\sigma - cos(\gamma) = 0 \tag{6.15}$$

from which the relative velocity at station 2 is calculated retaining the positive solution of the equation. The force coefficient is estimated using Raymer's correlation for the flow over a flat plate [151] with the Reynolds number based on the blade chord:

$$C_T = \frac{0.455}{log(Re^{2.58})(1 + 0.144M^2)^{0.65}} \tag{6.16}$$

It is demonstrated that the rothalpy flux is conserved in steady, adiabatic and inviscid flows [114]. For viscous flows, however, the friction with the casings raises the rothalpy by 1-2% for each rotor blade row [130]. As evidenced by the bulky separation regions present, the effect of flow viscosity is magnified in backflow operation and is expected to promote greater rothalpy rises across the rotor blade. However, to a first order, it is considered that the conservation of rothalpy still holds reasonably well in reverse flow conditions. By applying the conservation of rothalpy between stations 1 and 2, the static temperature at station 2 is found to be:

$$T_2 = T_1 + \frac{1}{2c_p}(U_2^2 - U_1^2 + W_1^2 - W_2^2) \tag{6.17}$$

The change in annulus area along the stage is confined to stations 2 and 3, whereas between stations 1 and 2 the annulus radii are taken as constant. By applying the momentum equation in the y direction and the mass flow continuity equation, the relative flow angle and relative velocity at station 3 can be determined:

$$tan(\beta_3) = \frac{\rho_3 A_3 W_2 sin(\beta_2)}{\rho_1 A_1 W_1 sin(\beta_1)} \tag{6.18}$$

$$W_3 = \frac{W_2 sin(\beta_2)}{sin(\beta_3)} \tag{6.19}$$

The static pressure at station 3 is obtained by applying the momentum equation in the x direction, combined with mass flow continuity as follows:

$$p_3 = p_2\frac{A_2}{A_3} + \rho_1 W_1 cos(\beta_1)\frac{A_1}{A_3}\left[W_2 cos(\beta_2) - W_3 cos(\beta_3)\right] \tag{6.20}$$

Finally, the static temperature at station 3 is given by the conservation of enthalpy between stations 2 and 3 since there is no blade present:

$$T_3 = T_2 + \frac{1}{2c_p}(V_2^2 - V_3^2) \tag{6.21}$$

The equations in the case of a stator row are similar to the ones for a rotor, except that the relative quantities are absolute, and the conservation of rothalpy for a stationary vane turns into enthalpy conservation.

In order to calculate the total to static or total to total pressure coefficients across the machine it is necessary to know the compressor exit total pressure and the compressor inlet static or total pressures. The flow properties should be calculated starting from the last stator and proceeding backwards up to the compressor inlet. For calculation convenience, in order to compare the computational results with the available experimental data it has been opted to prescribe the flow conditions at the inlet rather than at the outlet. Therefore, an iterative procedure will be used in order to determine the outlet conditions that match the data at the inlet. As a first guess, the outlet static conditions (temperature, pressure and corrected mass flow) are imposed to be equal to those at the inlet. The result is used to refine the initial guess using a Newton-Raphson method. The differences in the calculated static pressure and mass flow for subsequent time steps are used as the error handles that are targeted to values below a certain threshold. On the other hand, the temperature is unconstrained and free to develop.

6.5.3 Code results for user defined constant values of k_{coeff}

The direct application of the reverse flow model to Gamache's, Turner's and Day's compressors for the pressure loss suggested by Moses and Thomason, i.e. $k_{coeff} = 0.15$, yields results that depart considerably (differences of the order of 100%) from the experimental data in most of the cases. This may well happen since the expression published by Moses and Thomason was derived from very limited rig data [132].

The reverse flow model was carefully calibrated in order to find the value of the pressure losses that would match those found in the experimental data. A value of k_{coeff} 0.035 was consistently found to produce a reasonable agreement with the available experimental data. Figures 6.14a and 6.14b show the results obtained by the model compared with the rig data from Gamache's medium reaction build of a constant annulus three stage compressor for two different values of k_{coeff} at two shaft speeds. The same exercise was repeated for the high reaction build of the same compressor (figs. 6.15a and 6.15b). It is worth noticing that the agreement shown is obtained in terms of both total to static and total to total pressure coefficients.

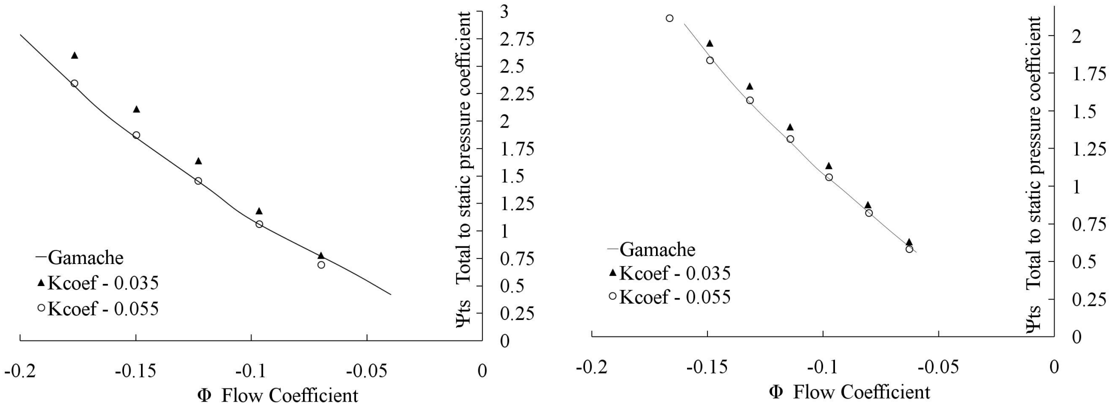

(a) *Shaft speed 1,170rpm* **(b)** *Shaft speed 1,800rpm*

Figure 6.14: *Reverse flow map for Gamache's compressor medium reaction build at two spool speeds.* Ψ *versus* Φ *for two different values of* k_{coeff}*. Numerical results*

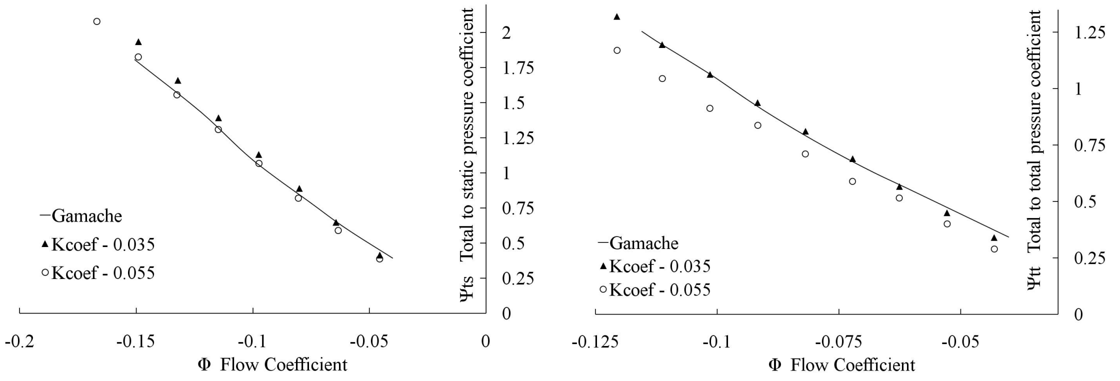

(a) *Shaft speed 1,800 rpm* **(b)** *Shaft speed 2,400 rpm*

Figure 6.15: *Reverse flow map for Gamache's compressor high reaction build at two spool speeds.* Ψ *versus* Φ *for two different values of* k_{coeff}*. Numerical results*

The effect of spool speed on the computational results is depicted in figure 6.16. Figure 6.17 illustrates the comparison between Koff's original model and the methodology proposed in this work. A slightly better agreement is obtained with the presented approach for high flows whereas Koff's model is found closer to the experimental data for lower reverse flow coefficients. However, although the overall prediction of compressor performance in backflow is satisfactory, the examination of the data broken down into stages unveils important deficiencies in the methodology. As stated previously, the program is devised so that it iterates to find the outlet conditions that satisfy the imposed conditions at the compressor inlet (IGV). The curves plotted in figures 6.14a to 6.17 are derived from flow magnitudes at the IGV inlet (imposed) and at the compressor outlet (calculated). In that case, it is enough for the flow conditions at the compressor outlet to be reasonably close to the experimental data for the code to provide reasonable results.

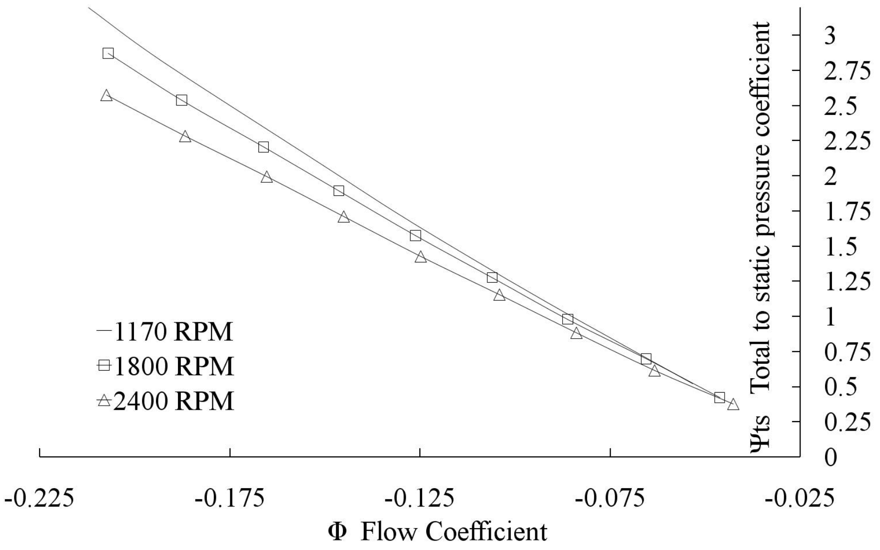

Figure 6.16: *Reverse flow map for Gamache's compressor high reaction build for several rotational speeds. Numerical results*

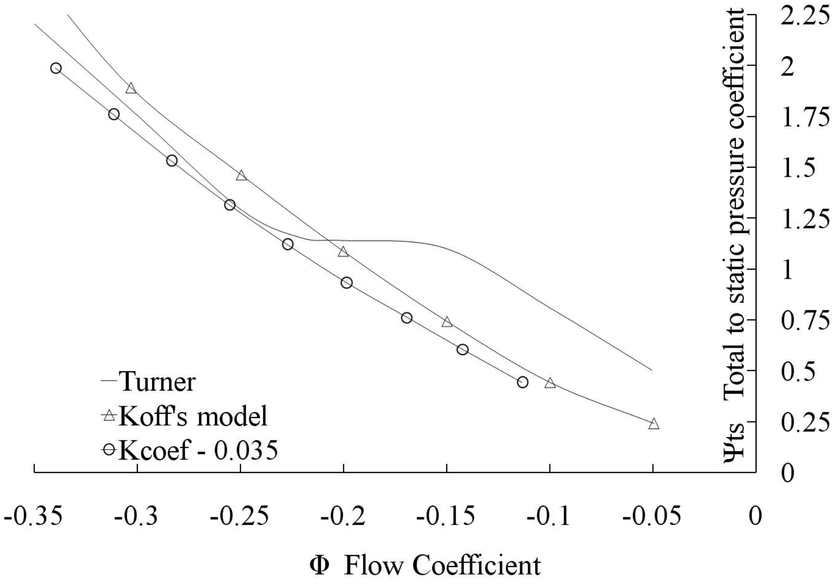

Figure 6.17: *Reverse flow map for Turner's compressor at 2,500 rpm. Numerical results for Koff's and current models*

Figure 6.18 illustrates this effect. Continuous lines represent the experimental data measured by Gamache at the axial gap between vanes for two flow coefficients, low (LF $\Phi = -0.04$) and moderate (MF $\Phi = -0.04$). Dotted lines show the calculated stage by stage performance of the compressor at such flow conditions. It can be observed how the relative differences are accrued and cancel out to produce a close agreement with the experimental conditions measured at the compressor S3 outlet. As expected, pressure losses are negligible across the last stator since the flow enters the compressor parallel to the vane metal angle at the trailing edge and hence remains smooth and attached along the channel. Furthermore, computations show an inverted trend compared to experiments for the greatest pressure losses occur across rotors as opposed by the pressure rise reported by Gamache. For the moderate flow case relative differences across stators and rotors make up in pairs so that the computed results match the experiments closely at each stator inlet. Besides, and yet again contrary to rig measurements, losses across stationary vanes are milder than those for rotors.

Figure 6.19 confirms such divergence. The numerical results do not show a noticeable change in static pressure coefficient if the compressor inlet guide vane is not included in the calculations. However, the significant experimental pressure drop across the IGV is evident at the sight of the marked margin between the continuous and dotted lines of figure 6.19. Moreover, the pressure loss across the IGV is magnified for greater reverse flow coefficients. This behaviour is consistent and can be generalised to any stator at backflow conditions, except for the compressor outlet guide vane for which flow losses are minimal.

The breakdown of compressor performance into stages provides additional useful information to further understand the flaws of the described methodology (fig. 6.20). Since the pressure loss over the third stator, S3, is insignificant, the rig results for the last stage constitute a measurement of the pressure rise attained across the rotor. Such pressure gain seems to increase continuously for greater backflow rates. The pressure loss across stators has a severe impact on the subsequent

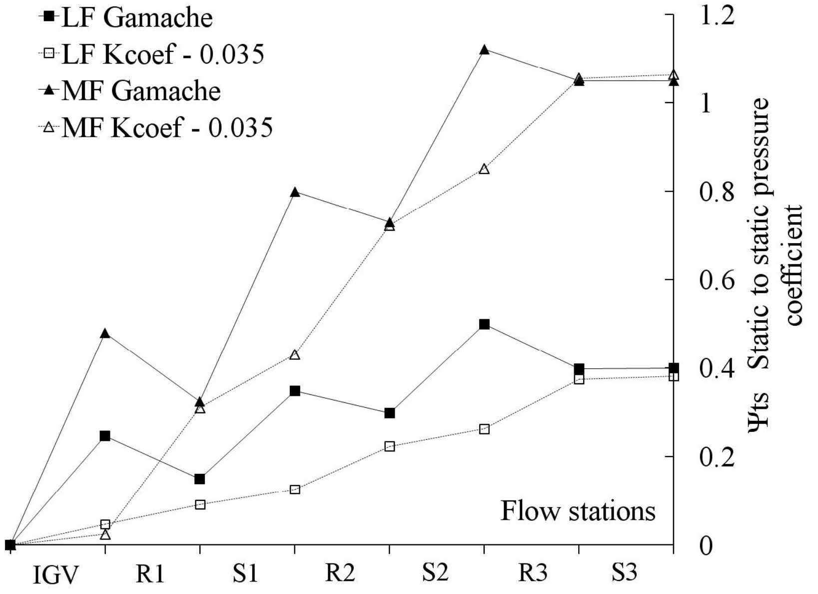

Figure 6.18: *Stage by stage Gamache's medium reaction build at 2400 rpm for low and moderate flow coef. Experimental and numerical results*

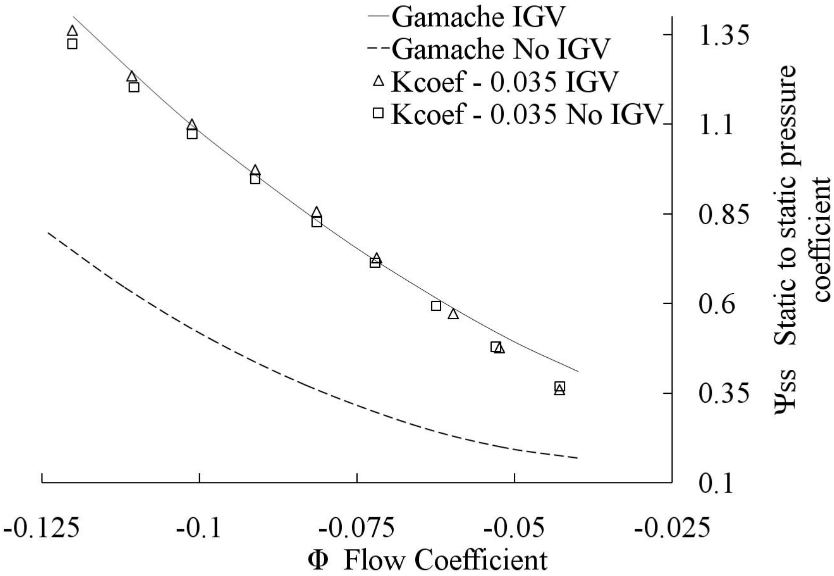

Figure 6.19: *Gamache's medium reaction build. Experimental and numerical results upstream and downstream of the IGV row*

stages; such marked pressure drop offsets the otherwise comparable pressure rise across rotors towards an overall net loss. The numerical results show that the greater pressure loss obtained across stages 1, 2 and 3 is compensated by the mild loss introduced by the inlet guide vanes.

The analysis of the total temperature profile along the compressor (fig. 6.21) reveals that the total temperature increases continuously towards the inlet, particularly across the rotors. This is reasonable since the energy imparted to the flow by the spool rotation translates into a temperature

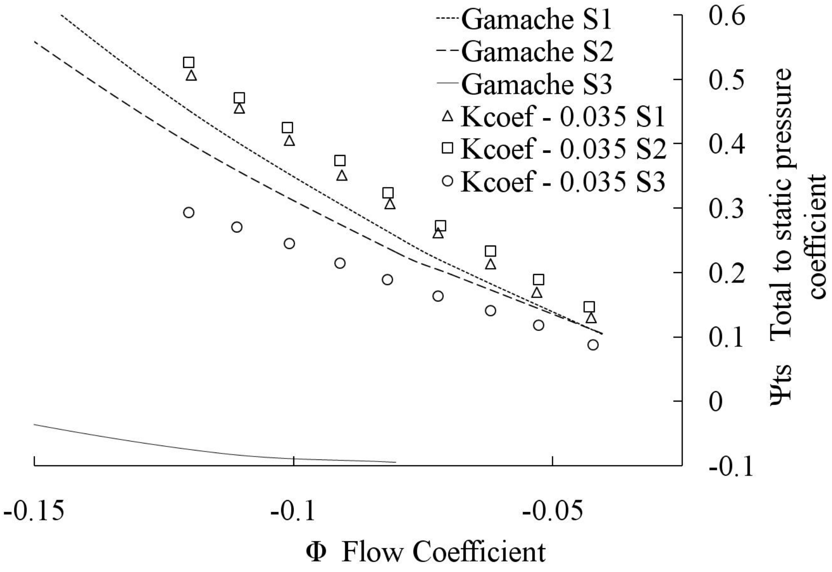

Figure 6.20: *Gamache's medium reaction build broken down into stages. Experimental and numerical results*

rise of the flow. The assumption of conservation of enthalpy across stator vanes seems divorced from fact, and the slight temperature rise achieved is an indication of the error made by modelling the flow as inviscid. Nothing can be said a priori about the correctness of the conservation of rothalpy, although it is suspected that differences notably greater than 2% will occur. The departure of the total temperature from the experiments accrues to values about twice the rig's at the compressor inlet.

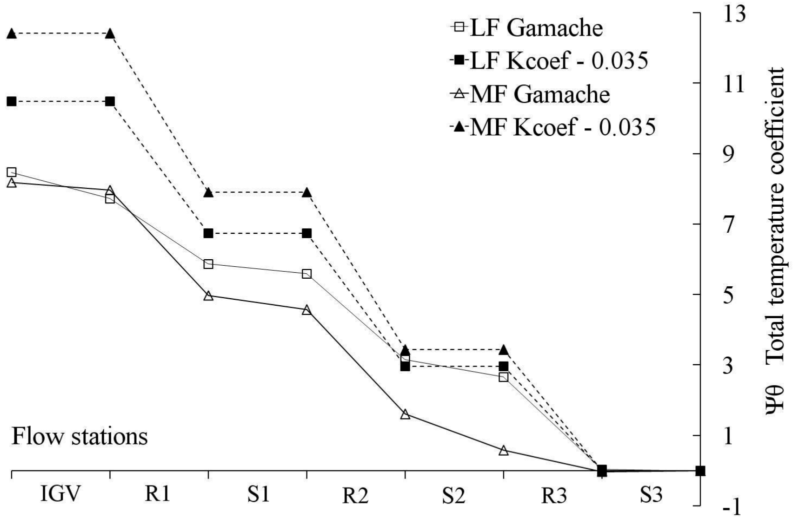

Figure 6.21: *Gamache's moderate reaction build at 2400 rpm for low and moderate flows. Experimental and numerical results*

6.5.4 Calibration of k_{coeff} on a stage by stage basis

At the light of the previous discussion and of equation 6.12, it is clear that positive values of k_{coeff} will fail to produce a static pressure rise across rotor vanes and hence adhere to the experimental performance recorded by Gamache. Therefore, in order to achieve a static pressure rise across rotors (in reverse flow), the pressure loss must be such that $k_{coeff} < 0$. The present work suggests calibrating the loss factor differentiating between rotor and stator vanes in order to pursue not only an overall agreement with the experiments but on an individual stage basis as well. For each blade row the value of k_{coeff} that produces a perfect match of the calculations with the rig data was obtained manually.

The only stage to stage static pressure rise data available for validation is that published from Gamache's compressor, but only at a rotational speed of 2,400 rpm. Since the difference of the experimental data for his two compressor builds is small, the calibration of k_{coeff} is rendered only for the medium reaction build. Gamaches stage to stage results are available at a low, moderate and high flow coefficients and the calibration of the code's results is carried out separately for each flow regime.

The values of k_{coeff} that best match Gamache's experimental data are grouped for each flow coefficient in table 6.1 and plotted in figure 6.22, for each rotor and stator of the three stages and the IGV. The last stator's flowfield is calculated using a different method, since it is assumed that no separation occurs on these blades. The pressure rise across the rotor exhibits a consistent value of k_{coeff} close to -1.2 for the whole range of flow coefficients analysed. On the other hand, the value for stator vanes shows a gentle rise for lower flow coefficients and increases sharply for very low flows. This is related to the fact that the velocity across the vane becomes very small and the flow seems to develop in an erratic fashion with abnormal pockets of highly entropic separated flow present in the axial spacing of the blade rows. Attention is drawn to the fact that the scatter of the results is minimised for higher backflow regimes. This suggests that while for lower flows the pressure loss suffers from a certain dependency on the blade geometrical features, for high flow coefficients blade row geometry has a somewhat secondary effect. Also, the unwavering values observed across rotor blades may arise from the effective accommodation and dissipation of the flow uniformities generated by the stators achieved by the blade rotation. This explanation would support the view that blade geometry is of secondary importance in reverse flow, particularly across rotors, and is reinforced by the uniformity of the spanwise flow profiles measured by Gamache at the leading and trailing edges of the compressor blades.

Table 6.1: *Gamache's medium reaction compressor at 2400 rpm.* k_{coeff} *calibration.*

C_x/U	IGV	R1	S1	R2	S2	R3	S3
Low (-0.038)	15.02	-1.06	11.6	-1.15	10.84	-1.2	X
Moderate (-0.098)	0.374	-1.175	0.351	-1.25	0.276	-1.18	X
High (-0.199)	0.05	-1.29	0.05	-1.27	0.05	-1.27	X

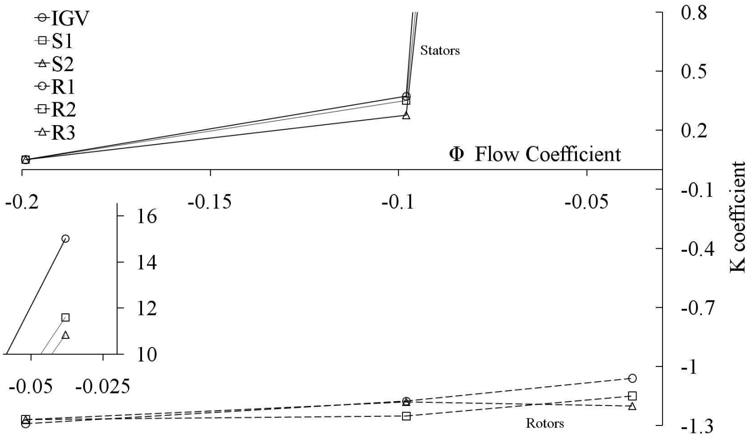

Figure 6.22: *Stage by stage Gamache's medium reaction build at 2400 rpm for low and moderate flow coef. Experimental and numerical results for k_{coeff} calibration*

By fitting the values of k_{coeff} derived for both builds of Gamaches compressor it is possible to produce two separate expressions that correlate the value of k_{coeff} against flow coefficient. Results for Gamache's medium reaction build compressor at the moderate reverse flow conditions were generated utilising such expressions and are shown in figure 6.23. The overall and the stage by stage agreement are reasonable throughout the whole length of the machine.

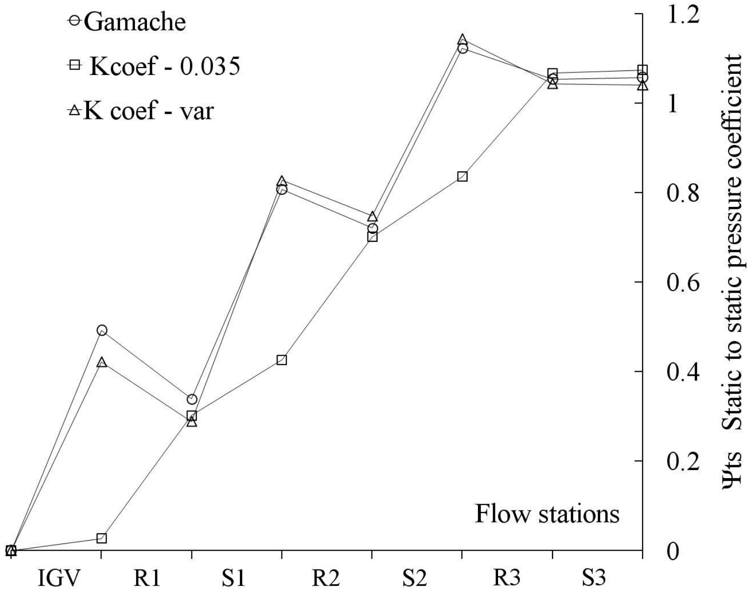

Figure 6.23: *Gamache's medium reaction build at several rotational speeds for variable k_{coeff}.*

Further to Gamache's compressor, the data supplied by Day on a four stage constant annulus compressor were used as a benchmark to test the usefulness of the described approach. Unfortunately, the stage by stage performance of Day's compressor in reverse flow is not available in the public domain for a thorough comparison to be possible. The calculated total to static pressure coefficient plotted in figure 6.24 deviates from the test data for moderate backflow regimes since the model does not seem to be able to capture the curvature of the compressor characteristic. Calculated and recorded performance come closer for both ends of the range of flow regime under study.

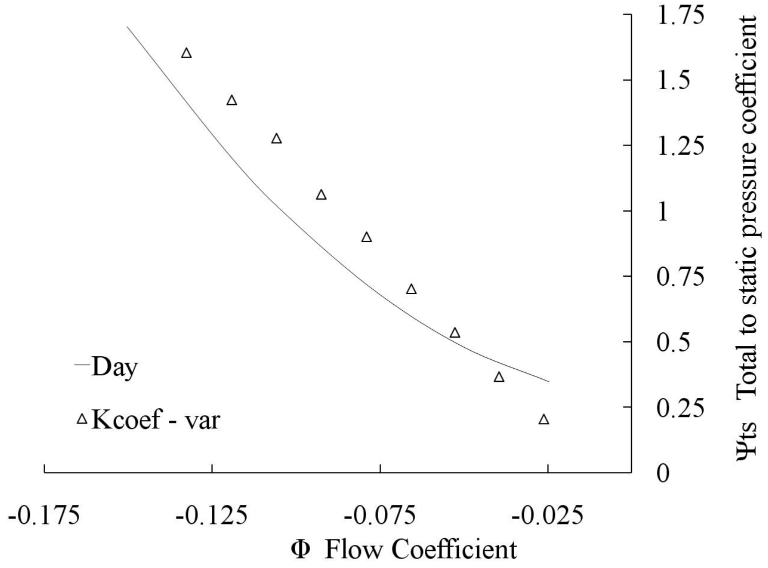

Figure 6.24: *Day's four stage axial compressor. Experimental and numerical results for variable* k_{coeff}.

6.6 Concluding remarks and future work

Extended reverse flow compressor maps are a necessary input for a performance model of a shaft failure event. In particular, the compressor delivery pressure, p_{30t}, is the most important parameter that determines the terminal speed of the turbine. Therefore the progression of p_{30} during the event needs to be accurately calculated for a reliable simulation of the event. The current research is accountable for the provision of reverse flow maps that are required by compressor transient models to simulate the pre and post stall operation of the compressor.

The calculation of compressor reverse flow characteristics is rather challenging due to the unsuitability of forward flow techniques to solve the strong separated flows that occur in backflow. Moreover, the very limited data available to the research constitutes however a major hurdle for the successful validation of any reverse flow model. This research used a stage stacking technique to develop the extended compressor map from CFD derived characteristics of the last two stages of a modern eight stage axial compressor. The stage stacking technique is formed by a system of eleven equations with eleven unknowns, two of which are substituted by graphic correlations obtained from CFD.

While the methodology is generic and can be applied to any axial compressor, the pressure coefficient and adiabatic efficiency obtained from CFD are dependent on the blade stagger angle and the cascade solidity of the particular compressor analysed. It is recommended that the work continues with the CFD simulation of compressor stages in reverse flow for a range of stagger angles and blade spacing to constitute a wide database to extend the applicability of the technique.

The chapter also investigated the suitability of two-dimensional models based on first principles to calculate the compressor backflow characteristics. These models present with the advantage that CFD simulations are not required to derive the extended characteristic. However, the main limitation of two-dimensional approaches was found to be their inability to capture the strong radial flows over rotor blades.

In an attempt to overcome the limitations associated with two-dimensional approaches, the pressure loss across the blade rows have been modelled with the inclusion of a pressure loss coefficient that includes three-dimensional effects and that has been calibrated against the stage data available from Gamache's experiments. The static pressure calibration was carried out through the manual selection and testing of several empirical k coefficients for each rotor and stator row. The application of the new methodology has proven efficient to simulate the compressor stage by stage performance in reverse flow in a quick and robust manner.

Comparison of the results against the very limited experimental data available is satisfactory and differences are suggested to occur due to the limitations of the assumptions made; particularly the conservation of enthalpy and rothalpy and the complete and effective mixing of the flow after a blade row prior to the next blade passage.

The research work should continue with the application of the methodology to a multistage compressor and comparison with the CFD based stage stacking technique.

Appendix 6A - First principles applied to compressor blades in reverse flow

This appendix covers the application of first principles to compressor blades in reverse flow, in conjunction with some assumptions that simplify the flow field. Consider the control volume depicted in figure 6.25 that shows a compressor blade in reverse flow.

The flow is assumed to be two-dimensional, steady and incompressible. Blade solidity is assumed to be high enough for the blades to be considered flat plates. The flow separates at the leading edge and the separation covers a fraction μ of the blade pitch. Downstream of the trailing edge the blade is asssumed to be fully mixed prior to the next blade row.

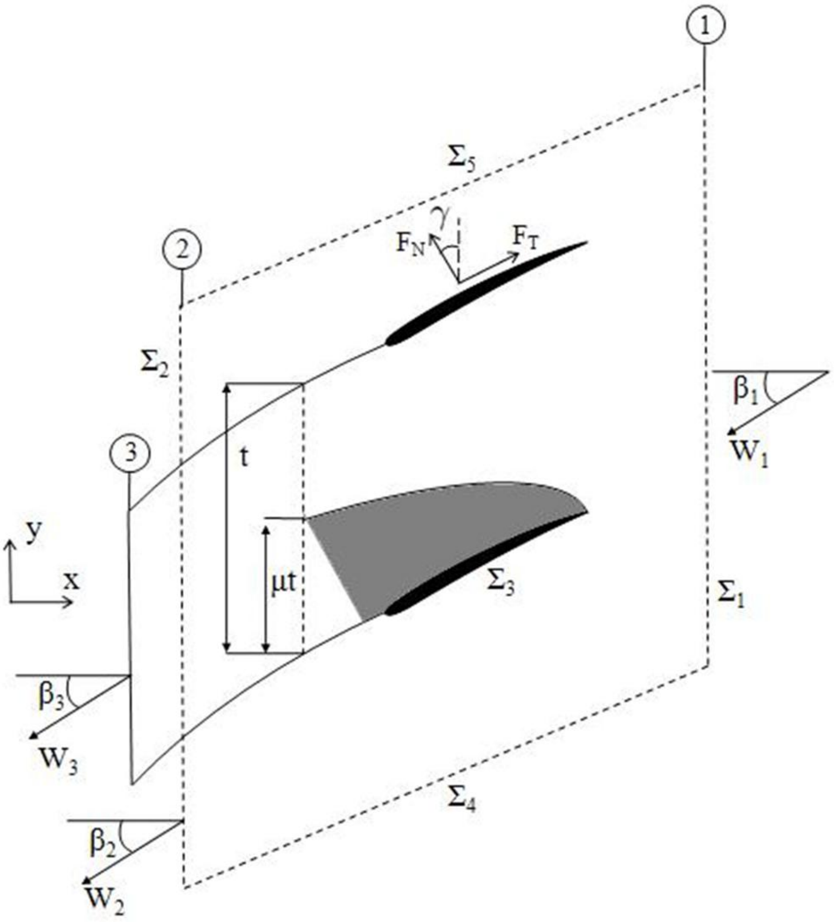

Figure 6.25: *Compressor reverse flow model - Control volume*

The uniformity of the flow on the boundaries allows for the application of the equations of Navier-Stokes to the domain in their integral form. The momentum equation between stations 1 and 2 takes the form:

$$\underbrace{\frac{d}{dt}\int_{\Omega}\rho\vec{v}d\Omega}_{=\vec{0}}+\int_{\Sigma}\rho\vec{v}\left(\vec{v}-\vec{v_c}\right)\cdot\vec{n}d\sigma=-\int_{\Sigma}p\cdot\vec{n}d\sigma+\underbrace{\int_{\Omega}\rho\vec{f_m}d\Omega}_{=\vec{0}}+\int_{\Sigma}\overline{\overline{\tau}}'\cdot\vec{n}d\sigma \tag{6.22}$$

The convective term in the equation is zero on surfaces $\Sigma_{3,4,5}$ either because $\vec{v}=0$ or because the speed is perpendicular to $\vec{n}$. The flow is considered inviscid on surfaces $\Sigma_{4,5}$. This assumption is true for isolated blades where these surfaces are far away from the blade, but for blades in cascade it may be defficient. The pressure integral can be offset by the ambient pressure, p_∞, so that the total sum extended to all surfaces cancel out. Hence, only the gauge pressure on surfaces $\Sigma_{1,2}$ give a non zero component. On surfaces $\Sigma_{1,2}$ tensor $\overline{\overline{\tau}}'$ is zero because on those surfaces the flow is uniform. On the other hand, the force exerted on the fluid by the blade is given by

$$\int_{\Sigma_3}\left(-p\vec{n}+\overline{\overline{\tau}}'\cdot\vec{n}\right)d\sigma=\vec{F}=F_T\left(cos(\gamma)\vec{i}+sin(\gamma)\vec{j}\right)+F_N\left(-sin(\gamma)\vec{i}+cos(\gamma)\vec{j}\right) \tag{6.23}$$

Equation 6.23 can be projected on the x and y axes to yield

$$\vec{i})\quad -\rho_2W_2^2cos^2\beta_2s\,(1-\mu)+\rho_1W_1^2cos^2\beta_1s=(p_2-p_1)s+F_Tcos\gamma-F_Nsin\gamma \tag{6.24}$$

$$\vec{j})\quad -\rho_2W_2^2sin\beta_2cos\beta_2s\,(1-\mu)-\rho_1W_1^2sin\beta_1cos\beta_1s=-F_Tsin\gamma+F_Ncos\gamma \tag{6.25}$$

After some algebra, it can be written that:

$$F_T=-\rho_2W_2^2cos\beta_2s(1-\mu)cos(\gamma-\beta_2)+\rho_1W_1^2cos\beta_1scos(\gamma+\beta_1)-(p_2-p_1)s \tag{6.26}$$

And the force coefficient in the tangential direction is:

$$C_T=\frac{F_T}{\frac{1}{2}\rho_1W_1^2c}=\frac{2}{\rho_1W_1^2\sigma}\left[\rho_2W_2^2cos\beta_2(1-\mu)cos(\gamma-\beta_2)\right]-2\frac{cos\beta_1cos(\gamma+\beta_1)}{\sigma}-\frac{(p_2-p_1)}{\sigma\rho_1W_1^2} \tag{6.27}$$

On the other hand, the continuity equation between stations 1 and 2 can be termed as follows:

$$\underbrace{\frac{d}{dt}\int_V\rho d\Omega}_{\vec{0}}+\int_\Sigma\rho(\vec{v}-\vec{v_c})\cdot\vec{n}d\sigma=0 \tag{6.28}$$

$$\rho_1W_1cos\beta_1s=\rho_2W_2cos\beta_2s(1-\mu) \tag{6.29}$$

By substitution of 6.29 into 6.27

$$C_T = \frac{2}{\rho_1 W_1^2 \sigma} \left[\rho_2 W_2^2 \frac{W_1}{W_2} cos\beta_1 cos(\gamma - \beta_2) \right] - 2\frac{cos\beta_1 cos(\gamma + \beta_1)}{\sigma} - \frac{(p_2 - p_1)}{\sigma \rho_1 W_1^2} \tag{6.30}$$

Equation 6.30 is included in section 6.5.2 as equation 6.14, and the model equations are thoroughly described next in that section.

Chapter 7

Compressor inlet guide vane loss, deviation and stall modelling

7.1 Introduction

During normal, unstalled operation of the engine the position of the variable geometry of the compressor is fixed for a given spool speed by the schedule that is mapped in the control logics of the engine. Variable geometry blade rows are moved by a fuel powered actuator that is connected to the vanes by a piston rod. During normal transient manoeuvres, the response of the control system and the actuator is fast enough to follow the change in shaft speed and restrain the compressor from surging or choking.

In rapid failure scenarios, however, the actuating mechanism is not able to catch up with the very rapid changes undergone by the flow and lags considerably behind. This variable geometry malschedule jeopardises the stability of the compression system; it can surge the engine or prevent it from recovery.

Performance calculations use compressor maps that are obtained from rig data. However, the experimental tests are conducted only at conditions in the neighbourhood of the prescribed schedule and do not cover all the many possible schedules. Therefore, the modelling of the shaft over-speed event requires an analytical methodology to obtain malscheduled compressor maps.

The current research uses an industry proprietary mean line compressor performance algorithm (VU59) developed by Wright [192] to obtain the compressor map for any combination of the variable geometry settings. The agreement that can be obtained with the compressor prediction algorithm is remarkable; however, the treatment given to the flow across the inlet guide vanes is inaccurate and needs to be revisited.

This chapter covers the development of pressure loss, deviation and stall correlations for the flow across the inlet guide vane of modern axial compressors. The correlations are derived from an extensive series of CFD simulations of an IGV and first rotor of a modern axial compressor for a range of flow incidences and conditions. The correlations are validated against experimental compressor maps avaliable to the research from the industrial sponsor.

The improved version of the compressor performance prediction program constitutes a generic tool able to produce compressor maps for malscheduled variable geometry vanes. The chapter ends with the provision of an example of such maps for three positions of the actuation mechanism. The compressor maps can be readily integrated into a whole engine performance model to simulate the shaft failure event.

7.2 Brief description of VU59

The performance that can be attained by a well-designed multistage compressor is determined by the choices made for a number of global parameters such as aspect ratio, solidity, tip Mach numbers, tip clearances, stage loading, flow turning, reaction and so on. These choices have to be made early in the design process and are paramount for the success of the design. No amount of subsequent development effort can correct a poor design where the basic selection of those global parameters is inconsistent with the objectives pursued by the design.

The design of an axial compressor is always a compromise between the requirements for high efficiency, high loading, acceptable part-speed performance and sufficient values of the surge margin. One-dimensional aerothermal codes use relatively simple mean line calculations to allow for the investigation of trade-offs between efficiency, loading and operating range of the compressor.

VU59 is the name of a Rolls-Royce proprietary Fortran computer program for running multistage axial compressor preliminary 1D design calculations. The program input comprises values of annulus coordinates, aerofoil geometric parameters such as space/chord ratio, thickness/chord ratio, blade angles and tip clearance and the shaft rotational speeds at which overall performance characteristics are to be predicted.

The calculation uses the Lieblein based empirical correlations contained in [193] and [128] to calculate the loss, turning and annulus wall blockage growth across the blades, and provides the user with the overall performance characteristics of the compressor. These correlations are in most cases an attempt to fit experimental data with tailored expressions. They are a generalisation and as such, they may not provide satisfactory results for a particular compressor. Besides, those models are usually developed on the assumption that the mechanisms that generate the loss are independent and give rise to separate loss factors, and this assumption may not be very accurate. Usually each model focuses on enhancing the prediction of a particular loss factor and then those factors are added up to make up the total loss across the blade row.

7.2.1 Description of the calculations

7.2.1.1 Calculation of choke and surge flows

Surge and choke points delimit the range of the unstalled portion of the compressor characteristics. Automated calculations to obtain the full characteristic are carried out as follows:

For each shaft speed calculations start by the program iteratively guessing values of the compressor inlet mass flow at which it thinks this might be achieved at the given shaft speed. In turn, for each of these guessed inlet mass flows the blade row stacking calculations are called and the program attempts to calculate the aerodynamic conditions right through the compressor to arrive at a value of the overall pressure ratio and efficiency at the guessed mass flow. If the guessed mass flow is not appropriate - compressor choked or stalled - then the program uses some intelligence to run at a more appropriate mass flow until a satisfactory initial flow is found.

After finding a satisfactory initial mass flow the program increments the inlet mass flow in small steps. For each incremented mass flow the blade row stacking calculations are called and the overall adiabatic efficiency is calculated. If a flow increment takes the mass flow beyond choke for the given speed then the code sets a flag that causes the flow increment to be halved. The iteration continues until the mass flow increment is smaller that a given value, 10^{-3}, when the mass flow is taken to be the choking mass flow.

The iteration scheme for finding the surge flow involves succesively reducing the mass flow from the intial flow value and calling the blade row stacking calculations described before to calculate blade row and overall performance at each mass flow. When three succesive mass flows are found which encompass a maximum of the overall total pressure ratio a quadratic curve fit is then fitted through these points and the mass flow corresponding to the maximum of this curve is easily found.

Having found surge and choke flows it remains only to fill the rest of the characteristic. The initial flow is discarded and the distribution of mass flows between surge and choke is determined by a sinusoidal function that spreads points at a fairly equally spaced intervals along the chic. The blade row calculations described before are then run at each mass flow to calculate blade row and overall performance.

7.2.1.2 Calculations for each operating point

The aforementioned correlations are used in conjunction with a blade row stacking technique to solve iteratively the continuity and Euler work equations for each blade row successively through the compressor. The stacking technique calculates a full set of mean line aerodynamic parameters (i.e. total velocities, whirl angles, pressures, temperatures, Mach numbers) at every blade row inlet and exit plane for a range of inlet mass flows for each correspondent speed line. A further correlation is then used to calculate the inlet mass flow at which the compressor surges at a given rotational speed. The iterative calculations run as follows (fig. 7.1): first of all, the mean line velocity triangles are obtained solving 1-D Euler and mass flow continuity equations. The annulus wall blockage, rotor and stator loss coefficients can be derived applying blade loss and blockage empirical correlations. From those coefficients and the stage pressure ratio the stage temperature rise can be obtained and the velocity triangles are calculated again. The process is repeated iteratively until consistent values of mean-line velocity triangles, blade row losses and annulus wall blockage are found. Once the program has converged, the remainder blade angles are then derived from correlations of incidence and deviation.

Output from the calculations consist of tabulations of the input data, together with formatted pages of predicted blade row data, stage data and overall performance data.

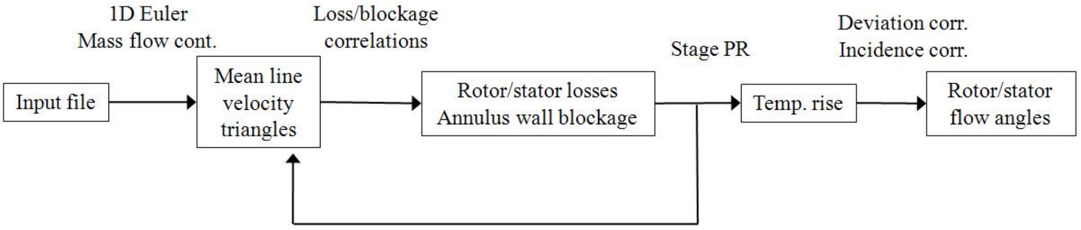

Figure 7.1: *VU59 performance code iterative structure*

7.2.2 Limitations of the code

VU59 has several limitations that must be borne in mind for a proper result analysis. These are:

- The code is a mean line based analysis. 3D effects are not considered and therefore the results are less representative for big compressors and fans. In those cases the variations along the blade span can not be disregarded.
- The method has been proved not to predict the turn-over of characteristics as surge line is approached.
- The empirical correlations employed in the calculations are based on DCA or parabolic aerofoils. Any other type of aerofoil is approximated by one of those two types. Moreover, the program employs several correlations and parameters based on old investigations like the Liebleins diffusion factor, Raley stalling incidence, De Haller number and so on, that may not be adaptable to new compressor designs. It is only the experienced compressor aerodynamicist who will determine the grade of confidence on the results the program provides.

However, the major limitation arises in the calculation of surge margin. The IGV loss and stall models used in VU59 are discussed next.

7.2.3 VU59's loss and stall modelling

7.2.3.1 Introduction to pressure loss models

[1] The prediction of axial compressor performance experienced a breakthrough when Lieblein [110] succeeded in tying down blade profile losses by correlating such losses to wake geometrical parameters that can in turn be linked to the blade geometry through the diffusion factor. The total pressure loss across the compressor is then calculated by adding up the individual losses - mainly broken down into profile, secondary and shock losses - for each blade row. Although Lieblein himself never referred to the diffusion factor for incidences other than minimum loss incidence, others have used it for a wider range of incidence angles [98][170] and so Lieblein's based methodologies have

---

[1] Lieblein based loss models are abundant in the literature and a comprehensive description of such models is out of the scope of this thesis.

become the standard for the calculation of losses in turbomachinery. However, this approach is no longer valid when a determined incidence angle is surpassed: at that point the flow detaches from the aerofoil surface and merges into big separation bubbles and recirculation zones that make the pressure coefficient experience a sudden rise. The wake rapidly becomes indistinct due to transient effects and attempts to predict the profile losses based on wake characteristics and the aforementioned diffusion factor are then somewhat fruitless (fig. 7.2a and 7.2b). It is for these reasons that the design of inlet guide vanes at off-design conditions usually relies on cascade tests, flat plate experimental rigs and CFD calculations.

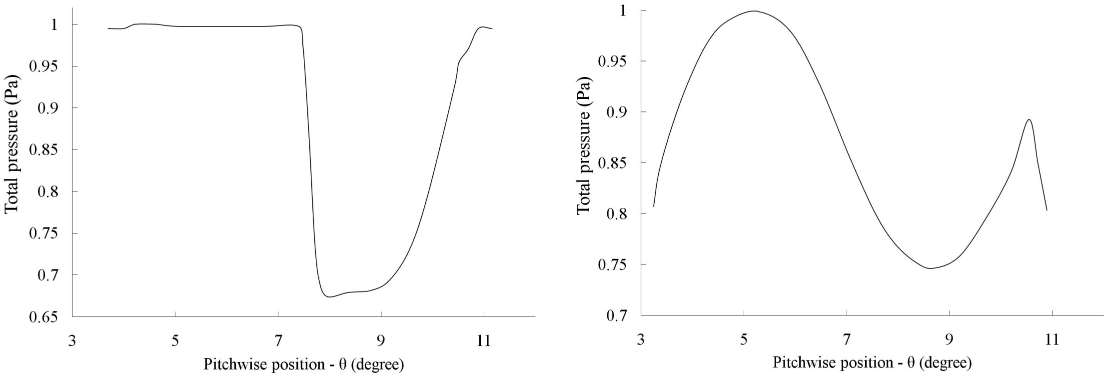

(a) *Incidence* 2° **(b)** *Incidence* 45°

Figure 7.2: *Wake profile one chord downstream of the trailing edge*

Moreover, a search of public domain literature revealed that the attention given to this topic by the turbomachinery community is scarce, save for those studies undertaken by Coppinger and Swain on centrifugal compressor design [36][35].

7.2.3.2 Simplified IGV loss and deviation model

VU59 uses a very simple model that is derived by assuming inviscid and steady state flow without mass forces. Appendix 7B shows that these assumptions applied to a control volume whose boundaries are infinitely far upstream and donwstream of the domain yield:

$$\frac{p_{1t} - p_{2t}}{\frac{1}{2}\rho v_2^2} = sin^2\alpha \tag{7.1}$$

This equation is weighted with a number coefficients to provide a better adjustment to experimental data available to the company. For what concerns the flow deviation at the trailing edge of the IGV, VU59 does not acount for this and considers that the flow leaves the IGV at the metal angle of the trailing edge.

7.2.3.3 Stalling incidence model

The stalling and optimum incidences are obtained from two empirically derived expressions that depend on the stagger and the solidity of the cascade. These are the following:

$$i_{stall} = A + B\sigma - C\Theta \tag{7.2}$$

$$i_{stall} = X + Y\sigma - Z\Theta \tag{7.3}$$

where the constants A, B, C, X, Y and Z are given by figures 7.3a and 7.3b respectively.

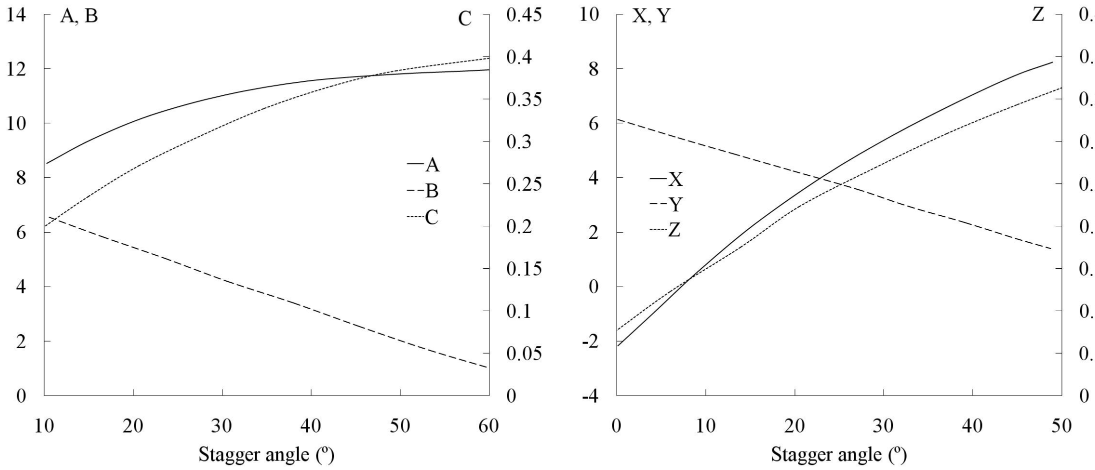

(a) *Stalling incidence* **(b)** *Optimum incidence*

Figure 7.3: *Coefficients for Raley's stalling and optimum incidence correlations. From [128]*

7.2.3.4 Results obtained with the original loss and stall models in VU59

The ability of VU59 to succesfully predict the performance of modern multistage compressors was tested by applying the code to two different eight stage axial compressors. The predicted compressor maps are shown in figures 7.15 and 7.5 and are compared with characteristics obtained experimentally for both compressors at the same aerodynamic speed. The agreement in terms of capacity between the two sets of data is good at high speeds but deteriorates markedly at part speed, when the IGV loss prediction is more inaccurate. In both cases, however, the stall point is severely overpredicted. The prediction of the efficiency peak follows closely the rig data, although the calculations yield slightly high values at low speeds for the first compressor.

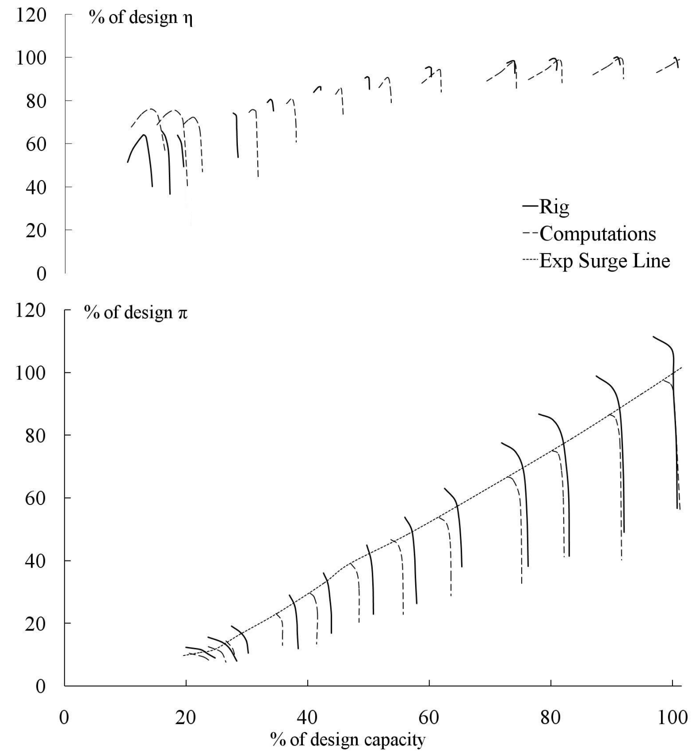

Figure 7.4: *Simplified IGV loss model - Results for axial compressor A*

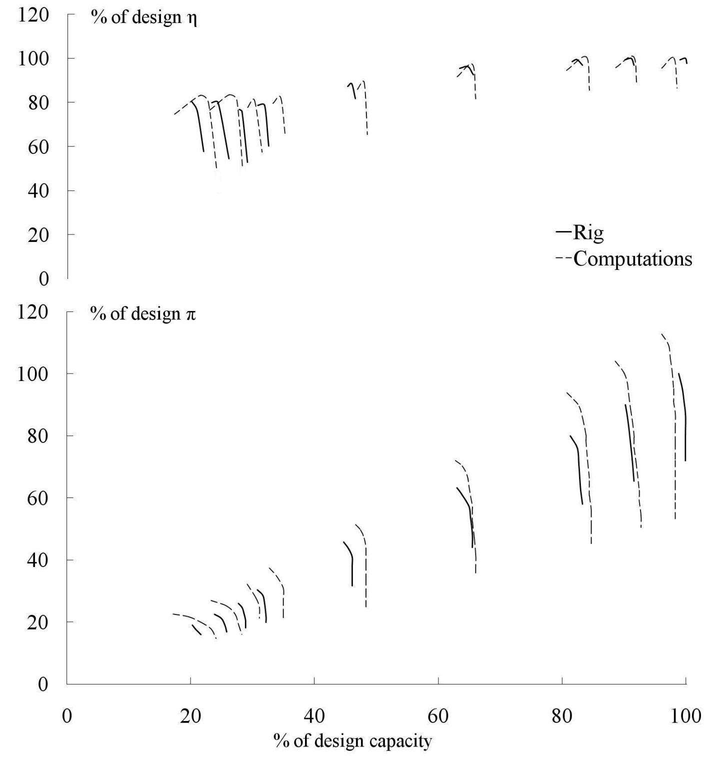

Figure 7.5: *Simplified IGV loss model - Results for axial compressor B*

7.2.3.5 Limitations of the loss and stall calculations

The existence of a variety of loss and stall correlations in the literature is partly historical, but it is also due to their inadequacy.

The treatment given to the pressure loss exhibits important deficiencies. The simplified expression does not account for the arrangement in cascade of the vanes that limit the extent of the flow separation. Flow viscosity is disregarded and assumes that the flow is fully mixed before it reaches the downstream rotor. In the case of stall calculations, the main limitation arises from the fact that stall is a strongly three-dimensional phenomenon and one-dimensional models are quite unable to capture this properly.

Experienced designers are aware of the limitations of these methods and use a mixture of judgement and analysis to decide which to use, or which to believe. An example of this is the way in which the surge margin of a compressor might be estimated by the designer.

Another reason why the designer's judgement is necessary is that most correlations, by their nature, are based on older designs, and embody the behaviour of earlier types of compressors. In particular, Raley stalling incidence is based on cascade tests of British 10% thick C4 profiles even though no such blade sections are used in modern compressors.

7.3 CFD simulation and loss modelling of inlet guide vanes

7.3.1 Geometry definition

Besides the radial flow on the compressor blades several important peculiarities pertaining to the flow across a compressor IGV are to be borne in mind when defining the geometry to be analysed. First of all, the air flow entering the compressor is usually deflected prior to the inlet in a "S" shaped duct - named swan neck duct - to be brought closer to the engine shaft so that the blades are subjected to smaller mechanical stresses, amongst other benefits. However, the requirement for shorter and lighter engines is at odds with the need for a smooth duct to avoid flow separation and zones of low energy fluid next to the hub surface. Moreover, provided that the hub and shroud casings are not flat, the clearance between the IGV tip and the casing varies as the vane is rotated, modulating the pressure loss. And last, aggravated by the increasingly reduced axial spacing between vanes in modern engines, the augmented width of the wake downstream of the trailing edge of the IGV at high incidence angles boosts the losses caused by the wake-rotor interaction. As a result, a detailed 3D geometry that comprises the swan neck duct, the uncambered IGV and the first compressor rotor is necessary to obtain trustful results and account for the aforementioned effects, as opposed to 2D IGV-only cascade simulations. The geometry assembly is shown in figure 7.6.

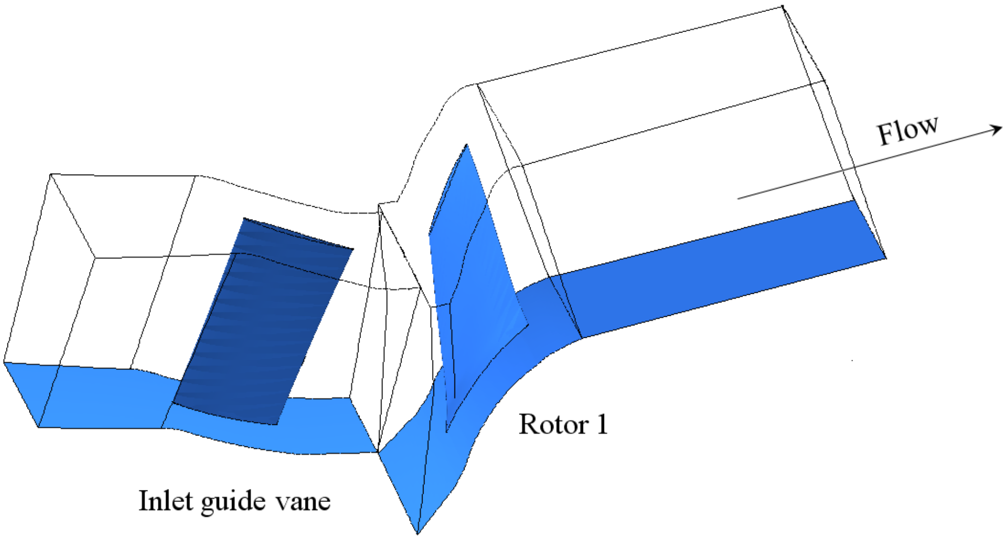

Figure 7.6: *CFD simulation domain - Inlet guide vane and first compressor rotor*

7.3.2 Flowfield across the inlet guide vanes

[2] Inlet guide vanes are designed to interfere as little as possible with the flow at maximum take-off conditions (100% NRT). An uncambered flat plate aligned with the flow introduces as little loss as possible 7.7a. As the IGV closes the flow detaches from the blade surface and forms a small bubble first that grows progressively until it finally occupies the whole length of the blade chord 7.7b. For the closed position of the vane the separation is stronger and the flow is forced to cross the passage in a fast and narrow jet 7.7c. This behaviour is analogous to that over supercritical thin wing profiles. Figure 7.8 contains the schematics of the flow over such type of wing profile and the pressure coefficient distribution on the extrados of the wing for a range of incidence angles. The flow across the vane passage follows the same pattern but unlike a wing at very high incidences, is not able to fully separate as the presence of the adjacent blades in the cascade prevent this.

7.3.3 Pressure loss results

Two different CFD studies have been conducted for the specified geometry. In the first set accurate engine conditions have been imposed as boundary conditions to derive the IGV performance at several operating points along the running line of the engine. Results for the pressure loss across the IGV and the deviation at the IGV trailing edge are plotted in figures 7.9 and 7.10. As expected the loss and deviation are minimal at high speed since the IGV is aligned with the incoming flow. Both losses and deviation raise progressively as the IGV is skewed closed and reaches a maximum for the closed position of the IGV that corresponds to the maximum stagger angle and therefore the maximum incidence. The trends present in figure 7.9 are justified as follows:

---

[2] For a comprehensive description of the operation of inlet guide vanes and their schedule the reader is directed to section 9.2

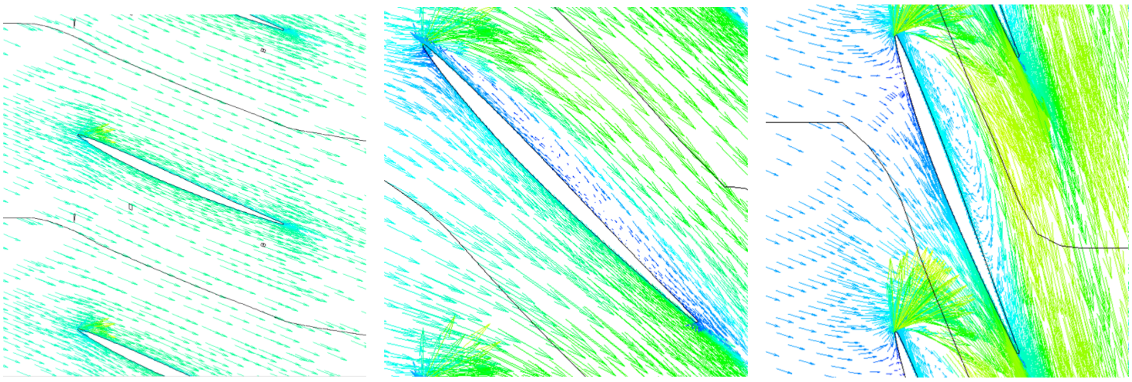

(a) *Design speed - 100% NRT* **(b)** *90% NRT* **(c)** *70% NRT*

Figure 7.7: *Flow velocity vectors across the inlet guide vane - Separation regions*

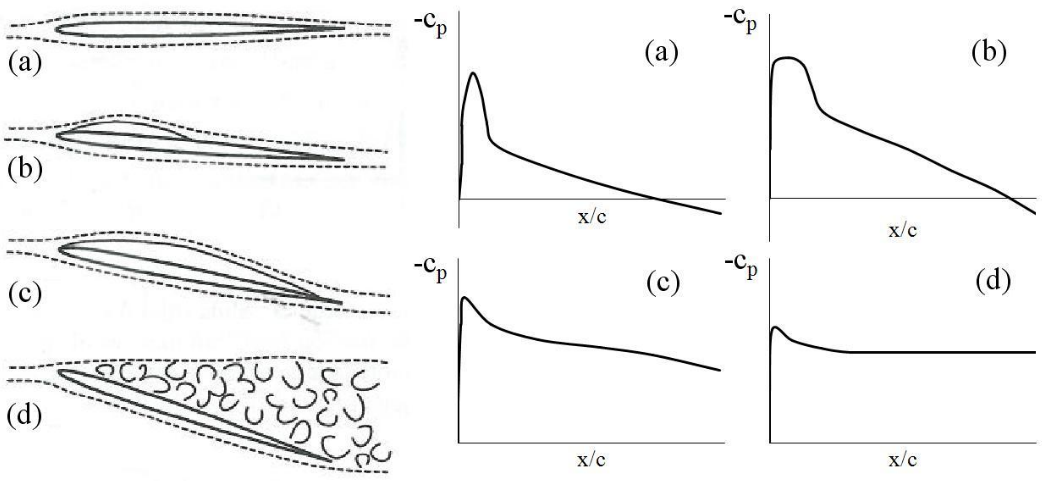

Figure 7.8: *Schematics of the flow field on the suction surface of a supercritical thin wing with incidence and distribution of pressure on the suction surface. From [125]*

- At low speeds the losses should be high on account of the incidence of the flow, which is far from its optimum value. However, this effect is compensated with the decrease in Mach number at the inlet of the IGV that makes the pressure loss drop.

- At high speeds, the opposite occurs. Whereas the Mach number is higher, the incidence is close to the optimum value and limits the loss. It is because of this reason that there is a minimum value of the pressure recovery factor that corresponds with the highest speed at which the IGV is completely closed.

On the other hand, figure 7.10 illustrates the weak dependency of the deviation angle with the mass flow, and therefore the IGV inlet Mach number as demonstrated by the plateau present at low speeds for the closed position of the IGV.

These results are corroborated when the pressure loss and the deviation are represented against the IGV stagger angle (figs. 7.11a and 7.11b). Particularly, for the IGV completely closed (100% setting) the decrease in pressure loss is caused by the fall in inlet Mach number.

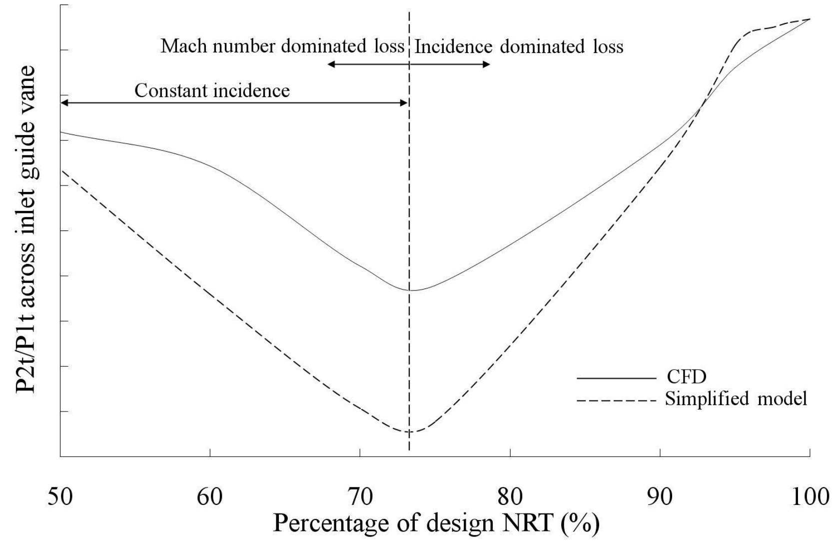

Figure 7.9: *Inlet guide vane pressure loss - Simplified and CFD derived losses*

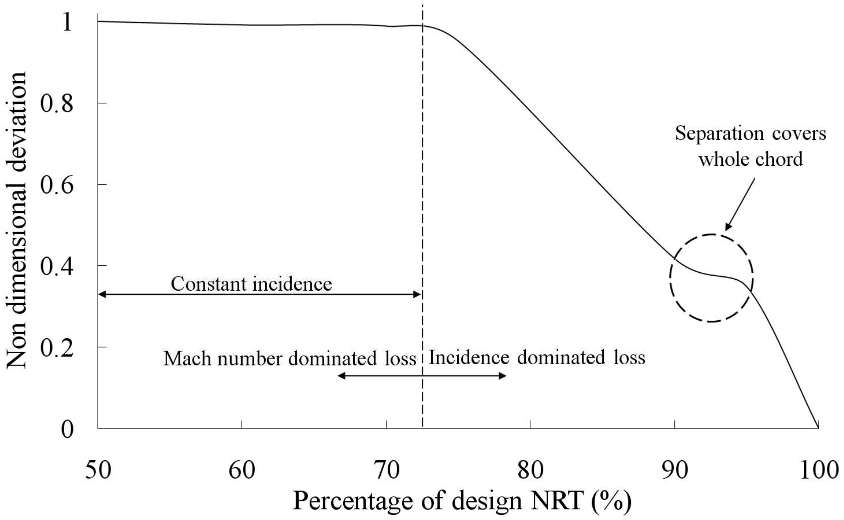

Figure 7.10: *Flow deviation at the trailing edge of the inlet guide vane versus rotational speed*

In the second set of simulations, three different positions of the IGV (open, intermediate and closed) for a range of different mass flows and incidence angles have been investigated. The aim is the provision of a grid of cases towards the extrapolation of the results for a greater applicability of the model to other compressors and flow conditions. With this objective in mind, plots for the pressure loss coefficient and the deviation angle for a fixed inlet Mach number and for a fixed incidence angle have been derived and are grouped in figures 7.12a to 7.14b. Several conclusions can be drawn from these plots:

- Losses across the IGV can be more than 30 times greater for the closed position of the IGV than for the open position at design conditions.
- Results corroborate the fact that most of the loss models experience a rapid pressure loss coefficient rise for incidences higher than 5° degrees.

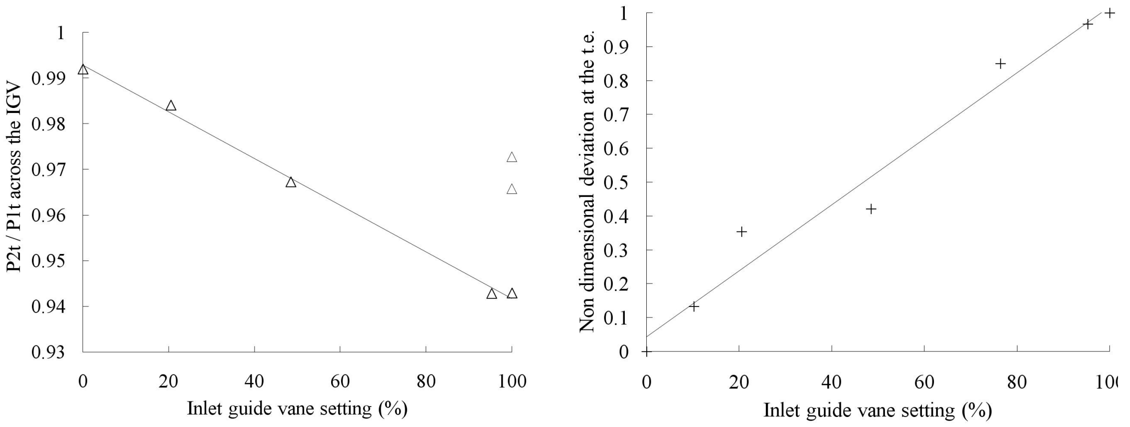

(a) *Pressure loss* **(b)** *Deviation at the trailing edge*

Figure 7.11: *Inlet guide vane pressure loss and deviation versus flow incidence*

- For a given incidence, losses rise as the stagger is increased because of the narrowing of the flow passage. For example, at an incidence angle of 0° and taking as a reference the losses for the open setting of the IGV, pressure loss is twofold the design value for the intermediate setting and almost threefold for the closed.

- As expected, pressure loss decays as Mach number rises at a rate that is greater for more closed settings of the IGV.

- Deviation also rises as the IGV is closed and falls with Mach number due to the straightening effect caused by greater air flows through the vane passage.

Assuming that to a first order, for a given geometry (same chord length, solidity, span, etc.), the loss and deviation depend only on the incidence angle and the inlet Mach number, any desired values for flow and deviation can be obtained by linear interpolation on figures 7.12a and 7.14a. To account for the effect of Mach number the pressure loss value is then corrected by interpolating in figures 7.13 and 7.14b. In this fashion the CFD simulations have been implemented in the form of several tables into VU59 for their validation of the results against compressor rig data.

7.3.4 Stalling incidence correlations

The constants A, B and C in equation 7.2 and shown in figure 7.3a date back to 1966 [148] and hence are not representative of the state of the art of modern axial compressors. By fitting more recent experimental data available to the research from the industrial sponsor it was found that a reduction in stalling incidence of 5% throughout the whole compressor operating envelope provided an adequate prediction of the stalling point.

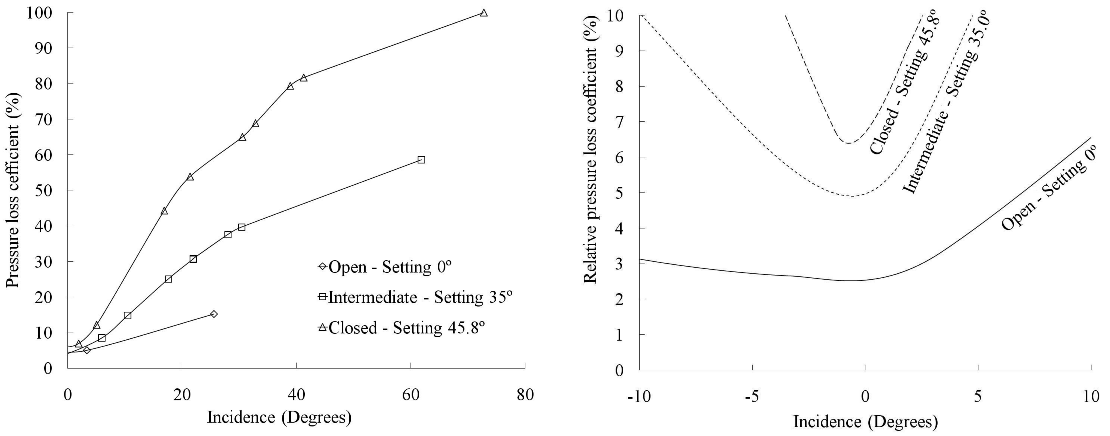

(a) *Complete range* **(b)** *Detail*

Figure 7.12: *Relative total pressure coefficient across the inlet guide vane for three angle settings as a function of incidence*

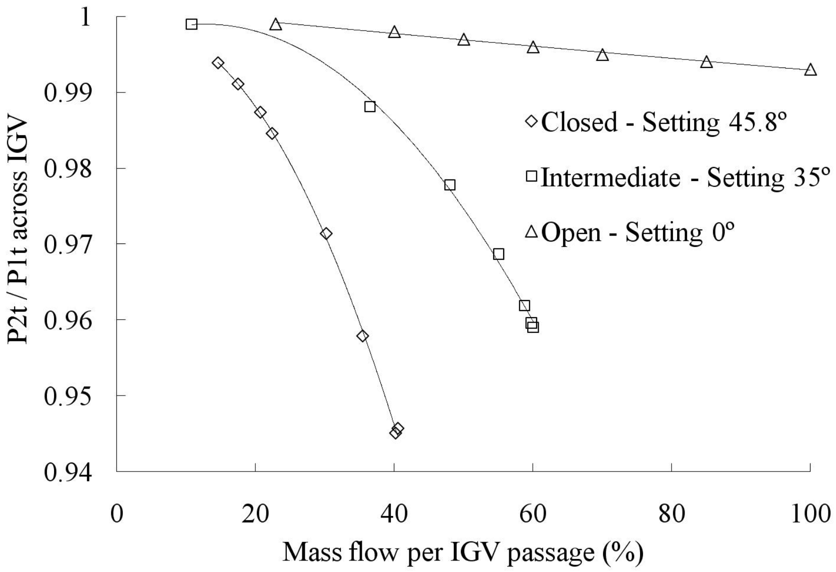

Figure 7.13: *Total pressure versus flow for a range of setting angles of the inlet guide vanes as a function of the mass flow through the passage*

7.3.5 Validation of the results

VU59's original loss and stall models were replaced by CFD derived correlations for loss, flow deviation and stalling incidence. Results for compressors A and B show a good agreement of predicted capacity with experimental data not only at low speeds but throughout the whole operating envelope of the machines (figs. 7.15 and 7.16). The predicted efficiency is in line with the test efficiency over the running range of the compressor for both machines. Overall, the gain in accuracy is very significant at low speed.

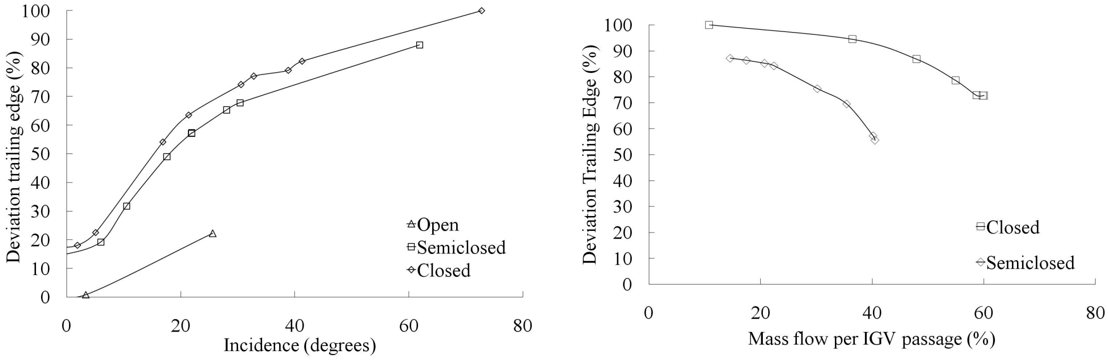

(a) *versus incidence* **(b)** *versus mass flow through the passage*

Figure 7.14: *Flow deviation at the trailing edge of the IGV as a function of incidence and mass flow*

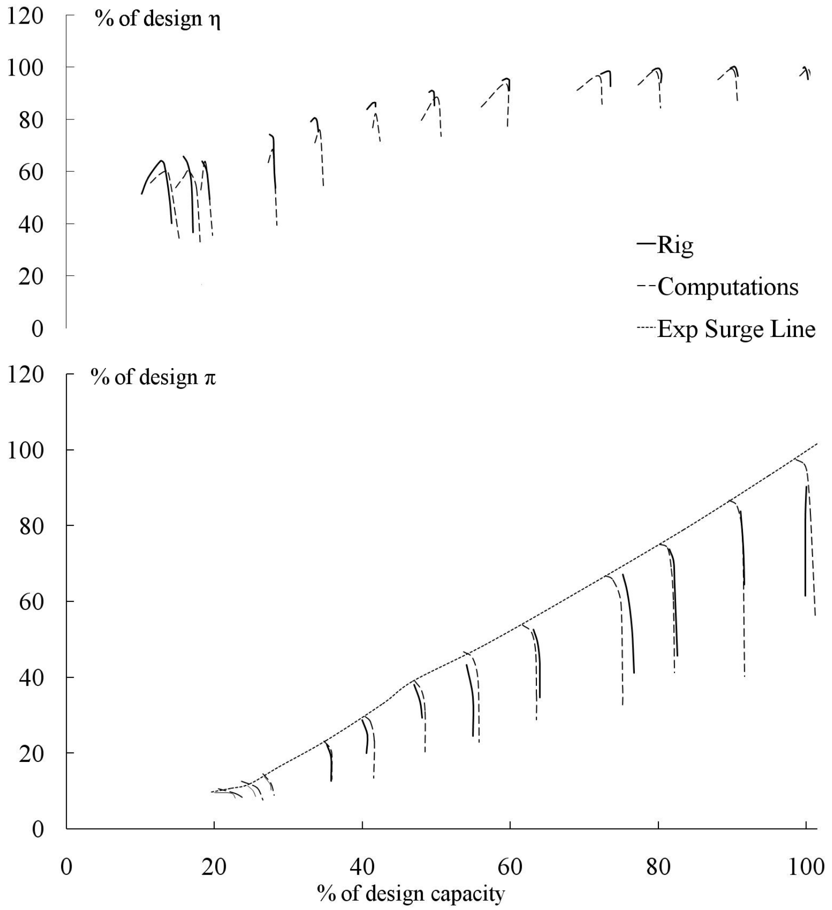

Figure 7.15: *IGV loss, stall and deviation model - Results for axial compressor A*

7.4 Malscheduled variable geometry compressor maps

During a shaft failure event the actuator of the variable geometry is not fast enough to follow the rapid changes of flow conditions and the variable geometry setting is not commensurate with the speed of the shaft. It is necessary to cater for this in engine performance models by calculating

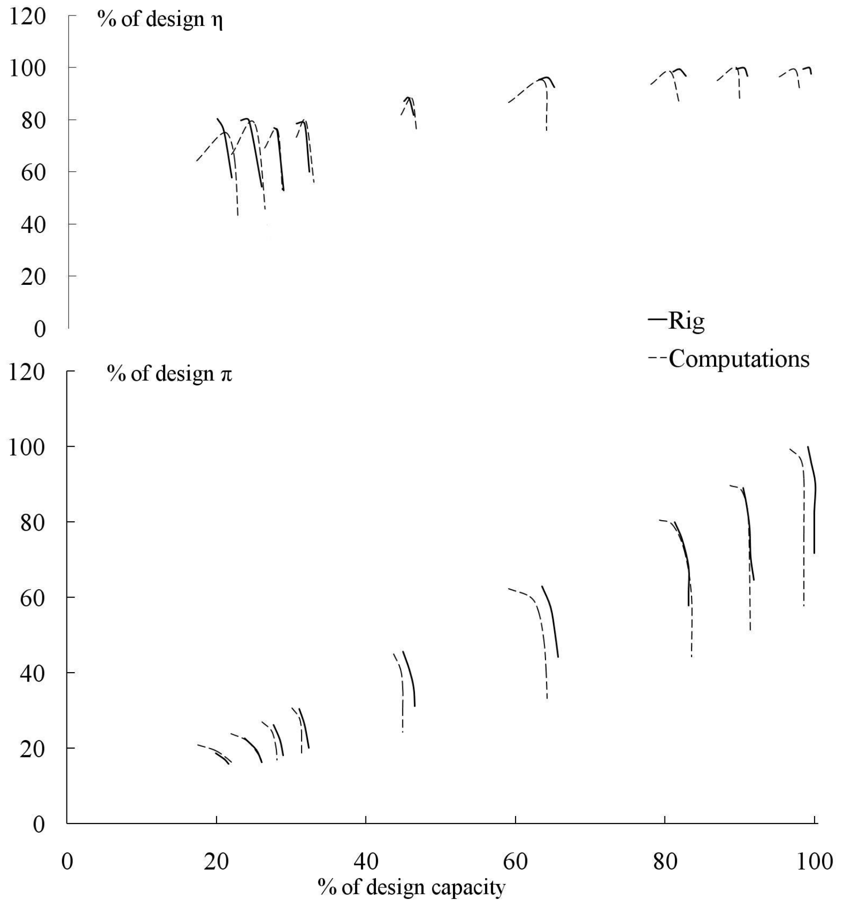

Figure 7.16: *IGV loss, stall and deviation model - Results for axial compressor B*

maps for any combination of the variable geometry setting and spool speed. This maps can also be used to simulate a failure of the actuating mechanism in which the variable geometry was stuck in given position for any shaft speed. To this purpose VU59 is an inexpensive and quick tool to provide such maps for any generic axial compressor.

An example of a set of malscheduled compressor maps is attached in appendix 7B, for the open, closed and intermediate setting of the variable geometry. As expected, the open position of the variable geometry causes a marked drop in surge margin and flow efficiency at part load. If the actuator fails to the closed position the flow capacity of the compressor is sternly reduced - 50% of the design capacity at the design aerodynamic speed.

7.5 Concluding remarks and recommendations for future work

A complete performance model to simulate the progression of a shaft failure event requires the provision of compressor maps for any possible malscheduled combination of shaft speed and variable geometry setting. An appropriate methodology to generate such compressor maps is to use a compressor off-design mean line performance code provided by the industrial sponsor. However, the treatment given by such tool to the pressure loss, deviation and stalling incidence of the flow across the inlet guide vane was found inaccurate and needed to be revisited.

The aim of this chapter is to report on the work carried out to improve the loss, deviation and stall models of the flow across an inlet guide vane in order to enhance the modelling capability of the compressor performance prediction program. Three-dimensional CFD simulations are used to derive correlations throughout the running range where the standard Lieblein-based loss models are no longer of any use. The validity of the correlations is proven by comparing against experimental data obtained from two modern high by pass ratio engine compressors.

Although the simulations have explored the effect of the main flow properties affecting the flow losses - namely incidence and mass flow -, the correlations derived from CFD are geometry dependent, and further analysis is required to extend the applicability of the model to include the effect of the vane cascade geometry.

The compressor maps calculated with the CFD derived correlations are adequate from a whole engine transient performance model viewpoint. The thorough study of compressor loss models and their extension into a truly generic model based on first principles, in a fashion similar to Lieblein's model, is out of the scope of this research. Significantly more work is needed to develop such a model; however, the results and data obtained from the CFD simulations constitute an outstanding starting point onto which further work towards a more general and upgraded loss and deviation model can be conducted.

Appendix 7A - A theoretical deviation of IGV loss

Consider the inlet guide vane as being a simply flat plate set at an angle to the axial inflow and producing an exit flow at an angle α to the axial diretion. in and a control volume similar to 6.25. The application of the continuity (eq. 6.28) and momentum equations (eq. 6.22) to such control volume under the usual assumptions of inviscid and steady state flow without mass forces in the blade direction yield:

$$v_1 = v_2 cos\alpha \tag{7.4}$$

$$p_1 scos\alpha + \rho_1 s v_1^2 cos\alpha = F_d + p_2 scos\alpha + \rho_2 s v_2^2 cos\alpha \tag{7.5}$$

where F_d denotes the drag force imposed by the blade surface boundary layers, in effect the profile loss. Dividing through by $scos\alpha$ and introducing the total pressure in incompressible flow $p_t = p + 1/2\rho v^2$ the momentum equation gives

$$p_{1t} - p_{2t} = \frac{F_d}{scos\alpha} + \frac{1}{2}\rho_2 v_2^2 - \frac{1}{2}\rho_1 v_1^2 \tag{7.6}$$

Divinding by the outlet dynamic head, substituting 7.4 into 7.6 and considering no profile loss ($F_d = 0$) the pressure loss is then

$$\frac{p_{1t} - p_{2t}}{\frac{1}{2}\rho v_2^2} = sin^2\alpha \tag{7.7}$$

Appendix 7B - Malscheduled compressor maps

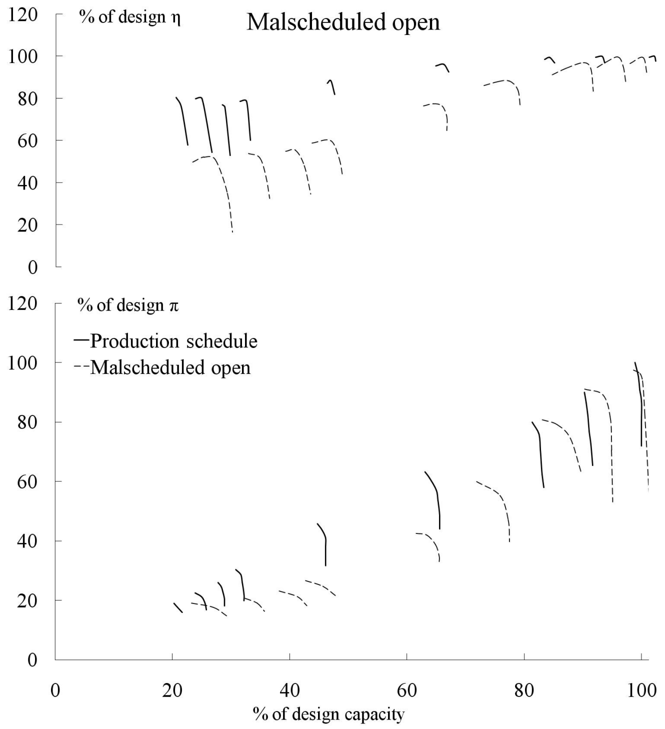

Figure 7.17: *Compressor map for variable geometry malscheduled in the open position*

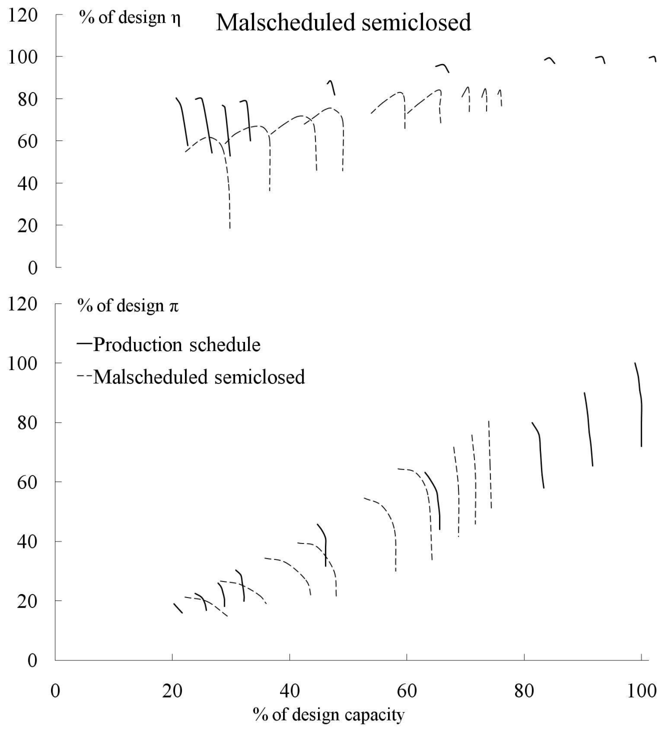

Figure 7.18: *Compressor map for variable geometry malscheduled in the semiclosed position*

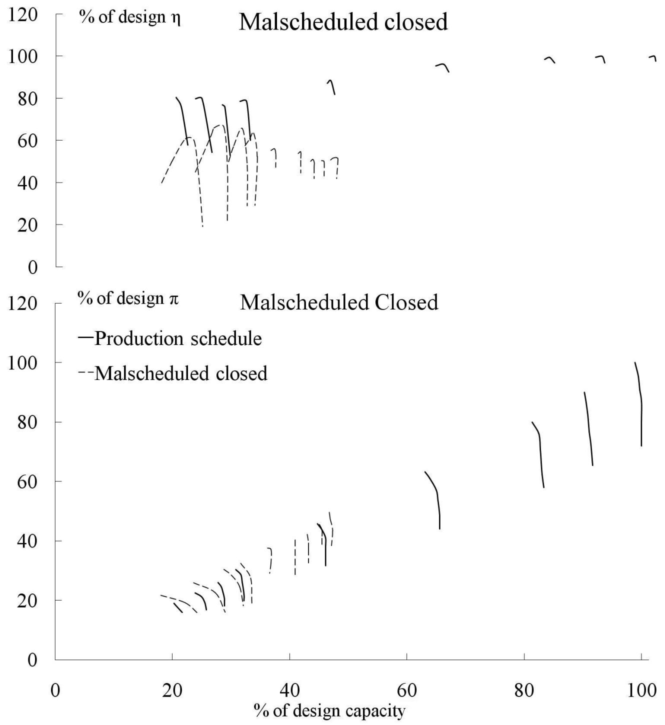

Figure 7.19: *Compressor map for variable geometry malscheduled in the closed position*

Chapter 8

Whole engine modelling

8.1 Introduction

The previous chapters (4 to 7) render the work carried out to model the performance of the different engine components and systems during a shaft over-speed event. These included the extension of component maps at far off-design conditions and for malscheduled settings of the variable geometry and methodologies to predict the rapid transient behaviour of the secondary air system. Once all these elements are in place, the research must continue with the vertical integration of the models and maps into a whole engine model to predict the transient performance of the engine during the event, and eventually ascertain the terminal speed of the over-speeding turbine disc.

This chapter covers the initial steps taken towards the integration of the component models into an “all in one” tool to model the over-speed. The chapter starts with the description of the current strategies that are employed to simulate the shaft over-speed event. The research continues with the appraisal of the previous modelling work available in the literature, and the lessons that can be learnt from such work. The chapter then elaborates on the preliminary work carried out to investigate the suitability an engine transient performance model available from the industrial sponsor to serve as a baseline onto which the extended component maps and models can be integrated. The chapter ends with recommendation to take the research forward and complete the integration of the models into a single tool.

8.2 Current modelling strategies

Modelling a shaft over-speed that has been triggered by a control system or fuel system failure is radically different from the modelling of shaft breakages. This is so because in the former cases the engine does not surge immediately after the failure, the over-speed is not so abrupt and the engine remains matched throughout the event.

8.2.1 Shaft failure events

Present strategies to model a shaft failure event need to distinguish between an unstalled and a stalled compression system (see section 1.7.2). This arises from the inadequacy of current whole engine performance models to capture the compressor surge and recovery sequence adequately and account for all the heavily interrelated phenomena relevant to a surge event. In a very loose sense it can be considered that clean located failures are less likely to surge immediately after the failure because of the lack of compressor imbalance and the mild vibration exerted on the engine by the failure.

Whole synthesis performance programs are appropriate to model the event if there is no surge. They can also be employed to determine the instant after the failure when the compression system runs out of stability margin and surges because of the mismatch between spool speeds or to assess if surge recovery is thermodynamically possible after the initial vibrations have faded away. These programs are also particularly suited to model low pressure shaft failures in a relatively simple manner by imposing the fuel flow dependency with time into the model.

Free running turbine models [39] are appropriate if the engine surges and runs down locked in stall. These models require the prescription of the stalled compressor characteristics and the compressor delivery pressure and temperature schedules during the event as the main input items. In most cases such profile is not accurately known and the pressure is assumed to decay exponentially from its value at the onset of the surge sequence. However, these models are not capable of providing a reliable answer if the compression system recovers or does not surge in the first place.

8.2.2 Control and fuel system failures

Control failures that lead to an over-speed event are relatively easy to model because the engine remains matched throughout the event. However, standard engine performance maps generally do not suffice because the shaft speeds are in excess of the range of speeds at which engine components are tested in experimental rigs. Care needs to be taken when extrapolating experimental component characteristics and it is essential to estimate the order of magnitude of the error made when doing so. The methodologies discussed in the previous chapters provide means of producing such extended maps and constitute a noteworthy enhancement to the modelling capability of this type of failures.

8.3 Previous work on shaft failure modelling

When the current research started in 2007, there was not one study in the literature that dealt with the prediction of the engine performance after a shaft failure. In 2009 a conference paper was presented in Florida at the annual ASME Turbo Expo conference by Matthias Haake in which a simple performance model was employed to estimate the terminal speed of the turbine of a two shaft turbofan after a shaft breakage [72]. Although useful from a qualitative point of view, the model involves a considerable amount of uncertainty: the crude estimates used to model some of the phenomena involved in the event, the large empiricism associated with a number of parameters of the model and the fact that some engine component models were not thoroughly validated raise important questions about its reliability.

In essence the approach used by Haake is based on the substitution of the compressor brick of a standard performance modular program by a one-dimensional stage by stage finite difference scheme algorithm. The model relies on the extended compressor characteristic to calculate the pre and post stall performance of the compressor. The post stall behaviour of the engine is calculated by artificially imposing an exponential decay law on the axial force on the blade. This equation is forced to adhere to experimental results by varying a time constant that is empirical and depends on the compressor being considered. This is a bodge that makes the model particular to a given compressor design and prevents its application to other machines. The model also accounts for blade tangling effects by assuming that the energy dissipated as friction from the contact is proportional to the forces acting on the disc and proportional to a friction coefficient.

Other major simplifications and limitations of the model include:

- The compressor performance in reverse flow and stall is highly three-dimensional; it is not two-dimensional and certainly not one-dimensional, and hence one-dimensional models cannot capture this effect. The three dimensional character of the flow field across compressor stages in reverse flow has been discussed in chapter 6
- The model uses the turbine exit capacity derived from a standard turbine map as a boundary condition for the calculations. As discussed in chapter 4, the velocity triangles downstream of an over-speeding turbine rotor are highly distorted and the flow incidence on the following row of nozzle guide vanes affects significantly the capacity of the downstream turbine. The capacity of the downstream turbine is therefore a function of the speed of the over-speeding turbine.
- The model scales the reverse flow compressor characteristics obtained by Gamache from a constant annulus three stage compressor to derive the extended characteristic of a ten stage variable annulus compressor. This is an estimate that is likely to introduce significant uncertainty on the results.
- The performance of the internal air system is not considered in the calculations. Haake's model considers the axial load on the turbine disc to depend only on the pressure exerted on the turbine blades. However, the pressure inside the cavities of the air system is of the same order as the pressures in the main gas path and hence the total axial force on the disc can be radically different to that predicted by Haake's model.
- After the failure, the turbine disc can bounce back after the initial impact, re-open the rim rear gap of the turbine and equalise the pressures in the gas path and the cavities of the air system, altering dramatically the axial load on the turbine disc. This needs to be accounted for in the model by coupling the performance of the air system with a model of the mechanical interaction of the contact between turbine structures. (see section 5.10)
- It will be later demonstrated in this chapter that the combustor performance is paramount to determine the behaviour of the whole engine performance. The relationship between the compressor operation (whether it flames out or remains lit during the event) and whether the engine recovers from surge or locks into stall is complex, and hence it needs to be investigated and accounted for.

8.4 Preliminary whole engine model integration studies

Once models and extended maps for the different engine components are in place the next step in the research is the integration of the component data into a single transient performance model. The industrial sponsor suggested evaluating the suitability of a proprietary pre and post stall engine performance model (BX04) programmed in RRAP to serve as an adequate baseline to capture all the interrelated phenomena that occurs during an over-speed. Particularly important was to investigate whether the model would predict the stall and recovery patterns that can be observed in modern three shaft engines, since there was the suspicion that the program was tailored to fit the particular behaviour of the engine it was developed for.

8.4.1 Rolls Royce Aerothermal Performance suite

The Rolls Royce Aerothermal Performance (RRAP) code is a Fortran computational platform developed to carry out design point, off-design and transient performance calculations of gas turbine engines. The program allows the user to build any desired engine architecture by stacking up different modules that can be called from an engine main routine. Some modules correspond to the engine components and others account for various phenomena such as bleeds, heat input or duct losses. The interface between modules is accomplished by means of vectors that contain the thermodynamic properties of the flow at the engine stations.

The calculations for each operating point or each time step in transient simulations are carried out by guessing some variables that are required to read component maps such as shaft speeds or compressor lines. The calculations then proceed sequentially to solve the flow from the intake back to the nozzle. Some of the flow properties and magnitudes derived from the calculations need to satisfy certain compatibility equations (work balance on the shafts, mass flow continuity, prescribed engine handle,...). These magnitudes are called “Matching Quantities”. A Newton Rhapson scheme varies the guessed variables until the matching quantities are within a prescribed threshold. Figure 8.1 shows an example of a RRAP performance model of a two shaft turbofan that is run to a target value of the engine thrust, F_N. Seven guessed variables (inner and outer fan and compressor velocities and lines and fuel flow) are changed until seven matching variables (flow capacities at different stations, nozzle areas and the prescribed engine thrust) are all converged to a given value.

Engine routines are compiled and built into executable files that can simulate the performance of any engine with the same arrangement. This is possible because the engine component modules solve generic equations that are not geometry dependent to calculate the flow at their outlet. Component characteristics particular to a given geometry are provided to the model in the form of graphical correlations and parameters obtained chiefly in component rigs.

8.4.2 BX04 - Single shaft transient performance engine model

BX04 is a single shaft engine transient model developed by Nicholas Merriman at Cranfield University in 1994 supported by the Rolls-Royce defence aerospace group in Bristol. His PhD

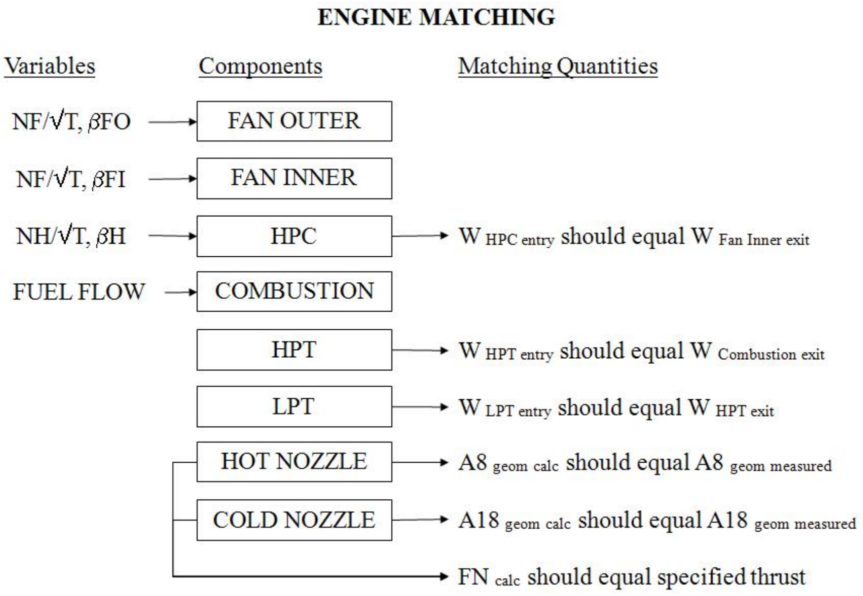

Figure 8.1: *Example of possible engine matching for a two shaft turbofan model*

thesis is a pioneering attempt to provide the Rolls-Royce Aerothermal Performance suite (RRAP) with pre and post stall modelling capability.

Merriman replaced RRAP's standard compressor and combustor modules to allow for the flow to discharge from the combustion chamber through the compressor. In addition to this substitution of modules, the engine routine was modified by inserting intercomponent volumes and heat transfer modules between engine components that are able to account for high frequency flow disturbances. By doing so it is assumed that the transient performance of the engine can be assimilated to its instantaneous steady state performance. Details of the high frequency mass packing method are confidential and cannot be discussed here.

BX04 relies heavily on the experimental pre and post stall data collected by Alex Wilson and Christopher Freeman [190][191] in a set of experiments carried out on a Viper engine. Surge recovery lines were also measured in the experiments and were also used by Merriman in his model. The compressor reverse flow characteristics were scaled from Greitzer's reverse flow compressor that has already been discussed in chapter 6. The unstable compressor characteristics are obtained by interpolation with a cubic polynomial technique between the recovery and reverse flow characteristics (fig. 8.2).

8.4.2.1 Compressor recoverability after surge

The capability of gas turbine engines to recover from surge is related to geometrical and aerothermal features. Edward Greitzer [70] ideated a flow parameter that linked such features with the stability

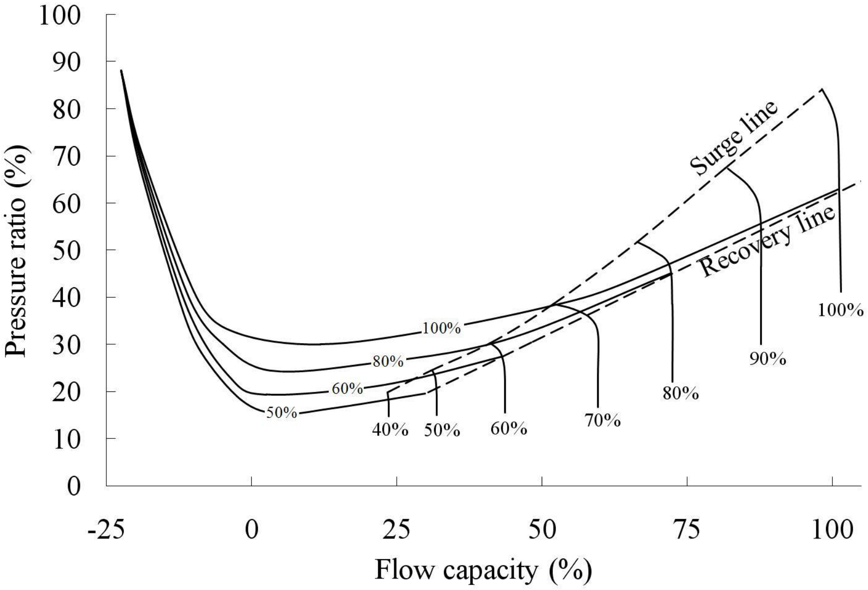

Figure 8.2: *Extended Viper compressor map. Adapted from [124]*

behaviour of the compressor:

$$B = \frac{U}{2a}\sqrt{\frac{V_p}{A_c L_c}} \tag{8.1}$$

where U is the compressor blade speed, V_p is the plenum volume, A_c is the compressor duct flow area and L_c is the total length of compressor and ducts. Greitzer concluded [71] that low values of B lead to rotating stall while big values of surge lead to surge. In current large turbofan engines, stall is the typical outcome at low powers and surge followed by recovery is typical at high powers (fig. 8.3). At conditions close to maximum take-off the engine is likely to surge and flame out. The recovery and relight sequence varies between events since ignition plugs are energised only at given time intervals. Since p_{30t} it is the most important parameter to determine the driving force of the over-speeding turbine it is paramount that a whole engine shaft failure model captures this behaviour accurately.

8.4.2.2 Original results

The original model considers that the combustor flames out when the FAR is greater than 0.037, and relights automatically if the mass flow through the compressor exceeds a given value. Moreover, after the compressor stalls the combustion efficiency is assumed to decay exponentially following a law that is calibrated with an artificial coefficient. One of the outcomes of this chapter is the finding that these are purely bodges that lack of physical meaning and cannot be extrapolated to other scenarios.

Surge is induced in the model by introducing a rapid ambient temperature sinusoidal blip (temperature rise of 50K). Results show that the engine only recovers from stall at mid-high powers if the combustor flames out only for a brief period (6-10ms) and immediate relight follows

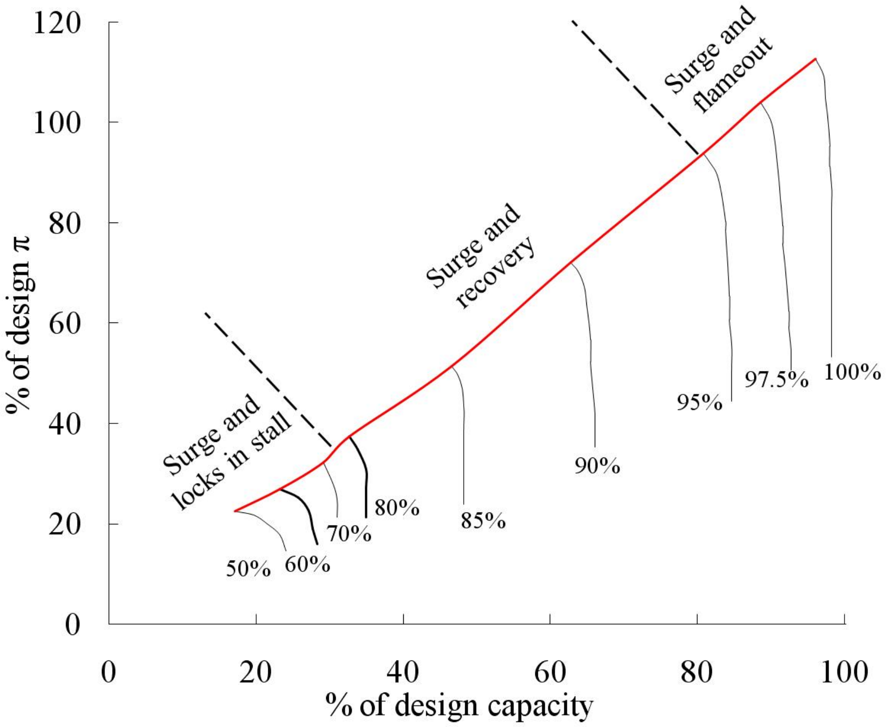

Figure 8.3: *Progression of the Viper surge event as a function of the power setting*

(fig. 8.4). If the combustor is forced to stay alight even beyond the stoichiometric FAR the engine locks in stall and is not able to recover (see 8.4).

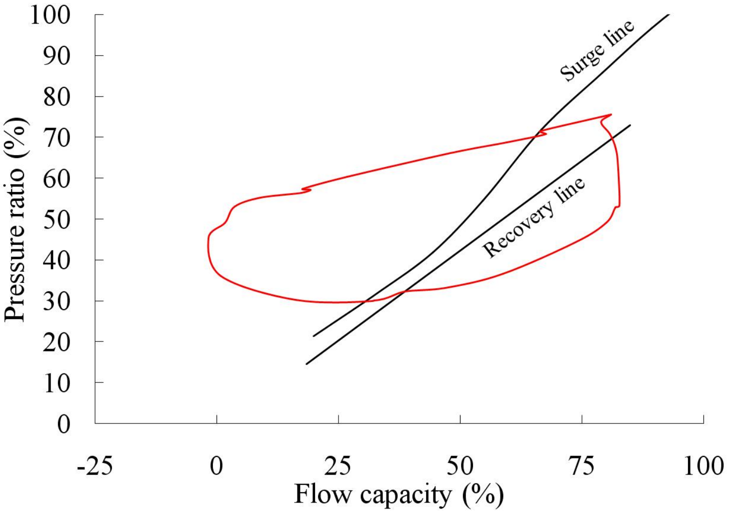

Figure 8.4: *Viper engine model at MTO conditions - Original BX04 model. Combustor switches off for FAR greater than 0.037*

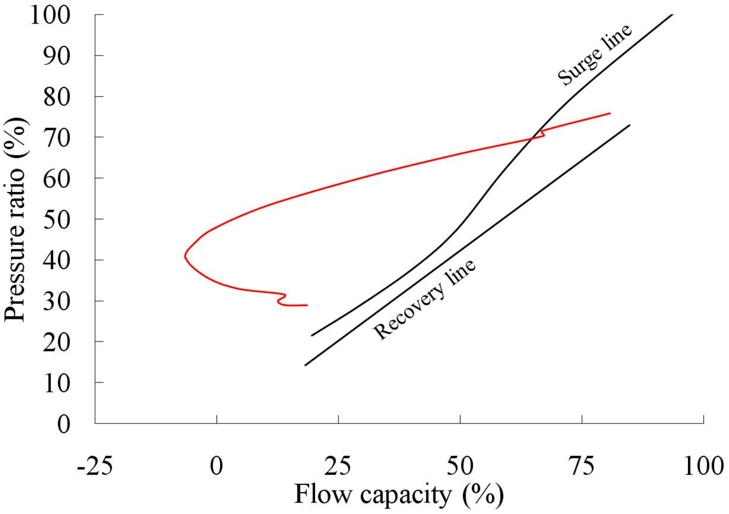

Figure 8.5: *Viper engine model at MTO conditions - Original BX04 model. Combustor remains lit during the event*

8.4.2.3 Model's sensitivity to mass packing volumes and the simulation time step

The sensitivity of the model to the size of the mass packing volume inserted between components was investigated by including an additional volume at the compressor outlet. As it could be expected, a larger mass packing volume stores more mass flow that is discharged through the intake during the blowdown (fig. 8.6a and 8.6b). However, large volumes hinder the ability of the gas dynamic equation set to capture high frequency flow disturbances, and the program is not able to converge to a solution.

The effect of the time step of the simulations is shown in figures 8.7a and 8.7b. A smaller time step allows a better coverage of the surge cycle that can be defined more accurately and changes the calculated cycle considerably.

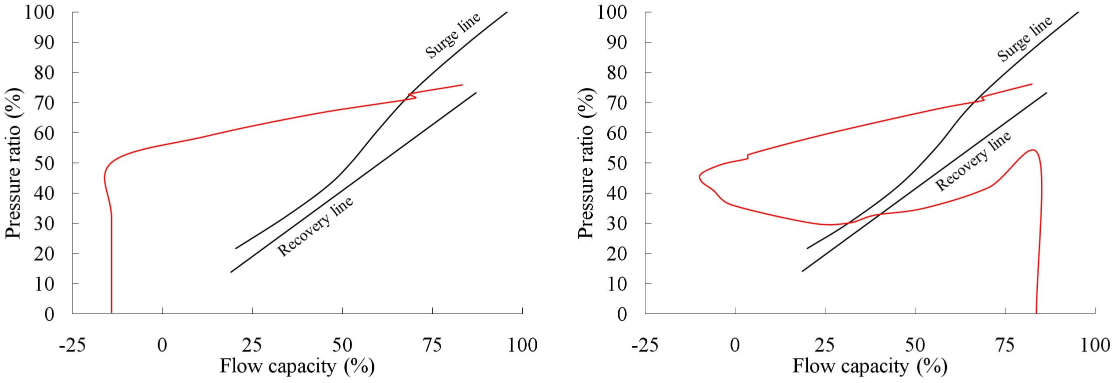

(a) *Volume 200%* **(b)** *Volume 70%*

Figure 8.6: *Viper engine model at MTO conditions - Effect of compressor mass packing volume with respect to the real compressor volume. Combustor remains lit during the event*

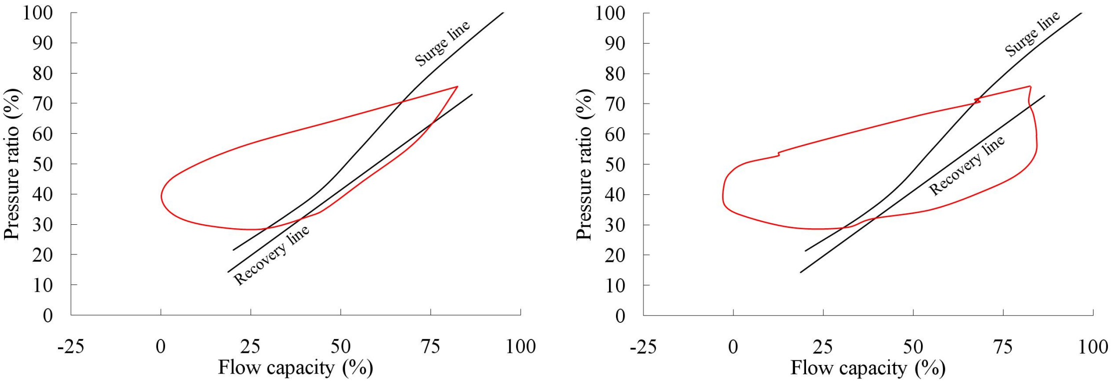

(a) *Time step 1ms* **(b)** *Time step 0.1ms*

Figure 8.7: *Viper engine model at MTO conditions - Effect of simulation time step. Combustor switches off for FAR greater than 0.037*

8.5 Concluding remarks and recommendations for future work

The component models and extended maps reported in the previous chapters are ready to be integrated in a whole engine transient performance program to simulate the progression of a shaft failure event. This chapter discusses some preliminary studies that have been carried out to investigate the suitability of a proprietary pre and post stall transient engine model (BX04) to capture the complex interrelated behaviour of the combustor and the compressor during the shaft failure.

It has been found that BX04 uses some strong assumptions to fit the stalling behaviour exhibited by a single shaft turbojet that is used as a benchmark. Some of this assumptions - combustor flame out for fuel to air ratios greater that a given value, and instantaneous relight once the compressor capacity exceeds a certain value - are not representative of the behaviour of modern large turbofan engines. If the combustor remains lit during the event results from the model show that the compressor locks in stall and is unable to recover.

It is recommended that the research work continues with the critical appraisal of existing transient performance models to accurately predict the behaviour of the engine at pre and post stall conditions, and the assessment of their suitability to be integrated into a whole engine transient model to simulate the over-speed.

Chapter 9

Compressor variable geometry schedule optimisation

9.1 Background and research scope

The design of axial compressors is driven by the pursuit of maximum flow efficiency at design conditions whereas at part speed the requirement for adequate surge margins prevails. Unfortunately these are conflicting objectives since the stability aids that improve the surge margin impair the adiabatic efficiency of the machine. In particular, compressor variable geometry is employed to raise the surge line at part speed for the provision of an adequate surge margin at the expense of increased pressure losses. The variable geometry schedule is typically obtained from expensive and time consuming rig tests that go through a vast combination of possible settings on a trial and error basis. Moreover, extensive testing is also undertaken to assess the relative impact of variable vane settings on overall surge margin, adiabatic efficiency and flow capacity.

The objective of this research is to develop a methodology based on stochastic optimisation methods - a genetic algorithm to be precise - coupled with a compressor off-design performance prediction code (VU59) to obtain the most flow efficient variable geometry schedule of an axial compressor while keeping a user defined value of the surge margin throughout the whole operating envelope of the machine. The final tool has shown its potential as a quick, effective and inexpensive approach to obtain such schedule, saving time and rig resources.

However, it is important to be aware of the fact that the optimiser produces only single point solutions and does not provide much information about the shape of the merit function; it may well be that small changes of the schedule around the optimised point or noise into the system cause a marked drop in the efficiency if gradients of the merit function are steep. Hence, for the sake of design robustness, the optimisation methodology is completed with a thorough investigation of the impact of small changes of the variable geometry schedule around the datum not only on flow capacity, isentropic efficiency and surge margin of the compressor in isolation but also on the spool speed and hence on the performance of its driving turbine.

9.2 Compressor variable geometry fundamentals

It is a known fact that at part speed the reduction in the axial velocity of the flow through an axial compressor overcomes the reduction in the spool speed and so pushes the early stages towards surge. There are a few methods available to the designer to alleviate this undesired part speed compressor behaviour, usually known as “part speed crutches”, that include multi spooling, handling bleeds and variable geometry stator blade rows as the most common. In particular, handling bleeds achieve an increased mass flow through the early stages of the compressor - for an increased axial velocity and therefore a reduced incidence angle - by dumping overboard at a mid stage the excess of flow that would choke the rear stages otherwise. On the other hand, variable IGVs and VSVs redirect the air towards their respective downstream rotors so that the incidence angle to those rotors is kept well within an acceptable range away from the stalling incidence (fig. 9.1). It is generally accepted that a variable geometry stator row is required for each additional stage beyond 5 [185].

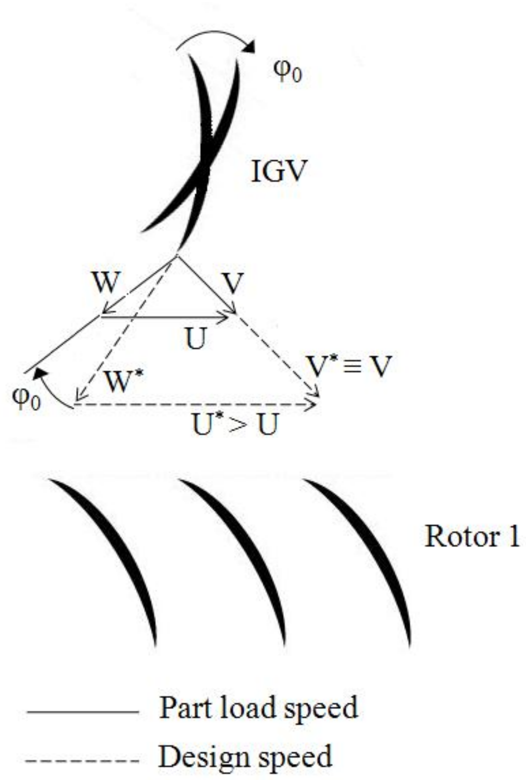

Figure 9.1: *Variable geometry operation fundamentals*

The effect attained with variable geometry or bleeds is however different (fig. 9.2); whereas the air bleed promotes a lower working line thanks to the additional turbine work required to compress the air bled overboard, by skewing the compressor variable blade rows the surge line is drastically raised at the expense of increased pressure losses across the variable vanes. Consequently, to supply the same mass flow and pressure for a closed variable geometry setting, the compressor must rematch itself and its speed must rise to compensate the drop in work across the variable stages, or conversely, for a constant speed, the closure of early stage variable geometry vanes push the speed lines to lower mass flows. On the other hand, at high spool speeds the impact of the variable geometry is subtler since stall is controlled by the rear stages and early stages migrate towards choke. At those conditions, by further opening the variable vanes, the blade passage sectional area is increased and the compressor is able to swallow a larger mass flow; that is, increases its capacity. If the VSVs settings are rescheduled in such manner, the compressor is said to be upflowed. Variable geometry also plays an important role in transient operation of the engine: the schedule may be reset during accelerations and decelerations to provide additional surge margin and counteract the pernicious effect of heat soakage until the engine stabilises again.

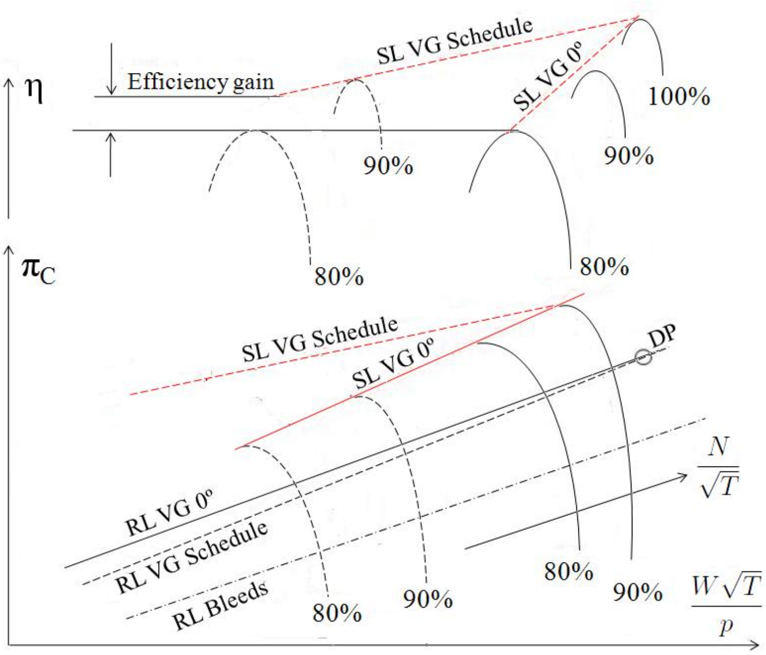

Figure 9.2: *Effect on bleeds and variable geometry on the compressor map*

To a first order, the position of the working line on the compressor map is considered unaffected by any re-stagger of the blade rows, although strictly speaking it is a function of the compressor efficiency that indeed varies with changes in the blade row stagger angle. Tipically, the improvement in compressor efficiency promoted at part speed will move the working line to lower pressure ratios pivoting around the design point on the map.

In power generation applications the low pressure spool must run at a speed synchronised with the grid frequency, usually 50 or $60Hz$. The variable vanes and the bleed valves are operated jointly to accommodate changes in power demand; in other words, at the same firing temperature and spool speed the attainable pressure ratio and mass flow are modulated to meet the load requirements. In aero applications on the other hand, variable blade rows are optimised for flow efficiency at high speed, and for part-speed surge margin at low speeds. It is for this reason that the IGVs are generally devised as thin flat or little cambered profiles aligned with the flow - no swirl component is introduced in the oncoming flow - at nominal conditions for minimum pressure losses. To restrain the compressor from surge at off-design conditions the flat plates are skewed inasmuch as the incidence to the first rotor is acceptable at the cost of a remarkable rise in pressure loss that emerges as the flow breaks away from the plate.

9.2.1 Variable vanes schedule eduction

The IGV/VSVs and bleed valve settings are usually mapped into the engine control unit versus the aerodynamic speed of the compressor so that the compressor geometry and bleeds are univocally defined for a given spool speed[1]. During the engine design process the VIGVs and VSVs are devised and optimised for design point operation following the usual rules and numerical procedures. Conversely at off-design conditions, the settings that make up the IGV/VSV schedule are usually obtained from rig tests in which a large number of possible combinations of the variable stator settings is tested and compared. This trial and error process is carried out for the whole operating envelope of the compressor and, although effective, it is also lengthy and expensive. The aim of this work is to engineer a computational tool able to deliver the most flow efficient IGV/VSV schedule that conforms to a user prescribed minimum surge margin. In so doing, not only the required experimental trials could be shortened and made cost effective but the rig resources could be employed in other tasks as well.

During the tests the variable stator rows are moved independently from each other by means of separate mechanical actuators that permit the blades to be restaggered at the controller's will. Nevertheless, for simplicity, weight and cost reasons production engines are equipped with a single mechanical actuator that is connected to the unison rings and the rings in turn with each variable row by a lever (fig. 9.3). Therefore, the movement of the VSVs rows obeys a fixed proportionality that is a function of certain geometrical parameters of the gearing mechanism (fig.9.4). The proportionality constant can be changed to fit a determined optimised schedule - in fact to obtain such constant is the object of the aforementioned rig trials - but once fixed it constrains the movement of the stator rows; i.e. for a given turn of the VSV_1, φ_1, the VSV_2 is forced to rotate an angle φ_2, equal to λ times φ_1. It is clear that a non linear response of the system is desirable from an aerodynamic point of view, but such benefits are offset by the mechanical simplicity of a single actuator system. As an example, figure (fig. 9.5) shows the datum schedule for the three variable rows of the eight stage axial compressor employed in the current study.

The optimisation of the variable geometry schedule of a compressor in isolation provides spurious solutions. A point on the working line - defined by a determined value of the non dimensional mass flow and a given pressure ratio - can be achieved with different settings of the variable geometry rows. However, it is unlikely that for those different configurations the speed at which the compressor runs would be the same. Any change in spool speed will have an impact on the efficiency of its correspondent downstream turbine and although the compressor efficiency may be raised the turbine efficiency can plummet[2] and the overall performance of the engine can turn out to be impaired. It is for this reason that the variable geometry schedule of a compressor should be derived in conjuction with its associated turbine. However and to a first order, it is not unreasonable to assume that the characteristic is flat for most of the power range for modern turbines.

---

[1] This may be overrun for transient operation. Also, from a stability point of view, variable geometry would be better correlated against mass flow, but reliable and dependable measurements of engine mass flow are complicated to obtain.

[2] This is likely to happen at low power settings when the turbine is not choked for turbines whose stators choke.

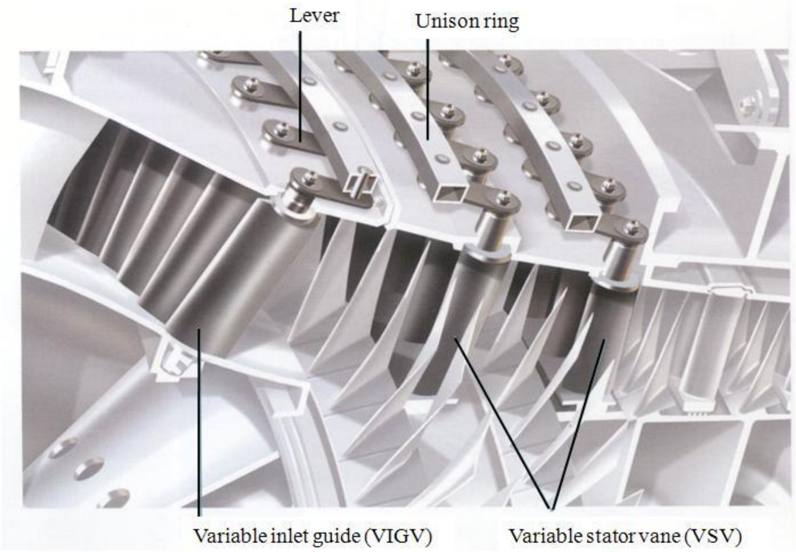

Figure 9.3: *Compressor variable geometry actuation mechanism. From* **??**

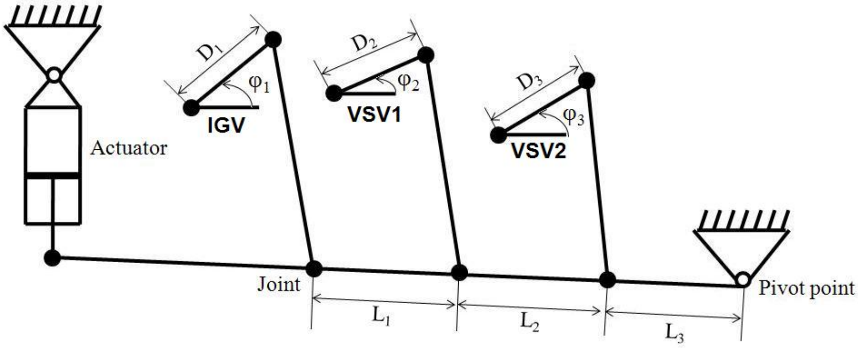

Figure 9.4: *Compressor variable geometry system schematics*

9.3 Genetic algorithm optimiser

9.3.1 General arrangement

A genetic algorithm (GA) based optimiser has been chosen to obtain the most flow efficient variable geometry schedule with user specified surge margin criteria. The choice of such method is dictated by the properties of the problem to be optimised. To be precise the algorithm handles three degrees of freedom (φ_0, φ_1 and φ_2), and this fact gives rise to multiple local optima for a myriad of angle combinations. Moreover, loss and stall models used to calculate compressor aerodynamics are generated from empirical data and are usually expressions that fit the mentioned data or in some cases losses are given in tabular form from which any operating point is found by interpolation. Furthermore, the prediction of the compressor performance is a highly constrained problem - e.g. De Haller number and Lieblein's equivalent diffusion factors are parameters that restrict the design space. The problem is therefore multimodal and highly constrained, and as such is suitably tackled with GAs, in contrast with classical gradient based numerical approaches like those undertaken by Dennis and Schnabel [42], Fletcher [52] and Rao [150] that perform better

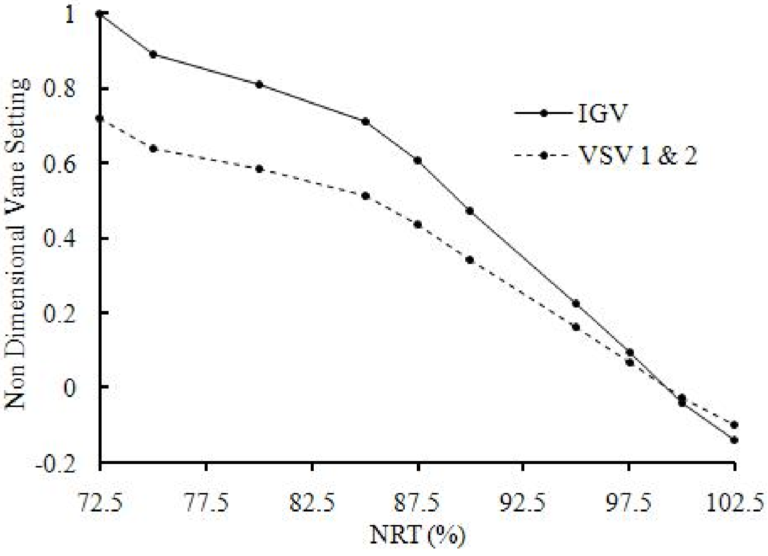

Figure 9.5: *Compressor variable geometry datum schedule*

for smooth functions where the shape of the objective function is known beforehand. On top of all, the problem is characterised by conflicting design options that make a trial and error approach tedious and ineffective. Particularly, surge margin is commonly enhanced by design decisions that impair the compressor efficiency. GAs have been successfully applied to virtually every aspect of the design of gas turbines: from models ideated for combustor design [45], to engine inlet design [54] or axial compressors aerodynamic design [91], engine components map generation techniques [27] and blade aerofoil design based on a parameterization of Beziers curves [64][134]. This type of optimiser has also been coupled with computational fluid dynamics techniques to narrow the design space and alleviate the time required to complete CFD based designs [50]. Wider scopes of application for the GA's include intercooled recuperated turbofan design [188] or even jet engine controller design [31].

In this work a genetic algorithm was developed from scratch. An "off the shelf" algorithm was not used because its possible inclusion in future Rolls-Royce performance codes would infringe copyright law. The code was programmed in Matlab and was coupled with a Fortran 1D mean line analysis code to predict the performance of the compressor. The interface between both codes is accomplished by means of txt data files. The GA generates the txt data files that encode the compressor geometry and characteristics required by the Fortran code as an input. In turn, the prediction code assesses the fitness of the rticular chromosome and generates a new txt data file that contains the predicted compressor performance to be read by the GA. The program structure is sketched in (9.6).

One of the results provided by the mean line analysis code is the mass flow that the compressor is passing at a given aerodynamic speed. By skewing the variable geometry of the compressor the aerodynamic speed at which a determined mass flow passes through the compressor changes. To a first order, for the engine to operate at given condition, it is the value of the air flow and pressure ratio that must be kept constant, rather than the aerodynamic speed of the compressor since this varies when the variable geometry of the compressor is skewed. Prior to the application to any genetic operator, this effect is accounted for in the algorithm by means of a loop that finds the

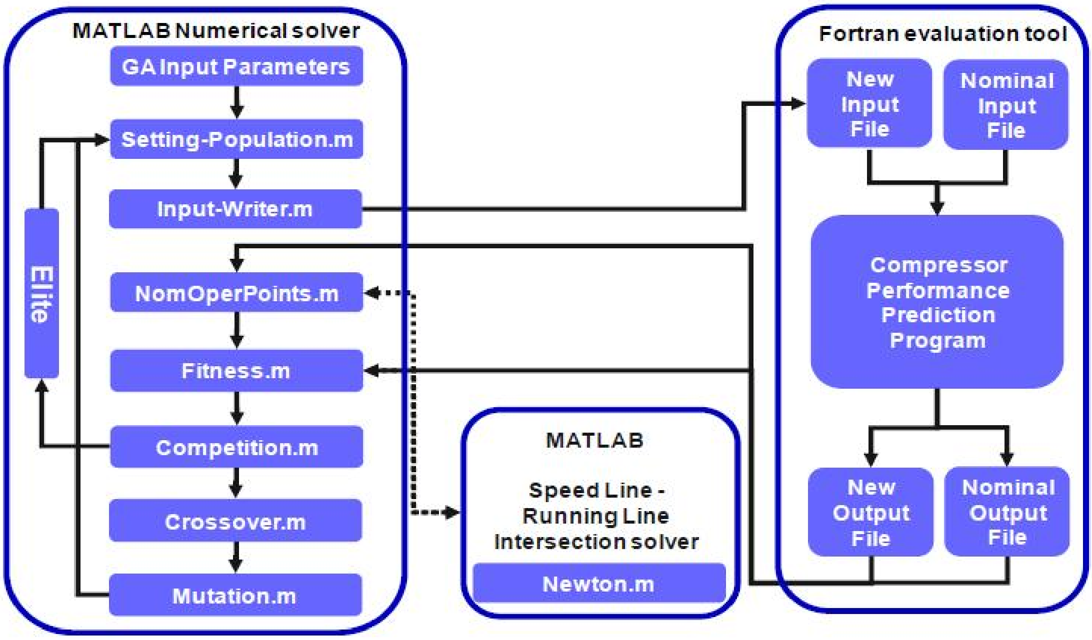

Figure 9.6: *Genetic algorithm structure*

spool speed at which the mass flow and pressure ratio are within an error of 10^{-3} of their datum values. (fig. 9.7).

9.3.2 Algorithm structure

The genetic algorithm had its breakthrough with the work undertaken by Holland [79] and Goldberg [68]and belongs to a group of heuristic optimisation techniques like the simulated annealing [94], the particle swarm optimisation [90] or the Tabu search [67]. The premise onto which the genetic algorithm is founded is to mimic the natural selection by which only the strongest individuals make it to survival while less fit individuals die away. The main advantage of the GA lies in its robustness and its ability to avoid getting trapped in local maxima once the algorithms parameters are tuned by means of a sensitivity analysis. This is guaranteed by the algorithm's mechanisms that produce diversity in the population, particularly the number of chromosomes per generation and the rate of mutation. Moreover, genetic algorithms surpass other design techniques like CFD in that the latter can be prohibitively time expensive.

The code operates by generating a random population of compressors where the IGVs/VSVs schedule is encoded into a string of zeros and ones so that it can be easily handled mathematically. The program then translates such strings to input files that are read by the prediction program to evaluate the performance of each individual of the population. The fitness subroutine assigns to every compressor a fitness value that corresponds in the simplest case to the adiabatic efficiency of such compressor. The proximity of the working line to the surge line can be accounted for in the calculations implicitly in the fitness function by penalising those solutions with a small surge margin or by rejecting any individuals that violate a given surge margin constraint. Once the fitness of every individual has been obtained they are subjected to the genetic operators. First the chromosomes are selected randomly in pairs and forced to compete so that the fittest of the two

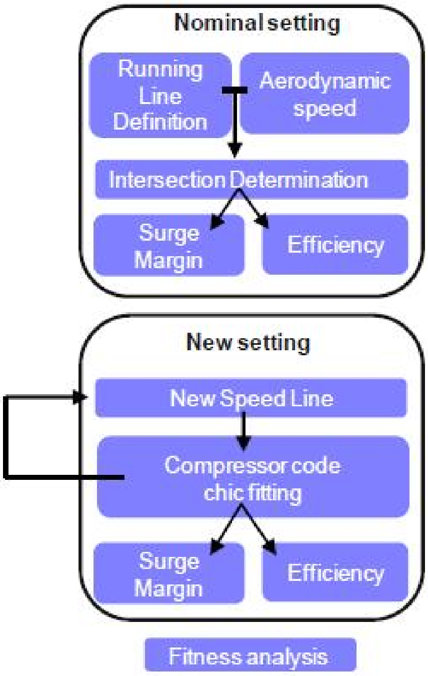

Figure 9.7: *Aerodynamic speed calculation loop*

replaces the less fit in the original population in what it is known as a “tournament selection”. The resultant individuals are randomly selected to mate and generate an offspring population. The children are generated by a so called multipoint crossover strategy in which each bit of the offspring is randomly chosen as the correspondent bit from either of the parents. Lastly, following natural genetics, the population is subjected to a degree of mutation that transmutes a prescribed percentage of bits in the population to its opposite value with the purpose of introducing diversity in the search space. In order to assure that the fittest individuals are not discarded from the population and hence accelerate the convergence of the code to the solution, after the competition the ensuing chromosomes with the highest fitness value are separated from the lot and set aside in an “elite” group that is exempted from undergoing any further transformation during that generation. To conclude the calculations the program runs mutation free for a number of generations in what is called a damping process to let the program converge to a solution. The algorithm stops when the average fitness of the population equals the fitness of the fittest individual; that is, when all the individuals in the population have become the fittest.

9.3.2.1 Validation - Benchmark functions

To investigate the capabilities of the algorithm to accurately predict the location of global maxima and assess the sensitivity of the code to the different algorithm control parameters the program has been subjected to trial by several benchmark functions with multiple local maxima, given by the following expressions (functions A to D):

$$z = 20\left[\frac{sin\sqrt{0.1+(x-4)^2+(y-4)^2}}{\sqrt{0.1+(x-4)^2+(y-4)^2}}\right] \quad for\ 0 \leq x \leq 20,\ 0 \leq y \leq 10 \tag{9.1}$$

$$z = 1 - [xsin(4x) + 1.1ysin(2y)] \quad for\ 0 \leq x \leq 20,\ 0 \leq y \leq 10 \tag{9.2}$$

$$z = 1 - [ysin(4x) + 1.1xsin(2y)] \quad for\ 0 \leq x \leq 20,\ 0 \leq y \leq 10 \tag{9.3}$$

$$z = \frac{\left[cos^2x - cos^2y\right]^2}{\sqrt{x^2+y^2}} \quad for\ 0 \leq x \leq 20,\ 0 \leq y \leq 10,\ xy > 0.75,\ x+y < 15 \tag{9.4}$$

The results provided by the code are grouped in table 9.1, and are found to agree closely with the maxima found analytically by the method of Lagrange multipliers. The runs are carried out for 100 chromosomes per generation, during 300 generations. The number of competitions per generation is 120 after which the resultant chromosomes are crossed 100 times. The mutation rate is 10%, 5 elements are kept within the elite and the algorithm ends with the damping generations required for the code to converge. The calculations are completed in 10 seconds.

Table 9.1: *Benchmark function optimiser results*

Benchmark	GA Result	Analytical Result	Dev (%)
9.1	$f(3.999, 4.000) = 19.6633$	$f(4.000, 4.000) = 19.6633$	0
9.2	$f(9.040, 8.668) = 19.5547$	$f(9.039, 8.668) = 19.5547$	0
9.3	$f(9.039, 8.664) = 19.5619$	$f(9.039, 8.668) = 19.5547$	0.037
9.4	$f(1.585, 0.477) = 0.3755$	$f(1.585, 0.473) = 0.3793$	-1.012

Figure 9.8 plots the evolution of the fitness value of the best specimen and the average of the population for the function 9.4 as the calculations progress. The results show that within the first 40 generations the algorithm is able to capture at least one chromosome with a fitness value of 0.37 whilst for the remainder of the generations the program explores other regions of the design space. The average fitness of the population rises gently over 90 generations (continuous trend line) while the population is subjected to mutation. For the last generations the absence of mutation allows the code to rapidly converge to the final solution.

9.3.2.2 Genetic algorithm performance

The performance of the GA is heavily dependent on the right choice of input parameters, and care must be put to assure that the program has not been trapped in any local maxima. On the other hand, an excessively conservative approach would eventually find the right solution to the problem but at the cost of a dramatic increase in computational time. Therefore, it is of the utmost importance to carry out a sensitivity analysis to tune the algorithm. The effect of the input parameters on the algorithm's behaviour in outline is:

- A number of competitions greater than the number of chromosomes (around 20%) improves the convergence.

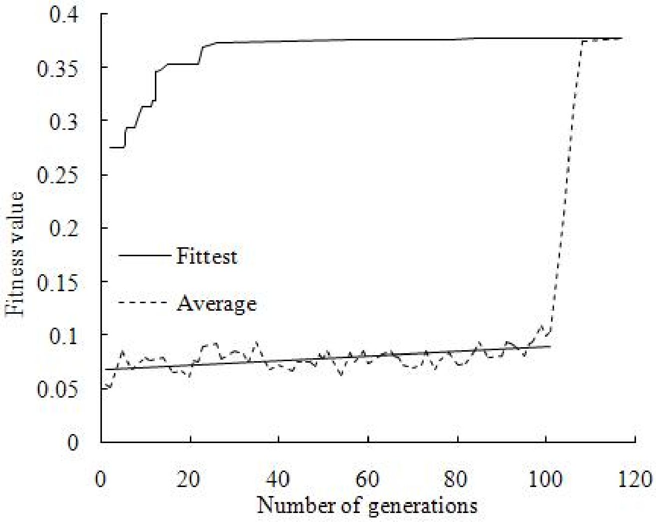

Figure 9.8: *Maximum and average fitness evolution for the baseline case - Function 9.4*

- A small percentage of mutation (1-5%) may hinder the algorithm from finding the solution and the code can be trapped on local maxima. Conversely, if the mutation is excessive (20%) the program eventually finds the global maximum but it behaves as a random search technique.

- The number of elements in the elite group should not represent a large percentage of the population as this delays unnecessarily the convergence to the solution.

- There is a threshold of generations and chromosomes below which there is no guarantee that the global maximum is found. This is demonstrated by the erratic behaviour of the algorithm for runs with less than 100 chromosomes and a small number of generations. Figures 9.9 and 9.10 illustrate this behaviour, and are an indicator of the repetitiveness of the algorithm. Particularly figure 9.10 groups the results of the maximum deviation from an average of 5 identical runs for the same operating point. The 30% deviation that appears for 50 chromosomes shows that the algorithm fails to reach the global maximum unequivocally.

The sensitivity of the algorithm to the number of generations and the percentage of mutation is investigated by three different sets of runs. In the baseline case the number of competitions is increased 70% from the baseline case (300 generations, 120 competitions, 100 individuals, 10% mutation) whereas in cases B and C the percentage of mutation is modified to 20% and 2% respectively. Increasing the number of competitions results in a less effective coverage of the design space compared to the baseline as illustrated in figures 9.11a and 9.11b where each individual is plotted as a red dot. This is reasonable since the number of different individuals that make it through the competition operator and are allowed to mate is sternly reduced by increasing the competitions.

Other effects associated to the increase in the number of competitions are:

- The number of generations required to damp the solution (mutation deactivated) and converge to the fittest individual is generally reduced.

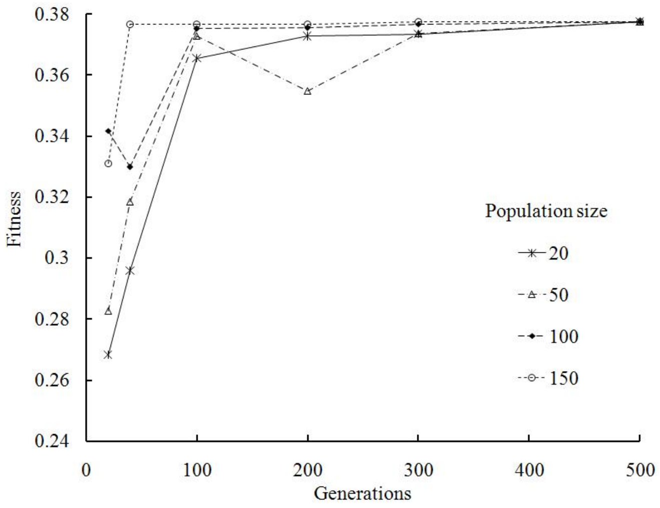

Figure 9.9: *Average function values versus number of generations - Function 9.4*

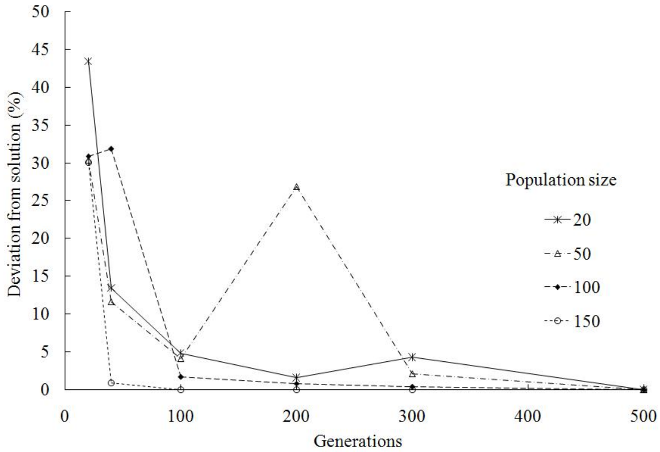

Figure 9.10: *Dev. of results from final averaged values versus number of generations - Function 9.4*

- The number of generations required to find the location of the global maximum is normally greater. This is a consequence of the previous - greater number of generations without mutation results in a worse coverage of the design space.

- The average fitness value reached during the fluctuation period is also higher.

- Overall, the final solution value is slightly improved and the deviation minimised when compared to the same percentage reduction in mutation rate. The major drawback of increasing the competitions lies on the non linear dependency of the time required for the cases to run with the number of competions that the individuals have to go through each generation.

It is found that an increase in the mutation rate has the opposite effect to any increments in the number of competitions. As an example, figure 9.12 shows the evolution of the calculations for the baseline (10% mutation) and the high and low mutation scenarios (20% and 2% mutation). It can be observed that the average fitness of the population in the initial phase is slightly higher for

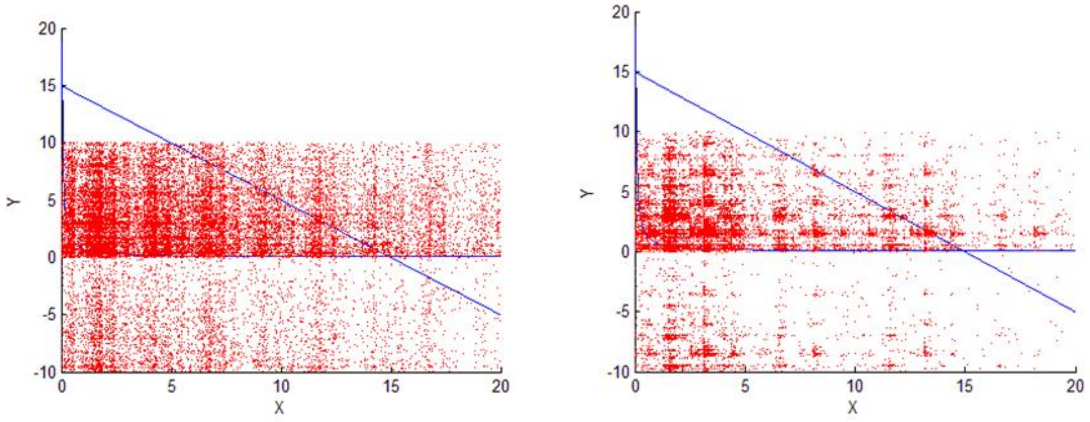

(a) *Baseline Case* **(b)** *High competitions, case A*

Figure 9.11: *Design space coverage - Effect of no. of competitions. Function 9.4*

moderate values of the mutation rate and increases sharply for the low mutation case. Thereafter the mutation operator is switched off and the algorithm is allowed to converge to the final solution, and it does so in a reasonably quick manner (less than 20 generations). On the other hand, for high values of mutation the algorithm performs poorly in that after a lower average initial phase, it behaves erratically for almost 100 generations until it is eventually able to pick and bring the fittest individual out of the crowd. Furthermore, although the reduction in mutation rate rises the average of the fitness of the population, the coverage of the search space is less efficient and the code is more likely to get trapped in local extremities (fig. 9.13b).

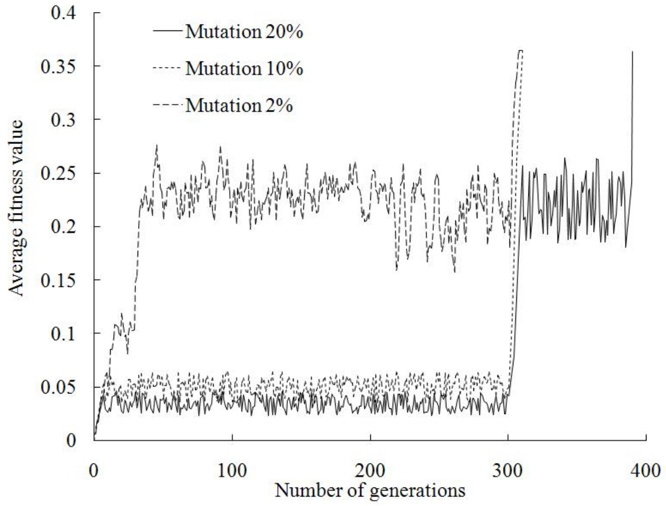

Figure 9.12: *Average fitness evolution for several mutation rates - Function 9.4*

9.3.3 VU59 - Compressor performance prediction program

The code employed to evaluate the fitness function for each compressor is a mean line Fortran Rolls-Royce proprietary computer program used to obtain the preliminary off-design performance of axial flow compressors. Its performance and capabilities have already been discussed in this

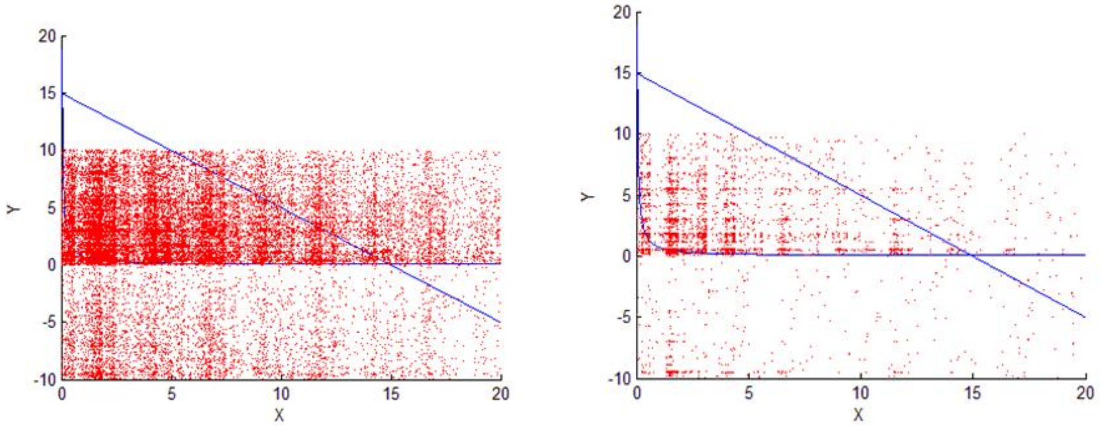

(a) *Baseline Case* **(b)** *Low mutation rate, case C*

Figure 9.13: *Design space coverage - Effect of mutation rate. Function 9.4*

manuscript and the interested reader is referred to section 7.2 for further details.

9.3.4 Practical case - Optimisation of an eight stage axial compressor variable geometry schedule

9.3.4.1 Unconstrained spool speed

To illustrate its capabilities the program has been applied to a state-of-the-art compressor of a modern high by pass ratio turbofan that features a VIGV row and two rows of VSVs, for a defined value of the minimum surge margin admissible (SM1). The population size of the algorithm is 100 individuals that run over 300 generations with a 10% mutation rate. The design parameters that can be changed in the program are three: IGV, VSV1 and VSV2 settings are allowed to vary 10 degrees around the datum.

The progression of the algorithm for this real-world optimisation problem is depicted in figure 9.14. The algorithm starts with a fittest individual with an efficiency of 0.45 and rises to an average of 0.65 after 5 generations. During 295 generations it explores the design space and as a result the efficiency of the fittest individual rises slowly up to 0.8243 after 95 generations. During the remaining 200 generations the algorithm does not find a fitter individual. After the mutation is switched off, it takes 4 generations for the GA to converge to the solution.

The resultant schedule is plotted in figures 9.15 and 9.16 for the IGV and VSV1 and 2 respectively in conjunction with the nominal schedule currently used in production engines. The optimised solution exhibits a clear trend towards a more opened position of the IGV row with respect to the datum. The first row of variable geometry is more opened at high speeds and gets progressively closer to the nominal down to 85%NRT; then it matches the original schedule until the solution departs again slightly from the nominal for the lower region of the speed range. The second row of variable vanes on the other hand, is more open at the top end of the speed range and more closed for the remaining of the speed range. The subtle change in efficiency trend that is present at 85%NRT for all three scenarios is caused by the operation of the bleed valves that are

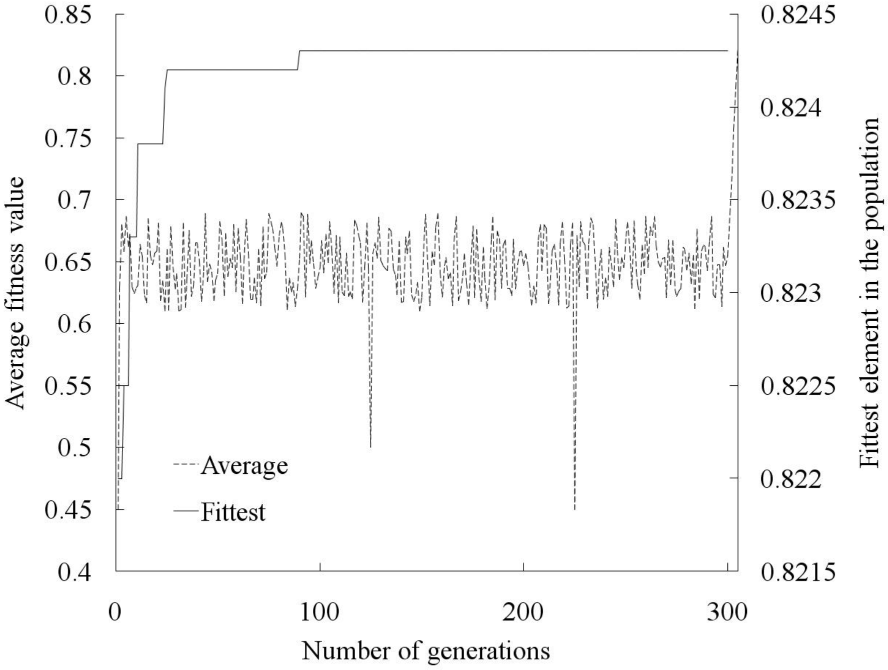

Figure 9.14: *VSV optimisation - Progression of the calculations*

scheduled to open at such speed (fig. 9.17). The opening of the valves allows the compressor to reach slightly higher efficiencies since the required surge margin for engine operation is provided by dumping the air overboard through the bleed valves rather than giving up adiabatic efficiency.

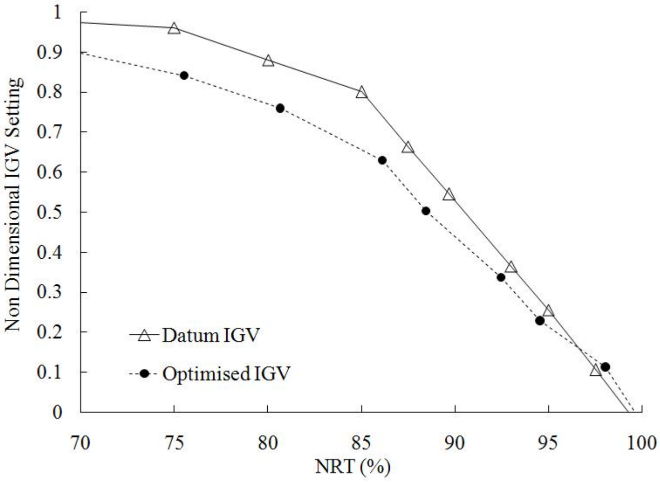

Figure 9.15: *Most flow efficient IGV schedule for no constraints in spool speed and SM1*

Figure 9.18 summarises the benefits that can be obtained by applying the proposed new methodology. As expected, at high speed the gain in compressor efficiency obtained is minimal as the compressor blading is optimised for flow efficiency at design conditions. Results show that a marked rise in compressor efficiency can be attained with respect to the nominal schedule utilising the new methodology, in particular at partial speed operation, for different values of the minimum surge margin required for engine operation. The continuous line labelled SM1- refers to

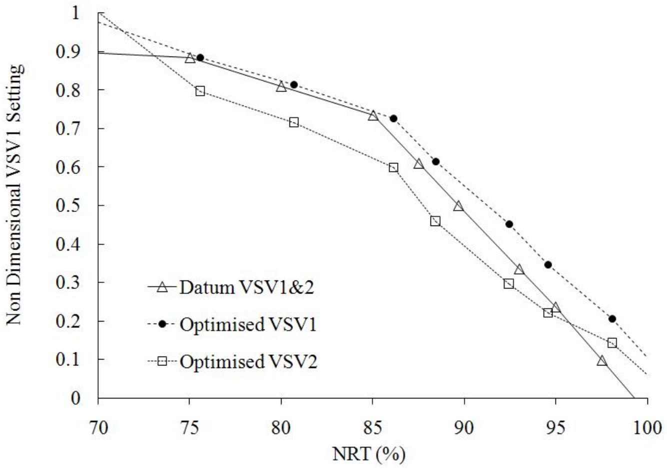

Figure 9.16: *Most flow efficient VSV schedule for no constraint in spool speed and SM1*

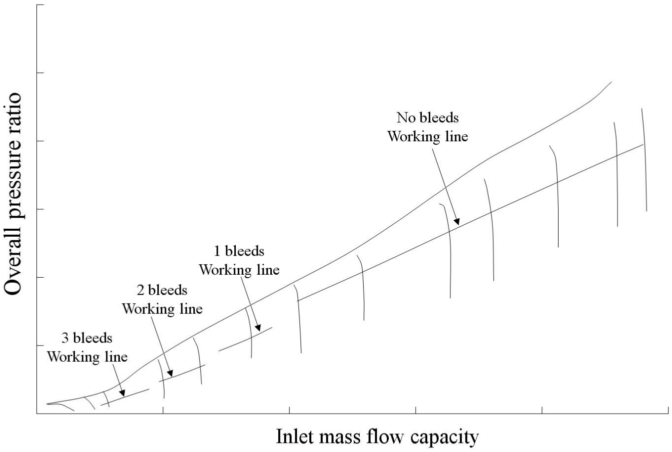

Figure 9.17: *Notional compressor bleed valves schedule*

the maximum adiabatic efficiency that can be attained with the same surge margin prescribed for the datum schedule throughout the operating speed range. The SM2 line shows the maximum flow efficiency that can be obtained for the nominal surge margin increased by 5%. It is noticeable that for both scenarios the compressor efficiency is still higher than the datum, despite the increase in surge margin required from the machine in the SM2 case.

9.3.4.2 Limited spool speed variation admissible

The mentioned efficiency gain of figure 9.18 was obtained at the expense of a considerable decrease in spool speed (fig. 9.19). On the other hand, the careful scrutiny of the results suggests that the capacity of this particular compressor is chiefly controlled by the stagger of the inlet guide vanes. This may be explained by the fact that by opening the IGVs pressure losses across the guide vane fall significantly, and this is enough to compensate the worse pressure loss expected from the first rotor. For the compressor to supply the same mass flow and pressure ratio - same operating point - the increase in capacity caused by the IGVs reschedule is offset by the mentioned decay in aerodynamic speed.

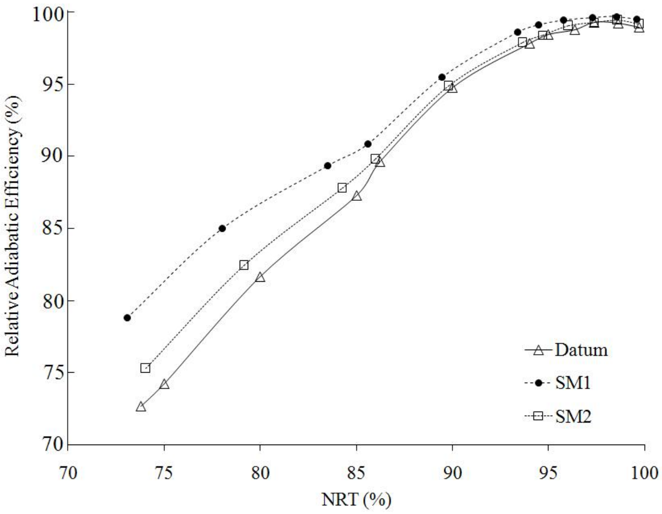

Figure 9.18: *Optimised schedule efficiency*

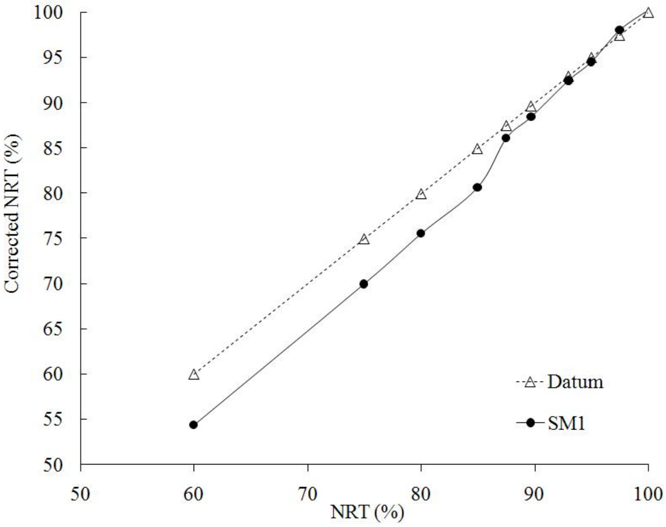

Figure 9.19: *Optimised schedule aerodynamic speed*

As a result of this, the effect of the VSVs settings on the solution is veiled by such dominant role of the IGV and spool speed on the optimised schedule. Consequently, it seems of particular interest to examine the results when the IGV schedule is frozen and the speed variation allowance of the solution is limited to 2%. To that end, an array of simulations has been completed in order to compare such case (labelled as Constrained) and a surge margin constraint free solution (Free) with the performance obtained with the nominal schedule (Datum). The results are grouped in figures 9.20 to 9.23.

The adiabatic efficiency of the resulting compressors is shown in figure 9.20. It is noted that a pronounced efficiency gain can be obtained at the expense of a reduced surge margin - this not only occurs with respect to the nominal schedule but even compared to the optimised case for the nominal surge margin and unlimited shaft speed change, SM1. The efficiency rise is more evident at low speeds. For the constrained case the increase in efficiency is less marked but still noticeable.

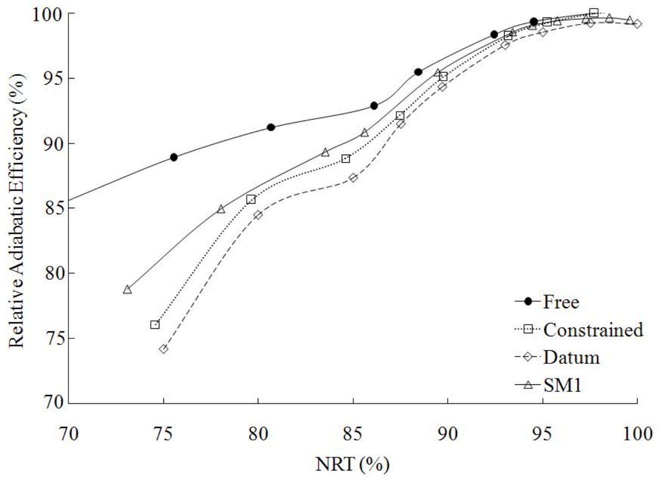

Figure 9.20: *Optimised schedule isentropic efficiency - Effect of spool speed constraint*

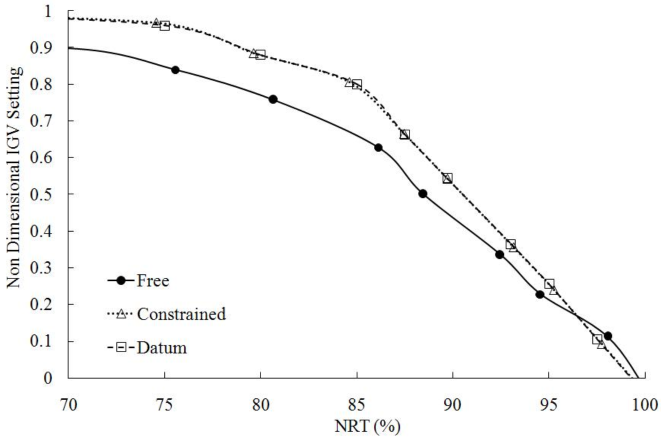

Figure 9.21: *Optimised IGV schedule - Spool speed variation constrained to 2%*

Figures 9.21, 9.22 and 9.23 contain the optimised IGV and VSV schedules for the three scenarios under study. The surge margin constraint free solution exhibits a clear trend towards a more opened position of the IGV row with respect to the datum. VSV1s are more opened at high speeds and get progressively closer to the nominal down to 85%NRT; then the schedule matches the original schedule until the solution departs again slightly from the nominal for the lower region of the speed range. The second row of variable vanes on the other hand, is more open at the top end of the speed range and more closed for the remaining of the speed range.

The results obtained for the case in which the IGV movement and the variation in aerodynamic speed have been restricted reinforce the suspicion that the inlet guide vanes exert a heavy control on the flow capacity. This is corroborated by the fact that, although the spool speed is restricted to a narrow range and hence is not a valid mechanism to offset the change in compressor capacity caused by the vanes restagger, both the VSV1 and 2 optimised settings remain close to the surge margin constraint free scenario. The main difference that can be found between the surge margin free and speed constrained cases consists in a small closure of the first and second variable rows between 85% and 95% of the nominal rotational speed.

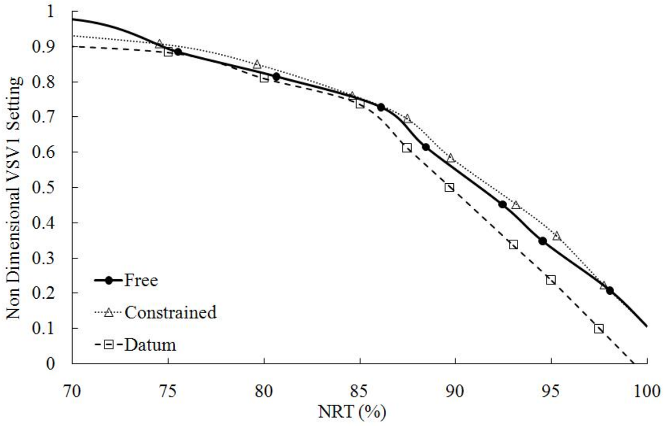

Figure 9.22: *Optimised VSV1 schedule - Spool speed variation constrained to 2%*

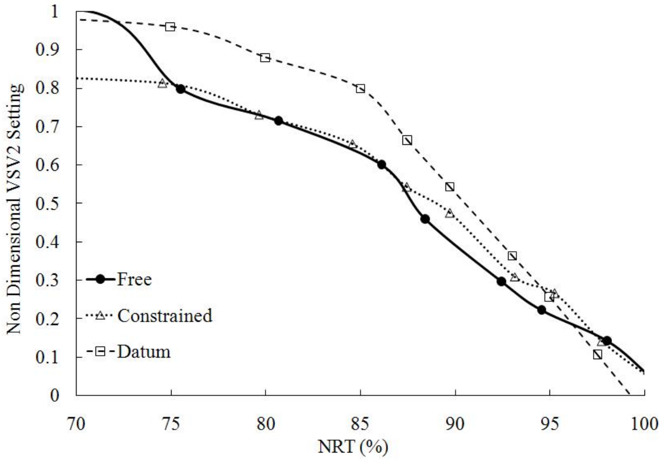

Figure 9.23: *Optimised VSV2 schedule - Spool speed variation constrained to 2%*

9.3.4.3 Surge margin dependent optimised schedule

Figures 9.18 and 9.20 point out the strong link existent between the compressor efficiency and the minimum surge margin. In order to gain a better insight into this relationship a number of simulations have been completed for increasingly restrictive values of the constraint in surge margin. The first set of simulations, labelled as “Free SM”, was unconstrained and serves as a reference for further simulations. The subsequent simulations discard compressors whose surge margin is smaller than 105, 110 and 115% of the margin obtained for the most flow efficient compressor in the constraint free case. The resulting schedules are plotted in figures 9.24 to 9.26. The optimised IGV and VSV2 schedules exhibit a strong tendency towards opened positions. The departure from the nominal is greater for lower rotational speeds. On the other hand, the first row of variable vanes shows the opposite trend, although the deviation from the nominal is less pronounced. The IGV and VSV1 schedules are grouped around the unconstrained solution while the VSV2 settings fall close to the datum schedule as the requirement of surge margin increases.

At low speeds VSV1 settings for the 105% surge margin case depart suddenly from the general trend exhibited by all simulations. This is explained by the fact that, in an attempt to comply with

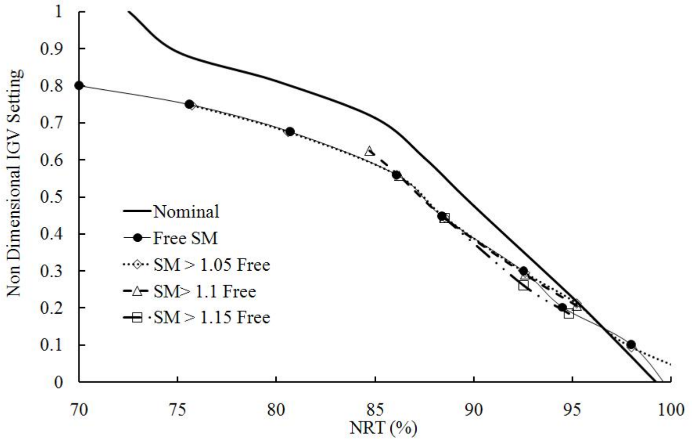

Figure 9.24: *Optimised IGV schedule - Surge margin dependency*

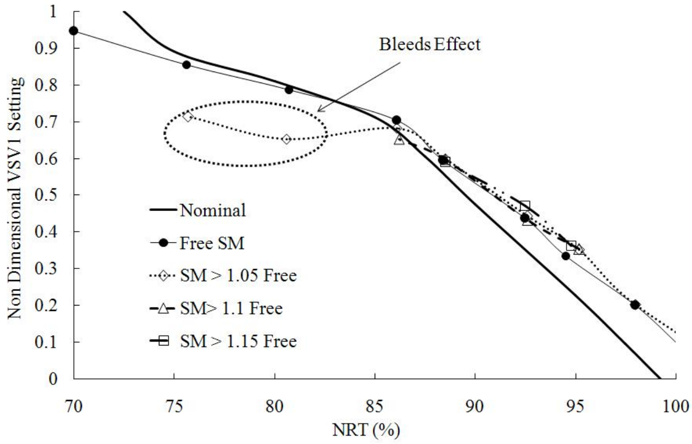

Figure 9.25: *Optimised VSV1 schedule - Surge margin dependency*

such a severe constraint, the algorithm finds a characteristic line that is more inclined so that it falls on a lower segment of the running line (fig. 9.27). In this manner the surge margin is greatly enhanced. For some of the remaining cases the algorithm fails to find any compressors that satisfy the requirements. It is for such reason that some of the lines included in figures 9.24 to 9.26 do not show any values for low speeds.

Figure 9.28 shows the deviation of the optimised compressor adiabatic efficiency from the datum at such particular speed as a function of the surge margin requirement inputted to the algorithm. The first point of each curve represents the value of surge margin when the algorithm runs unconstrained. As expected, all curves are monotonically decreasing since by limiting the minimum value of surge margin some highly efficient compressors no longer comply with the demanded criteria and die out within the algorithm. For most of the speeds apart from 100% and 97.5% there is an initial plateau across which the efficiency decays smoothly and then plummets to values well below the nominal.

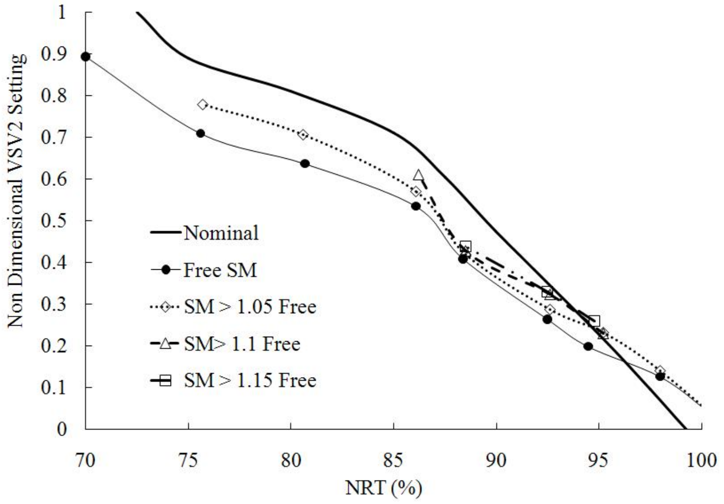

Figure 9.26: *Optimised VSV2 schedule - Surge margin dependency*

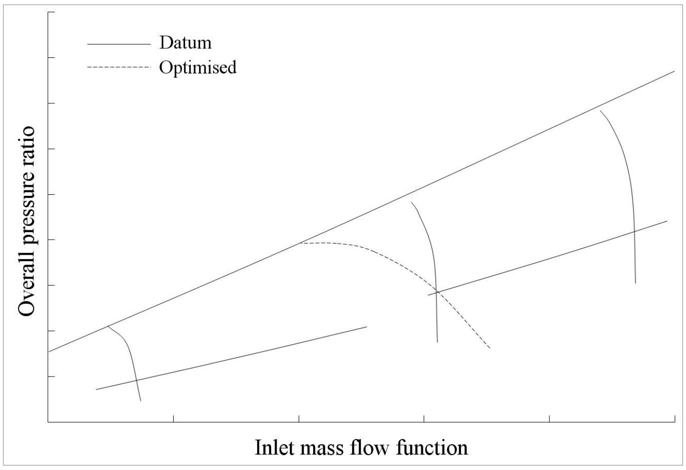

Figure 9.27: *The effect of bleeds - Surge point movement to lower segments of the running line*

9.4 Combined compressor - turbine response to variable geometry setting changes

9.4.1 Effect of shaft speed changes on the combined compressor - turbine efficiency

Results so far suggest that a gain in compressor efficiency close to 1% with respect to the nominal could be achieved for surge margins above 10%. A point on the working line - defined by a determined value of the non dimensional mass flow and a given pressure ratio - can be achieved with different settings of the variable geometry rows. However, it is unlikely that, for those different configurations, the speed at which the compressor runs would be the same. For the particular compressor under investigation the efficiency rise is obtained at the expense of a reduction in rotational speed that can be as high as 5% (fig. 9.19). In any case, any change in spool speed will have an impact on the efficiency of its correspondent downstream turbine and although the compressor efficiency may be raised the turbine efficiency can plummet and the overall performance of the engine can turn out to be impaired. It is for this reason that the variable geometry schedule

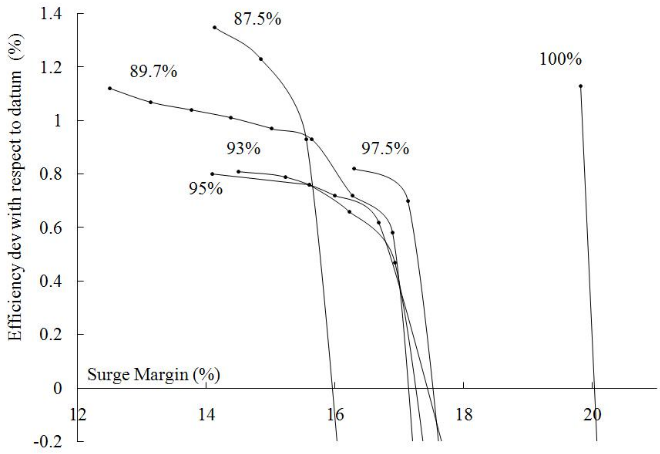

Figure 9.28: *Optimised efficiency vs surge margin for a range of aerodynamic speeds*

of a compressor should be derived in conjuction with its associated turbine. To this regard and to a first order the working line position on the compressor map is regarded as unaffected by any re-stagger of the blade rows, although strictly speaking it is a function of the compressor efficiency that indeed varies with changes in the blade row stagger.

Experimental turbine maps led to the conclusion that a shaft speed change of 1% translates into a fixed change in turbine efficiency, $\Delta\eta_t$, (faster being better) and this seems pretty consistent across the whole power range of the turbine. In this work it has also been assumed that the compressor and its associated turbine have about the same exchange rates. This means that reducing the shaft speed by 1% due to an increased compressor capacity will reduce the turbine efficiency by $\Delta\eta_t$. If the gain in compressor efficiency is less than this then it is a net loss (i.e. the compressor has to gain more than $\Delta\eta_t$ efficiency for each 1% speed loss to be in profit). On the other end, for any rise of the shaft speed the combined efficiency will capitalise on the turbine efficiency improvement to make up for any fall in compressor efficiency or add to a possible gain. A combined efficiency that can be taken as an objective measure of the overall performance of the new variable geometry setting is then defined as:

$$\Delta = \Delta\eta_c + \Delta NRT \cdot \Delta\eta_t \tag{9.5}$$

In order to evaluate the effect of variable geometry on the combined efficiency defined above every possible combination of the vanes settings was examined in a range of ±4° around the nominal. Figure 9.29 shows that the maximum variation of the shaft speed experiences a rapid increase up to 3% for speeds lower than 85% of the nominal. Minimum shaft speeds that can be achieved are slightly more than 2% lower than the datum also for the slowest end of the speed range analysed.

The study of figure 9.30 brings to light several facts. The continuous line represents the gain or loss in compressor efficiency that can be induced by restaggering the variable geometry. In turn, the discontinuous line is the combined efficiency of the couple compressor - turbine. First of all, it can be noticed that whereas the potential gain in compressor efficiency that could be reached

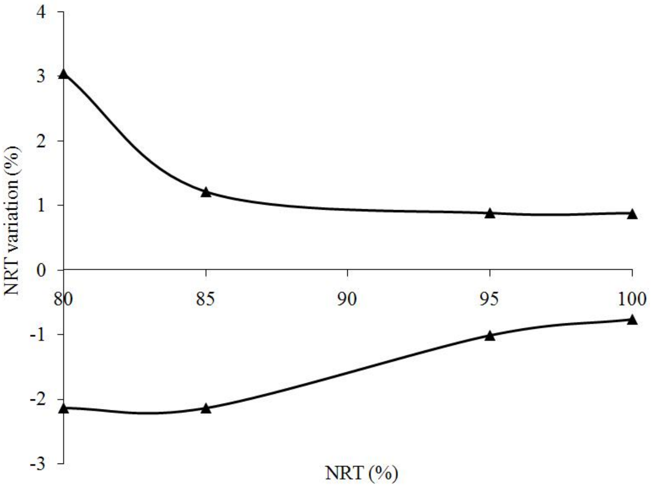

Figure 9.29: *Maximum and minimum spool speed variation for ±4 ° stagger change of the variable vanes*

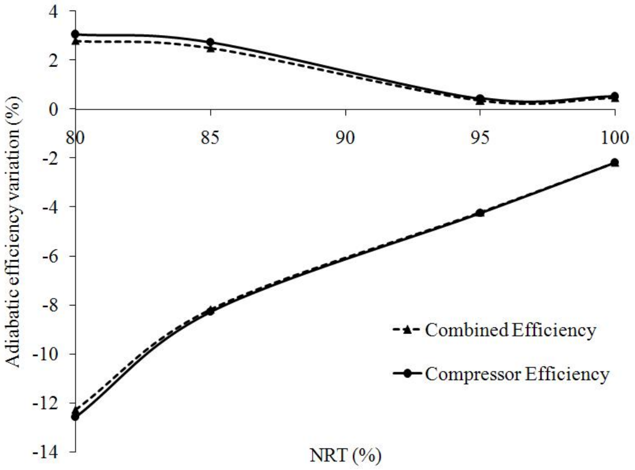

Figure 9.30: *Maximum and minimum isolated compressor and combined adiabatic efficiency variation for ±4 ° stagger change*

is above 2% the possible loss could be fivefold. Second, at high speeds the nominal efficiency is very close to the maximum achievable and the potential gain is slim; yet again this is expected since the compressor geometry is devised to maximise the flow efficiency at design point. Third, for the particular compressor and turbine under study, the effect of the shaft speed reduction on the turbine efficiency is negligible save for low speeds where the potential efficiency gain may be lessened by 0.3%. Fourth, the pernicious effect of the speed reduction on the turbine efficiency is exacerbated at lower speeds since the speed drop is more accentuated. And last, the earlier approximation of the proportionality between turbine efficiency and shaft speed is deficient for low speeds for the turbine characteristic is far from flat at those operating points. The impact of variable geometry settings on compressor surge margin is illustrated by figure 9.31. For the given compressor geometry the maximum surge margin that can be obtained is as high as 24%, more than adequate for a civil high bypass ratio turbofan. The minimum is 4% and appears at 85%NRT. The further increase in minimum surge margin at lower speeds can be explained by the position of the first bleed valve between 80% and 85%NRT, as discussed earlier.

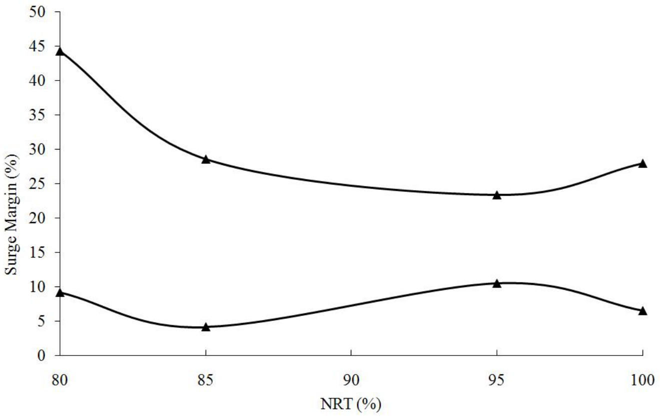

Figure 9.31: *Maximum and minimum surge margin attainable for a ±4° stagger change of the variable vanes*

9.4.2 Parallel coordinates representation of the effect of variable geometry settings

The genetic algorithm constitutes a reliable and inexpensive method to derive the most flow efficient schedule of the variable geometry for a user defined value of the surge margin. It is reasonable to suggest that movements of the variable vanes towards the optimum found by the algorithm are likely to enhance the compressor efficiency for a determined surge margin requirement. However, it may be the case that a movement of the vanes away from the optimum can in some cases also increase the flow efficiency, although the gain expected will be less than the optimum. On the other hand, it is also possible that the solution found by the optimiser delivers the best performance only across a very narrow range of settings around the optimum, and hence give rise to what is known as a "cliff-edge" design. To identify such scenarios and favour robust designs, it would be desirable to map the compressor efficiency and surge margin over a fine grid of variable geometry settings around the nominal. Unfortunately, since there are three rows of variable vanes the visualisation of the design space on classic three-dimensional Cartesian coordinates is unfeasible.

Parallel coordinates representation as introduced by Inselberg in 1985 [84] provides a suitable approach to reduce the visualisation of multidimensional design vectors to a two-dimensional space. Other researchers like Kipouros et al [93] have successfully applied this methodology to post process multi-objective design optimisation methods on turbomachinery aerodynamics. In essence, the design parameters are the abscissas and their range of variation is plotted on the ordinates' axis. Each individual of a population has certain values of its design parameters that are joined to form a line. The colour of such line is used as a metric to measure the relative variation of the performance magnitude under study. It is then possible to identify regions of high and low values of the performance magnitudes and redirect the design efforts towards those areas of interest.

In this work, 4096 stagger combinations of the compressor variable geometry that correspond to a small sample of the search space have been examined for values of the IGV and VSV settings that range from $-4°$ to $+4°$ around the nominal. Figure 9.32 groups the results for four performance magnitudes under study for a range of shaft speeds: compressor adiabatic efficiency variation, shaft speed variation, combined cycle variation as defined by equation 9.5 and surge margin variation all with respect to the datum values. Blue regions point to high values of the mentioned parameters whereas red indicate that the parameters are below the nominal. The conclusions that can be drawn from this study are:

- The effect of spool speed (second column) in the tendency of combined efficiency (third column) with respect to the tendency of efficiency variation of the compressor on its own (first column) can be disregarded. This is attributed to the low rate of turbine efficiency variation $\Delta\eta_t$ featured by the particular compressor - turbine couple under study. It is left for further work to investigate the effect of the particular value of $\Delta\eta_t$ on the combined efficiency.
- The results show a marked drop in spool speed for combinations of open IGV settings and closed VSV1s and VSV2s that becomes more pronounced at both ends of the range of shaft speeds investigated. The aerodynamic speed is also rather insensitive to stagger changes at 85% of the nominal speed.
- The compressor efficiency drops for combinations of closed VSV2s and open IGVs and VSV1s and this tendency is accentuated for lower shaft speeds. Nevertheless, some high efficiency values can be obtained for opened IGVs and closed VSV1s and VSV2s as shown by the blue interspersed lines among the red regions in some cases. This suggests that, while the IGV may control the flow, its effect on the compressor efficiency is somewhat modest.
- It can be observed that opening the second row of variable geometry enhances the efficiency, save perhaps at design speed. At 100%NRT compressor efficiency seems quite insensitive to movements of the first and second rows of variable vanes. These trends are found in agreement with the results produced by the algorithm for the optimum schedules and shown by earlier figures (9.24 to 9.26).
- There is a generalised tendency towards increased surge margins when all the three vanes are closed except for 80%NRT when the surge margin is maximised for values close to the datum. This is suspected to happen due to the effect of bleeds on the running line as explained earlier. Throughout the whole speed range there is however a consistent degradation of the surge margin when the vanes are opened, exacerbated in the case of the first variable vanes.
- For all parameters studied, the interspersed colours distinguishable in some regions denote that the particular variable vane row has a modest effect on the performance parameter examined and is dominated by one or both of the two other vane rows.

9.5 On the accuracy and limitations of the methodology

This chapter has demonstrated that the genetic algorithm performs correctly in the optimisation of mathematical problems. The accuracy of the particular results showed for the optimisation of the variable geometry of a particular compressor depend only on the ability of the compressor performance code to capture the flow phenomena appropriately. It has already been demonstrated in a previous section 7.2 that the code is capable of capturing relative changes in flow capacity - and so spool speed variations - and compressor efficiency with changes of variable geometry settings with a high degree of accuracy. Surge margin prediction, however, is a complete different matter. The compressor responds to changes in vane settings in complex three-dimensional ways to this input: vortices change size and trajectory, wakes interact, leakage quantity changes, Reynolds number changes, high loss fluid radially migrates, mixing is modulated, separations form or are suppressed. A 1D mean line calculation is quite unable to predict these effects, yet it determines the performance of the machine. True that the 1D calculation could be provided with perfect data to force a solution with the real compressor characteristic, but such data is not available to this research, and if it did, the same data would be useless for any other machine. Hence, the ability of mean line codes to successfully predict the detailed stability margin of an axial flow compressor may perhaps be a distant challenge.

In any case, despite the uncertainty associated to mean line calculations of the surge margin and thanks to the proven ability of VU59 to yield valid capacity and efficiency predictions, the efficiency gain predicted by the optimiser (fig.9.28) guarantees that, with disregard to their associated surge margin, there are a number of vane schedules that show greater compressor efficiencies than the datum. This constitutes a major benefit of the presented methodology for it narrows the schedules whose stability margin should be further investigated down to only a few possible configurations, cutting down on time and money spent in rig tests.

9.6 Concluding remarks and recommendations for future work

This chapter addresses the application of a genetic algorithm to the selection of stator schedules in a multirow compressor. The aim of the chapter is to divulge the discussed methodology rather than comment on the results obtained since these will undoubtedly depend on the particular compressor under study.

Stochastic optimisation methods and in particular genetic algorithms have been found as a powerful and adequate methodology suited to derive the most flow efficient schedule of the variable geometry of an axial compressor. The genetic algorithm optimiser described in this chapter constitutes a very efficient methodology that replaces “trial and error” and “one factor at a time” experimental approaches.

Satisfactory results have been obtained using a 1D mean line code to predict the compressor efficiency. Besides, the modular character of the tool enables the researcher to substitute the compressor evaluation tool with 2D or 3D models for an enhanced accuracy of the results. The methodology enables the user to assess the impact of some design decisions at part speed operation during the design phase of the engine and in so doing promotes a better understanding of the expected performance of the compressor at part speed. This state of the art tool is suited to be upgraded to carry out the coupled optimisation of the bleeds and variable geometry schedules for a greater applicability of the tool.

Whereas it could be argued that the prediction of surge margin with 1D mean line codes is not completely accurate, the demonstrated ability of the compressor performance prediction algorithm employed by this research to capture efficiency and capacity variations with changes in the variable geometry schedule guarantees that the configurations shown in figure 9.28 have all better flow efficiencies than the datum. The accurate determination of the surge margin for all these cases could be assessed by other tools or perhaps rig tests. In any case, there is an obvious benefit that comes from the fact that the amount of variable geometry configurations that need to be tested further has been reduced greatly. VU59 employs the empirically correlations published by Miller and Wasdell [128] to calculate incidence that stalls the compressor blades. It is recommended that the research continues with the investigation of other surge correlations and blade stalling such as that published by Aungier [9].

For the particular compressor under scrutiny the efficiency gain attainable can reach values close to 1%, with a marked decreased of spool speed. Furthermore, the strong relationship between the adiabatic efficiency and the surge margin of the compressor is investigated and reported. The effect of variable bleeds on the results is also accounted for an explained.

Since the change in rotational speed can impair the turbine efficiency, its effect has been examined and accounted for by an efficiency change that is proportional to the spool speed variation. At the sight of experimental data available to the research, the validity of this approach is adequate for the power range analysed. However, for lower speeds this assumption may need to be revisited since the slope of the turbine characteristic will turn steeper and not constant. Although for the couple compressor-efficiency studied the change in turbine efficiency is negligible, this will depend strongly on the particular machines considered. The thorough analysis of this effect is left for further research.

In order to complete the results produced by the code, a parametric analysis was carried out in which the compressor performance is monitored for small variations of the variable geometry settings around the datum. For the particular compressor analysed results show that ample variations of the compressor efficiency, shaft speed and surge margin are obtainable by the restagger of the variable geometry.

The work is completed with the application of a simple yet effective technique used to reduce the visualisation of multidimensional space problems to two-dimensional plots. This enables the identification of trends and tendencies of some compressor performance parameters for any reschedule of the variable geometry.

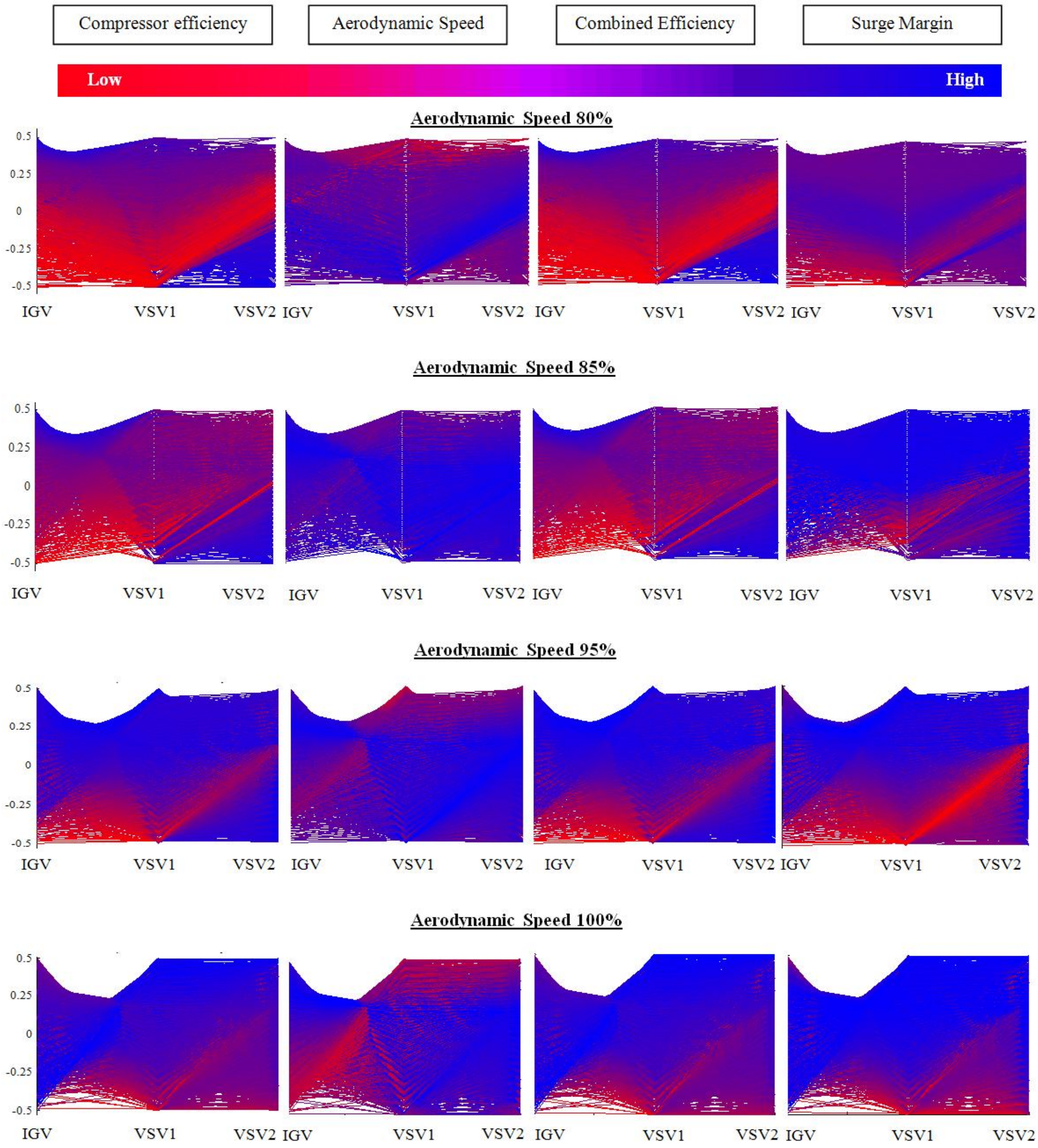

Figure 9.32: *Parallel coordinates visualisation of the compressor efficiency, spool speed, combined efficiency and surge margin for 4 stagger change of the variable vanes*

Chapter 10

Thermodynamic gas models effect on jet engine performance simulation

10.1 Background and research scope

One of the basic problems faced by any fluid engineer is the calculation of the thermodynamic state of a working fluid that has undergone a process to a final equilibrium state. To achieve this goal, further to the principles of conservation of mass, conservation of energy (first principle) and entropy rise (second principle), in the case of a simple compressible system it shall be known:

1. Either a thermodynamic potential function $U(S, V)$, $A(V, T)$, $G(T, p)$ or $H(p, S)$ since by their successive derivation all the properties and coefficients that define the system can be determined.
2. Or two compatible equations of state that can be integrated to produce a thermodynamic potential; e.g. $V = V(T, p)$ and $S = S(T, p)$ to yield $G(T, p)$.
3. Or three thermodynamic coefficients and an integration constant. For example, $\alpha(T, p)$, $k_T(T_0, p)$ and ρ_0 can be integrated to give the equation of state $v = v(T, p)$ from $dv/v = \alpha dT - k_T dp$. With the equation of state and a correlation for $c_p(T, p_0)$ it is immediate to obtain variations of internal energy, enthalpy and entropy.
4. Or a suitable combination of the previous such as an equation of state $f(V, p, T) = 0$ and $c_p(T, p_0)$.

Of all these possibilities, the last one is most used as the relation between p, v and T, along with the relationship of specific heats with temperature at low pressure are the properties more straightforwardly measurable. The evaluation of properties such as internal energy, enthalpy and entropy can be carried out subsequently through calculations based on such empirically derived magnitudes. Therefore it is evident that the provision of fundamental equations that enable the calculation of properties of interest from properties directly measurable like (p, v, T) and $Cp(T, p_0)$ is of paramount importance for any thermodynamic process under study.

Nonetheless, in many cases the empirical data available to calculate the thermodynamic state of a given substance is insufficient, despite the fact that the mathematical relationships needed to derive u, h and s may have been unequivocally established. It is then that appropriate modelling methods to predict the fluid state deem necessary. The use of a generalised compressibility factor, Z, is perhaps the most common technique used to correlate p, v and T when sufficient experimental data is lacked of. Other methods include those derived from the principle of corresponding states, pure theoretical approaches such as the virial equation or efforts to fit mathematically through a set of coefficients an array of data obtained experimentally .

For what concerns the gas turbine engineer, whether it is to predict the engine performance or post process the data obtained from a test rig, virtually every performance calculation relies on some kind of gas model, and it is the perfect gas idealisation the most commonly used. However, the accuracy and reliability of the ideal gas equation is usually taken for granted and the attention paid hitherto to its limitations may be inadequate. Although for single calculations the errors associated to such calculations may be negligible, it is in iterative procedures like compressor performance prediction algorithms or off-design whole engine performance simulations that even small errors can be accrued and become significant. A thorough literature survey has shown that there is no comparison between the different gas models for air available in the public domain in the range of operating conditions of interest to the gas turbine engineer. Since the compressibility factor (as defined in equation 10.3) in most of the gas turbine operating envelope rises with pressure and temperature[1], the departure of the behaviour of real gases from that projected by the perfect gas model becomes increasingly important given the pursuit for higher pressure ratios and temperatures of modern gas turbines manufacturers (fig.10.1) and needs to be investigated.

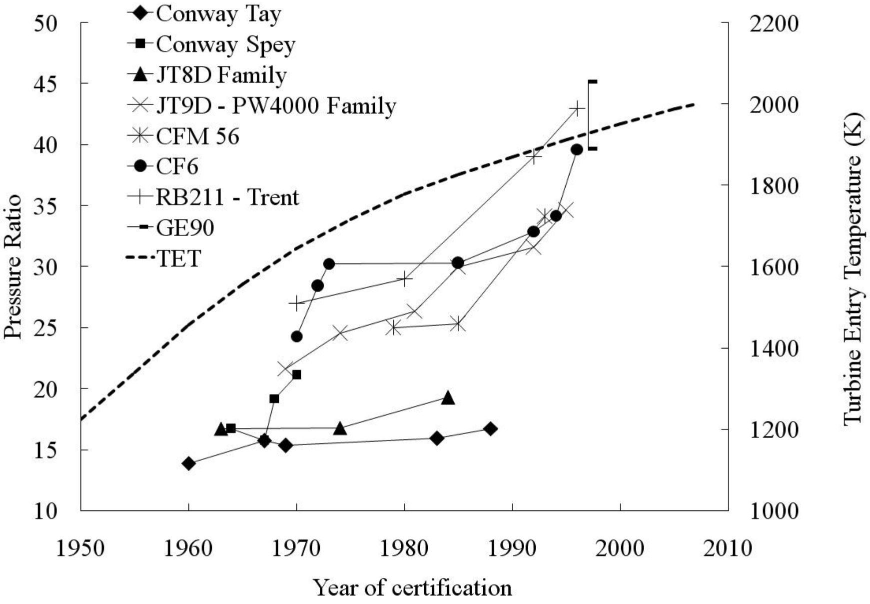

Figure 10.1: *Gas turbine operating envelope evolution over the years. Adapted from [85] and [14]*

---

[1] The compressibility factor exhibits a maximum at temperatures around $750K$

The first part of the work reported in this chapter provides a comparison of the accuracy of different generic gas equations to predict the thermodynamic properties of air at different states of pressure and temperature. The second part of the chapter quantifies the deviation from ideal of isolated components and whole engine performance calculations with different thermodynamic gas models.

10.2 Equations of state for gases

Because[2] each of them is targeted to predict specific properties at a particular range of conditions for determined substances, the number of equations of state that have been proposed to model the behaviour of gaseous and liquid substances is rather large. Further to the idealisation of the perfect gas model, any equation of state can be classified according to its origin, as illustrated by figure 10.2.

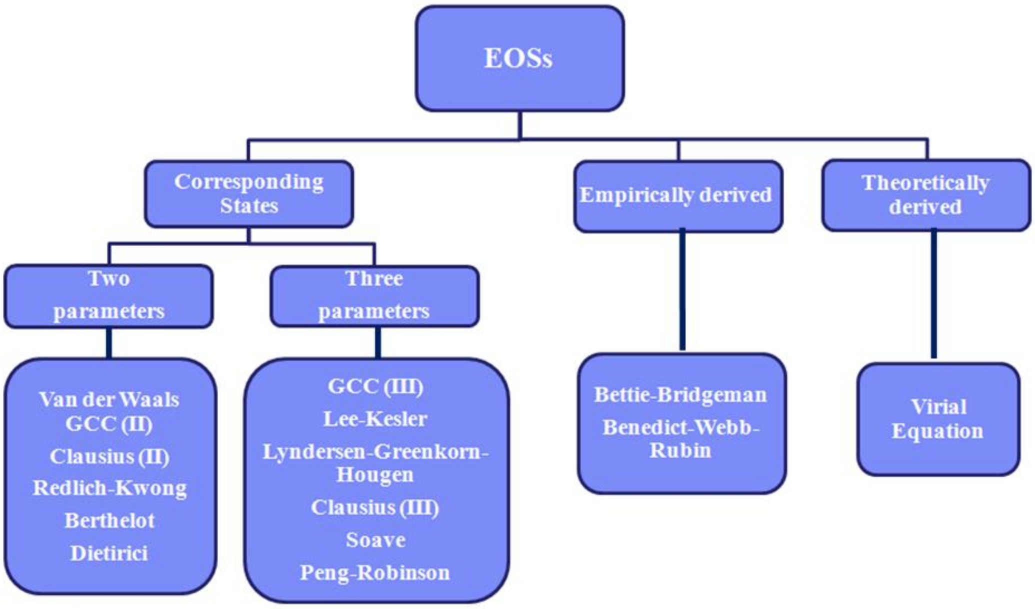

Figure 10.2: *Classification of the most common equations of state according to their origin*

10.2.1 The prefect gas equation

The works of Boyle, Charles and Dalton fructified into the formula known today as the perfect or semi-perfect gas equation of state, $pv = RT$. To contrive that expression, the kinetic gas theory assumes that for semi-perfect gases the volume occupied by the gas molecules themselves is negligible when compared to the bulk volume occupied by the gas and that the intermolecular forces are also insignificant. Those conditions hold better the lower the pressure of the fluid is -or

---

[2] This section is circumscribed to the study of monocomponent, simple, compressible systems. For these systems Kline and Koenig [95] showed that two known thermodynamic properties are sufficient to determine unequivocally the thermodynamic properties of the system

density for that matter -; that is:

$$pv = RT \quad when \quad p \rightarrow 0 \tag{10.1}$$

However, unless the pressure is reasonably low and the temperature relatively high the gases will not show this behaviour. Therefore, one of the simplest way to overcome these limitations is to introduce a correction factor, Z, known as the compressibility factor, in the form:

$$pv = ZRT \tag{10.2}$$

The compressibility factor represents the ratio of the real specific volume to the specific volume yielded by the semi-perfect gas equation at the same conditions of pressure and temperature:

$$Z = \frac{v_{real}}{v_{sp}} \tag{10.3}$$

Experiments have shown that the value of the compressibility factor on the critical point for most substances[3] ranges from around 0.20 to 0.30 depending of the substance under consideration [74].

10.2.2 Equations based on the law of corresponding states

10.2.2.1 The equation of van der Waals

The first attempt to eliminate the semi-perfect gas assumptions - negligible intermolecular forces and no volume occupied by the gas molecules themselves - is due to Van der Waals in 1873. It acknowledges the fact that the attraction forces between molecules reduce the gas pressure below the value provided by the semi-perfect gas assumption. It can be demonstrated [181] that the pressure correction is inversely proportional to the square of the specific volume:

$$p_{real} = p_{sp} - \frac{a}{v^2} \tag{10.4}$$

Furthermore, due to the finite volume indeed occupied by the gas molecules - more noticeable at high pressures - the volume in the perfect gas equation is replaced by $(v - b)$ where b represents the volume excluded by one mol of gas. Hence van der Waals proposed the following expression:

$$\left[p + \frac{a}{v^2}\right](v - b) = RT \tag{10.5}$$

At low pressures, the volume occupied by the gas is large and the interaction between molecules is negligible, and so equation (10.5) reduces to the perfect gas equation. The major limitation that Van der Waals' EOS presents is the real dependency of the constants a and b with temperature

---

[3] For light substances like hydrogen fluoride the critical compressibility factor is as low as 0.12.

that have to be obtained experimentally for a range of temperatures. However, bearing in mind that the critical isothermal curve has an inflection point with an horizontal tangent on the critic point ($\frac{\partial p}{\partial v}|_{T_c} = 0$; $\frac{\partial^2 p}{\partial v^2}|_{T_c} = 0$), a and b are derived in most cases by imposing that the equation of van der Waals has a triple root on that point[4],$(v - v_c)^3 = 0$, to yield:

$$a = 3p_c{v_c}^2 = \frac{27}{64}\frac{R{T_C}^2}{p_c} \tag{10.6}$$

$$b = \frac{v_c}{3} = \frac{RT_c}{8p_c} \tag{10.7}$$

The gas equation can be expressed in reduced magnitudes p_r, T_r and v_r to give:

$$p_r = \frac{8T_r}{3v_r} - \frac{3}{{v_r}^2} \tag{10.8}$$

Note that in the equation (10.8) above there are no variables that relate to any characteristic specific to the gas studied, and so it can be applied independently of the gas under scrutiny. Therefore, two different gases with two equal reduced magnitudes will have the remaining reduced magnitudes equal, although their actual state will be different. This is known as the 'law of corresponding states'.

The gas equation can be expressed now in terms of Z, p_r and T_r:

$$Z = Z(p_r, T_r) \tag{10.9}$$

After some algebra:

$$Z^3 + (\frac{p_r}{8T_r} + 1)Z^2 + \frac{27}{64}\frac{p_r}{8{T_r}^2}Z - \frac{27}{512}\frac{p_r^2}{{T_r}^3} = 0 \tag{10.10}$$

That is:

$$Z^3 - f_1(p_r, T_r)Z^2 + f_2(p_r, T_r)Z - f_3(p_r, T_r) = 0 \tag{10.11}$$

When calculated with equation (10.10) on the critical point, Z_c is found to be 0.375, far from the values observed experimentally. This constitutes one major flaw of the EOS of van der Waals, although the match of the equation to the experimental data improves far from the critical point. However, the historical value of this equation is undeniable since many later equations are nothing but modifications and evolutions of Van der Waals'.

---

[4] Some equations cannot be reduced to a cubic polynomial in volume, such as Dieterici's; in those cases the constants are obtained by obliging ($\frac{\partial p}{\partial v}|_{T_c} = 0$; $\frac{\partial^2 p}{\partial v^2}|_{T_c} = 0$) to be satisfied directly.

Table 10.1: *Two parameter EOS based on the law of corresponding states*

van der Waals	$p = \frac{RT}{v-b} - \frac{a}{v^2}$
Berthelot	$p = \frac{RT}{v-b} - \frac{a}{Tv^2}$
Dieterici	$p = \frac{RT}{v-b} e^{\frac{-a}{vRT}}$
Clausius (II)	$p = \frac{RT}{v-b} - \frac{a}{(v+b)^2 T}$
Redlich-Kwong	$p = \frac{RT}{v-b} - \frac{a}{\sqrt{T} v(v+b)}$

Table 10.2: *Two parameter EOS - Analytical values for a, b, R and Z_c*

Equation	a	b	R	Z_c
van der Waals	$3v_c^2 p_c$	$\frac{v_c}{3}$	$\frac{8}{3}\frac{v_c p_c}{T_c}$	$\frac{3}{8} = 0.375$
Berthelot	$3v_c^2 p_c T_c$	$\frac{v_c}{3}$	$\frac{8}{3}\frac{v_c p_c}{T_c}$	$\frac{3}{8} = 0.375$
Dieterici	$v_c^2 p_c e^2$	$\frac{v_c}{2}$	$\frac{1}{2}\frac{v_c p_c}{T_c}$	$\frac{2}{e^2} = 0.271$
Clausius (II)	$\frac{108}{25}\frac{T_c^3 v_c^2}{p_c}$	$\frac{v_c}{5}$	$\frac{16}{5}\frac{v_c p_c}{T_c}$	$\frac{5}{16} = 0.312$
Redlich-Kwong	$\frac{1}{2^{1/3}-1}\sqrt{T_c} v_c^2$	$(2^{1/3} - 1)v_c$	$3\frac{v_c p_c}{T_c}$	$\frac{1}{3} = 0.333$

Lydersen, Greenkorn and Hougen [113] observed that Z_c varies between 0.22 and 0.29 with a modal value of 0.27 for most gases. They prepared tables (GCC) for $Z_c = 0.27$ and correction factors for $Z_c < 0.27$ and $Z_c > 0.27$ and obtained a good agreement for both liquid and vapour phases.

10.2.2.2 Other two parameters equations based on the law of corresponding states

With the focus on addressing the explained deficiencies shown by van der Waals' thermal equation, several modifications were proposed on the assumption that $(\partial u/\partial v)_T = f(T)g(v)$. Between them, perhaps the most popular are those proposed by Berthelot [18], Dieterici [47], Clausius [34] and Redlich - Kwong [152] (Table 10.1). In the same fashion as explained for the EOS of van der Waals, expressions for the constants a and b and values for the critical compressibility factor, Z_c can be calculated and are grouped in table 10.2.

10.2.2.3 Three parameters equations based on the law of corresponding states - The acentric factor

Due to the non sphericity of the molecules and their different polarity equation (10.9) covers only a reduced number of substances. In 1955 Pitzer [144] named simple fluids those whose molecules are spherical (spherical molecular symmetry) and for whom force fields and quantum effects are negligible (Argon, Krypton and Xenon comply with this definition, and other gases like CH_4, N_2 and CO are reasonably close). For these gases Pitzer observed that the saturation pressure, ${p_r}^*$, when $T_r = 0.7$, was such that $log({p_r}^*)|_{T_r=0.7} = -1$, and so the acentric factor was defined as:

$$\omega = -1 - log({p_r}^*)|_{T_r=0.7} \tag{10.12}$$

The acentric factor is an indicator of the departure of a gas from the simple fluid type defined by Pitzer. Hence, the law of corresponding states reads now that all gases with the same acentric factor possess the same compressibility factor when compared with identical values of p_r and T_r. The compressibility factor suggested by Pitzer is expressed mathematically as:

$$Z = Z^0(p_r, T_r) + \omega Z^1(p_r, T_r) \tag{10.13}$$

This expression was later reviewed by Lee and Kesler [105] to extend its range of applicability. In order for the vapour pressure and liquid density to be predicted more accurately, Soave [165] introduced in 1972 a new parameter named the α function with the following suggested expression:

$$\alpha(T, \omega) = [1 + m(\omega)(1 - T_r^{1/2})]^2 \tag{10.14}$$

where $m(\omega)$ is a polynomial function of the acentric factor. The equation of Soave can be then expressed as:

$$[p + \frac{a\alpha}{v(v+a)}](v - b) = RT \tag{10.15}$$

In 1976 the Peng-Robinson equation was developed [142] in an attempt enhance the accuracy of the predictions in the neighbourhood of the critical point:

$$(p + \frac{a\alpha}{(v(v+b) + b(v+b))})(v - b) = RT \tag{10.16}$$

Although the equations mentioned are perhaps the most widely known, a myriad of new equations or further modifications to those explained here have been devised for more specific and particular purposes, such as those by Patel-Teja [141], Mathias - Copeman [119] or Stryjek - Vera [167].

10.2.3 Empirically derived equations and the Virial EOS

10.2.3.1 Empirically derived EOS

Equations with more than three parameters have been proposed in the literature in an effort to fit the experimental data particular to each gas under scrutiny. One of their main drawbacks is the need for experimental data to derive them since the equation coefficients are not expressed as a function of the critical magnitudes. Among those, perhaps the most used are those by Beattie and Bridgeman [16] (10.17) and Benedict, Webb and Rubin [17] (10.18).

$$p = RT\rho + (B_0RT - a - \frac{R_c}{T^2})\rho^2 + (-B_0bRT + A_0a - \frac{RB_0c}{T^2})rho^3 + \frac{RB_0bc\rho^4}{T^2} \tag{10.17}$$

$$p = RT\rho + (B_0RT - A_0 - \frac{C_0}{T^2})\rho^2 + (bRT - a)\rho^3 + \alpha a\rho^6 + \frac{c\rho^3}{T^2}(1 + \gamma\rho^2)e^{-\gamma\rho^2} \tag{10.18}$$

Although in principle it may be considered that equations (10.17) and (10.18) ought to be more accurate than two parameter equations, Redlich-Kwong has shown a better behaviour for simple molecules like Argon [164]. For more complex molecules (10.17) and (10.18) provide better results at high T_r and v_r, but overall agreement with Redlich - Kwong's EOS is similar [164]. This fact, coupled with its simpler mathematical handling and the ability to relate the equation constants to the critical point makes Redlich - Kwong particularly attractive for engineering applications.

10.2.3.2 The Virial equation

The virial equation of state (19) was proposed by Kamerlingh and Onnes in 1901 resorting only to statistical mechanics considerations. It has the form:

$$Z = \frac{pv}{RT} = 1 + \frac{B(T)}{v} + \frac{C(T)}{v^2} + \frac{D(T)}{v^3} + \ldots \tag{10.19}$$

where coefficients B, C, D,... are called virial coefficients and depend solely on the temperature and the substance being dealt with. These coefficients are related directly with the intermolecular forces existent between groups of molecules. For example, coefficient B describes interactions between pairs of molecules, C between triplets and so on. These interactions can be expressed as rather complicated integrals of the intermolecular forces, so that, if the intermolecular forces were known as a function of the separation between molecules for whatever combination of molecules possible, it would be possible to calculate the integrals without the need for any experimental data to derive the equation coefficients. However this task is tremendously complicated and has not been completed except for simplified cases for the second coefficient of the virial EOS. Moreover, the equation is not easy to handle and so its application to engineering problems is almost discarded.

10.2.4 Tailored EOS for air. Lemmon's equation of state

The experimental $p - v - T$ data available in the public domain for air was fitted by Lemmon et al. [106][140] into a tailored EOS explicit in Helmholtz energy with independent variables of temperature and density. In the absence of experimental data for temperatures above $873K$ and $70MPa$ Nitrogen data was used to predict air properties up to $2000K$ and $2000MPa$. The equation consists of two terms; the first accounts for the ideal gas contribution to the Helmholtz energy and the second represents the contribution due to the deviation from ideal:

$$A(\rho_r, T_r) = A_{sp}(\rho_r, T_r) + A_R(\rho_r, T_r) \tag{10.20}$$

In essence, the equation is a sum of numerous terms that are functions of some 50-odd coefficients whose relative weight is modulated as temperature and density change. This equation is claimed to have an associated uncertainty of the calculated density of 0.5% for temperatures above 873K and 70MPa, and it rises to 1.0% at 2000K and 2000MPa. Although this equation yields results far more accurate than most of the EOS previously discussed, its use in recursive calculations is hampered because the complexity of the equation increases the computational time significantly. An additional major flaw of this equation is that its tailored nature make it unable to handle combustion products satisfactorily (see 10.4.2)

10.2.5 Experimental $p - v - T$ data available for air for gas turbine calculations

To the authors' knowledge, there are eleven references in the public domain listed in table 10.3 that group an overall 1525 experimental $p - v - T$ points for air, ranging from 0.01 to $304MPa$ and from 61 to $873K$. However, the vast majority of the data was obtained for either very high or low values of pressure and temperature that are out of the environmental operating envelope of the gas turbine.

Table 10.3: *References on experimental $p - v - T$ data available for air*

Reference (Year)	No. of points	Temperature range (K)	Pressure range (MPa)
Amagat (1893)	78	273 - 318	0.10 - 304.0
Blanke (1977)	110	61 - 170	0.01 - 4.9
Holborn and Schultze (1915)	42	273 - 473	1.98 - 10.0
Howley et al. (1994)	286	67 - 400	1.06 - 35.2
Kozlov (1968)	348	288 - 873	1.21 - 72.2
Michels et al. (1954a)	157	273 - 348	0.73 - 228.0
Michels et al. (1954b)	199	118 - 248	0.56 - 102.0
Penning (1923)	62	128 - 293	2.52 - 6.20
Rogovaya and Kaganer (1960)	10	273	4.71 - 8.6
Romberg (1971)	124	84 - 122	0.02 - 2.0
Vasserman et al. (1976)	109	77 - 199	2.62 - 59.8
Overall	1525	61 - 873	0.01 - 304.0

10.2.5.1 Operational envelope of the civil aero gas turbine

The jet engine of a tipical civil aircraft ($\pi_c = 50$ as a notional value for overall pressure ratio) operates within an environmental envelope (Fig. 10.3) that is limited on its left by the compression of the ambient air on a cold ISA day at zero flight speed and whose upper limit is given by increasing flight Mach number and ambient temperature at the highest pressure ratio of the cycle. For unburnt air, the right limit of the envelope is marked by the flight altitude at the highest cycle pressure ratio. The lower boundary of the envelope is determined by the conditions at the highest flight altitude and the highest flight speed. The actual slope of the margins of the envelope depends on the efficiency at which the compression occurs. Air conditions further right to the unburnt air envelope are only attainable by combustion products, for which thermodynamic calculations are carried out from individual species data rather than as a constant mixture of gases. Similarly, the lowest cycle temperature and pressure occur at the conditions labelled in figure 10.4.

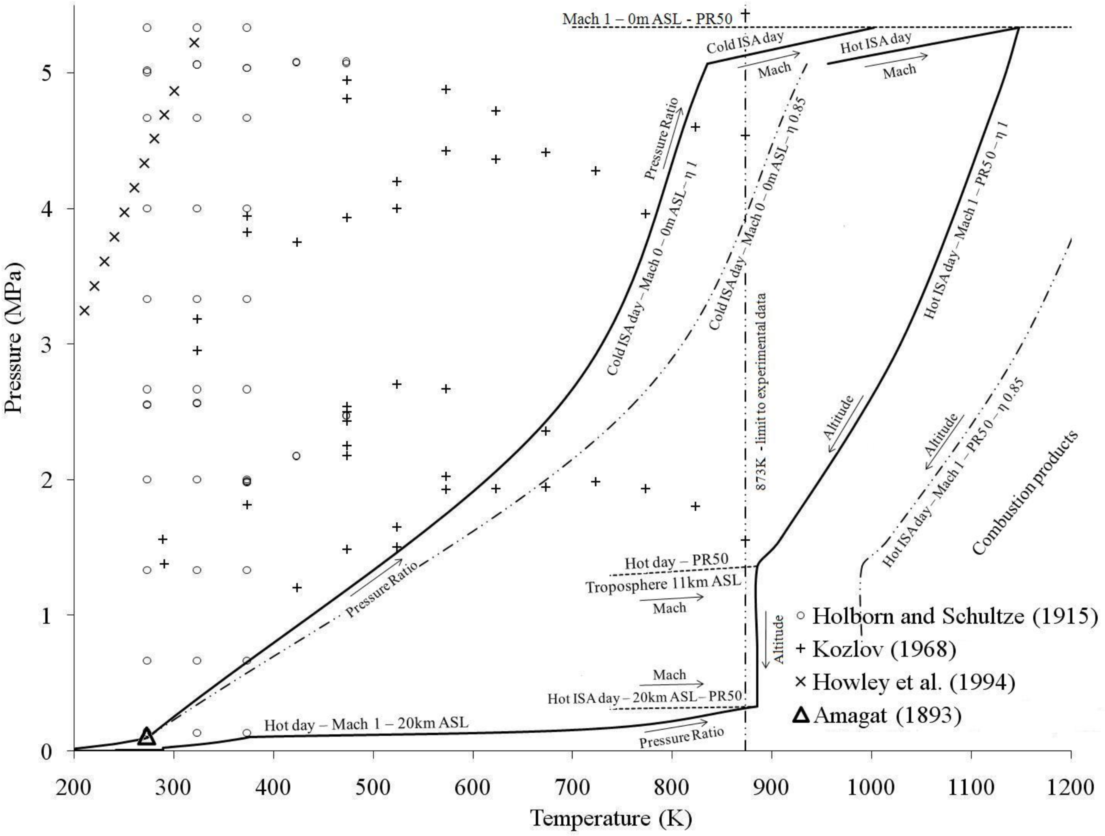

Figure 10.3: *Pressure and temperature envelope for gas turbine engines and experimental data available at such conditions*

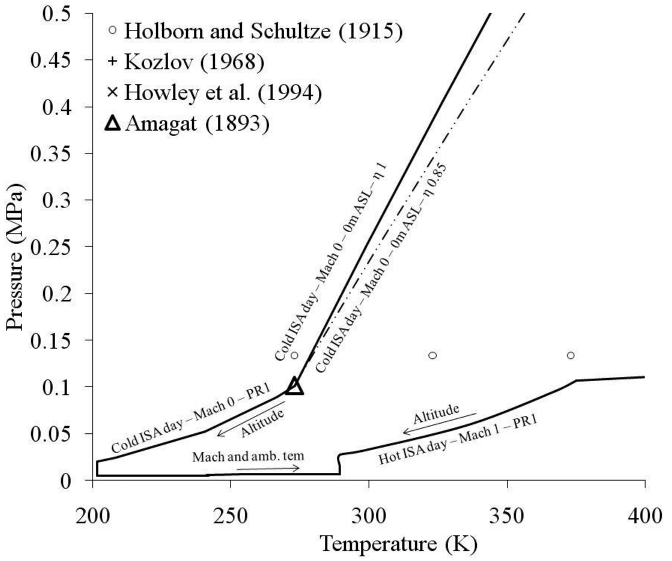

Figure 10.4: *Pressure and temperature envelope for gas turbine engines and experimental data available at such conditions. Detail*

Out of the aforementioned literature available only 15 points from two references, eleven from [99] and four from [78], contain data that fall within the isentropic jet engine environmental

Table 10.4: *Experimental $p-v-T$ data available for air inside the environmental operating envelope of the engine*

Reference	Temp. (K)	Press. (MPa)	Sp. Vol. (m^3/Kg)	Ideal EOS Dev (%)
Kozlov [99]	523.15	1.5049	0.10035	0.56
	623.15	1.9364	0.09314	0.83
	673.15	1.9454	0.10020	0.88
	673.15	2.3600	0.08264	0.93
	723.15	1.9864	0.10532	0.78
	773.15	1.9363	0.11545	0.73
	773.15	3.9598	0.05687	1.47
	823.15	1.8035	0.13193	0.69
	823.15	4.6027	0.05224	1.76
	873.15	1.5554	0.16212	0.61
	873.15	4.5406	0.05608	1.60
Holborn and Schultze [78]	273.15	0.1333	0.58811	0.00
	323.15	0.1333	0.69621	0.06
	373.15	0.1333	0.80414	0.09
	373.15	0.6667	0.16094	0.16

operating envelope, with pressures that range from $0.023MPa$ (ambient static pressure at eleven kilometres ASL on an ISA cold day) to $5MPa$ (HPC delivery pressure) and temperatures greater than $208.0K$ (ambient temperature at eleven kilometres ASL on an ISA cold day). These experimental points are grouped in table 10.4. The ideal gas assumption is found to underpredict the air properties by up to 1.5% especially at pressure values typical of high pressure compressor outlets. Note that, at the time of writing this manuscript, only the experimental data was available and the accuracy of the measurements taken by the different researchers remained to be established. Thus, it is advised to treat the results and more particularly the older data from Holborn and Schultze consequently.

10.2.6 Accuracy of the equations of state in the operating envelope of the gas turbine

The accuracy of the equations of state most commonly used in engineering was investigated for those experimental data sets of table 10.3 that cover the range of gas properties closest to those encountered in modern jet engines. Table 10.5 groups the averaged absolute error and the standard deviation of such error for nine EOS compared with the rig data produced by Kozlov [99], Holborn and Schultze [78] and Howley et al [82]. The absolute averaged error provides a measurement of the accuracy of the EOS, whereas the standard deviation is an indication of the dispersion of the equation. The most striking fact that can be observed from the results is the ineptitude of the ideal gas approximation to yield reasonable predictions at high pressures with errors that can be greater than 15% in some cases. On the other hand, three EOS exhibit a superior behaviour over the rest: Peng-Robinson, Soave and Redlich-Kwong. The latter is particularly attractive since it is the only

Table 10.5: *Accuracy of several equations of state in the operating envelope of a gas turbine*

	Howley $67 - 400K$ $1.06 - 35.2MPa$		Kozlov $288 - 873K$ $1.21 - 72.2MPa$		Holborn $273 - 473K$ $1.98 - 10MPa$		All data $67 - 873K$ $1.06 - 72.2MPa$	
	A (%)	St. D (%)	A (%)	St. D (%)	A (%)	St. D (%)	A (%)	St. D (%)
Ideal	5.59	4.23	15.44	12.35	1.30	1.08	11.39	11.76
VDW	4.78	3.31	2.99	2.25	2.14	1.20	3.14	2.45
Cla (II)	2.43	2.72	6.82	5.65	0.43	0.35	5.00	5.41
Ber	9.83	4.79	2.97	3.21	2.56	1.79	4.02	4.22
RK	1.85	1.20	4.04	2.64	0.87	0.43	3.14	2.57
Cla (III)	6.12	6.15	11.25	8.83	1.42	0.82	8.72	8.52
Soa	3.17	1.41	1.03	0.99	1.01	0.62	1.38	1.29
PR	2.28	1.86	0.94	0.88	0.23	0.23	1.03	1.21
Lemmon	0.069	0.37	0.086	0.07	0.069	0.11	0.080	0.19

two parameter equation that shows results comparable to higher order EOS. Unlike Soave and Peng-Robinson and further to its simplicity and robustness, Redlich-Kwong has the added benefit that its constants can be determined from the critical gas properties. As expected, the tailored Lemmon's equation is considerably and consistently more accurate than any other equation, at the expense of a much increased complexity.

The results provided by the mentioned EOS for the experimental points of table 10.4 show a comparable performance of Soave's, Peng-Robinson's and Lemmon's equations, with Berthelot and Redlich-Kwong close behind (Fig. 10.5). However, it is only Lemmon, Peng-Robinson and Soave, in this order, that are consistently accurate for broader conditions and in principle can be considered consistent inside the whole operating envelope of figure 10.3 as well.

10.2.6.1 Conditions of maximum deviation from the ideal gas assumption for a given pressure

The deviation from ideal of the different gas models is not linear with neither temperature nor pressure and hence the location of the maximum value of the compressibility factor changes accordingly. The compressibility factor predicted with all the gas models explained previously exhibit the same trend: at low temperatures the volume occupied by the real gas is smaller than the ideal, but this turns over progressively until at a given temperature the compressibility factor is maximum. For higher temperatures the ratio between the real and ideal volume decays asymptotically to 1 (Fig. 10.6).

The occurrence of the maximum compressibility factor for three EOS as a function of pressure and temperature is depicted in figure 10.7. Although for the three equations the position of the maximum deviation from ideal falls with temperature as pressure rises, there is a significant variation (around $300K$) of the particular values at which the maximum happens. In any case,

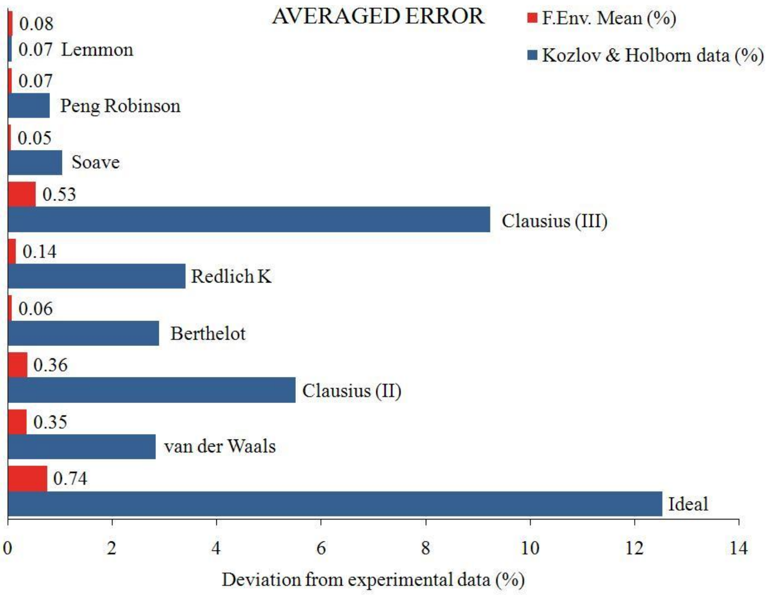

Figure 10.5: *Average error for different EOS in the operating envelope of the gas turbine and for Kozlov and Holborn data*

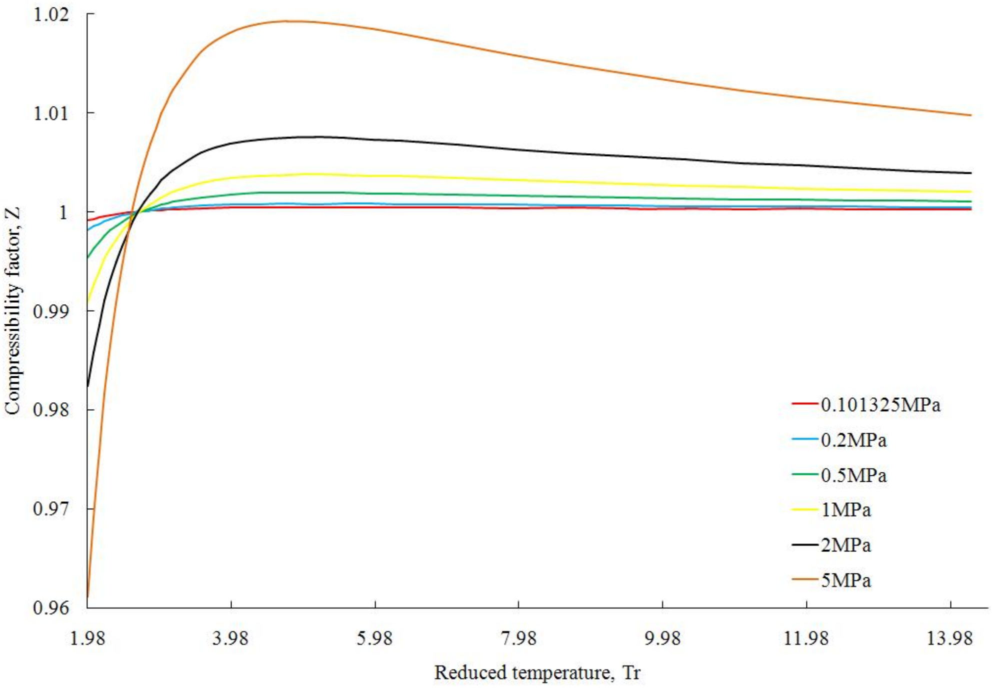

Figure 10.6: *Compressibility factor for Lemmon EOS for a range of temperature and pressure*

the maximum occurs in the neighbourhood of $750K$ and this suggests that the greatest errors introduced by the ideal gas assumption occur at conditions similar to those encountered at the outlet of modern HPCs rather than at the combustor exit contrary to what could be commonly believed[5]. Hence, deviations from ideal are smaller for higher and lower temperatures.

---

[5] However, departures of measured thermodynamic properties from predictions at the combustor outlet could still be greater aggravated by inappropriate calculation of gas mixtures and chemical equilibrium

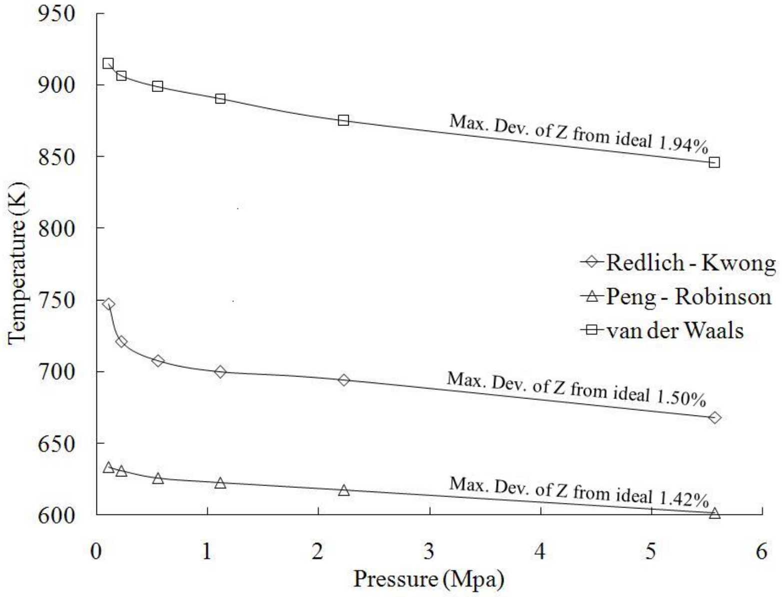

Figure 10.7: *p and T conditions for maximum Z*

10.3 Elementary thermodynamic properties and calculation of simple processes

This section ellaborates on the analysis of simple gas properties derived from the equations of state - heat coefficients and speed of sound - and simple compressions to provide an initial estimation of the results to be expected. This prepares the ground to understand the results of whole engine simulations. The deviation of the results from ideal for any magnitude are defined as:

$$Dev(\%) = \frac{real - ideal}{ideal} \cdot 100 \tag{10.21}$$

Consequently, magnitudes predicted by real models greater than the ideal are positive and smaller negative.

10.3.1 Specific heat coefficient at constant pressure

The specific heat coefficient becomes important in gas turbine performance simulations chiefly in the calculation of the energy balance on the engine shafts. It determines the temperature change of the working fluid across engine components for a given enthalpy variation. Its effect is also noticeable in the calculation of the ratio of specific heats, γ. Figure 10.8 shows the deviation from ideal of C_p calculated with three different EOS at three different temperatures. Both temperature and gas model have a comparable effect in the results, with deviations that can reach 0.5% in some desfavourable cases. Results are consistent with the existence of the mentioned maximum in Z at temperatures of the order of $750K$.

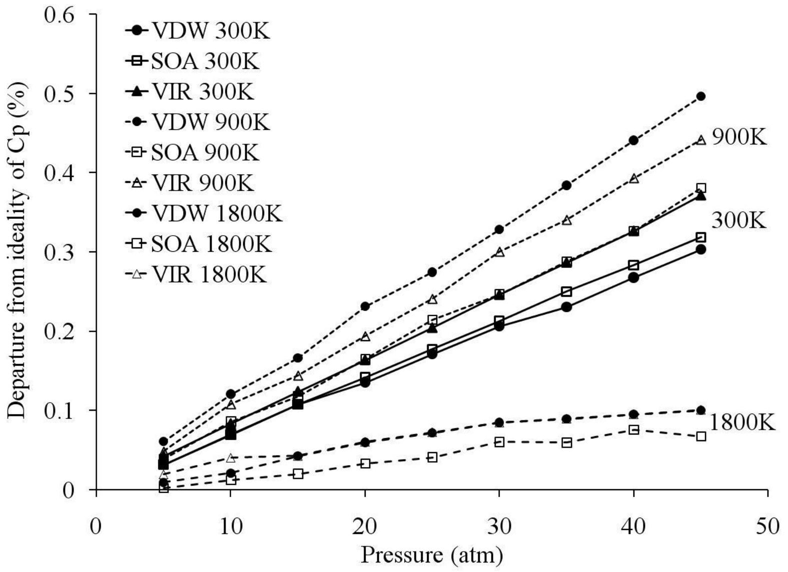

Figure 10.8: *Specific heat coefficient at constant pressure for several gas models and temperatures*

10.3.2 Speed of sound

The importance of the role that speed of sound plays in the prediction of engine performance lies in the calculation of mass flows through choked engine sections since the calculated flow velocity at sonic conditions vary. For each equation of state, the speed of sound is calculated by iteration from the definition (10.22) by imposing no entropy change in equation (10.23).

$$a = \sqrt{\frac{\partial p}{\partial \rho}}|_s \tag{10.22}$$

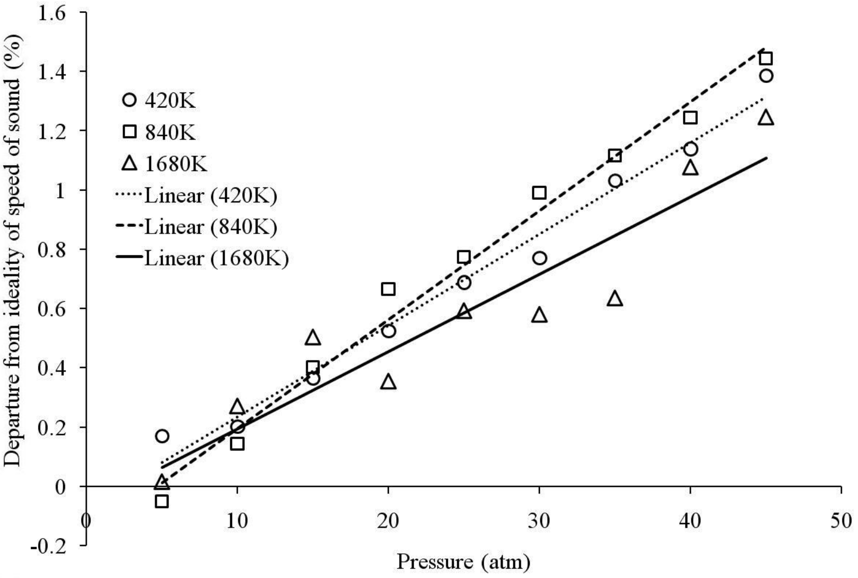

Figure 10.9: *Deviation of the speed of sound from the ideal gas model for van der Waals' EOS at several temperatures*

Figure 10.9 shows the deviation of the speed of sound for the equation of van der Waals with respect to the ideal speed of sound. The plot reveals that the departure decreases with temperature up to a cetain maximum to decrease again for high temperatures, yet again in agreement with the occurence of a maximum value of Z at around $750K$ as mentioned earlier in the text. To a first order, the deviation is a linear function of temperature, although the data present greater scatter at high temperatures.

10.3.3 Simple air compressions - effect of pressure ratio

The analysis of simple processes provides a valuable starting point to interpret whole engine simulations. For this purpose, a series of single compressions of air have been completed with several EOS varying the pressure ratio demanded from the compressor. The air is initially at $1atm$ and $300K$ and the politropic efficiency is considered constant ($\eta_p = 0.92$). Figure 10.10 reveals that the ideal gas assumption underpredicts the enthalpy gain of the compression; or in other words, the work input demanded by the compressor to achieve the same pressure ratio is greater. Although not exactly proportional to C_p in real gas models (see equation 10.24), to a first order this is consistent with the greater C_p predicted by real gas equations (Fig. 10.8). Hence for a single compression to a given pressure, real gases predict higher final temperatures than ideal processes.

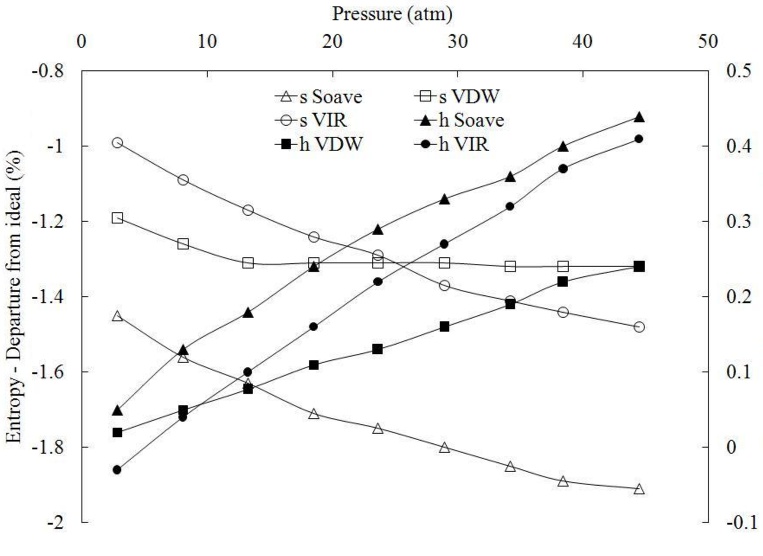

Figure 10.10: *Deviation of entropy and enthalpy from the ideal gas assumption for several EOS at several temperatures*

Entropy gains, on the other hand, are overpredicted by the ideal gas model. These simulations consider that the polytropic efficiency is constant for all EOS under analysis and this can give rise to distorted results. Turbomachinery efficiency maps are derived from calculations that are based on the measurement of the final pressure and temperature. It is evident that both real and isentropic enthalpy variations for the same final temperature are different depending on the equation of state used. As a result, the use of efficiency as a metric to measure the departure of a real process from isentropic may change slightly. However, this is of relative importance because the calculation of the final thermodynamic state of the air using an efficiency map would be perfectly accurate as long as the gas model used to build the map and to perform the calculations afterwards is the same.

10.4 Engine performance simulations

The impact of the different EOS on the prediction of engine performance is quantified by simulating the three spool high bypass ratio turbofan sketched in figure 10.11 with a 0 dimensional gas turbine performance prediction code. The main cycle parameters are grouped in table 10.6 and are chosen as representative values of those of a modern civil aircraft engine.

Table 10.6: *Engine cycle main parameters at design point*

Overall Pressure Ratio	46 ($15 \times 6.5 \times 4.8$)
Bypass Ratio	8.5
Turbine Entry Temperature	$1800K$
Takeoff Thrust	$330KN$
Inlet Mass Flow	$1180Kg/s$
Specific Fuel Consumption	$8g/KN\ s$

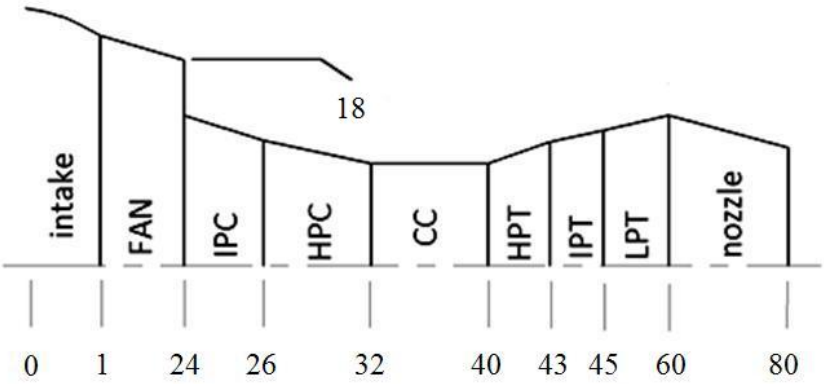

Figure 10.11: *Engine configuration and station numbering*

10.4.1 The Turbomatch scheme for gas turbine performance simulation

Turbomatch is a modular Fortran 0-D engine performance prediction code whose first version was developed by MacMillan [115] in 1974 based on the work of Palmer [139] at Cranfield University. The program consists of various subroutines that model the components performance and that are called up only as they are required so that the engine is “pieced together” by the user. This allows for a significant degree of flexibility to investigate alternative engine configurations and operating conditions. The software structure comprises three hierarchy levels: a master control program governs a set of engine component routines which, in turn, refer to some common thermodynamic data blocks. The flexibility of such approach is also convenient to the present study since it permits the easy modification of the thermodynamic data in the bottom level without any side-effects to the higher two blocks.

Turbomatch performs the design point calculation prior to any other off-design case. During this phase, the intake and nozzle geometries as well as the component maps are defined on the basis of the specified mass flow for an adapted nozzle. Then, when dealing with off-design conditions, the geometry of the engine is fixed and the code iterates on some guessed quantities until a converged solution is found. Details on the solution of the off-design problem are presented in [115].

Turbomatch treats the flow through the engine as dry air up to the combustor inlet and thereafter the flow dissociates into combustion products. The program uses pseudocritical values of the temperature and pressure of the resulting mixture calculated by adding up the critical temperature and pressure of the individual components weighed by their molar fraction. The EOS then yield an averaged compressibility factor for such pseudocritical properties. This methodology to calculate the thermodynamic properties of mixtures is known as the "Kay's rule". Other common rule that is commonly employed in gas turbine calculations is the Gibbs'-Dalton's Law: the thermodynamic properties of each chemical species at a given pressure and temperature are interpolated from the JANAF thermochemical tables [29] and the properties of the mixture are derived by adding them up weighed by the molar fraction they have in the mixture.

10.4.2 Whole engine calculations

10.4.2.1 Engine cycle calculations for unchoked nozzles

The prediction of the thermodynamic properties of the working fluid at each engine station is the base upon which all performance calculations (sfc, thrust, efficiencies) rest. For design (table 10.6) and off-design conditions, using TET as the calculations handle, the cycle and the deviations from ideal of several equations of state are plotted in figures 10.12 to 10.15. The ideal gas cycle is represented by the discontinuous line (left vertical axis) and the deviation from ideal of the different gas models can be read on the right vertical axis. The cycle line is labelled with the engine station numbers in agreement with figure 10.11. The equations investigated were those that were found more accurate after the experimental data survey: Redlich-Kwong (R-K), Soave (S), Peng-Robinson (P-R), Lemmon (L+PR) and Virial (VIR). However, since Lemmon's EOS was tailored to fit experimental data, it is not suited to predict the thermodynamic state of other compounds like gas turbine combustion products using neither the Gibbs'-Dalton's Law nor Kay's rule. Consequently, in this study Lemmon's equation was used in combination with Peng-Robinson's EOS; the former was used up to the HPC outlet and the latter from that station downstream.

Figures 10.12 and 10.13 show the total pressure evolution along the engine at the different engine stations for design and off-design conditions, running the model to a prescribed TET or fuel flows respectively. All real models underpredict the gas pressure in the engine with respect to ideal. The deviation is greater for Peng-Robinson's and Soave's EOS and exceeds 3.5% whereas the combined Lemmon's and Peng-Robinson's equations in turn produce the smallest departure. Differences from ideal rise monotonically up to the combustor inlet, and decrease subtly thereafter. This is consistent with the existence of the maximum in compressibility factor at about HPC outlet conditions. One plausible[6] explanation for this behaviour is that for a given temperature and pressure, a compressibility factor greater than 1 gives a smaller density and therefore mass flow through the engine sections compared to the ideal model. For a constant T_{40}/T_{24} and assuming that the effect of the deviation from ideal has a second order effect on the running line, the reduction in capacity causes a drop in spool speed and hence a smaller pressure ratio.

---

[6] Explaining and understanding the results is not a trivial but a quite obscure exercise. The deviation from ideal is positive for some magnitudes and negative for others, and thus magnitudes derived from complex calculations will vary depending on the relative importance of the deviation from ideal of each variable invoked in the calculations.

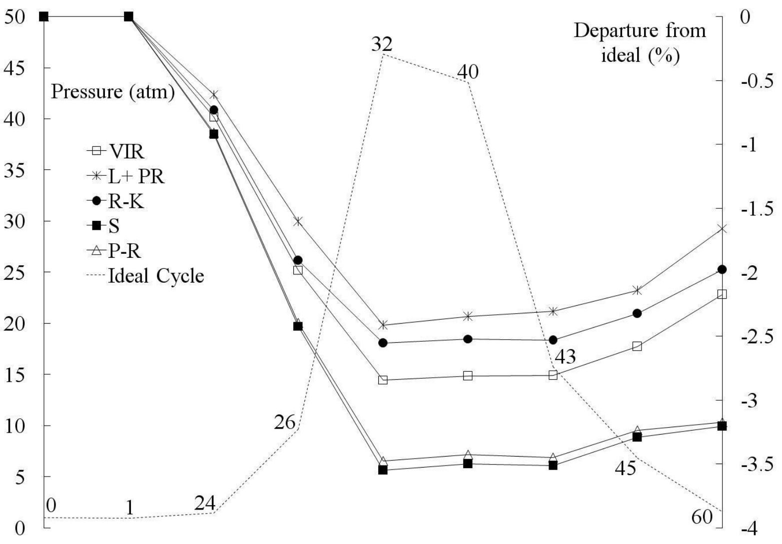

Figure 10.12: *Engine cycle pressure at design conditions at each station and departure from the ideal gas assumption for several gas models*

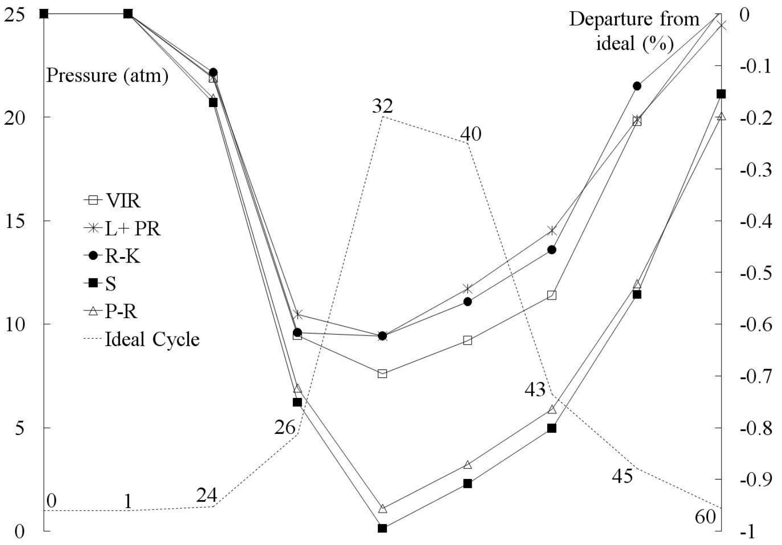

Figure 10.13: *Engine cycle pressure at off-design conditions at each station and departure from the ideal gas assumption for several gas models - Fuel flow* $0.8Kg/s$

As expected due to the lower temperatures and pressures of the cycle, the off-design case exhibits the same behaviour but with overall smaller deviations (fig. 10.13). The on design calculation determines the exit area of the nozzle so that it is adapted at SLS conditions (static pressure equals the ambient at the nozzle exit at Mach 1). Lower TET temperatures at SLS conditions will unchoke the nozzle and expand the flow at the outlet of the engine to total conditions closer to the ambient - hence lower jet velocity. As a result, deviations from ideal tend to zero at station 60.

Figures 10.12 and 10.13 are paired up with figures 10.14 and 10.15 in that they show the same design and off-design operating points. The deviation of the cycle temperatures at design conditions pivots around the TET because this is the calculations handle (fig. 10.14).

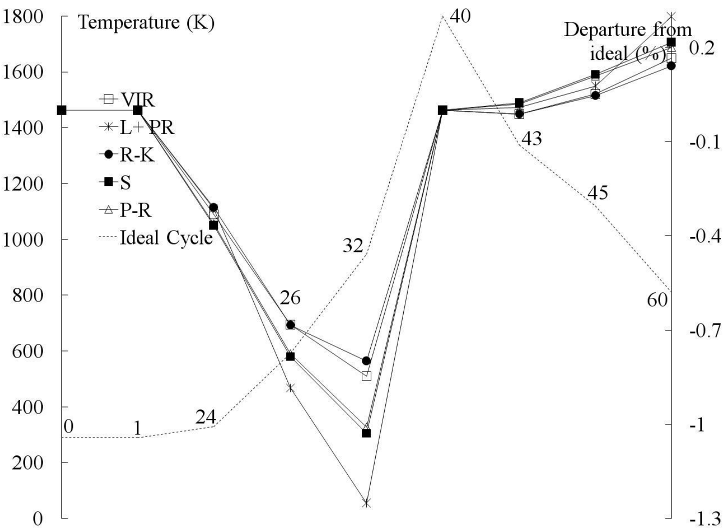

Figure 10.14: *Engine cycle temperature at design conditions at each station and departure from the ideal gas assumption for several gas models*

Predicted temperature leaps are smaller across compressors and greater across turbines for real models compared with the ideal gas assumption. This is compatible with the lower pressure ratio yielded by real models (fig. 10.12) that lead to lower compressor work and hence lower compressor outlet temperatures. The turbines are in turn required to produce less work, and hence temperature drops are smaller when calculated with real gas models.

At off-design conditions however, since the engine model runs to fuel flow rather than to a temperature value, the temperature deviation profiles are no longer anchored to the TET value. Figure 10.15 conveys the clear message that real models show that 1% drop in compressor pressure ratio produces the same compressor delivery temperature than the ideal and it translates to turbine outlet temperature gains of roughly the same order.

10.4.2.2 Engine cycle calculations for choked nozzles

Results so far have been obtained for adapted or unchoked nozzles. This limits the deviation of real models from ideal because static pressure at the outlet of the nozzle is set to atmospheric. Deviations pivot around two fixed points: T_{40} and p_{80}. If the nozzle is choked, however, the boundary condition of static pressure at the nozzle exit is replaced by imposing sonic flow at its throat. Unlike the static pressure that is a fixed value for whatever gas model used, the temperature and pressure that yield a sonic Mach number change with the EOS being used. This causes greater deviations of the real models from ideal at the outlet of the LPT (fig. 10.16). Temperature profiles, on the other hand, are not very sensitive to the operation regime of the nozzle (fig. 10.17)

10.4.2.3 Whole engine performance calculations

The previous sections have prepared the ground for whole engine performance analyses. While the cycle results shown in the previous epigraph are of interest mainly to the engine manufacturer, the accuracy of whole engine performance simulations has a broader impact outside the engine company. One of the roles of the performance office of any engine manufacturer is to develop

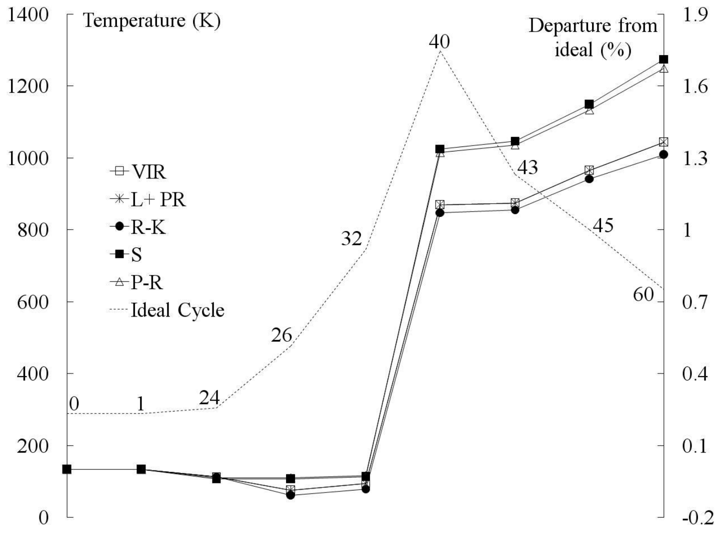

Figure 10.15: *Engine cycle temperature at off-design conditions at each station and departure from the ideal gas assumption for several gas models - Fuel flow* $0.8Kg/s$

Table 10.7: *Departure from the ideal gas assumption of whole engine performance parameters for several equations of state at design conditions - TET = 1800K*

EOS	SFC	Specific Thrust	Flow capacity $\frac{W\sqrt{T}}{P}$
	$\frac{g}{kNs}$	$\frac{Ns}{kg}$	$\frac{sK^{0.5}}{m^3}$
Ideal	7.912	279.92	0.197
		Deviation from ideal (%)	
RK	-1.05	-1.23	-1.00
Soa	-0.97	-1.72	-1.46
PR	-0.95	-1.70	-1.47
Lemmon + PR	-0.63	-1.19	-0.94
Virial	-1.07	-1.33	-1.08

performance customer decks that allow the airframer to carry out integration and mission analysis calculations. To this regard, deviations of the order of 1% on the results provided by the customer deck can have a profound impact on the mission design and analysis.

Design point deviations of specific fuel consumption, specific thrust and engine mass flow capacity from ideal of several gas model are grouped in table 10.7. As it has been the norm in previous results, relative differences between Soave's and Peng - Robinson's EOS are imperceptible. Deviations from ideal for all the equations oscillate around -1% with the coupled Lemmon Peng - Robinson model slightly off the general trend.

For off-design conditions TET was no longer the handle and instead the engine model was run to a given fuel flow. Performance parameters have to be compared against the engine handle as this is the only magnitude that remains constant for all calculations. If results were compared against say, for example, TET, this would lead to inaccuracies since TET changes for each gas model used in the simulations.

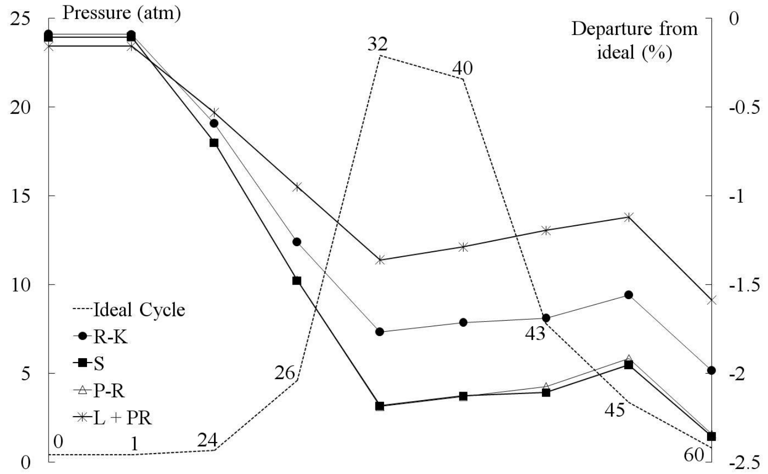

Figure 10.16: *Engine cycle pressure at off-design conditions at each station and departure from the ideal gas assumption for several gas models - Choked nozzle. Fuel flow* $1.34 Kg/s$

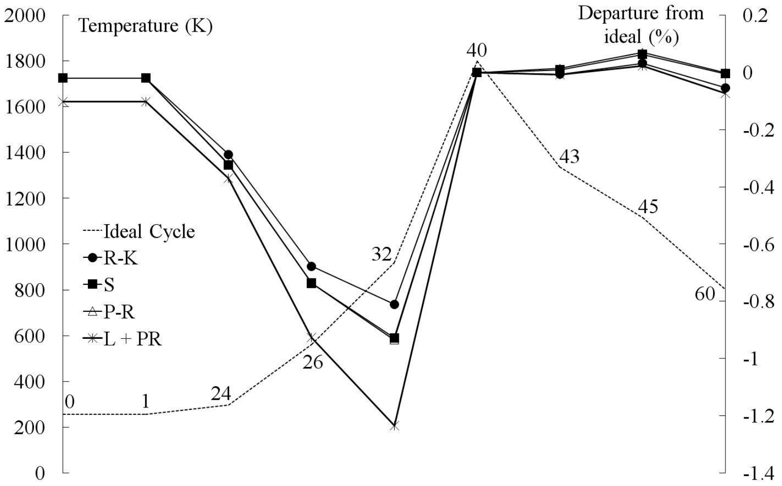

Figure 10.17: *Engine cycle pressure at off-design conditions at each station and departure from the ideal gas assumption for several gas models - Choked nozzle. Fuel flow* $1.34 Kg/s$

TET predicted for the various real models is found to be offset from the ideal case by a constant amount for each EOS, and this is quite consistent throughout the whole operating regime of the engine (fig. 10.18).

Departures from ideal of the specific fuel consumption diminish at high power, with Soave and Peng - Robinson being the furthest from ideal (fig. 10.19). It could generally be said that real models overpredict the SFC by around 0.6% when compared with the ideal gas assumption.

The departure of specific thrust (fig. 10.20) and mass flow capacity (fig. 10.21) from ideal follow the same trend. Deviations fall with power, yet again with Peng - Robinson and Soave's yielding the results most deviated from ideal. At part load, real models seem to underpredict specific thrust and capacity by around 3% when compared with the ideal gas.

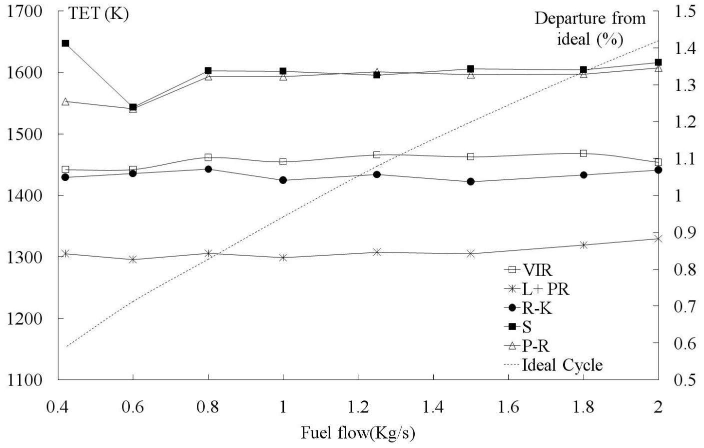

Figure 10.18: *Turbine entry temperature versus fuel flow and departure from the ideal gas assumption of several gas models*

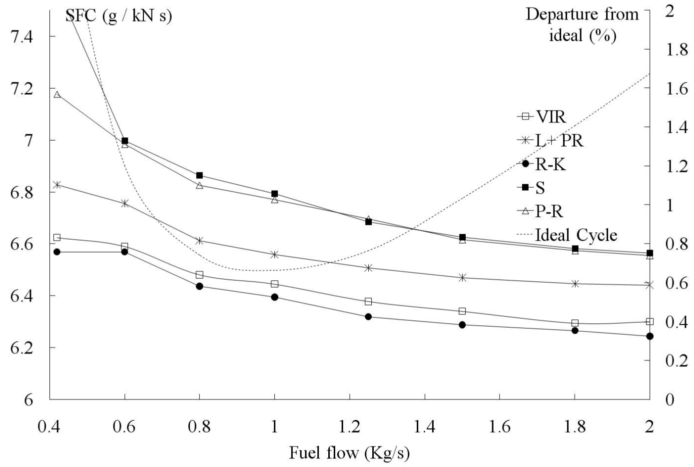

Figure 10.19: *Specific fuel consumption versus fuel flow and departure from the ideal gas assumption of several gas models*

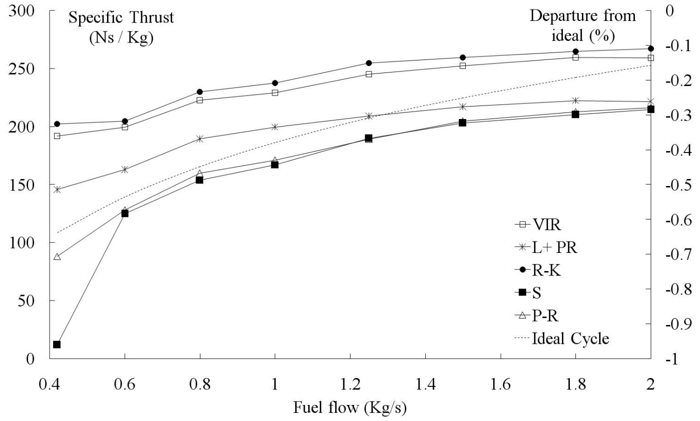

Figure 10.20: *Specific thrust versus versus fuel flow and departure from the ideal gas assumption of several gas models*

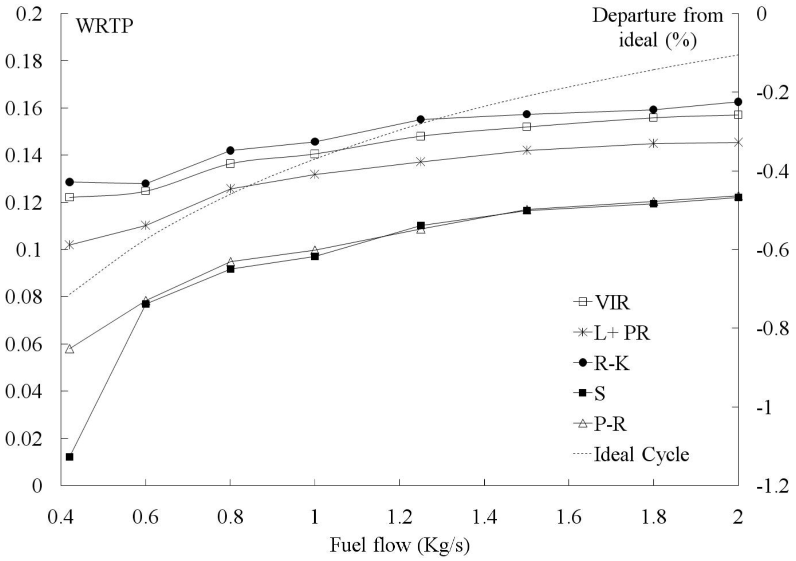

Figure 10.21: *Engine flow capacity versus fuel flow and departure from the ideal gas assumption of several gas models*

10.4.2.4 Contribution of the different engine components to the deviation from ideal

The contribution of each engine component to the deviation from the ideal gas assumption of the results shown in this chapter is not clear since deviations from ideal at a given engine station are propagated in the calculations upstream and downstream to other components. The impact of each engine component on the deviation from the ideal gas assumption was quantified by running design point simulations in which the Peng Robinson equation was used to calculate the flow across a single engine component while the rest of the engine was calculated with the ideal gas assumption. Results show that the high pressure components account for around 50% of the deviation. This is in agreement with the maximum exhibited by the in compressibility factor at temperatures around 750K at high pressures. The intermediate and low pressure systems follow, with the intake and the nozzle causing around 6% of the departure from ideal.

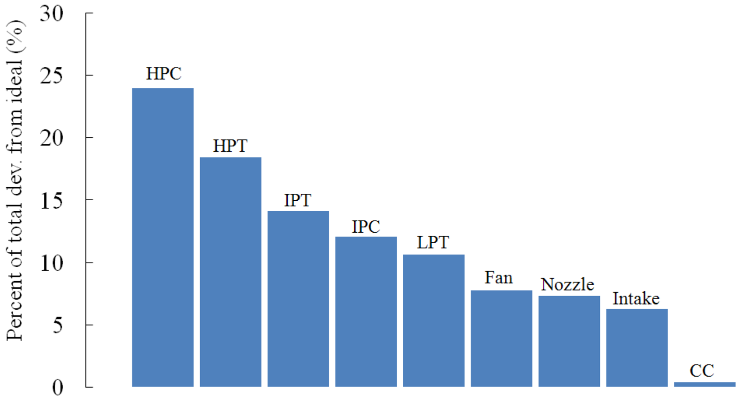

Figure 10.22: *Relative engine component contribution to the departure from the ideal gas assumption*

10.5 Concluding remarks and recommendations for future work

The accuracy of the perfect gas equation is taken for granted in most turbomachinery design and analysis softwares, including performance simulation tools. While the effect of chemical dissociation has been studied in the past [88][21], it is surprising that in spite of their extended use, the appraisal of gas equations of state for turbomachinery applications has not been undertaken in the past. Performance models in particular are routinely used by engine and aircraft manufactures for several purposes, including preliminary engine design, mission analysis, market studies and test support. Therefore, the estimation of their accuracy is crucial to determine the reliability of such widely used tools. This chapter has looked at the accuracy of commonly used equations of state for gases to predict the $p - v - T$ state of air and their impact on whole engine performance simulations. On a general note, it is likely that the perfect gas assumption may not be adequate for other commonly used tools like CFD and its accuracy in this context should be investigated.

The ability of gas models to predict the $p - v - T$ state of air was investigated thoroughly for the very limited experimental data available in the public literature for the operating conditions of a modern turbofan engine. Deviations from experimental data of the ideal gas model can reach 1.76% in the worst case analysed. The tailored Lemmon equation has shown a marked superior performance over any other equation of state at any conditions of pressure and temperature. However its use in performance calculations is severely hampered by its complexity and its large number of coefficients. Peng Robinson equation shows a similar performance in the range of pressures and temperatures of interest and therefore is recommended as a convenient alternative.

As a rule of thumb, it could be said that non ideal gas models predict pressures and temperatures at maximum take-off conditions 2% and 1% lower that the ideal gas assumption on the high pressure spool of modern high bypass ratio turbofans. In terms of the overall predicted performance of the engine this translates into roughly 0.5% less thrust and 2% more in SFC than that predicted by the ideal gas model.

Given the scarcity of experimental data available in the range of operation of the gas turbine it would be definitely useful to design and carry out rig tests to produce a reliable database against which the different models can be compared. The experimental facility used by the National Institute of Standards and Technology in the United States to obtain $p - v - T$ data of different substances is an outstanding starting point to design an experimental rig.

It is advised that the research continued with the assessment of the impact of different gas mixing rules on engine performance simulations, in a similar fashion as the work completed for the equations of state. The flow downstream of the combustor is composed of chemical species in equilibrium and the overall thermodynamic state of the mixture is calculated by some form of mixing rule. This is generally an average of the properties of each of the species present in the mixture weighed, for example, by their molecular fraction.

Appendix 10A - Path integration

The goal pursued here is the calculation per unit mass of the enthalpy, entropy and internal energy of a simple monocomponent compressible system that evolves between two equilibrium states, initial (1) and final (4). It can be demonstrated [187] that differential variations of h, s and u of such a system can be written in terms of the variables (T, v) in the following manner:

$$ds = \frac{c_v}{T}dT + \frac{\partial p}{\partial T}|_v dv \tag{10.23}$$

$$dh = [c_v + v\frac{\partial p}{\partial T}|_v]dT + [T\frac{\partial p}{\partial T}|_v + v\frac{\partial p}{\partial v}|_T]dv \tag{10.24}$$

$$du = c_v dT + [T\frac{\partial p}{\partial T}|_v - p]dv \tag{10.25}$$

These expressions will be useful for data expressed as follows:

- Equation of state expressed as $p = p(T, v)$
- Specific heat at constant volume known as a function of T and p along an isochor line, v^0; that is, $c_v = c_v(T, p, v^0)$

$$c_v(T, v) = c_v^0(T) + T\int_{v^0}^{v} \frac{\partial^2 p}{\partial T^2}|_v dv \tag{10.26}$$

The choice of variables (T, v) is dictated by the form of the EOS described previously, $p = p(T, v)$; it is an uncomplicated algebraic exercise to obtain dh, ds and du in variables (p, T) or (p, v) for EOS of the form $v = v(p, T)$ and $T = T(p, v)$ respectively. Furthermore, if the specific heat coefficient c_v in equations [10.23 - 10.25] is not known it can be derived from the generalised relationship between c_v and c_p, provided that c_p is given[7]:

$$c_p - c_v = T\frac{\partial v}{\partial T}|_p\frac{\partial p}{\partial T}|_v = T\frac{\alpha^2 v}{k_T} \tag{10.27}$$

Bearing in mind that the energetic variables h, s and u are point functions, their value at two different states 1 and 4 can be evaluated independently of the process undergone by the fluid inbetween those two states. Hence, for calculation purposes and regardless of the real gas evolution, a fictional three stage process that comprises two isothermal and one isochor evolutions can be ideated, so that the evolution $2-3$ occurs at a constant reference specific volume, v^0, for which c_v is known as a function of pressure and temperature. Therefore:

- Evolution 1 → 2: $T = T_1 = T_2$; $dT = 0$, $dv \neq 0$

---

[7] Expressions for c_p are abundant in the literature. Take for instance [185] where c_p is given for dry air and combustion products as a function of static temperature at a reference pressure.

- Evolution 2 → 3: $v = v_2 = v_3 = v^0$; $dT \neq 0$, $dv = 0$
- Evolution 3 → 4: $T = T_3 = T_4$; $dT = 0$, $dv \neq 0$

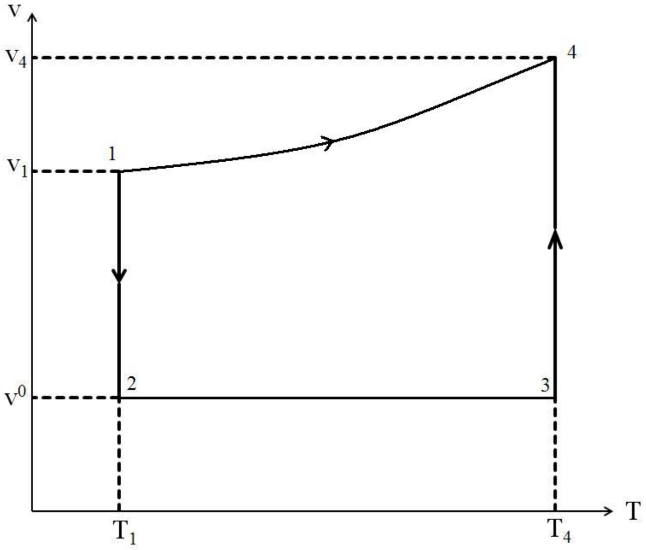

Figure 10.23: *Path integration from an initial state 1 and a final state 4*

For values of the reference specific volume v^0 such that $v^0 >> 1$ ($\rho \rightarrow 0$, perfect gas) the evolution between points 2 and 3 corresponds to a semi-perfect gas like evolution and processes $1-2$ and $3-4$ represent the departure from semi-perfect gas due to compressibility.

Chapter 11

Conclusions, contribution to knowledge and way forward

The simulation of the transient engine performance after a shaft failure is one of the most difficult problems in the engine to analyse. It requires a very high degree of integration of aerothermal and mechanical effects into a single tool to account for all the very complex and interrelated phenomena involved in the event.

This research pursues a better understanding of the engine behaviour during the over-speed and the enhancement of the current modelling capability of the event. The approach adopted in the work is to develop far off-design component modelling methodologies for the provision of extended component characteristics that can be integrated into a single "all in one" engine transient performance model. Such components have been completed and are ready to be integrated in the shaft over-speed modelling tool. The research has also carried out a preliminary study to investigate the suitability of an industry proprietary code to capture the complex stalled performance of the compressor and the combustor after the failure.

On the other hand, the collaboration with Rolls-Royce triggered the opportunity to conduct research in other aspects of the field of engine performance engineering. In particular the research makes noteworthy contributions to the optimisation of variable geometry schedules, inlet guide vane loss and deviation modelling and the effect of the thermodynamic gas modelling on the simulation of gas turbine performance.

The following sections summarise the contribution to knowledge made by the present work and provide detailed guidelines to continue the research in the future.

11.1 Contribution to knowledge and deliverables

This study has gone some way towards enhancing the current modelling capability of shaft failure events. However, apart from the results particular to the engines and scenarios analysed, the greatest value of this research lies on the wide applicability of the novel methodologies developed to derive the performance of engine components at far off-design conditions. The findings from this study make the following contributions to the current literature:

1. *CFD simulation of an over-speeding turbine during an IP shaft failure event.* The simulations provide a preliminary insight to understand the flow field that develops across the IP turbine rotor and the first stage of the LPT.
2. *Design of a cascade rig for turbine vanes at high negative incidences.*
3. *Extensive experimental database of turbine NGV at high negative incidences.* The data is amenable to be used as a validation platform for numerical simulations. The data was delivered to the sponsor for validation of proprietary CFD codes, numerical tools and methodologies.
4. *Investigation of the capability of CFD to simulate losses in highly separated turbine flows.* This study provides a measurement of the order of magnitude of the error of CFD to calculate separated turbine flows.
5. *Flow visualisation of the secondary flow across turbine vanes at high incidences.* Data available in the public domain is limited to incidence angles down to $-53°$. The flow visualisation of the flow over a turbine NGV at as much as $-113°$ help to understand the flow development across the turbine passage at such far off-design conditions.
6. *Extended turbine loss model.* The data obtained from the NGV test rig allowed extending commonly used turbine loss models that can be used early in the turbine design process.
7. *Methodology to derive turbine maps during an over-speed of the upstream shaft.* The stage splitting/stacking technique developed in chapter 4 replaces the performance of the first stage in the whole turbine map when the upstream shaft over-speeds. The turbine maps obtained with this methodology can be integrated in whole engine performance simulation decks.
8. *Internal air system dynamics model.* Although extensive research has been carried out on the modelling of internal air systems, all models of the air system published in the literature are limited to steady state conditions and no single study exists which adequately deals with the transient performance of the system. Chapter 5 covers the development of a modular tool that can simulate the transient performance of the secondary air system and is able to handle reverse and supersonic flow along the system. The configuration of the air system can be changed readily making it a very flexible tool to assess the response of the system to rapid transients. The software and its manual have been delivered to Rolls-Royce to be included in the company's tool set.
9. *Methodology to calculate the endloads on turbine discs during rapid transients.* The air system model provides the evolution of the pressure in the cavities of the system that can be integrated to provide the evolution of the axial loads on the turbomachinery discs.
10. *Database of the performance of compressor blades in reverse flow.*
11. *Methodology to derive extended compressor maps in reverse flow.* The stage stacking technique described in chapter 6 uses the compressor characteristics obtained from CFD to derive the compressor map at reverse flow conditions. In a similar fashion to the turbine map,

the extended compressor characteristics can be integrated in the “all in one” performance tool to model the shaft over-speed.

12. *Extension of compressor reverse flow 2D models.* Analytical two-dimensional models based on first principles of compressor blades in reverse flow are not reliable because of their inability to capture the strong three-dimensional flows present across rotor blades. The methodology proposed in this thesis accounts for the three-dimensional effects of the flow by the introduction of a novel coefficient connected to the high pressure loss across the blades in reverse flow.

13. *IGV loss, deviation and stall models.* Commonly used compressor pressure loss, deviation and stall models are not suited to calculate the very high incidence flows on compressor variable geometry vanes. Loss, deviation and stall correlations for a range of flow conditions and flow angles were developed and used to predict the characteristics of two state-of-the-art axial compressors for a range of shaft speeds. Results show a close agreement between the rig data and the results from the calculations.

14. *Compressor variable geometry optimiser.* The genetic algorithm based optimiser described in chapter 9 provides and inexpensive methodology to find the most flow efficient schedule that conforms to a prescribed value of the surge margin. The software and accompanying manuals have been delivered to Rolls-Royce to be integrated into the company’s tool set.

15. *Appraisal of common gas equations of state to predict the $p - v - T$ state of air.* The ability of the most common equations of state to predict the $p - v - T$ state of air was critically assessed. It was concluded that the equations of Redlich-Kwong and Peng-Robinson are the best compromise between the accuracy of the results and the complexity of the equation.

16. *Investigation of the effect of gas models on engine performance simulation.* This study quantified the deviations of whole engine performance calculations carried out with real gas model from the ideal gas assumption.

11.2 Recommendations for further work

While there are well established methodologies to predict the behaviour of the engine when the high pressure or low pressure shaft fail, there are still many open questions pertaining the modelling of the failure of the intermediate pressure shaft. It is clear that the progression of a shaft failure event is very complex to model and much additional work will be required before a complete understanding of the phenomenon is possible. It is hoped that the current study will stimulate more work in this field.

11.2.1 Whole engine modelling

The isolated component models and performance maps developed in this work are in place ready to be used in whole engine performance calculations. The future work should be directed towards the vertical integration of such maps into a whole engine transient model to simulate the shaft over-speed event. On the other hand, thanks to the modular nature of the multidisciplinary tool to model the over-speed, the models of the individual engine components can be superseded by improved models once they become available.

11.2.2 Engine component modelling

This research has originated many questions in need of further investigation. In addition to the conclusions at the end of each chapter, suggestions to carry on the work on the different research topics are detailed next.

11.2.2.1 Turbine Aerodynamics

The studies conducted to quantify the loss in flow capacity of turbine vanes at high negative incidence are based on a given vane geometry. Geometrical features such as cascade solidity, flow turning and the stagger angle of the vanes should be investigated for a wider applicability of the results. Further to numerical studies, possible future studies using a similar experimental set up are apparent.

11.2.2.2 Compressor reverse flow modelling

Although the methodology to derive the extended compressor characteristics in reverse flow is valid for any compressor, results shown in chapter 6 are peculiar to the compressor geometry simulated with CFD. Blade geometry effects are considered to be of second order but further analysis is required to support this claim. Moreover, the database of the performance of compressor blades in reverse flow should be completed with the simulation of wider conditions of operation and compressor geometries.

11.2.2.3 Air system dynamics modelling

The qualitative description of the flow along the air system of gas turbines in steady state is abundant in the literature. The modelling of the steady state performance of air systems is common place among engine manufacturers and is also relatively well documented. The modelling of the transient performance of the SAS has not been studied in the past, chiefly because it is only relevant in rapid failure scenarios. The complex nature of the vortical flow within the system adds considerably to the intractability of the problem.

The current research has provided an excellent modelling platform to model the response of the air system to rapid transients. The modular nature of the code makes it suitable of being upgraded to include further elements in the network. To this regard, it is suggested that other elements of the air system are included in the network such as cooling holes, brush seals and flow junctions. Future research should also concentrate on the investigation of the effect of heat input into the system.

11.2.2.4 Inlet guide vanes loss, deviation and stall modelling

The IGV loss, deviation and stall models presented in chapter 7 are derived from the 3D CFD simulation of an IGV and the first rotor of an intermediate pressure compressor. Correlations link pressure loss and deviation against IGV setting angle and mass flow in a very simple manner. Considerably more work will need to be done towards the generalisation of the models by supporting the correlations with the physics based analysis of the flow, in a similar fashion to Lieblein's work. Preliminary studies on the connection between pressure losses and deviation and the force coefficients on the blades have yielded promising results [33].

11.2.2.5 Variable geometry optimiser

The main limitation of the work carried out to find the most flow efficient schedule of the variable geometry of an axial compressor is the limited accuracy of one-dimensional approaches to calculate the surge margin. The correlations employed in this work are those due to Raley that are thirty years old.

It is suggested that further research focuses on the appraisal of other methodologies - Aungier's model could be a good starting point - to predict the surge margin of axial compressors. The optimiser can be readily modified to integrate other means of calculating the surge margin for a greater accuracy of the tool.

11.2.2.6 Thermodynamic gas modelling effect on engine performance simulation

The thorough survey of the public literature showed a very limited amount of experimental $p{-}v{-}T$ measurements available for air in the range of operation of the gas turbine. The design and test of an experimental rig should be undertaken for the provision of comprehensive data to validate models and carry out performance calculations.

Equally important as the estimation of the accuracy of gas models to calculate the $p - v - T$ state of air is the investigation of the suitability of different mixing rules to calculate the state of combustion products. It is advised that a similar study to that completed here for the equations of state is conducted to evaluate the accuracy of different mixing rules.

Bibliography

[1] R.B. Abernethy, R.P. Benedict, and R.B. Dodwell. Asme measurement uncertainty. *Journal of fluids engineering*, 107:161–164, 1985.

[2] AIAA. Guide for the verification and validation of computational fluid dynamics simulations. *AIAA paper*, (G-077-1998), 1998.

[3] A. Alexiou, N.J. Hills, C.A. Long, A.B. Turner, L.S. Wong, and J.A. Millward. Discharge coefficients for flow through holes normal to a rotating shaft. *International Journal of Heat and Fluid Flow*, 21:701–709, 2000.

[4] A. Alexiou and K. Mathioudakis. Secondary air system component modelling for engine performance simulations. In *ASME Turbo Expo 2008*, number GT2008-50771, 2009.

[5] E.A. Amagat. *Ann. Chem. Phys.*, 29:68, 1893.

[6] A. Ameri. NASA rotor 37 CFD code validation. glenn-ht code. In *47th AIAA Aerospace sciences meeting including the new horizons forum and aerospace exposition*, number AIAA 2009-1060, 2009.

[7] M. Arias. Compressor VIGV and VSV schedule optimisation. MSc thesis, Cranfield University, School of Engineering, 2008.

[8] T. Arts, H.L. Boerrigter, J.M. Buchlin, M. Carbonaro, G. Degrez, R. Denos, D. Fletcher, D. Olivari, M.L. Riethmuller, and R.A. Van den Braembussche. *Measurement techniques in fluid dynamics.* von Karman Institute for Fluid Dynamics, 2^{nd} edition, 2001.

[9] R.H. Aungier. *Axial-flow compressors: a strategy for aerodynamic design and analysis.* ASME Press, 2003.

[10] Several Authors. *Verification and validation of computational fluid dynamics.* Von Karman Institute - Lecture series 2000-08, 2000.

[11] Several Authors. Flow in rotating components - discs, cylinders and cavities. *Engineering science data unit (ESDU)*, (Data item 07004), 2007.

[12] Several Authors. Performance prediction and simulation of gas turbine engine operation for aircraft, marine, vehicular, and power generation. *Final report of the RTO applied vehicle technology panel (AVT) task group AVT-036*, 2007.

[13] Several Authors. Labyrinth seal flow. *Engineering sciences data unit (ESDU)*, (Data item 09004), 2009.

[14] D.R. Ballal. Progress in aero engine technology (1939-2003). In *AIAA/ASME/SAE/ASEE Joint Propulsion Conference and Exhibit, AIAA 2003-4412*, 2003.

[15] K. Bammert and P. Zehner. Measurements of the perfomance of an air turbine stage at positive and negative mass flow and rotational speed (four-quadrant characteritics). *Journal of Turbomachinery*, 100:22–29, 1978.

[16] J.A. Beattie and O.C. Bridgeman. A new equation of state for fluids. i. application to gaseous ethyl ether and carbon dioxide. *Journal of the American Chemical Society*, 49(7, pages =), 1927.

[17] M. Benedict, G.B. Webb, and L.C. Rubin. An empirical equation for thermodynamic properties of light hydrocarbons and their mixtures: I. methane, ethane, propane and n-butane. *Journal of Chemical Physics*, 8(4):334–345, 1940.

[18] D. Berthelot. Sur une méthode purement physique pour la détermination des poids moléculaires des gaz et des poids atomiques de leurs éléments. *Journal de Physique Théorique et Appliquée*, 8, 1899.

[19] R.S. Bessel. *The thermodynamics and gas dynamics of internal combustion engine*, volume 1. Clarendon Press, 1982.

[20] W. Blanke. Proceedings of the 7th symposium of thermophysics properties. *The American Society of Mechanical Engineers*, page 461, 1977.

[21] B. Bottin. Computation of thermodynamic properties of arbitrary perfect gas mixtures at low pressures and high temperatures. *Von Karman Institute for fluid dynamics*, Technical note 195, 1997.

[22] S.G. Brown. Private conversation, 2010.

[23] C. Calcagni. Secondary air system dinamics modelling during shaft failure. MSc thesis, Cranfield University, School of Engineering, 2008.

[24] C. Calcagni, L. Gallar, V. Pachidis, and P. Pilidis. Development of a one-dimensional dynamic gas turbine secondary air system model part ii: assembly and validation of a complete network. In *ASME Turbo Expo 2009*, number GT2009-60051, 2009.

[25] A. Cantarero. Experimental and numerical investigation of turbine NGVs at high negative incidence. MSc thesis, Cranfield University, School of Engineering, 2010.

[26] T. Cebeci, J.P. Shao, F. Kafyeke, and E. Laurendeau. *Computational fluid dynamics for engineers*. Springer, 2005.

[27] J.K. Changduk Kong and C. Lee. Components map generation of gas turbine engine using genetic algorithms and engine performance deck data. *ASME paper*, (GT 2006-90975).

[28] B. Charnley, L. Gallar, and E. Giordano. High speed flow evaluation using particle image velocimetry. In 2^{nd} *joint EVI-GTI / PIWG international gas turbine instrumentation conference*, number 016, 2008.

[29] M.W. Chase. *NIST-JANAF Thermochemical Tables*, volume 9. Journal of Physical and Chemical Reference Data Monographs, 4^{th} edition, 1998.

[30] J.W. Chew, J.M. Owen, and J.R. Pincombe. Numerical predictions for laminar source-sink flow in rotating cylindrical cavity. *Journal of Fluid Mechanics*, 143:451–466, 1984.

[31] A. Chipperfield and P. Fleming. Multiobjective gas turbine engine controller design using genetic algorithms. *IEEE Transactions on Industrial Electronics*, 43(5), 1996.

[32] S.H. Chue. Pressure probes for fluid measurements. *Prog, Aerospace Sciences*, 16(2):147–223, 1975.

[33] R. Cirligeanu. IGV loss model generalisation. MSc thesis, Cranfield University, School of Engineering, 2010.

[34] R. Clausius. Ueber das verhalten der kohlensure in bezug auf druck, volumen und temperatur. *Annalen der Physik und Chemie*, 245(3):337–357, 1880.

[35] M. Coppinger and E. Swain. Numerical analyses and development of an industrial centrifugal compressor inlet guide vane system. *CFD in fluid machinery design*, 1998.

[36] M. Coppinger and E. Swain. Performance prediction of an industrial centrifugal compressor inlet guide vane system. *Journal of the IMechE - Part A: Journal of power and energy*, 214, 2000.

[37] W.G. Cornell. The stalled performance of cascades. In *Proceedings of the second U.S. national congress of applied mechanics*, 1954.

[38] S. Curzons. Private conversation, 2010.

[39] G. Cutts and R. Pilling. Computer users guide for bd29 - ip shaft break synthesis program cug. *Rolls-Royce internal report PTR41849*, 2005.

[40] M.L. Davin. Compressor performance modelling at reverse flow conditions. MSc thesis, Cranfield University, School of Engineering, 2008.

[41] I.J Day. Axial compressor performance during surge. *Journal of Propulsion and Power*, 10(3), 1994.

[42] J.E. Dennis and R.B. Schnabel. *Numerical methods for unconstrained optimisation and nonlinear equations.* Prentice Hall, 1983.

[43] J.D. Denton. Some limitations of turbomachinery CFD. In *ASME Turbo Expo 2010*, number GT2010-22540, 2010.

[44] M. D'Erasmo. Numerical/CFD analysis of turbine NGVs at high incidence. MSc thesis, Cranfield University, School of Engineering, 2009.

[45] A. Despierre. Gas turbine combustor design using genetic algorithms. MSc thesis, Cranfield University, School of Engineering, 1996.

[46] A. Despierre, P.J. Stuttaford, and P.A. Rubini. Preliminary gas turbine cobustor design using a genetic algorithm. *ASME paper*, (97-GT-72), 1997.

[47] C. Dietirici. *Ann. Phys.*, 69:685, 1899.

[48] J. Dunham. Cfd validation for propulsion system components. *AGARD Advisory Report*, (355), 1998.

[49] J.C. Dutton and R.E. Coverdill. Experiments to study the gaseous discharge and filling of vessels. *International Journal of Engineering Ed*, 13(2):123–134, 1997.

[50] R. Duvigneau and M. Visonneau. Single and multiobjective optimisation for high fidelity cfd using genetic algorithms. In *Evolutionary methods for design optimisation and control, 19-21 September, Athens, Greece*, 2001.

[51] M.M. Felling, R.H. Page, H.H. Korst, and R.A. White. An experimental analysis and demonstration of the non-steady flow in a shock tube. *Journal of Engineering Ed.*, 14(1):59–66, 1998.

[52] R. Fletcher. *Practical methods of optimisation.* Wiley, 1987.

[53] J. Fritz. *Partial differential equations.* Springer, 4^{th} edition, 1991.

[54] A. Gaiddon and D.D. Knight. Multicriteria design optimization of integrated three-dimensional supersonic inlets. *Journal of Engineering for Power*, 19:456–463, 2003.

[55] L. Gallar, M. Arias, V. Pachidis, and P. Pilidis. Compressor variable geometry schedule optimisation using genetic algorithms. In *ASME Turbo Expo 2009*, number GT2009-60049, 2009.

[56] L. Gallar, M. Arias, V Pachidis, and R. Singh. Stochastic axial compressor variable geometry schedule optimisation. *Journal of Aerospace Science and Technology*, 2010. accepted for publication on the 24^{th} of August 2010.

[57] L. Gallar, C. Calcagni, V. Pachidis, and P. Pilidis. Development of a one-dimensional dynamic gas turbine secondary air system model part i: Tool components development and validation. In *ASME Turbo Expo 2009*, number GT2009-60058, 2009.

[58] L. Gallar, M. D'Erasmo, V. Pachidis, and R. Singh. CFD assissted design of a nozzle guide vane cascade rig for high negative incidence angle. In 4^{th} *Symposium on integrating CFD and experiments in aerodynamics*, 2009.

[59] L. Gallar, V. Pachidis, and V. Pilidis. Compressor IGV off design performance and loss modelling. In *International Symposium on Air Breathing Engines*, number ISABE 1221, 2009.

[60] L. Gallar, G. Torres, V. Pachidis, and V. Pilidis. 3D CFD analysis of turbine nozzle guide vanes performance at shaft over-speed conditions. In *International Symposium on Air Breathing Engines*, 2011. Accepted for publication in ISABE conference 2011.

[61] L. Gallar, I. Tzagarakis, V. Pachidis, and R. Singh. Compressor performance 2D modelling at reverse flow conditions. In *ASME Turbo Expo 2010*, number GT2010-23428, 2009.

[62] R.N. Gamache. *Axial Compressor Reversed Flow Performance.* PhD thesis, Massachusetts Institute of Technology, 1985.

[63] R.N. Gamache and E.M. Greitzer. Reverse flow in multistage axial compressors. *Journal of Propulsion and Power*, 6(4):461–474, 1990.

[64] B.A. Gardner and M.S. Selig. Airfoil design using a genetic algorithm and an inverse method. *AIAA paper*, (2003-0043), 2003.

[65] T. Ghisu, Parks, G.T. Jarrett, J.P., and P.J. Clarkson. Multi-objective optimization of aero-engine compressors. In *The future of gas turbine technology, 3^{rd} International conference*, 2006.

[66] A. Gill, T.W. von Backstrom, and T.M. Harms. Fundamentals of four-quadrant axial flow compressor maps. *Journal of the IMechE - Part A: Journal of power and energy*, 221:1001–1010, 2007.

[67] F. Glover and M. Laguna. *Tabu Search.* Kluwer Academic Publishers, 1997.

[68] D.E. Goldberg. *Genetic Algorithms in Search, Optimization and Machine Learning.* Addison-Wesley Professional, 1989.

[69] J.P. Gostelow. *Cascade Aerodynamics.* Pergamon Press, 1^{st} edition, 1984.

[70] E.M. Greitzer. Surge and rotating stall in axial flow compressors, part i: Theoretical compression system model. *Journal of Engineering for Power*, 98:190–198, 1976.

[71] E.M. Greitzer and F.K. Moore. A theory of post-stall transients in a axial compressor system. part ii:application. *Journal of Engineering for Gas Turbines*, 108:231–240, 1986.

[72] M. Haake, R. Fiola, and S. Staudacher. Multistage compressor and turbine modeling for the prediction of the maximum turbine speed resulting from shaft breakage. In *ASME Turbo Expo 2009*, number GT2009-59049, 2009.

[73] C. Hah. Large eddy simulation of transonic flow field in NASA rotor 37. *NASA Technical Memorandum*, (215627), 2009.

[74] G. N. Hatsopoulos and J. H. Keenan. *Principles of general thermodynamics.* Wiley, 1965.

[75] C. Hirsch. *Numerical computation of internal and external flows*, volume 2. Wiley, 1990.

[76] C. Hirsch. *Numerical computation of internal and external flows*, volume 1. Elsevier, 2007.

[77] H.P. Hodson and R.G. Dominy. The off-design performance of a low pressure turbine cascade. *Journal of Turbomachinery*, 109:201–209, 1987.

[78] L. Holborn and H. Schultze. Uber die druckwage und die isothermen von luft, argon und helium zwischen 0 und 200c. *Annalen der Physik*, 352(16):1089–1111, 1915.

[79] J.H. Holland. *Adaption in natural and artificial systems.* University of Michigan Press, 1975.

[80] C.W. Hong and Huang G.H. Numerical computation of unsteady gas flow in the ducts of reciprocating engines. *Numerical Heat Transfer - Part A*, 32:769 – 785, 1997.

[81] J. Howard. *Sub-idle modelling of gas turbines; altitude relight and windmilling.* EngD thesis, Cranfield University, School of Engineering, 2007.

[82] J.B. Howley, J.W. Magee, and W.M. Haynes. *Int. J. Thermophys.*, 15(5):801, 1994.

[83] H. Iacovides and I.P. Theofanopoulos. Turbulence modelling of axisymmetric flow inside rotating cavities. *International Journal of Heat and Fluid Flow*, 12:2–11, 1991.

[84] A. Inselberg. The plane with parallel coordinates. *Visual Computer*, 1:1942–1948, 1985.

[85] Janes Information Group. *Jane's aero engines 16*, 1996.

[86] W.P. Jones and B.E. Launder. The calculation of low-reynolds-number phenomena with a two-equation model of turbulence. *International Journal of Heat and Mass Transfer*, 16:1119–1130, 1973.

[87] H.D. Joslyn and R.P. Dring. Negative incidence flow over a turbine rotor blade. *Journal of the ASME*, (83-GT-23), 1983.

[88] M. Katsourou. Implementation of accurate gas properties on gas turbine simulations. MSc thesis, Cranfield University, School of Engineering, 2005.

[89] J. Kaye and E.C. Elgar. Modes of adiabatic and diabatic fluid flow in an annulus with an inner rotating cylinder. *Transactions of the ASME*, 80:753–765, 1958.

[90] J. Kennedy and R. Eberhart. Particle swarm optimization. *Proceedings of the IEEE Int. Conf. on Neural Networks*, pages 1942–1948, 1995.

[91] A. Keskin and D. Bestle. Application of multi-objective optimization to axial compressor preliminary design. *Journal of Aerospace Science and Technology*, 10:581–589, 2006.

[92] T. Kipouros, D.M. Jaeggi, W. Dawes, G.T. Parks, and M. Savill. Multi-objective design optimisation for axial compressors. In *3rd Seminar in aerodynamic design optimisation (AOS 2005)*. Rolls-Royce plc., 2005.

[93] T. Kipouros, M. Mleczko, and M. Savill. Use of parallel coordinates for post analyses of multi-objective aerodynamic design optimisation in turbomachinery. In *49th AIAA/ASME/AHS/ASC Structures, Structural Dynamics and Materials conference, AIAA 2008-2138*, 2008.

[94] S. Kirkpatrick, C.D. Gelatt, and M.P. Vecchi. Optimization by simulated annealing. *Science*, 220(4598):671–680, 1983.

[95] S.J. Kline and F.O. Koenig. The state principle - some general aspects of the relationships among the properties of systems and discussion. *Journal of Applied Mechanics*, pages 29–34, 1957.

[96] S.G. Koff. Stalled flow characteristics for axial compressors. MSc thesis, Massachusetts Institute of Technology, 1983.

[97] S.G. Koff and E.M. Greitzer. Axisymmetrically stalled flow performance for multistage axial compressors. *Journal of Turbomachinery*, 108:216–223, 1986.

[98] W.M. Konig, D.K. Hennecke, and L. Fottner. Improved blade profile loss and deviation angle models for advanced transonic compressor bladings: Part i - a model for subsonic flow. *Journal of Turbomachinery*, 118:73–87, 1996.

[99] A. Kozlov. Experimental investigation of the specific volumes of air in the 20 - 600 °c temperature range and 20 - 700 bar pressure range. *Dissertation for Candidate of Technical Science, Moscow Power Engineering Institute*, 1968.

[100] K.J. Kutz and T.M. Speer. Simulation of the secondary air system of aero engines. *Journal of Turbomachinery*, 116:306–315, 1994.

[101] B. Lakshminarayana. An assessment of computational fluid dynamic techniques in the analysis and design of turbomachinery the 1990 freeman scholar lecture. *Journal of fluids engineering*, 113, 1991.

[102] L.D. Landau and E.M. Lifschitz. *Fluid Mechanics - Course of theoretical physics*, volume 6. Pergamon Press, 2^{nd} ed edition, 1987.

[103] L.S. Langston. Secondary flows in axial turbines - a review. *Annals of the New York Academy of Sciences - Heat transfer in gas turbine systems*, 934:11–26, 2001.

[104] L.S. Langston, M.L. Nice, and R.M. Hooper. Three dimensional flow within a turbine cascade passage. *Journal of Engineering for Power*, 99:21–28, 1977.

[105] B.I. Lee and M.G. Kesler. A generalized thermodynamic correlation based on three-parameter corresponding states. *Journal of the American Institute of Chemical Engineers*, 21(3):510–527, 1975.

[106] E.W. Lemmon, R.T. Jacobsen, S. G. Penoncello, and D.G. Friend. Thermodynamic properties of air and mixtures of nitrogen, argon, and oxygen from 60 to 2000 k at pressures to 2000 mpa. *Journal of Physical and Chemical Reference Data*, 29(3):331–385, 2000.

[107] S. Lieblein. Analysis of experimental low-speed loss and stall characteristics of two-dimensional compressor blade cascades. *NACA Research Memorandum*, E57A28, 1957.

[108] S. Lieblein. Loss and stall analysis of compressor cascades. *Journal of basic engineering*, pages 387–400, 1959.

[109] S. Lieblein and W.H. Roudebush. Theoretical loss relations for lowspeed two-dimensional-cascade flow. *NACA Technical Note*, 3662, 1956.

[110] S. Lieblein, F.C. Schwenk, and R.L. Broderick. Diffusion factor for estimating losses and limiting blade loadings in axial-flow-compressor blade elements. *NACA Research Memorandum*, E53D01, 1953.

[111] M.C. Llorens. Secondary air system dinamics modelling during shaft failure. MSc thesis, Cranfield University, School of Engineering, 2010.

[112] J.P. Longley. Calculating stall and surge transients. In *ASME Turbo Expo 2007*, number GT2007-27378, 2007.

[113] A.L. Lydersen, R.A. Greenkorn, and O.A. Hougen. Generalized thermodynamic properties of pure fluids. *University of Wisconsin, Eng. Expt. Sta. Rept.*, 4, 1955.

[114] F.A. Lyman. On the conservation of rothalpy in turbomachines. *Journal of Turbomachinery*, 115:520–526, 1993.

[115] W.L. Macmillan. *Development of a modular type computer program for the calculation of gas turbine off design performance.* PhD thesis, Cranfield Institute of Technology, College of Aeronautics, 1974.

[116] P. Marchal and C.H. Sieverding. Secondary flows within turbomachinery bladings. *AGARD*, CP-214, 1977.

[117] H. Martin. Labyrinth packings. *Engineering*, 85:35–38, 1908.

[118] H. Martin. Steam leakage in dummies of the ljungstrom type. *Engineering*, 107:1–3, 1919.

[119] P.M. Mathias and T.W. Copeman. Extension of the pzeng-robinson equation of state to complex mixtures: evaluation of the various forms of the local composition concept. *Journal Fluid Phase Equilibria*, 13:91–108, 1983.

[120] D. McGrath. Swirl effects on turbine capacity. MSc thesis, Cranfield University, School of Engineering, 2006.

[121] C.S. McNeil. *Efficient upwind algorithms for solution of the Euler and Navier-Stokes equations.* PhD thesis, Cranfield University, 1995.

[122] F. R. Menter. Zonal two equation $k-\omega$ turbulence models for aerodynamic flows. *AIAA Paper*, (93-2906), 1993.

[123] F. R. Menter. Two-equation eddy-viscosity turbulence models for engineering applications. *AIAA Journal*, 32:269–289, 1994.

[124] N.M. Merriman. *Simulation of aero engine pre and post - stall transient behaviour.* PhD thesis, Cranfield University, School of Engineering, 1994.

[125] J. Meseguer and A. Sanz Andrés. *Aerodinámica básica.* Publicaciones de la E.T.S.I. Aeronáuticos, 1^{st} edition, 2005.

[126] A. Michels, T. Wassenaar, J. M. H. Levelt, and W. de Graaf. *Appl. Sci. Res.*, 4:381, 1954.

[127] A. Michels, T. Wassenaar, J.M.H. Levelt, and W. de Graaf. *Appl. Sci. Res.*, 4:381, 1954.

[128] D.C. Miller and D.L. Wasdell. Off-design prediction of compressor blade losses. *IMechE.*

[129] M. Mohseni. *Compressor rotating stall and surge modelling.* Phd first year review report, Cranfield University, School of Engineering, 2009.

[130] J. Moore, J.G. Moore, and P.H. Timmis. Performance evaluation of centrifugal compressor impellers using three-dimensional viscous flow calculations. *Journal of Engineering for Gas Turbines*, 106:475–481, 1984.

[131] A.P. Morse. Numerical prediction of turbulent flow in rotating cavities. *Journal of Turbomachinery*, 110:202–215, 1988.

[132] H.L. Moses and S.B. Thomason. Axisymmetrically stalled flow performance for multistage axial compressors. *Journal of Turbomachinery*, 108(2), 1986.

[133] Y. Muller. Secondary air system model for integrated thermomechanical analysis of a jet engine. In *ASME Turbo Expo 2008*, number GT2008-50078, 2008.

[134] S. Obayashi, T. Tsukahara, and T. Nakamura. Cascade airfoil design by multiobjective genetic algorithms. *Genetic algorithms in engineering systems: innovations and applications*, (446), 2003.

[135] C.L. Ong and J.M. Owen. Boundary layer flows in rotating cavities. *Journal of Turbomachinery*, 111:341–348, 1989.

[136] C.L. Ong and J.M. Owen. Prediction of heat transfer in a rotating cavity with a radial outflow. *Journal of Turbomachinery*, 113:115–122, 1991.

[137] CFD Online. *Online forum for computational fluid dynamics.* www.cfd-online.com, Accessed in March 2008.

[138] J.M. Owen and J.R. Pincombe. Velocity measurements inside a rotating cylindrical cavity with a radial outflow of fluid. *Journal of Fluid Mechanics*, 99:111–127, 1980.

[139] J.R. Palmer. The “turbocode” scheme for the programming of thermodynamic cycle calculations on an electronic digital computer. Technical Report Report Aero 203, Cranfield Institute of Technology, College of Aeronautics, 1968.

[140] M.D. Panasiti, E.W. Lemmon, S.G. Penoncello, R.T. Jacobsen, and D.G. Friend. Thermodynamic properties of air from 60 to 2000 k at pressures to 2000 mpa. *International Journal of Thermophysics*, 20(1):218–228, 1999.

[141] N.C. Patel and A.S. Teja. A new cubic equation of state for fluids and fluid mixtures. *Journal of Chemical Engineering Science*, 37(3):463–473, 1982.

[142] D.Y. Peng and D.B. Robinson. A new two-constant equation of state. *Journal of Industrial and Engineering Chemistry Fundamentals*, 15:58–64, 1976.

[143] F.M. Penning. Communs. phys. lab. Technical Report 166, Univ. Leiden, 1923.

[144] K. Pitzer. The volumetric and thermodynamic properties of fluids. i. theoretical basis and virial coefficients. *Journal of the American Chemical Society*, 77:3427–3433, 1955.

[145] D. Pollard and J. Gostelow. Some experiments at low speed on compressor cascades. *Journal of Engineering for Power*, 89(3):427–436, 1967.

[146] A. Psarra. *Friction and wear modelling of turbines in contact.* PhD thesis, Cranfield University, School of Engineering, 2011.

[147] A. Psarra, V. Pachidis, and P. Pilidis. Finite element turbine blade tangling modelling following a shaft failure. In *ASME Turbo Expo 2009*, number GT2009-60144, 2009.

[148] R.M. Raley. Blading of axial flow compressors. *Rolls-Royce internal note RCR 90054*, 1966.

[149] N.B. Rao and N. Sidheswar. Influence of straight-through type of labyrinth gland parameters on the amount of air leakage. *India Engineering Journal-ME*, 56:176–181, 1976.

[150] S.S. Rao. *Engineering optimisation:theory and practice.* Wiley, 1996.

[151] D.P. Raymer. *Aircraft design: a conceptual approach.* AIAA Education series, 3^{rd} edition, 1999.

[152] O. Redlich and J.N.S. Kwong. On the thermodynamics of solutions. v. an equation of state. fugacities of gaseous solutions. *Journal of Chemical Reviews*, 44(1):233–244, 1949.

[153] L. Reid and R.D. Moore. Performance of single-stage axial- flow transonic compressor with rotor and stator aspect ratios of 1.19 and 1.26, respectively, and with design pressure ratio of 1.82. *NASA Technical Paper*, (1338), 1978.

[154] P.L. Roe. Approximate riemann solvers, parameter vectors and difference schemes. *Journal of Computational Physics*, 43:357–372, 1981.

[155] I.A. Rogovaya and M.G. Kaganer. *Russ. J. Phys. Chem.*, 34(9):917, 1960.

[156] H. Romberg. *VDI-Forsch-Verlag*, 543, 1971.

[157] S. Rousselot, D. Truffi, G. Doulgeris, S. Mistry, V. Pachidis, and P. Pilidis. Generation of a quasi 3-d map of a half-embedded ultra high bypass ratio turbofan intake on the wing of a broad delta wing airframe. In *ASME Turbo Expo 2008*, number GT2008-51008, 2008.

[158] A.L. Rowe. Shaft failure review - large fan engines. *Rolls-Royce internal report PTR90865*, 2003.

[159] A.L. Rowe. Private conversation, 2010.

[160] M. Salussolia. Thermodynamic gas model effect on gas turbine component and engine performance prediction. MSc thesis, Cranfield University, School of Engineering, 2010.

[161] T. Scanlon. Private conversation, 2010.

[162] H.D. Schulz and H.D. Gallus. Experimental investigation of the three dimensional flow in an annular compressor cascade. *Journal of Turbomachinery*, 110:467–478, 1988.

[163] S. Serrajotto. Swirl effects on turbine capacity, a CFD and experimental study. MSc thesis, Cranfield University, School of Engineering, 2005.

[164] K.K. Shah and G. Thodos. A comparison of equations of state. *Journal of Chemical Physics*, 57(3):30–37, 1965.

[165] G. Soave. Equilibrium constants from a modified redlich-kwong equation of state. *Journal of Chemical Engineering Science*, 27:11971203, 1972.

[166] C. Soria. Compressor VIGV and VSV schedule optimisation. MSc thesis, Cranfield University, School of Engineering, 2010.

[167] R. Stryjek and J.H. Vera. An improved peng-robinson equation of state for pure compounds and mixtures. *The Canadian Journal of Chemical Engineering*, 64:323–333, 1986.

[168] K.L. Suder. Experimental investigation of the flow field in a transonic, an axial flow compressor with respect to the development of blockage and loss. *NASA Technical Memorandum*, (107310), 1996.

[169] Q. Sun and I.D. Boyd. Flat-plate aerodynamics at very low reynolds number. *Journal of fluid mechanics*, 502:199–206, 2004.

[170] W.C. Swan. A practical method of predicting transonic-compressor performance. *Journal of Engineering for Power*, 83:322–330, 1958.

[171] M. Taylor. HP axial flow turbine aerodynamic design. In *Advances in turbomachinery aero-thermo-mechanical design analysis HP axial flow turbine aerodynamic design*, 2006. VKI Lecture series.

[172] J.F. Thompson, Z.U.A. Warsi, and C.W. Mastin. *Numerical grid generation.* Elsevier Science Publishers, 1985.

[173] G. Thorncroft, Patton J.S., and R. Gordon. Modelling compressible air flow in a charging or discharging vessel and assessment of polytropic exponent. In *AC 2007-2695, ASEE Annual Conference & Exposition*, 2007.

[174] D.L. Tipton, T.E. Scott, and R.E. Vogel. Labyrinth seal analysis. volume iii analytical and experimental development of a design model for labyrinth seals. *AF Wright Aeronautical Laboratories*, TR-85-2103 Volume III, 1986.

[175] E.F. Toro. *Riemann solvers and numerical methods for fluid dynamics.* Springer, 1999.

[176] G. Torres. 3D CFD analysis of turbine NGV at high negative incidence. MSc thesis, Cranfield University, School of Engineering, 2008.

[177] A.L. Treaster and A.M. Yocum. The calibration and application of five hole probes. *Technical Memorandum of the Institute for Science and Engineering of the Pennsylvania State University*, TM 78-10:54, 1978.

[178] K. Trutnovsky and K. Kotomori. *Berhrungsfreie dichtungen.* VDI Verlag, 1981.

[179] R.C. Turner and D.W. Sparkes. Complete characteristics for a single-stage axial flow fan. In *Thermodynamics and Fluid Mechanics Convention*, 1964.

[180] I. Tzagarakis. Compressor performance modelling at reverse flow conditions. MSc thesis, Cranfield University, School of Engineering, 2009.

[181] J.D. van der Waals. *On the continuity of the gaseous and liquid states.* PhD thesis, University of Leiden, 1873.

[182] A. Vasserman, E.A. Golovskii, E.P. Mitsevich, and V. A. Tsymarnyi. Measurement of the density of air at temperatures of 78 to 190 k up to pressures of 600 bars. *VINITI Deposition, Odessa Institute of Marine Engineering*, 2953:381, 1976.

[183] G. Vermes. A fluid mechanics approach to labyrinth seal leakage problem. *Transactions of the ASME of basic engineering*, 83:161–169, 1961.

[184] V. Volpe. Thermodynamic gas model effect on gas turbine component and engine performance prediction. MSc thesis, Cranfield University, School of Engineering, 2008.

[185] P.P. Walsh and P. Fletcher. *Gas turbine performance.* Blackwell Publishing, 2^{nd} edition, 1996.

[186] H.P. Wang, S.J. Olson, R.J. Goldstein, and E.R.G. Eckert. Flow visualisation in a linear cascade of high performance turbine blades. *Journal of Turbomachinery*, 119:1–8, 1997.

[187] K. Wark. *Thermodynamics.* McGraw-Hill, New York, 1988.

[188] M.W. Whellens, R. Singh, and P. Pilidis. Genetic algorithm based optimisation of intercooled recuperated turbofan design. *AIAA paper*, (2003-1210), 2003.

[189] D.C. Wilcox. Re-assessment of the scale-determining equation for advanced turbulence models. *AIAA Journal*, 26:1414.

[190] A.G. Wilson. *Stall and surge in axial flow compressors.* PhD thesis, Cranfield University, School of Engineering, 1994.

[191] A.G. Wilson and C. Freeman. Stall inception and development in an axial flow aeroengine. *ASME Journal of Turbomachinery*, 116(2):217–225, 1994.

[192] P. Wright. Private conversation, 2010.

[193] P.I. Wright and D.C. Miller. An improved compressor performance prediction model. *ImechE*, (C423/028), 1991.

[194] A. Yamamoto. Review: Mechanism of secondary flows and losses within turbine blade rows. *Journal of Turbomachinery*, 14:234–241, 1986.

[195] A. Yamamoto. Production and development of secondary flows and losses in two types of straight turbine cascades:part 1 - a stator case. *Journal of Turbomachinery*, 109(2):186–194, 1987.

[196] A. Yamamoto. Production and development of secondary flows and losses in two types of straight turbine cascades:part 2 - a rotor case. *Journal of Turbomachinery*, 109(2):194200, 1987.

[197] A. Yamamoto. Interaction mechanisms between tip leakage flow and the passage vortex in a linear turbine rotor cascade. *Journal of Turbomachinery*, 110(3):329–339, 1988.

[198] A. Yamamoto. Endwall flow/loss mechanisms in a linear turbine cascade with blade tip clearance. *Journal of Turbomachinery*, 111(3):264–266, 1989.

[199] A. Yamamoto and H. Nouse. Effects of incidence on three-dimensional flows in a linear turbine cascade. *Journal of Turbomachinery*, 110(4):486–497, 1988.

[200] D.J. Ye, W.D. Liu, and L.W. Zhou. An experimental study on separated flow of large negative incidence in 2-d turbine cascade. In *Tokyo International Gas Turbine Congress and Exhibition*, number IGTC-15, 1987.

[201] P. Zachos, F. Pengue, V. P., Pachidis, and P. Pilidis. Flowfield investigation of a compressor cascade at high incidence - part II: Numerical analysis. In *ASME Turbo Expo 2009*, number GT 2009-59908, 2009.

[202] H. Zimmermann and K.H. Wolff. Comparison between empirical and numerical labyrinth flow calculations. *ASME paper*, (87-GT-86), 1987.